JYU DISSERTATIONS 215

Souvik Agasti

Theoretical and Numerical Studies of the Dynamics of Open Quantum Systems

UNIVERSITY OF JYVÄSKYLÄ
FACULTY OF MATHEMATICS
AND SCIENCE

JYU DISSERTATIONS 215

Souvik Agasti

Theoretical and Numerical Studies of the Dynamics of Open Quantum Systems

Esitetään Jyväskylän yliopiston matemaattis-luonnontieteellisen tiedekunnan suostumuksella
julkisesti tarkastettavaksi toukokuun 7. päivänä 2020 kello 12.

Academic dissertation to be publicly discussed, by permission of
the Faculty of Mathematics and Science of the University of Jyväskylä,
on May 7, 2020 at 12 o'clock noon.

JYVÄSKYLÄN YLIOPISTO
UNIVERSITY OF JYVÄSKYLÄ

JYVÄSKYLÄ 2020

Editors
Timo Sajavaara
Department of Physics, University of Jyväskylä
Ville Korkiakangas
Open Science Centre, University of Jyväskylä

Permanent link to this publication: http://urn.fi/URN:ISBN:978-951-39-8149-5

ISBN 978-951-39-8149-5 (PDF)
URN:ISBN:978-951-39-8149-5
ISSN 2489-9003

Preface

This work has been carried out at the Nanoscience Center in the Department of Physics at the University of Jyväskylä. The research work was supported by the Academy of Finland (contract no. 275245).

I would like to express my gratitude to Dr. Pekka Koskinen and Dr. Juha Merikoski for their support while writing and defending the thesis. I am also thankful to Dr. Muhammad Asjad, Dr. Subrata Chakraborty and Dr. Philippe Djorwé for their technical advice while working on this project. Further, I would like to thank my family and friends for their moral support.

Jyväskylä, May 2020

Souvik Agasti

Abstract

Open quantum systems have drawn attention over decades due to its applicability in the foundation of theoretical physics, e.g. statistical mechanics, quantum mechanics and condensed matter physics. The dynamics of open quantum systems has been described as separate entities from their surrounding environment that consists of a very large number of modes, somehow coupled to the mode of the system. Even though the exact solution of the dynamical behavior of the system is impossible to calculate, we obtain a tentative solution using the crucial Markov approximation. The input-output formalism of the quantum Langevin equation (QLE) has been considered as a useful tool which provides a semi-classical description of the dynamics of the system, whereas the master equation provides a complete picture of the dynamics of the system expressed in terms of density matrix. While studying the dynamics of nonlinear system/environment coupling using QLE, we see, for a small value of external field, that the steady state system field does not change much from the steady state field obtained in the absence of nonlinear dissipation. However, in a case where a stronger external field is applied, we see that the deviation becomes substantial from the solution of linear system. We also see that the nonlinear coupling introduces significant difference in the cavity fluctuation spectrum. The description, therefore, provides a potential explanation of parametric effects in terms of nonlinear dissipation phenomena associated with the nonlinear coupling.

Even though the theories developed in the context of open quantum systems have proven to be powerful tools, they do not provide a satisfactory platform to be implemented on non-linear Hamiltonians. We often approximate it by linearizing over nonlinear steady state field amplitude, and therefore, the interesting effects are often overlooked. The limitation of the analytics provokes us to simulate open quantum dynamics numerically. The numerical method consists of transformation of the environmental degrees of freedom to a one-dimensional many-body chain, and the computational technique includes numerical diagonalization and renormalization process.

The time-adaptive density matrix renormalisation group (t-DMRG) is known as one of the most powerful techniques for the simulation of strongly-correlated many-body quantum systems. In this thesis, along with the theoretical modeling, we implement DMRG numerical scheme for the simulation of canonical S/B model by mapping it to one-dimensional harmonic chain with nearest neighbor interactions, and use the method to investigate the dynamics of the free dissipative system. The thermalization of open quantum systems is also studied by generating minimally entangled typical thermal states (METTS) through imaginary time evolution, and real-time evolving an empty system in the presence of the thermal bath. Further, we simulate coherently driven free dissipative Kerr nonlinear system numerically using Euler's method by solving Heisenberg equation of motion and t-DMRG algorithm, and demonstrate how the numerical results are analogous to classical bistability. By comparing with analytics, we see that the DMRG numerics is analogous to the quantum-mechanical

exact solution obtained by mapping the equation of motion of the density matrix of the system to a Fokker-Plank equation. The comparison between two different numerical techniques shows that the semi-classical Euler's method determines the dynamics of the system field of one among two coherent branches, whereas DMRG numerics gives the superposition of both of them. Hence, DMRG-determined time dynamics undergoes generating non-classical states. Our approach of dealing with nonlinearity represents an important contribution in the developments of technique to study the dynamical and steady-state behavior of open quantum systems, which is a fundamental aspect of quantum physics.

Author's address Souvik Agasti
Department of Physics
University of Jyväskylä
Finland

Supervisors Senior Lecturer Pekka Koskinen
Department of Physics
University of Jyväskylä
Finland

Reviewers University Researcher Jyrki Piilo
Department of Physics and Astronomy
University of Turku
Finland

Senior University Lecturer Sorin Paraoanu
Department of Applied Physics
Aalto University
Finland

Opponent Associate Professor André Xuereb
Department of Physics
University of Malta
Malta

List of Publications

I J. Manninen, S. Agasti, and F. Massel, *Nonlinear quantum Langevin equations for bosonic modes in solid-state systems*; Phys. Rev. A **96**, 063830 (2017)

II Souvik Agasti; *Numerical simulation of Kerr nonlinear systems; analyzing non-classical dynamics*; J. Phys. Commun. **3**, 105004 (2019)

III Souvik Agasti; *Simulation of Matrix Product States For Dissipation and Thermalization Dynamics of Open Quantum Systems*; J. Phys. Commun. **4**, 015002 (2020)

IV Souvik Agasti; *Numerical Simulation of Free Dissipative Open Quantum System and Establishment of a Formula for* π; accepted to be published in AIP Conf. Proceedings.

The author has contributed to the theoretical calculations of the article **I**, and has investigated and written articles **II, III, IV** single-handedly.

Contents

1 Introduction

1.1 Brief Overview of Open Quantum Systems

An open quantum system is obtained by separating certain degrees of freedom from their surrounding environment. The theory of open quantum systems has been formulated in terms of well-established master equation, where the time evolution of the reduced density matrix is expressed by a first-order differential equation. The generator of this master equation has a very specific mathematical and physical structure, known as Lindblad structure which was proposed by Gorini, Kossakowski, and Sudarshan in 1976 [1], and independently by Lindblad in 1976 [2]. Considering a microscopic system-environment approach, the derivation of the master equation is done with the help of the Born-Markov approximation. The Markov process was first proposed by the Russian mathematician Andrey Markov in 1954 [3]. The process assumes that the future state of a stochastic process is dependent only on the present state, not on the sequence of past events, and therefore, assumes time locality by neglecting the past history of the system. The master equation approach is analogous to the Fokker-Plank equation for the Brownian motion in case of a classical system. In statistical mechanics, the Fokker-Planck equation is defined by a partial differential equation for the probability density function of the velocity of a particle under the influence random driving force. The equation was proposed first by Adriaan Fokker (1914) [4] and Max Planck (1917) [5], and it is also known as the Kolmogorov forward equation, after the independent discovery by Andrey Kolmogorov in 1931 [6]. The quantum-mechanical counterpart of the Fokker-Planck equation has been derived consistently by Bogoliubov and Krylov (1939) [7], and it is applicable for any microscopic system. The dissipative dynamics of the macroscopic variable of the system and the noise interference due to the coupling to the environment have been described by the input-output formalism of quantum Langevin equations (QLEs) [8, 9], which was derived using Heisenberg's equation of motion introduced in 1925 [10]. The QLE is an extension of the classical Langevin equation to the quantum regime [11]. The traditional classical Langevin equation was first introduced by Paul Langevin in 1908 [12]. It is a stochastic differential equation describing the time evolution of macroscopic variables of the system. The connection between the QLE and the stochastic differential quantum master equation have been established by Gardiner and Collett (1985) [13]. The description of the generalized QLE is given by Ford, Lewis and O'connell (1988) [14]. There the system suffers Markovian/non-Markovian random force due to the coupling

to an arbitrary heat bath, and therefore, it provides a complete macroscopic quantum description.

The techniques developed in the context of open quantum systems have remained useful in the establishment of the theory of quantum optics [8, 9], quantum statistical mechanics [15, 16], quantum information science [17, 18] and quantum cosmology [19, 20]. For instance, in the case of quantum information science, the theory has proven a powerful tool to study the interference in entanglement assisted quantum data processing [21, 22], information transmission, and quantum communication [23]. Besides, the theory of stochasticity in cosmological perturbations is formulated by using quantum master equation [19, 20, 24, 25], which has opened a window to study cosmological inflation [26–29] and the dynamics of black holes [30, 31].

Within this framework, nonlinear coupling between the system and environment has also been employed widely to model ultracold atomic systems [32–34], laser cooled trapped ion systems [35–37], and to study light matter interaction, especially in micro/nanomechanical or optomechanical systems [38, 39]. Further, strong coupling of mechanical motion to individual spin qubit [40, 41] and collective atomic spins [42–44] have drawn attention for having applications in spin control [45] and detection of mechanical motion [46–49].

For all nonlinear Hamiltonians discussed above, the theory of open quantum systems has been implemented with a linearized approximation. However, even though the model is simple, the method is not satisfactory to determine the exact dynamical behavior. We often overlook interesting effects when we cannot treat system/bath (S/B) interaction in a perturbative manner. Apart from the nonlinear S/B coupling, also, this analytical model exhibits limitation while determining the exact non-Markovian dynamics. The limitation of analytical methods provoke us for the numerical simulation of the time evolution, which is the main motivation of this work.

1.2 Quantum Simulation of 1D Lattice Systems

Over the years, many numerical techniques have been developed to simulate many-body quantum systems. For example, Monte Carlo method has remained popular to study the dynamical behavior and phase transition problems of Ising chain [50], Hubbard [51] and Bose-Hubbard model [52, 53]. The time-adaptive density matrix renormalisation group (t-DMRG) is known as one of the strongest techniques to investigate strongly-correlated many-body quantum system. The technique has often been used for some well-known models, e.g. Ising model [54, 55], Bose-Hubbard model [34, 52, 56] and Hubbard model [51, 57, 58], especially aiming to investigate quenching dynamics, magnetization, and properties associated with phase transitions. However,

in this thesis, we use the numerical scheme to simulate the dynamics of open quantum systems.

The DMRG technique was introduced first by S. R. White in 1992 [59] to determine the ground state of a many body system. Afterwards, a slightly different method has been attempted for the simulations at finite temperature, which is the purification of the density matrix, used successfully to study finite-temperature properties of quantum spin chains [60]. However, this simulation is often limited due to a subsequent growth of entanglement and the computational cost associated with it. In order to get rid of those problems, a complementary approach was introduced by S. R. White, where one generates a large number of sample pure states through imaginary time evolution, and calculates observables by taking average over them; this ensemble altogether generates an impact of a thermal state. This is *typically* known as minimally entangled typical thermal states (METTS) [61]. In this thesis, we use the algorithm for the first time for the generation of thermal bath and parameterize it to investigate their consequences in the determination of the thermalization of open quantum system.

Even though several attempts have been taken to generalize the DMRG technique to be used for time dependent calculations, the major step forward was taken by Vidal in 2003 [62] with certain crucial optimization and modification. The method makes the state able to be represented with a sufficiently small number of retained basis set which is referred to as "slightly entangled". The details of the modification of the algorithm will be explained in section 4.1. The method is known as time-evolving block decimation algorithm (TEBD) and we use the algorithm here to simulate the time dynamics of open quantum systems.

2 Theoretical Methods

The theory of open quantum systems has been formulated in terms of master equation, expressed in Lindblad form where the time evolution of the reduced density matrix is expressed by a first order differential equation. In this section, we establish a theoretical framework and discuss how to study the dynamical behavior of open quantum systems.

2.1 Theoretical Methods for Open Quantum Systems

We introduce a simple model of open quantum system and discuss the theoretical techniques to study its dynamics. We start by approaching master equation technique to determine the time evolution of the reduced density matrix in the interaction picture. After that, we derive quantum Langevin equation in the Heisenberg picture, which gives the equation of motion of the system field operator.

The following section is arranged by starting with the investigation of the behavior of the time evolution of a part of a bipartite quantum system without having full knowledge of the rest of others. Hereafter, we study the time dynamics of the density matrix of an individual system with the help of the master equation expressed in the Lindblad form. This is followed by establishing the quantum Langevin equation which gives the equation of motion of a system operator, and compare the two methods.

2.1.1 Evolution of the Reduced Density Operator

The time evolution of any system is represented by a map which connects the time evolved density matrix to the initial one $\rho_S(t) = \mathcal{M}\rho_S(0)$. The operator $\mathcal{M}$ is known as a superoperator which has the following properties: Linear, Trace preserving, Hermiticity preserving, and Positive (Completely positive) [63]. The time dynamics of the density matrix of the system (ρ_S) can also be expressed in terms of a first-order differential equation: $\dot{\rho}_S(t) = \hat{\mathcal{L}}\rho_S(t)$ where $\hat{\mathcal{L}}$ is a time-independent linear superoperator. The formulation satisfies both the linearity and the absence of memory preservity

condition of the system. The time evolved density matrix at time t can be deduced as

$$\rho_S(t) = e^{\hat{\mathcal{L}}t}\rho_S(0). \tag{2.1}$$

The entire system and the environment undergo a unitary time evolution, which can be mapped, ideally, as

$$\rho(t) = \mathcal{M}\rho(0) = \mathcal{U}_{SE}(t)\rho(0)\mathcal{U}_{SE}^{\dagger}(t)$$
$$\mathcal{U}_{SE}^{\dagger}\mathcal{U}_{SE} = 1,$$

where ρ is the density matrix of the combination of the system and environment and $\mathcal{U}_{SE}$ is the unitary time evolution operator. Since our interest is the time evolution of the system alone, we trace out the environmental part of the total density matrix to deal with the reduced density matrix of the system, which leads to see non-unitarity in the time-evolution of an individual system. We assume that the system and the environment are not entangled initially at time $t = 0$, meaning that the state of the whole system can be factorized, i.e. written as a tensor product of the state of the system and the environment. Therefore, the total density matrix can also be written as a product of the density matrices of the system and the environment, which we denote by saying $\rho(0) = \rho_S(0)\otimes\rho_E(0)$, where ρ_E are the density operators of the environment. After taking trace over the environment in order to determine the density matrix of the system, we obtain

$$\begin{aligned}\rho_S(t) &= \mathrm{Tr}_E\{\rho(t)\} = \mathrm{Tr}_E\{U_{SE}(t)\rho_S(0)\otimes|\psi_E(0)\rangle\langle\psi_E(0)|U_{SE}^{\dagger}(t)\} \\ &= \sum_{\mu}\langle\mu_E|U_{SE}(t)|\psi_E(0)\rangle\rho_S(0)\langle\psi_E(0)|U_{SE}^{\dagger}(t)|\mu_E\rangle,\end{aligned} \tag{2.2}$$

where $|\mu_E\rangle$ is the basis vector of the environment. Hereafter, we introduce a time-evolution operator for the system for each basis of the environment, named as Kraus operator [64]

$$\hat{M}_{\mu}(t) = \langle\mu_E|U_{SE}(t)|\psi_E(0)\rangle. \tag{2.3}$$

The Kraus operator is constructed by tracing out over the environmental degrees of freedom and therefore, leaving it as an operator of the system. The time evolution of ρ_S can be written using the Kraus representation as

$$\rho_S(t) = \sum_{\mu}\hat{M}_{\mu}(t)\rho_S(0)\hat{M}_{\mu}^{\dagger}(t). \tag{2.4}$$

It is worth noting that from the unitarity of the evolution operator $U_{SE}(t)$ one can see that

$$\sum_{\mu}\hat{M}_{\mu}^{\dagger}\hat{M}_{\mu} = \hat{1}_S. \tag{2.5}$$

One can establish the link between linear superoperator and the Kraus operator as

$$\mathcal{M}\rho_S = e^{\hat{\mathcal{L}}t}\rho_S = \sum_{\mu} \hat{M}_\mu(t)\rho_S \hat{M}_\mu^\dagger(t). \tag{2.6}$$

The state of the individual system evolves from pure to mixed through a non unitary time-evolution known as decoherence. Typically, the mixed state is a statistical ensemble of pure states which cannot be represented by a ket vector. Hence, unlike the pure state, the trace of the square of the density matrix of a mixed state always gives less than 1, even though the trace is always 1. The time evolution of the subsystem is considered to be a random process, which is treated by stochastic calculus. We determine the time evolution of the reduced density matrix in the following section.

2.1.2 Master Equation

The time evolution of the probability of a system occupying a certain state which is described by a set of first order differential equations, known as a classical master equation. The time variable is continuous here, and the rate of change of probability is expressed by a transition rate matrix, which is given by

$$\frac{dP_n}{dt} = \sum_{m>n} \left(A_m^n + B_m^n \bar{r}\right) P_m + \sum_{m<n} B_m^n \bar{r} P_m - \sum_{m<n} \left(A_n^m + B_n^m \bar{r}\right) P_n - \sum_{m>n} B_n^m \bar{r} P_n, \tag{2.7}$$

where P_n is the probability of occupying n^{th} state, A and B are the matrix of coefficients of spontaneous transition and stimulated transition respectively, and $\bar{r}$ is the energy density. It is often called the Pauli master equation, after being introduced by Pauli [65]. The quantum master equation extends to a quantum context of the classical master equation, where the dynamics of the full density matrix is taken for time-homogeneous and Markovian time evolution rather than considering just a set of probabilities.

In order to derive the quantum master equation, we start with the total Hamiltonian which is essentially given by

$$H = H_S + H_E + H_{int}, \tag{2.8}$$

where H_S, H_E, H_{int} are the system, bath and interaction Hamiltonians, respectively. Usually, the quantum master equation is derived in interaction picture and for that we express the interaction Hamiltonian as

$$H_{int}^{[new]} = e^{i(H_S+H_E)t} H_{int}^{[old]} e^{-i(H_S+H_E)t}. \tag{2.9}$$

The transformation of the Hamiltonian modifies the equation of motion of the total density matrix as $\dot{\rho}(t) = -i[H_{int}, \rho(t)]$, which simplifies to

$$\rho(t) = \rho(0) - i\int_0^t \mathrm{d}t'[H_{int}(t'), \rho(t')]. \tag{2.10}$$

Now, we replace the expression of the density matrix and iterate couple of times. The week perturbation allows us to neglect higher order integrals. Essentially, we get

$$\begin{aligned}\rho(t) =&\rho(0) - i\int_0^t \mathrm{d}t'[H_{int}(t'), \rho(0)] - \Bigg[\int_0^t \mathrm{d}t' \int_0^{t'} \mathrm{d}t''\Big(H_{int}(t')H_{int}(t'')\rho(0)\\ &+ \rho(0)H_{int}(t'')H_{int}(t') - H_{int}(t')\rho(0)H_{int}(t'') - H_{int}(t'')\rho(0)H_{int}(t')\Big)\Bigg]\\ =&\rho(0) - i\int_0^t \mathrm{d}t'[H_{int}(t'), \rho(0)] - \frac{1}{2}\mathbf{T}\Big[(\int_0^t \mathrm{d}t' H_{int}(t'))^2\rho(0)\\ &+ \rho(0)(\int_0^t \mathrm{d}t' H_{int}(t'))^2 - 2(\int_0^t \mathrm{d}t' H_{int}(t'))\rho(0)(\int_0^t \mathrm{d}t' H_{int}(t'))\Big],\end{aligned} \tag{2.11}$$

where $\mathbf{T}$ refers time ordering of the operators. By taking the partial trace over environmental degrees of freedom we obtain

$$\rho_S(\mathrm{d}t) = \rho_S(0) + [L, \rho_S(0)]\mathrm{d}B_t - \frac{1}{2}\left[\left(LL^\dagger\rho_S(0) + \rho_S(0)LL^\dagger - 2L\rho_S(0)L^\dagger\right)\mathrm{d}t\right], \tag{2.12}$$

which is the *master equation* expressed in the interaction picture in Lindblad form, where

$$L\mathrm{d}B_t = -i\mathrm{Tr}_E\{\int_0^{\mathrm{d}t} \mathrm{d}t' H_{int}(t')\rho(0)\}. \tag{2.13}$$

L is known as the *Lindblad operator* which describes quantum jump between different states of the system [8, 9] and $\mathrm{d}B_t$ refers to the Wiener process ($\mathcal{N}(0, \mathrm{d}t)$) that comes from the Brownian motion of the system. One can easily determine the relation $L^\dagger = -L$ from the expression of L given in Eq. (2.13). The part $\hat{L}\rho_S(0)\hat{L}^\dagger$ in Eq. (2.12) indicates a possible quantum jump between the states of the system, the terms $\rho_S(0)\hat{L}\hat{L}^\dagger$ and $\hat{L}\hat{L}^\dagger\rho_S(0)$ are there to normalize the density matrix if no jump occurs, and the term $[\hat{L}, \rho_S(0)]\mathrm{d}B_t$ generates stochastic fluctuation in the quantum jump.

In order to draw an analogy between classical and quantum master equations, we drop the second term in Eq. (2.12), which is associated with the stochastic fluctuation $\mathrm{d}B_t$ for the mean 0. Apparently, the positive terms of the last term represent gain of probability of a certain state due to the transitions from the other states in that state, and the negative terms represent loss of probability due to the transitions to other state from that state. One can visualize the similar phenomenon from the classical master equation given in Eq. (2.7) by choosing A and B matrices properly.

2.1.3 Quantum Langevin Equation

The classical Langevin equation is a stochastic differential equation that describes the motion of a particle which moves under the presence of an arbitrary external potential. The two-variable (x, p) Langevin equation is useful to model the Brownian motion of a particle moving in a potential field $V(x)$, as

$$\dot{x} = p/m \tag{2.14a}$$

$$\dot{p} = -V'(x) - \gamma p + \eta, \tag{2.14b}$$

where $\eta(x, \dot{x}, t)$ is the Brownian force which follows the correlation function $\langle \eta(t)\eta(t') \rangle = \delta(t - t')$. Quantum Langevin equation is a quantum-mechanical analogy of classical Langevin equation, in which the variables are expressed as operator quantities. In the following part, we derive the quantum Langevin equation from the operator commutation relation of quantum mechanics.

We consider a system that is coupled linearly with a multimode bath by the exchange of energy. The total Hamiltonian spanning the system, its environment, and the interaction between them is given in the Eq. (2.8), where the Hamiltonian of the isolated system given by $H_S = H_S(a, a^\dagger)$ exhibits a generic dependence on the annihilation (creation) operators a $(a^\dagger)$ associated with the system. The Hamiltonian for the thermal bath is represented by a set of bosonic oscillators:

$$H_E = \sum_k \omega_k b_k^\dagger b_k, \tag{2.15}$$

where $b_k^\dagger$ and b_k are the creation and annihilation operators of the kth bosonic mode, respectively. Note that we use a unit convention with $\hbar = 1$. Now consider the following coupling between the system and the environment

$$H_{int} = \sum_{\mathrm{k}} g_{\mathrm{k}} \left[F(a, a^\dagger) b_{\mathrm{k}}^\dagger + F^\dagger(a, a^\dagger) b_{\mathrm{k}} \right], \tag{2.16}$$

where $F(a, a^\dagger)$ is a generic function of the creation and annihilation operators of the system and g_k is the coupling constant of the kth mode. The bosonic commutation relations of the field operators is

$$\begin{aligned} [a, a] = [a^\dagger, a^\dagger] = [b_k, b_{k'}] = [b_k^\dagger, b_{k'}^\dagger] = 0, \\ [a, a^\dagger] = 1\,; \qquad [b_k, b_{k'}^\dagger] = \delta_{kk'}. \end{aligned} \tag{2.17}$$

The system operators naturally commute with the bath operators. The equation of motion of the annihilation operator of the bath in the Heisenberg picture is given by $\dot{b_k} = i[H, b_k] = i([H_E, b_k] + [H_{int}, b_k])$. Since b_k commutes with H_S, we get

$$\dot{b}_{\mathrm{k}}(t) = -i\omega_{\mathrm{k}} b_{\mathrm{k}}(t) - i g_{\mathrm{k}} F(a, a^{\dagger}). \tag{2.18}$$

Similarly, the equation of motion for any arbitrary system operator is $\dot{c} = i([H_S, c] + [H_{int}, c])$, which can be simplified as

$$\dot{c}(t) = i[H_{\mathcal{S}}, c(t)] + i \sum_{\mathrm{k}} g_{\mathrm{k}} \left([F, c] b_{\mathrm{k}}^{\dagger} + [F^{\dagger}, c] b_{\mathrm{k}} \right). \tag{2.19}$$

In order to obtain an equation of motion for the system field operator, we solve $b_k(t)$ formally from Eq. (2.18) and plug that expression in Eq. (2.19). Depending on initial or final condition, we can have two different solutions. For a given initial condition at the time $t_0 < t$, the solution is

$$b_{\mathrm{k}}(t) = e^{-i\omega_{\mathrm{k}}(t-t_0)} b_{\mathrm{k}}(t_0) - i g_{\mathrm{k}} \int_{t_0}^{t} e^{-i\omega_{\mathrm{k}}(t-t')} F\left(a(t'), a^{\dagger}(t')\right) \, \mathrm{d}t'. \tag{2.20}$$

By substituting Eq. (2.20) and its Hermitian conjugate into Eq. (2.19) we obtain

$$\begin{aligned} \dot{c}(t) = i[H_{\mathcal{S}}, c(t)] + i \sum_{\mathrm{k}} g_{\mathrm{k}} \Bigg\{ & [F, c] \left[e^{i\omega_{\mathrm{k}}(t-t_0)} b_{\mathrm{k}}^{\dagger}(t_0) + i g_{\mathrm{k}} \int_{t_0}^{t} e^{i\omega_{\mathrm{k}}(t-t')} F^{\dagger}(t') \, \mathrm{d}t' \right] \\ & + [F^{\dagger}, c] \left[e^{-i\omega_{\mathrm{k}}(t-t_0)} b_{\mathrm{k}}(t_0) - i g_{\mathrm{k}} \int_{t_0}^{t} e^{-i\omega_{\mathrm{k}}(t-t')} F(t') \, \mathrm{d}t' \right] \Bigg\}. \end{aligned} \tag{2.21}$$

Now, suppose that the discrete modes of the bath is dense enough so that it forms a continuous spectrum. Therefore, in case of a purely linear case, we introduce the density of states $D = \partial \mathrm{k} / \partial \omega_{\mathrm{k}}$. Note that D is independent of the mode index k, which allows us use the first *Markov approximation* by assuming the coupling constant g_{k} is independent of frequency [14]. We define

$$g_{\mathrm{k}}^2 = \frac{\gamma}{2\pi D}, \tag{2.22}$$

where γ is a the mode-independent constant. This helps us in simplifying the equation of motion of a. Namely, we find the identity

$$\begin{aligned} \sum_k g_n^2 e^{-i\omega_k(t-t')} &= \frac{\gamma}{2\pi D} \sum_k e^{-ik(t-t')/D} \\ &= \frac{\gamma}{2\pi D} 2\pi \delta((t-t')/D) = \frac{\gamma |D|}{D} \delta(t-t'). \end{aligned}$$

If we define the input field as [11, 13]

$$a_{in}(t) = -i\sqrt{\frac{1}{2\pi D}}\sum_{k} e^{-i\omega_k(t-t_0)}b_k(t_0), \tag{2.23}$$

we can write the Eq. (2.21) as

$$\begin{aligned}\dot{c}(t) = i[H_{\mathcal{S}}, c(t)] + i\sum_{\mathrm{k}}\sqrt{\frac{\gamma}{2\pi D}}\Bigg\{[F,c]\Bigg(e^{i\omega_{\mathrm{k}}(t-t_0)}b_{\mathrm{k}}^{\dagger}(t_0) + i\sqrt{\frac{\gamma}{2\pi D}}\int_{t_0}^{t} e^{i\omega_{\mathrm{k}}(t-t')}F^{\dagger}(t')\,\mathrm{d}t'\Bigg) \\ + [F^{\dagger},c]\Bigg(e^{-i\omega_{\mathrm{k}}(t-t_0)}b_{\mathrm{k}}(t_0) - i\sqrt{\frac{\gamma}{2\pi D}}\int_{t_0}^{t} e^{-i\omega_{\mathrm{k}}(t-t')}F(t')\,\mathrm{d}t'\Bigg)\Bigg\} \qquad (2.24) \\ = i[H_{\mathcal{S}}, c(t)] + \sqrt{\gamma}\Bigg\{[F,c]\Bigg(a_{\mathrm{in}}^{\dagger}(t) - \frac{\sqrt{\gamma}}{2}F^{\dagger}(t)\Bigg) + [F^{\dagger},c]\Bigg(-a_{\mathrm{in}}(t) + \frac{\sqrt{\gamma}}{2}F(t)\Bigg)\Bigg\},\end{aligned}$$

which finally gives us the quantum Langevin equation of motion for an arbitrary system operator. Note that all the operators in this formulation are local in time, meaning that the system has no memory, which reminds that the system has Markov property. Eq. (2.24) indicates that the time evolution is caused by three separate dynamics.

In case of simple harmonic motion, where the system Hamiltonian is given by $H_S = \omega_s a^{\dagger}a$, one can establish links between classical and quantum Langevin equation assuming that the system is coupled to the environment in such a way that the generic function becomes $F = (a^{\dagger} + a)$ and $i(a^{\dagger} - a)$. Essentially, we arrive the quantum Langevin equation for the quadrature $[x = a^{\dagger} + a, p = i(a^{\dagger} - a)]$ as

$$\dot{x} = \omega_s p \qquad \text{and} \tag{2.25a}$$

$$\dot{p} = -\omega_s x - \gamma p - 2i\sqrt{\gamma}(a_{in} - a_{in}^{\dagger}). \tag{2.25b}$$

Now, assuming the harmonic oscillator having a quadratic potential well ($V(x) = \frac{1}{2}kx^2$), we can compare classical and quantum Langevin equation by choosing $k = m\omega_s^2$ and $\eta = -2i\sqrt{\gamma}(a_{in} - a_{in}^{\dagger})$.

Input and output field

We have already presented the quantum Langevin equation in terms of the input noise caused by the initial condition of the bath. One can also define a similar equation using the output spectrum. This is done by substituting the final condition instead of the initial condition in the derivation of Eq. (2.20). Using this formalism and following

a similar procedure as here, one ends up with a time-reversed quantum Langevin equation,

$$\dot{c}(t) = i[H_{\mathcal{S}}, c(t)] + \sqrt{\gamma}\Big\{[F, c]\Big(- a^{\dagger}_{\rm out}(t) + \frac{\sqrt{\gamma}}{2}F^{\dagger}(t)\Big) + [F^{\dagger}, c]\Big(a_{\rm out}(t) - \frac{\sqrt{\gamma}}{2}F(t)\Big)\Big\}, \tag{2.26}$$

where

$$a_{out}(t) = i\sqrt{\frac{1}{2\pi D}}\sum_{k} e^{i\omega_k(t-t_f)}b_k(t_f), \tag{2.27}$$

where $t_f > t$ is the final state of the bath. The input field tells about the noise interference on the system generated by the environment which always has a positive contribution to the system field, whereas output field gives an idea about the amount of field coming out from the system. By choosing the generic function $F = a$ and $c = a$ and comparing between Eq. (2.24) and the (2.26), one gets

$$a_{out}(t) + a_{in}(t) = \sqrt{\gamma}a(t), \tag{2.28}$$

which determines the relation between output and input field. It is also referred as the boundary condition that relates the internal and external cavity fields [8].

2.1.4 Connection Between QLE and Master Equation

We derived the quantum Langevin equation derived for an arbitrary field operator of the system in Eq. (2.24), which is expressed in the Heisenberg picture while the master equation given in Eq. (2.12), is derived to represent the time dynamics of the density matrix in the interaction picture. In this section, we establish a link between these two representations and discuss about the consequences of two formalisms. Following master equation given in Eq. (2.12), one can deduce the time-evolution of the system operator a in Heisenberg picture as

$$\begin{aligned} a(dt) = a(0) &+ i[H_S, a(0)]dt \\ &- \frac{1}{2}(a(0)\hat{L}^{\dagger}\hat{L} + \hat{L}^{\dagger}\hat{L}a(0) - 2\hat{L}^{\dagger}a(0)\hat{L})dt \\ &+ (\hat{L}^{\dagger}a(0) + a(0)\hat{L})\mathrm{d}B_t. \end{aligned} \tag{2.29}$$

Now, considering a special case for the generic function in the interaction Hamiltonian

$$F(a, a^{\dagger}) = a, \tag{2.30}$$

we construct the Lindblad operator from Eq. (2.13) as [8, 9]

$$L\mathrm{d}B_t = \sqrt{\gamma}[a^\dagger(0)a_{in} - a(0)a_{in}^\dagger]\mathrm{d}t. \tag{2.31}$$

One can check whether it satisfies the relation $L^\dagger = -L$. The expression of Lindblad operator allows us to rewrite Eq. (2.29) as

$$\dot{a}(t) = i([H_S, a(t)] - \frac{\gamma}{2}a(t) + \sqrt{\gamma}a_{in}(t), \tag{2.32}$$

which is the Quantum Langevin equation for the annihilation operator in case of linear coupling between the system and environment which can be derived from the Eq. (2.24) by considering $c = a$. From left to right, they are the time evolution of the isolated system, the decay of the field amplitude, and the noise interference on the system caused by the environment. Substituting the expression of the Lindblad superoperator given in the Eq. (2.31) into Eq. (2.12), we reproduce the master equation in Schrödinger picture as

$$\begin{aligned}\dot{\rho}_S = -i[H_S, \rho_S] &+ \sqrt{\gamma}([a^\dagger(0), \rho_S(0)]a_{in} - [a(0), \rho_S(0)]a_{in}^\dagger) \\ &- \frac{\gamma}{2}[(N+1)(a^\dagger a\rho_S + \rho_S a^\dagger a - 2a\rho_S a^\dagger) \\ &+ N(aa^\dagger\rho_S + \rho_S aa^\dagger - 2a^\dagger\rho_S a) \\ &+ M(a^\dagger a^\dagger\rho_S + \rho_S a^\dagger a^\dagger - 2a^\dagger\rho_S a^\dagger) \\ &+ M^*(aa\rho_S + \rho_S aa - 2a\rho_S a)],\end{aligned} \tag{2.33}$$

where $N = dt\langle a_{in}^\dagger a_{in}\rangle$ and $M = dt\langle a_{in}a_{in}\rangle$. The terms proportional to M and M^* describe dephasing whereas the terms proportional to N and $N+1$ illustrate dissipation. The terms on the top row correspond to isolated time evolution of the system and the fluctuation due to external noise interference caused by bath, respectively. Since the system is coupled to a thermal bath, the action of random external noise and the dephasing terms vanish, leaving

$$\begin{aligned}\dot{\rho}_S = -i[H_S, \rho_S] &- \frac{\gamma}{2}[(N_{th}+1)(a^\dagger a\rho_S + \rho_S a^\dagger a - 2a\rho_S a^\dagger) \\ &+ N_{th}(aa^\dagger\rho_S + \rho_S aa^\dagger - 2a^\dagger\rho_S a)],\end{aligned} \tag{2.34}$$

where N_{th} is the thermal population of bath. For normalized ρ_S at temperature T, N_{th} becomes

$$N_{th}(\omega_k) = (e^{\frac{\hbar\omega_k}{k_B T}} - 1)^{-1}, \tag{2.35}$$

where k_B is the Boltzmann constant.

2.2 Decoherence and Dephasing

We introduce two important features of the evolution of open quantum systems coupled to a thermal bath at zero temperature. The difference in the coupling Hamiltonian

gives different features in the time evolution of the system. The features are amplitude and phase decay, and those are well explained by using master equation. The amplitude decay of a channel is a schematic model where we see spontaneous emission of photons from the system, whereas phase damping describes the transformation of the state of the system from pure to mixed, keeping the population unchanged.

2.2.1 Amplitude Decoherence

As an example to demonstrate the amplitude damping, we consider the case where a harmonic oscillator interacts with an empty bath with the exchange of photon, making the generic function $F(a, a^\dagger) = a$ in the interaction Hamiltonian. Such kind of system/reservoir coupling is often observed in the physics of quantum transport [66], photosynthetic complexes [67] and ultracold gases [68]. The coupling between the system and the bath determines the Lindblad jump operator as

$$L = -\sqrt{\gamma}a, \tag{2.36}$$

which makes the equation of motion of the density matrix of the system in interaction picture as

$$\dot{\rho}_S = -\frac{\gamma}{2}(a^\dagger a\rho_S + \rho_S a^\dagger a - 2a\rho_S a^\dagger). \tag{2.37}$$

Essentially, one can determine the decay equation of the field operator as

$$\langle \dot{a}(t)\rangle = \mathbf{Tr}\{a\dot{\rho}_S\} = -\frac{\gamma}{2}\langle a(t)\rangle. \tag{2.38}$$

One can obtain the same expression from the quantum Langevin equation given in the Eq. (2.32) by considering $a_{in}(t) = 0$. The occupation number ($n = a^\dagger a$) of the oscillator reduces as

$$\frac{\mathrm{d}n}{\mathrm{d}t} = a^\dagger \dot{a} + \dot{a}^\dagger a = -\gamma n, \tag{2.39}$$

which integrates to

$$n(t) = e^{-\gamma t} n(0). \tag{2.40}$$

Here, we see system population decays exponentially with time at the dissipation rate γ. The master equation indicates amplitude decoherence due to the transformation of particle from system to bath spontaneously over time.

2.2.2 Phase Decoherence

In order to understand phase decoherence, let us take an example where the mechanical object interacts with photons. For example, one can consider the interaction of

dust particle with light in the atmosphere. Collision of the particle with photon will not change the intensity of the field, but the state of the particle changes. We visualize the process from the formulation of open quantum system, explicitly from the master equation by considering that the bath is at zero temperature, and the generic function in the interaction Hamiltonian is $F(a, a^\dagger) = a^\dagger a$, giving the Lindblad operator

$$L = \sqrt{\gamma} a^\dagger a. \tag{2.41}$$

Such kind of situation generally appears in the case of electron-phonon coupling or optomechanical coupling, e.g. superconducting qubits [69–71], mechanical mode coupled to atomic spins [42–44] and spin boson systems [45, 48]. The Lindblad operator given in Eq. (2.41), determines the master equation in interaction picture as

$$\dot{\rho}_S = -\frac{\gamma}{2}[(a^\dagger a)^2 \rho_S + \rho_S (a^\dagger a)^2 - 2(a^\dagger a)\rho_S (a^\dagger a)]. \tag{2.42}$$

Here γ is interpreted as the scattering rate of reservoir photons when the system is singly occupied. To determine the state of the system, we express its density matrix in number basis

$$\rho_S = \sum_{n,m} \rho_{nm} |n\rangle\langle m|, \tag{2.43}$$

which gives the EOM of the elements of density matrix as

$$\dot{\rho}_{nm} = -\frac{\gamma}{2}(n-m)^2 \rho_{nm}, \tag{2.44}$$

and which integrates to

$$\rho_{nm}(t) = \exp\left(-\frac{\gamma t}{2}(n-m)^2\right) \rho_{nm}(0). \tag{2.45}$$

However, the population of the system remains unchanged in this process, which can be derived from the Eq. (2.42) as

$$\frac{\mathrm{d}\langle a^\dagger a\rangle}{\mathrm{d}t} = \mathbf{Tr}\{a^\dagger a \dot{\rho}_S\} = 0. \tag{2.46}$$

Here, we cannot see the amplitude decoherence, leaving us to investigate on the phase decoherence. To understand the phenomenon, let us start with a state

$$|c\rangle = \sqrt{p}|0\rangle + \sqrt{1-p}|n\rangle, \tag{2.47}$$

where p is the probability of occupying state $|0\rangle$. The initial density matrix of the system is constructed as

$$\rho_S(0) = |c\rangle\langle c| = p|0\rangle\langle 0| + \sqrt{p(1-p)}|0\rangle\langle n| + \sqrt{p(1-p)}|n\rangle\langle 0| + (1-p)|n\rangle\langle n|. \tag{2.48}$$

We see that the diagonal terms hardly change, but the off-diagonal terms in the density matrix dissipate like $\exp(-\gamma n^2 t/2)$. Hence, we lose the phase information of the initial cat state, and after infinite time the off-diagonal terms become zero, leaving the density matrix as

$$\rho_S(\infty) = p|0\rangle\langle 0| + (1-p)|n\rangle\langle n|. \tag{2.49}$$

Note that the initially prepared pure state of the system becomes mixed without changing the system population. The same behavior is found when the phase damping for a single qubit is studied [72]. The rate of decoherence is $\gamma n^2/2$. One can also consider a system coupled to a thermal reservoir which has a finite temperature, and in that case, the same phenomenon can be observed with much faster rate.

3 Nonlinear Coupling Between System and Environment

The linear S/B coupling given by the Hamiltonian

$$H_{\mathcal{S}-\mathrm{B}} = \sum g_{\mathrm{k}}^{\mathrm{B}} \left(a^{\dagger} b_{\mathrm{k}} + a b_{\mathrm{k}}^{\dagger} \right) \tag{3.1}$$

is not the most general situation. For example, the TLS bath which is modeled as a collection of spins $\mathbf{J}_k$ and the Hamiltonian of isolated TLS bath is $H_E^{TLS} = \sum_k \Omega_k J_k^z$. TLS modes are coupled collectively to the mode of the system. Therefore, we write the coupling Hamiltonian between system and TLS as

$$H_{\mathcal{S}-\mathrm{TLS}} = \sum_{\mathrm{k}} g_{\mathrm{k}}^{\mathrm{TLS}} \left(J_{+}^{\mathrm{k}} a^2 + J_{-}^{\mathrm{k}} a^{\dagger 2} \right). \tag{3.2}$$

3.1 Holstein-Primakoff Transformation

The Holstein-Primakoff realization allows us to substitute the spin operators with bosonic operators. The spin operators obey commutation relations

$$\left[J_z^{\mathrm{k}}, J_{\pm}^{\mathrm{k}} \right] = \pm J_{\pm}^{\mathrm{k}}, \qquad \left[J_{+}^{\mathrm{k}}, J_{-}^{\mathrm{k}} \right] = 2 J_z^{\mathrm{k}}. \tag{3.3}$$

The bosonic operators d_{k}, $d_{\mathrm{k}}^{\dagger}$ follow the commutation relation

$$\left[d_{\mathrm{k}}, d_{\mathrm{k}}^{\dagger} \right] = 1. \tag{3.4}$$

The spin operators which obeys Eq. (3.3) are mapped to the bosonic operators d_{k}, $d_{\mathrm{k}}^{\dagger}$, considering two possibilities, based on the physical situation that we want to describe. If the situation appears as the TLSs is mostly staying in ground state, we write $J_z^{\mathrm{k}} \simeq -j_{\mathrm{k}}$ where j_{k} is the index of representation which is associated with the spin $\mathbf{J}_{\mathrm{k}}$. This allows us to accept the following transformation:

$$J_z^{\mathrm{k}} = \hat{n}_{\mathrm{k}} - j_{\mathrm{k}}, \qquad J_{+}^{\mathrm{k}} = d_{\mathrm{k}}^{\dagger} \sqrt{2j_{\mathrm{k}} - \hat{n}_{\mathrm{k}}}, \qquad J_{-}^{\mathrm{k}} = \sqrt{2j_{\mathrm{k}} - \hat{n}_{\mathrm{k}}}\, d_{\mathrm{k}}, \tag{3.5}$$

where $\hat{n}_{\mathrm{k}} = d_{\mathrm{k}}^{\dagger} d_{\mathrm{k}}$.

We name this choice as HP$_-$. The operators J_z^{k}, $J_{\pm}^{\mathrm{k}}$ can be shown to fulfill the SU(2) commutation relations

$$\left[J_z^{\mathrm{k}}, J_+^{\mathrm{k}}\right] = \left[\hat{n}_{\mathrm{k}}, d_{\mathrm{k}}^{\dagger}\right] \sqrt{2j_{\mathrm{k}} - \hat{n}_{\mathrm{k}}} = J_+^{\mathrm{k}}, \qquad \left[J_z^{\mathrm{k}}, J_-^{\mathrm{k}}\right] = \sqrt{2j_{\mathrm{k}} - \hat{n}_{\mathrm{k}}}\,[\hat{n}_{\mathrm{k}}, d_{\mathrm{k}}] = -J_-^{\mathrm{k}}, \tag{3.6a}$$

$$\begin{aligned}\left[J_+^{\mathrm{k}}, J_-^{\mathrm{k}}\right] &= d_{\mathrm{k}}^{\dagger} \left(\sqrt{2j_{\mathrm{k}} - \hat{n}_{\mathrm{k}}}\right)^2 d_{\mathrm{k}} - \sqrt{2j_{\mathrm{k}} - \hat{n}_{\mathrm{k}}}\,\hat{n}_{\mathrm{k}}\,\sqrt{2j_{\mathrm{k}} - \hat{n}_{\mathrm{k}}} \\ &= \hat{n}_{\mathrm{k}}\,(2j_{\mathrm{k}} - \hat{n}_{\mathrm{k}} + 1) - 2j_{\mathrm{k}} + \hat{n}_{\mathrm{k}} - \hat{n}_{\mathrm{k}}\,(2j_{\mathrm{k}} - \hat{n}_{\mathrm{k}}) = 2J_z^{\mathrm{k}}.\end{aligned} \tag{3.6b}$$

In the limit $j_{\mathrm{k}} \to \infty$, we have

$$\frac{J_+^{\mathrm{k}}}{\sqrt{2j_{\mathrm{k}}}} = d_{\mathrm{k}}^{\dagger} \sqrt{\frac{2j_{\mathrm{k}} - \hat{n}_{\mathrm{k}}}{2j_{\mathrm{k}}}} = d_{\mathrm{k}}^{\dagger} \left(1 - \frac{\hat{n}_{\mathrm{k}}}{4j_{\mathrm{k}}} + \ldots\right) \simeq d_{\mathrm{k}}^{\dagger}, \tag{3.7a}$$

$$\frac{J_-^{\mathrm{k}}}{\sqrt{2j_{\mathrm{k}}}} \simeq d_{\mathrm{k}}, \tag{3.7b}$$

$$\frac{J_z^{\mathrm{k}}}{j_{\mathrm{k}}} = \frac{\hat{n}_{\mathrm{k}}}{j_{\mathrm{k}}} - 1 \simeq -1. \tag{3.7c}$$

Hence, the bosonic excitations those are described by d_{k} and $d_{\mathrm{k}}^{\dagger}$, correspond to (small) excitations around the $J_z^{\mathrm{k}} = -j_{\mathrm{k}}$ state. One can approximate system/TLS bath coupling as

$$H_{\mathcal{S}-\mathrm{HP}_-} = \sum_{\mathrm{k}} g_{\mathrm{k}}^{\mathrm{HP}} \left(d_{\mathrm{k}}^{\dagger} a^2 + d_{\mathrm{k}} a^{\dagger 2}\right) \tag{3.8}$$

with $g_{\mathrm{k}}^{\mathrm{HP}} = \sqrt{2j_{\mathrm{k}}} g_{\mathrm{k}}^{\mathrm{TLS}}$. Similarly, if the TLSs mainly belong to their excited state, one can write the mapping as

$$J_z^{\mathrm{k}} = j_{\mathrm{k}} - \hat{n}_{\mathrm{k}}, \qquad J_-^{\mathrm{k}} = d_{\mathrm{k}}^{\dagger} \sqrt{2j_{\mathrm{k}} - \hat{n}_{\mathrm{k}}}, \qquad J_+^{\mathrm{k}} = \sqrt{2j_{\mathrm{k}} - \hat{n}_{\mathrm{k}}}\, d_{\mathrm{k}}. \tag{3.9}$$

so that when $j_{\mathrm{k}} \to \infty$

$$\frac{J_+^{\mathrm{k}}}{\sqrt{2j_{\mathrm{k}}}} \simeq d_{\mathrm{k}}, \qquad \sqrt{\frac{2}{j_{\mathrm{k}}}} J_-^{\mathrm{k}} \simeq d_{\mathrm{k}}^{\dagger}, \qquad \frac{J_z^{\mathrm{k}}}{j_{\mathrm{k}}} = 1 - \frac{\hat{n}_{\mathrm{k}}}{j_{\mathrm{k}}} \simeq 1. \tag{3.10}$$

This corresponds to the description of small fluctuations around $J_z^{\mathrm{k}} = j_{\mathrm{k}}$ state. We indicate the condition as HP$_+$ which gives

$$H_{\mathcal{S}-\mathrm{HP}_+} = \sum_{\mathrm{k}} g_{\mathrm{k}}^{\mathrm{TLS}} \left(d_{\mathrm{k}} a^2 + d_{\mathrm{k}}^{\dagger} a^{\dagger 2}\right). \tag{3.11}$$

3.2 Linearization of the Quantum Langevin Equations

We therefore linearize the system accepting the presence of a strong coherent pump $\alpha_{\rm p} = \alpha_{\rm in} e^{-i\omega_{\rm p} t}$. Here, we derive the equations to describe the stationary state in a rotating frame of frequency $\omega_{\rm p}$ and the fluctuations around the stationary state. Focusing on Eq. (2.24), we obtain

$$\dot{a} = -i\left[a, H_{\mathcal{S}}\right] - \left(\frac{\kappa}{2} + \kappa_N a^\dagger a\right) a + \sqrt{\kappa} a_{\rm in} + 2\sqrt{\kappa_N} a^\dagger a_{\rm in}^{\rm TLS} \tag{3.12a}$$

$$\dot{a} = -i\left[a, H_{\mathcal{S}}\right] - \left(\frac{\kappa}{2} - \kappa_N a^\dagger a\right) a + \sqrt{\kappa} a_{\rm in} + 2\sqrt{\kappa_N} a^\dagger a_{\rm in}^{\rm TLS\dagger} \tag{3.12b}$$

in the presence of a strong, coherent pump $\alpha_{\rm p} = \alpha_{\rm in} e^{-i\omega_{\rm p} t}$. The first equation corresponds to HP_- and the second equation is for HP_+. We seek a solution by splitting up the cavity field in terms of steady state coherent field and thermal fluctuation around it in the form $a^{[old]} = \alpha + a^{[new]}$, which gives

$$\begin{aligned} -i\omega_{\rm p}\alpha + \dot{a} = -i\omega_{\rm c}\left(\alpha + a\right) - \left[\frac{\kappa}{2} + \kappa_N\left(\alpha^* + a^\dagger\right)\left(\alpha + a\right)\right]\left(\alpha + a\right) \\ + \sqrt{\kappa}\left(\alpha_{\rm in} + a_{\rm in}\right) + 2\sqrt{\kappa_N}\left(\alpha^* + a^\dagger\right) a_{\rm in}^{\rm TLS} \end{aligned} \tag{3.13a}$$

$$\begin{aligned} -i\omega_{\rm p}\alpha + \dot{a} = -i\omega_{\rm c}\left(\alpha + a\right) - \left[\frac{\kappa}{2} - \kappa_N\left(\alpha^* + a^\dagger\right)\left(\alpha + a\right)\right]\left(\alpha + a\right) \\ + \sqrt{\kappa}\left(\alpha_{\rm in} + a_{\rm in}\right) + 2\sqrt{\kappa_N}\left(\alpha^* + a^\dagger\right) a_{\rm in}^{\rm TLS\dagger}, \end{aligned} \tag{3.13b}$$

where without loss of generality we have assumed that $H_S = \omega_{\rm c} a^\dagger a$. Neglecting the fluctuation terms, we obtain the equation for the steady-state solutions

$$0 = i\Delta\alpha - \frac{\kappa}{2}\alpha - \kappa_N \alpha \left|\alpha\right|^2 + \sqrt{\kappa}\alpha_{\rm in} \tag{3.14a}$$

$$0 = i\Delta\alpha - \frac{\kappa}{2}\alpha + \kappa_N \alpha \left|\alpha\right|^2 + \sqrt{\kappa}\alpha_{\rm in}, \tag{3.14b}$$

where $\Delta = \omega_{\rm p} - \omega_{\rm c}$.

In Fig. 3.1 we plot the stationary value of the cavity field obtained from the Eq. (3.14a). As anticipated, when the driving field α_{in} is weak, the stationary solution does not deviate much from the solution obtained in the absence of nonlinear dissipation, for both the choices of the HP mapping ($HP_\pm$). However, when we increase the strength of the external drive, the stationary solution starts deviating from the solution we obtained in linear system. For the parameters chosen here, the amplitude difference is negligible, even though the phase difference noticeable, as it is seen in between $HP_\pm$ cases.

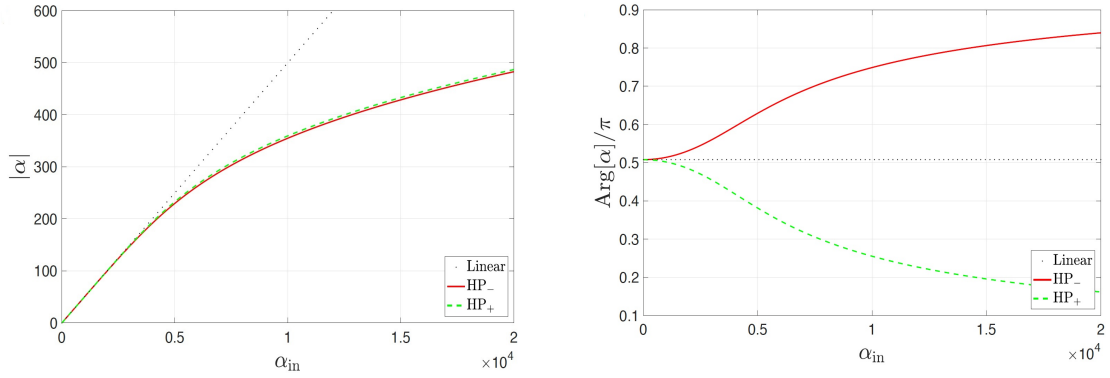

(a) (b)

Figure 3.1: Amplitude (a) and phase (b), for the stationary value (in a frame rotating at $\omega_{\rm p}$, see text) of the cavity field α in the presence of a driving $\alpha_{\rm in}$. Parameters: $\kappa_{\rm N} = 1.5 \times 10^{-4}$, $\Delta = 20$ (all quantities are expressed in units of κ). [Pub.- I] reproduced with permission.

From Eq. (3.13) the equation for the fluctuation around the steady-state solution value of α is expressed as

$$\dot{a} = \left[i\Delta - \left(\frac{\kappa}{2} + 2\kappa_N |\alpha|^2\right)\right] a - \kappa_N \alpha^2 a^\dagger + \sqrt{\kappa} a_{\rm in} + 2\sqrt{\kappa_N}\alpha^* a_{\rm in}^{\rm TLS} \tag{3.15a}$$

$$\dot{a} = \left[i\Delta - \left(\frac{\kappa}{2} - 2\kappa_N |\alpha|^2\right)\right] a + \kappa_N \alpha^2 a^\dagger + \sqrt{\kappa} a_{\rm in} + 2\sqrt{\kappa_N}\alpha^* a_{\rm in}^{\rm TLS\dagger}. \tag{3.15b}$$

The change in the effective damping rate $\kappa_{eff} = \kappa \pm 4\kappa_N |\alpha|^2$ in the presence of nonlinear ($HP_\pm$) coupling should be noted from Eq. (3.15). The ratio of the nonlinear effective damping rate to that linear one is plotted with the variation of input field, in Fig. 3.2, and it is seen that the nonlinear dissipative terms $\mp 2\kappa_N |\alpha|^2 a$ in Eq. (3.15) lead to the broadening/narrowing of the linewidth associated with the linearized response of the cavity field fluctuations, respectively.

3.3 Fluctuation Spectrum of the Nonlinear Model

In the presence of a strong, coherent pump, the system dynamics are affected by thermal fluctuations provided by the bosonic and the TLS baths. As hinted by Eqs. (3.15a, 3.15b), the existence of a parametric term introduces squeezing in the spectrum of the cavity for both cases. Here, we evaluate the spectrum of these fluctuations for the HP$_-$ case. One can also do a similar kind of derivation for the HP$_+$ mapping. One can obtained the fluctuation spectrum

$$S_\omega^\theta = \frac{1}{2}\langle\{X_\omega^\theta, X_{-\omega}^\theta\}\rangle, \tag{3.16}$$

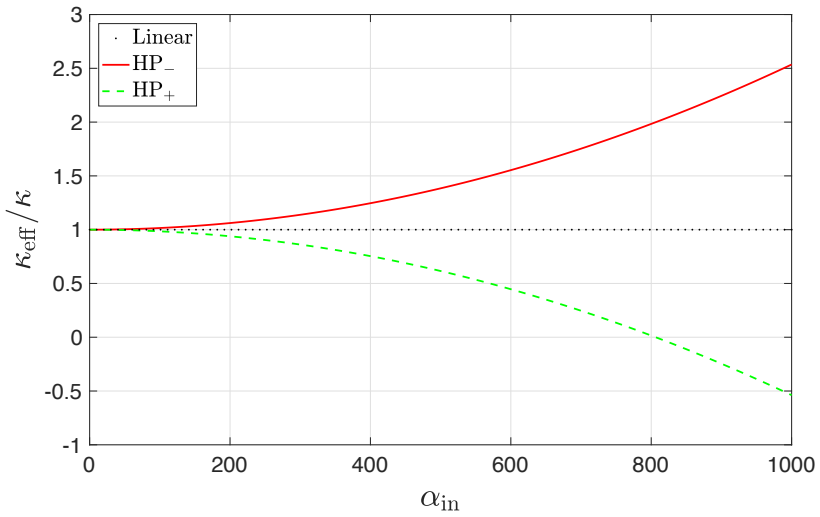

Figure 3.2: The total effective dissipation of the linearized models Eq. (3.15a) (red) and Eq. (3.15b) (dashed green) that correspond to the cases, where the majority of the TLSs are in the ground state/excited state, respectively. They are compared to the case of pure linear dissipation (black dots). Here we assume the system to be a simple cavity with $H_{\mathcal{S}} = \omega_{\mathrm{c}} c^{\dagger} c$. In the units of κ, the parameters are $\Delta = \omega_{\mathrm{p}} - \omega_{\mathrm{c}} = 20$ and $\kappa_N = 1.5 \times 10^{-4}$. [Pub.- I] reproduced with permission.

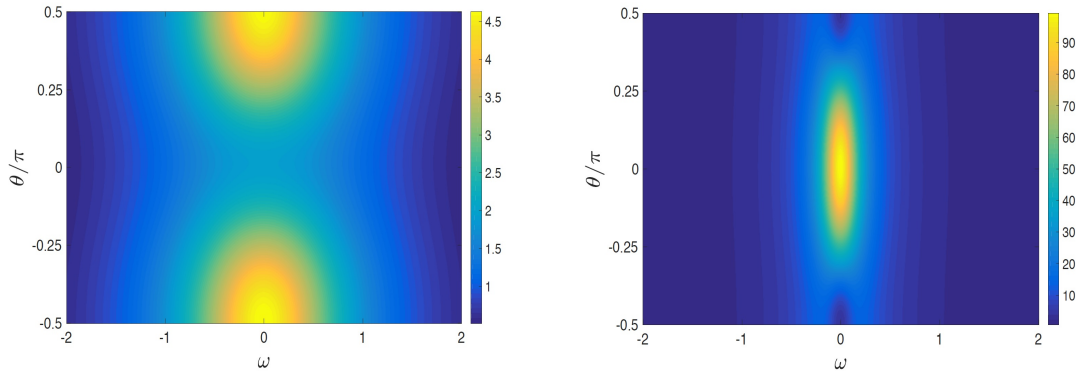

(a) (b)

Figure 3.3: Noise spectrum for the cavity field in the presence of an external drive $\alpha_{\mathrm{in}} = 700$, for (a) HP$_-$ and (b) HP$_+$ for $\langle a_{\mathrm{in}}^{\dagger} a_{\mathrm{in}} \rangle = \langle a_{\mathrm{in}}^{\mathrm{TLS}\dagger} a_{\mathrm{in}}^{\mathrm{TLS}} \rangle = 1$ (all other parameters as in Fig. 3.1). [Pub.- I] reproduced with permission.

with $X_{\omega}^{\theta} = 1/\sqrt{2}\left(a_{-\omega}^{\dagger} e^{i\theta} + a_{\omega} e^{-i\theta}\right)$, from the Fourier transformation of the QLE which is given in the Eq. (3.15a) and its Hermitian conjugate

$$\left[-i\left(\omega + \Delta\right) + \frac{\kappa}{2} + 2\kappa_N \left|\alpha\right|^2\right] a_{\omega} + \kappa_N \alpha^2 a_{-\omega}^{\dagger} = \sqrt{\kappa} a_{\mathrm{in},\omega} + 2\sqrt{\kappa_N}\alpha^* a_{\mathrm{in},\omega}^{\mathrm{TLS}} \tag{3.17a}$$

$$\left[-i\left(\omega - \Delta\right) + \frac{\kappa}{2} + 2\kappa_N \left|\alpha\right|^2\right] a_{-\omega}^{\dagger} + \kappa_N \alpha^{*2} a_{\omega} = \sqrt{\kappa} a_{\mathrm{in},-\omega}^{\dagger} + 2\sqrt{\kappa_N}\alpha a_{\mathrm{in},-\omega}^{\mathrm{TLS}\dagger}. \tag{3.17b}$$

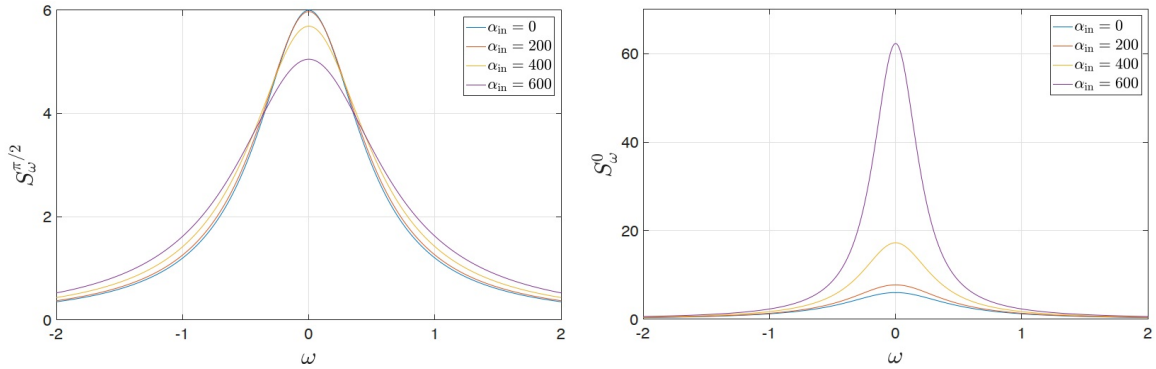

Figure 3.4: The cavity spectra related to the Holstein-Primakoff couplings (a) HP_- and (b) HP_+ for the largest uncertainty quadrature ($\theta = \pi/2$ and $\theta = 0$, respectively). Here the thermal populations of the bosonic and TLS baths are $n_{\mathrm{th}} = n_{\mathrm{th}}^{\mathrm{TLS}} = 1$, and in the units of κ, the other parameters are $\Delta = 20$ and $\kappa_N = 1.5 \times 10^{-4}$. [Pub.- I] reproduced with permission.

The usual convention of the Fourier transformation is used here, according to which

$$a_t = \int_{-\infty}^{\infty} \mathrm{d}\omega \exp\left(-i\omega t\right) a_\omega \qquad \text{and} \qquad a_t^\dagger = \int_{-\infty}^{\infty} \mathrm{d}\omega \exp\left(-i\omega t\right) a_{-\omega}^\dagger. \tag{3.18}$$

Defining

$$A = -i\left(\omega + \Delta\right) + \frac{\kappa}{2} + 2\kappa_N \left|\alpha\right|^2, \tag{3.19a}$$

$$B = \kappa_N \alpha^2, \qquad \text{and} \tag{3.19b}$$

$$C = -i\left(\omega - \Delta\right) + \frac{\kappa}{2} + 2\kappa_N \left|\alpha\right|^2, \tag{3.19c}$$

we express the QLE for the system as

$$\begin{pmatrix} a_\omega \\ a_{-\omega}^\dagger \end{pmatrix} = \frac{1}{AC - |B|^2} \begin{pmatrix} C & -B \\ -B^* & A \end{pmatrix} \begin{pmatrix} \sqrt{\kappa} a_{\mathrm{in},\omega} + 2\sqrt{\kappa_N}\alpha^* a_{\mathrm{in},\omega}^{\mathrm{TLS}} \\ \sqrt{\kappa} a_{\mathrm{in},-\omega}^\dagger + 2\sqrt{\kappa_N}\alpha a_{\mathrm{in},-\omega}^{\mathrm{TLS}\dagger}. \end{pmatrix} \tag{3.20}$$

Now, one can simplify the equation as

$$a_\omega = \chi_{\mathrm{d}}\left(\omega\right) a_{\mathrm{in},\omega} + \chi_{\mathrm{x}}\left(\omega\right) a_{\mathrm{in},-\omega}^\dagger + \chi_{\mathrm{d}}^{\mathrm{TLS}}\left(\omega\right) a_{\mathrm{in},\omega}^{\mathrm{TLS}} + \chi_{\mathrm{x}}^{\mathrm{TLS}}\left(\omega\right) a_{\mathrm{in},-\omega}^{\mathrm{TLS}\dagger}, \tag{3.21a}$$

$$a_{-\omega}^\dagger = \chi_{\mathrm{x}}^*\left(-\omega\right) a_{\mathrm{in},\omega} + \chi_{\mathrm{d}}^*\left(-\omega\right) a_{\mathrm{in},-\omega}^\dagger + \chi_{\mathrm{x}}^{\mathrm{TLS}*}\left(-\omega\right) a_{\mathrm{in},\omega}^{\mathrm{TLS}} + \chi_{\mathrm{d}}^{\mathrm{TLS}*}\left(-\omega\right) a_{\mathrm{in},-\omega}^{\mathrm{TLS}\dagger}, \tag{3.21b}$$

where

$$\chi_{\mathrm{d}}\left(\omega\right) = \sqrt{\kappa} C (AC - |B|^2)^{-1}, \tag{3.22a}$$

$$\chi_{\mathrm{x}}\left(\omega\right) = -\sqrt{\kappa} B (AC - |B|^2)^{-1}, \tag{3.22b}$$

$$\chi_{\mathrm{d}}^{\mathrm{TLS}}\left(\omega\right) = 2\sqrt{\kappa_N}\alpha^* C (AC - |B|^2)^{-1}, \qquad \text{and} \tag{3.22c}$$

$$\chi_{\mathrm{x}}^{\mathrm{TLS}}\left(\omega\right) = -2\sqrt{\kappa_N}\alpha B (AC - |B|^2)^{-1}. \tag{3.22d}$$

If the thermal populations of the baths are given by $\langle a_{\mathrm{in},\omega} a^{\dagger}_{\mathrm{in},\omega'}\rangle = (n_{\mathrm{th}}+1)\,\delta(\omega-\omega')$ and $\langle a^{\mathrm{TLS}}_{\mathrm{in},\omega} a^{\mathrm{TLS}\dagger}_{\mathrm{in},\omega'}\rangle = \left(n^{\mathrm{TLS}}_{\mathrm{th}}+1\right)\delta(\omega-\omega')$, the cavity spectrum can be written as

$$
\begin{aligned}
S^{\theta}_{\omega} =& \frac{1}{4}\Big[\left(|\chi_{\mathrm{d}}(\omega)|^2+|\chi_{\mathrm{x}}(-\omega)|^2\right)\langle\Big\{a_{\mathrm{in},\omega},a^{\dagger}_{\mathrm{in},\omega}\Big\}\rangle+\left(|\chi_{\mathrm{d}}(-\omega)|^2+|\chi_{\mathrm{x}}(\omega)|^2\right)\langle\Big\{a^{\dagger}_{\mathrm{in},-\omega},a_{\mathrm{in},-\omega}\Big\}\rangle\Big]\\
&+\frac{1}{4}\Big[\left(\chi_{\mathrm{d}}(\omega)\,\chi_{\mathrm{x}}(-\omega)\,e^{-i2\theta}+\chi^{*}_{\mathrm{d}}(\omega)\,\chi^{*}_{\mathrm{x}}(-\omega)\,e^{i2\theta}\right)\langle\Big\{a_{\mathrm{in},\omega},a^{\dagger}_{\mathrm{in},\omega}\Big\}\rangle\\
&\quad+\left(\chi_{\mathrm{d}}(-\omega)\,\chi_{\mathrm{x}}(\omega)\,e^{-i2\theta}+\chi^{*}_{\mathrm{d}}(-\omega)\,\chi^{*}_{\mathrm{x}}(\omega)\,e^{i2\theta}\right)\langle\Big\{a^{\dagger}_{\mathrm{in},-\omega},a_{\mathrm{in},-\omega}\Big\}\rangle\Big]\\
&+\frac{1}{4}\Big[\left(\left|\chi^{\mathrm{TLS}}_{\mathrm{d}}(\omega)\right|^2+\left|\chi^{\mathrm{TLS}}_{\mathrm{x}}(-\omega)\right|^2\right)\langle\Big\{a^{\mathrm{TLS}}_{\mathrm{in},\omega},a^{\mathrm{TLS}\dagger}_{\mathrm{in},\omega}\Big\}\rangle\\
&\quad+\left(\left|\chi^{\mathrm{TLS}}_{\mathrm{d}}(-\omega)\right|^2+\left|\chi^{\mathrm{TLS}}_{\mathrm{x}}(\omega)\right|^2\right)\langle\Big\{a^{\mathrm{TLS}\dagger}_{\mathrm{in},-\omega},a^{\mathrm{TLS}}_{\mathrm{in},-\omega}\Big\}\rangle\Big]\\
&+\frac{1}{4}\Big[\left(\chi^{\mathrm{TLS}}_{\mathrm{d}}(\omega)\,\chi^{\mathrm{TLS}}_{\mathrm{x}}(-\omega)\,e^{-i2\theta}+\chi^{\mathrm{TLS}*}_{\mathrm{d}}(\omega)\,\chi^{\mathrm{TLS}*}_{\mathrm{x}}(-\omega)\,e^{i2\theta}\right)\langle\Big\{a^{\mathrm{TLS}}_{\mathrm{in},\omega},a^{\mathrm{TLS}\dagger}_{\mathrm{in},\omega}\Big\}\rangle\\
&\quad+\left(\chi^{\mathrm{TLS}}_{\mathrm{d}}(-\omega)\,\chi^{\mathrm{TLS}}_{\mathrm{x}}(\omega)\,e^{-i2\theta}+\chi^{\mathrm{TLS}*}_{\mathrm{d}}(-\omega)\,\chi^{\mathrm{TLS}*}_{\mathrm{x}}(\omega)\,e^{i2\theta}\right)\langle\Big\{a^{\mathrm{TLS}\dagger}_{\mathrm{in},-\omega},a^{\mathrm{TLS}}_{\mathrm{in},-\omega}\Big\}\rangle\Big]\\
=&\frac{1}{2}\Big[|\chi_{\mathrm{d}}(\omega)|^2+|\chi_{\mathrm{d}}(-\omega)|^2+|\chi_{\mathrm{x}}(\omega)|^2+|\chi_{\mathrm{x}}(-\omega)|^2\\
&\quad+2\cos(2\theta+\phi)\,|\chi_{\mathrm{d}}(\omega)\,\chi_{\mathrm{x}}(-\omega)+\chi_{\mathrm{d}}(-\omega)\,\chi_{\mathrm{x}}(\omega)|\Big]\left(n_{\mathrm{th}}+\frac{1}{2}\right)\\
&+\frac{1}{2}\Big[\left|\chi^{\mathrm{TLS}}_{\mathrm{d}}(\omega)\right|^2+\left|\chi^{\mathrm{TLS}}_{\mathrm{d}}(-\omega)\right|^2+\left|\chi^{\mathrm{TLS}}_{\mathrm{x}}(\omega)\right|^2+\left|\chi^{\mathrm{TLS}}_{\mathrm{x}}(-\omega)\right|^2\\
&\quad+2\cos\left(2\theta+\phi^{\mathrm{TLS}}\right)\left|\chi^{\mathrm{TLS}}_{\mathrm{d}}(\omega)\,\chi^{\mathrm{TLS}}_{\mathrm{x}}(-\omega)+\chi^{\mathrm{TLS}}_{\mathrm{d}}(-\omega)\,\chi^{\mathrm{TLS}}_{\mathrm{x}}(\omega)\right|\Big]\left(n^{\mathrm{TLS}}_{\mathrm{th}}+\frac{1}{2}\right),
\end{aligned}
\tag{3.23}
$$

where $\phi^{(\mathrm{TLS})} = \mathrm{Arg}\left[\chi^{(\mathrm{TLS})}_{\mathrm{d}}(\omega)\,\chi^{(\mathrm{TLS})}_{\mathrm{x}}(-\omega)+\chi^{(\mathrm{TLS})}_{\mathrm{d}}(-\omega)\,\chi^{(\mathrm{TLS})}_{\mathrm{x}}(\omega)\right]$.

The Eq. (3.23) shows squeezing in the cavity spectrum for HP_{-} mapping and it is also possible to draw a parallel picture for HP_{+} mapping starting from Eq. (3.15b). From Fig. 3.3, we see how the cavity fluctuation spectrum exhibits a clear dependence on the phase θ for both the cases. In Fig. 3.4(a) we have plotted the cavity spectrum for the HP_{-} and Fig. 3.4(b) presents the spectrum related to HP_{+} coupling. Both the cases the plots are given for the largest uncertainty quadrature [(a)$\theta = \pi/2$ for HP_{-} and (b) $\theta = 0$ for HP_{+}]. The interesting feature that we see is the linewidth broadening in (a) as the driving field α_{in} increases, whereas in (b) the linewidth becomes narrower.

4 Numerical Methods

As we see in the previous chapter, the linear S/B coupling is not the most general situation. The linearization technique implemented before is not a satisfactory method to study exact dynamical behavior. Apart from nonlinear S/B coupling, this method is also limited to provide exact solution of non-Markovian dynamics. These limitations of analytical methods motivates for the numerical simulation of the time evolution, which includes transformation of the S/B coupling model to a many-body chain and the computational method consists of numerical diagonalization and renormalization process. In the following section, we provide an explanation in detail describing the computational technique, and followed by the mapping of S/B coupling model to a one-dimensional chain.

4.1 Time-evolving Block Decimation Algorithm

The simulation of a many-body quantum system having a large number of lattice sites is a difficult task due to the rapid increase in the number of parameters associated with the size of the Hilbert space. For example, one can consider the Hubbard model with N lattice sites, $N_\downarrow$ spin-down, and $N_\uparrow$ spin-up fermions, the dimension of the corresponding Hilbert space is

$$W_H(N, N_\uparrow, N_\downarrow) = \frac{(N!)^2}{(N - N_\uparrow)!N_\uparrow!(N - N_\downarrow)!N_\downarrow!}, \tag{4.1}$$

which is a very large number and increases almost exponentially with the number of lattice sites N. In case of Bose-Hubbard model with N lattice sites and N' bosons, the associated Hilbert space is

$$W_{BH}(N, N') = \frac{(N' + N - 1)!}{(N - 1)!N'!}, \tag{4.2}$$

which also becomes huge when the size of the system increases. For the calculation of the ground-state properties and the simulation of the time-evolution of a many body quantum system of feasible sizes, one has to invest a huge effort into the development

of numerical methods. The linear growth of the size of the system causes exponential increase in the size of the Hilbert space which also costs exponential increase in computational resources.

Over last few decades, many numerical approaches have been developed to calculate the time evolution and the ground states of many-body quantum systems which bypasses the trouble of storing the coefficients of the entire Hilbert space. The approaches include sampling in Quantum Monte-Carlo methods [50–53], performing in Density Matrix Renormalisation Group (DMRG) methods [34, 51, 52, 54–58]. The DMRG method was first introduced by S. R. White in 1992 [59] to determine the ground state of a one dimensional system, keeping in mind that the system is large. Even though several attempts have been attempted to generalize the basic DMRG methods to apply on time dependent calculations [73], the major step forward was taken by Vidal in 2003 [62] where he proposed a method in which the truncated Hilbert space was modified at each time step so that the representation of the state satisfied some optimal criteria. The method is often referred to as the Time Evolving Block Decimation Algorithm (TEBD), which has been used for the treatment of Ising chain model [74], Hubbard model [68], master equations in case of dissipative systems, and systems at finite temperatures [75].

4.1.1 State Representation

The state of an N site 1-D lattice system is expressed in terms of local Hilbert space of each lattice site which consists M^N-dimensional basis

$$|\psi\rangle = \sum_{i_n=1}^{M} c_{i_1 i_2 .. i_N} |i_1, i_2, .., i_{N-1}, i_N\rangle, \tag{4.3}$$

where M is the dimension of local Hilbert space and $|i_n\rangle$ is the basis states in the local Hilbert space at site n. The trick of the algorithm is the representation of this state as a convenient decomposition into a series of tensors:

$$c_{i_1 i_2 .. i_N} = \sum_{\alpha_1,.,\alpha_{N-1}=0}^{\chi} \lambda^{[1]}_{\alpha_1} \Gamma^{[1]i_1}_{\alpha_1\alpha_2} \lambda^{[2]}_{\alpha_2} \Gamma^{[2]i_2}_{\alpha_2\alpha_3} \cdot ... \cdot \lambda^{[N]}_{\alpha_N} \Gamma^{[N]i_N}_{\alpha_N\alpha_{N+1}} \lambda^{[N+1]}_{\alpha_{N+1}} \tag{4.4}$$

The representation of the state is known as matrix product states (MPS). The decomposition of the pair of sites is performed by singular value decomposition (SVD), which generates bipartite splitting between any two local Hilbert spaces in the chain. The details of the decomposition procedure are explained in the following section.

However, the Γ tensor has dimension $N \times M \times \chi \times \chi$, where χ is the predetermined Schmidt number. The index n within square brackets stands for the corresponding site. The λ tensor keeps the Schmidt values for the partition between two consecutive bond. After analyzing the computational complexity, one can conclude by saying that rather than treating M^N coefficients of the initial term, it is always efficient to deal with $MN\chi^2 + (N+1)\chi$ terms, which are obtained after the decomposition of the state.

Schmidt decomposition

The state of any bipartite system ($|\psi\rangle \in H_A \otimes H_B$) can be decomposed into two subsystems such as

$$|\psi\rangle = \sum_{\alpha} \lambda_\alpha |\phi_\alpha^A\rangle \otimes |\phi_\alpha^B\rangle, \tag{4.5}$$

where the states $|\phi_\alpha^A\rangle$ and $|\phi_\alpha^B\rangle$ are orthonormal states of H_A and H_B, respectively. The representation is obtained from the Schmidt decomposition, and the real and positive Schmidt coefficients λ_α satisfy $\sum_\alpha \lambda_\alpha^2 = 1$ and

$$\langle \phi_\alpha^A | \psi \rangle = \lambda_\alpha |\phi_\alpha^B\rangle.$$

To derive Schmidt decomposition, we start with two orthonormal bases $|j_A\rangle$ and $|k_B\rangle$ of H_A and H_B, respectively. Let the dimension of H_A and H_B be M_A and M_B, respectively, so that the state $|\psi\rangle$ can be expanded in terms of bases vectors

$$|\psi\rangle = \sum_{j,k}^{M_A,M_B} c_{j,k} |j_A\rangle \otimes |k_B\rangle, \tag{4.6}$$

where the complex numbers $c_{j,k}$ are the elements of the matrix C of dimensions $M_A \times M_B$. The singular value decomposition generates two unitary matrices U and V of dimensions $M_A \times M_A$ and $M_B \times M_B$, respectively, and an $M_A \times M_B$ diagonal matrix D with real and non-negative entities, such that $C = UDV$. Using the SVD we can re-express the state as

$$|\psi\rangle = \sum_{j,k}^{M_A,M_B} \sum_{\alpha}^{\chi} u_{j,\alpha} d_{\alpha,\alpha} v_{k,\alpha} |j_A\rangle \otimes |k_B\rangle = \sum_{\alpha}^{\chi} \lambda_\alpha |\phi_\alpha^A\rangle \otimes |\phi_\alpha^B\rangle, \tag{4.7}$$

where $|\phi^A_\alpha\rangle = \sum_j u_{j,\alpha}|j_A\rangle$, $|\phi^B_\alpha\rangle = \sum_k v_{k,\alpha}|k_B\rangle$, and $\lambda_\alpha = d_{\alpha,\alpha}$. The orthonormality of $|\phi^A_\alpha\rangle$ and $|\phi^B_\alpha\rangle$ is ensured by the unitarity of U and V.

The Schmidt rank, $\chi \leq \min(M_A, M_B)$, is used to measure the entanglement between two subsystems A and B in quantum information theory. Larger values of χ correspond to more entanglement, and when $\chi = 1$, the system is in a product state.

To obtain matrix product state for the full chain, we consider the first bipartite splitting between site 1 and the rest of the chain: $[1] : [2..N]$:

$$|\psi\rangle = \sum_{i_1,\alpha_2=1}^{M,\chi} \Gamma^{[1]i_1}_{\alpha_2} \lambda^{[2]}_{\alpha_2} |i_1\rangle |\phi^{[2..N]}_{\alpha_2}\rangle. \tag{4.8}$$

In the next step, we split the rest of the chain separating in between site 2 and the rest of the others: $[2] : [3..N]$ giving us

$$|\phi^{[2..N]}_{\alpha_2}\rangle = \sum_{i_2,\alpha_3=1}^{M,\chi} \Gamma^{[2]i_2}_{\alpha_2\alpha_3} \lambda^{[3]}_{\alpha_3} |i_2\rangle |\phi^{[3..N]}_{\alpha_3}\rangle \tag{4.9}$$

Substituting it into the Eq. (4.8), we get

$$|\psi\rangle = \sum_{i_1,\alpha_2=1}^{M,\chi} \Gamma^{[1]i_1}_{\alpha_2} \lambda^{[2]}_{\alpha_2} \Gamma^{[2]i_2}_{\alpha_2\alpha_3} \lambda^{[3]}_{\alpha_3} |i_1\rangle |i_2\rangle |\phi^{[3..N]}_{\alpha_3}\rangle. \tag{4.10}$$

By repeating this process until the end of the chain, we obtain the decomposed form of the coefficient $c_{i_1 i_2 .. i_N}$ which is expressed in the Eq. (4.4). The construction of the MPS ensures that the vectors $\lambda^{[1]}_{\alpha_1}$ and $\lambda^{[N+1]}_{\alpha_{N+1}}$ are nonzero only when $\alpha_1 = \alpha_{N+1} = 1$.

Validity of truncated decomposition

The physical significance of the Schmidt decomposition is understood from the reduced density operator of the subsystem A obtained by tracing out the subsystem B from the full density matrix: $\rho_A = \mathrm{Tr}_B[\rho] = \sum_\alpha \lambda_\alpha |\psi^A_\alpha\rangle\langle\psi^A_\alpha|$. In quantum information theory, the entanglement between two subsystems A and B is identified by the von Neumann entropy, which is determined from the eigenvalues of the reduced density operators:

$$S_A = -\mathrm{Tr}[\rho_A \log_2 \rho_A] = -\sum_\alpha \lambda_\alpha^2 \log_2 \lambda_\alpha^2. \tag{4.11}$$

The fact that the eigenvalues of the reduced density operators are same for both subspaces, ensures that the von Neumann entropy of the two subsystems A and B are same for the pure state of a composite system.

The von Neumann entropy provides a theoretical lower bound on the number of qubits required to express the information of the subsystem A (or B). The cutoff limit of the dimension of the Schmidt vector (χ) comes from the fact that the eigenvalues of the reduced density matrix decay exponentially with the increment of $\alpha(\lambda_\alpha \approx \exp(-K\alpha)$, where $K > 0$), and beyond the cutoff limit, it is expected that λ_α becomes reasonably low to be neglected. The lower bound of the Schmidt rank is given by $\chi \geq 2^{S_A}$. In case of 1D systems, the von Neumann entropy diverges logarithmically at a critical point. However, in the case of higher dimensional systems the decay of the eigenvalues is too slow, and therefore, it demands a large value of χ which makes the TEBD simulation inefficient. In another way, one can say that due to low entanglement or smaller value of the von Neumann entropy, in case of one dimensional systems truncation of Hilbert space is a good and efficient approximation, but the higher-dimensional systems demands a large number of states to achieve accuracy, and hence, the TEBD simulation has poor performance [76].

4.1.2 Operator on Lattice Chain

Single-Site Gate

A single site operator updates the Γ tensor of a particular site

$$\Gamma'^{[k]i_k}_{\alpha_k\alpha_{k+1}} = \sum_j^M U^{i_k}_{j_k} \Gamma^{[k]j_k}_{\alpha_k\alpha_{k+1}}, \tag{4.12}$$

which is performed in the order of $\chi^2 M^2$ operations.

Two-Site Gate

The implementation of a two-site gate on an MPS is dependent on SVD, which plays a crucial role in the time evolution and measurements. The implementation is based upon updating the tensors of two neighboring sites n and $n+1$. The double site operator U acting on the two sites changes the basis of these sites and entanglement.

In order to apply the gate operator, first we write the state expressing in terms of Schmidt eigenvectors to the left and the right of the pair of the sites:

$$|\alpha\rangle = |\phi_{\alpha}^{[1....(n-1)]}\rangle \tag{4.13a}$$
$$|\gamma\rangle = |\phi_{\gamma}^{[(n+2)....N]}\rangle, \tag{4.13b}$$

with tensor product symbols $|\alpha i_n i_{n+1}\gamma\rangle = |\alpha\rangle \otimes |i_n\rangle \otimes |i_{n+1}\rangle \otimes |\gamma\rangle$. By expressing it as a sum of matrix product, we can construct a fourth order tensor Θ as

$$|\psi\rangle = \sum_{\substack{i_n, i_{n+1}=1 \\ \alpha,\beta,\gamma=1}}^{M,\chi} \underbrace{\lambda_{\alpha}^{[n]} \Gamma_{\alpha\beta}^{[n]i_n} \lambda_{\beta}^{[n+1]} \Gamma_{\beta\gamma}^{[n+1]i_{n+1}} \lambda_{\gamma}^{[n+2]}}_{\Theta_{\alpha\gamma}^{i_n i_{n+1}}} |\alpha i_n i_{n+1}\gamma\rangle. \tag{4.14}$$

Next, we apply the operator to update the tensor

$$\tilde{\Theta}_{\alpha\gamma}^{j_n j_{n+1}} = \sum_{\beta=1}^{\chi} \sum_{i_n, i_{n+1}=1}^{M} U_{i_n i_{n+1}}^{j_n j_{n+1}} \lambda_{\alpha}^{[n]} \Gamma_{\alpha\beta}^{[n]i_n} \lambda_{\beta}^{[n+1]} \Gamma_{\beta\gamma}^{[n+1]i_{n+1}} \lambda_{\gamma}^{[n+2]}, \tag{4.15}$$

which has $M^2\chi^2$ basis states in total, which is then reduced to χ^2 states by taking SVD on newly constructed Θ tensor. The SVD generates the diagonal matrix with magnitudes arranged in an exponentially reducing manner. We truncate the λ tensor for the highest χ values to finalize the updated state.

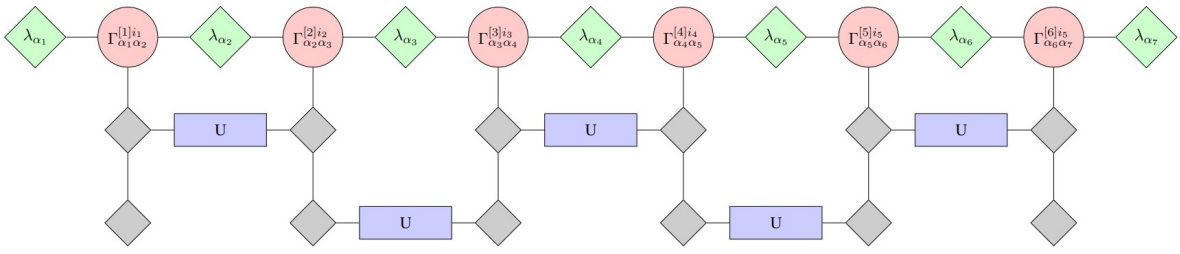

Figure 4.1: The quantum circuit for simulating a time evolution: alternating operation on odd and even pair. [Pub.- II,III] reproduced with permission.

4.1.3 Time Evolution

Real-Time Evolution

In order to do the numerical simulation for the real time evolution, we split the double site Hamiltonian in odd and even sites.

$$H = \sum_{i \text{ odd}} H_{i,i+1} + \sum_{i \text{ even}} H_{i,i+1} = F + G \tag{4.16}$$

According to the Suzuki-Trotter expansion, we do time evolution of the alternate lattice sites. The first order expansion is

$$U = e^{-iHdt} = e^{-iFdt}e^{-iGdt} + O[dt^2], \tag{4.17}$$

which generates an error in the order of dt^2. To minimize the time error, we generally use the second order ST expansion which comes with the error of the order dt^3.

$$U = e^{-iHdt} = e^{-iFdt/2}e^{-iGdt}e^{-iFdt/2} + O[dt^3] \tag{4.18}$$

The diagrammatic representation is given in Fig. 4.1. However, the time error can even be reduced by applying Forest-Ruth formula, which gives Trotter error of the order $O(\mathrm{d}t^6)$. The formula of the decomposition is given by [77]

$$e^{-iHdt} = e^{-iF\theta dt/2}e^{-iG\theta dt}e^{-iF(1-\theta)dt/2}e^{-iG(1-2\theta)dt}e^{-iF(1-\theta)dt/2}e^{-iG\theta dt}e^{-iF\theta dt/2}, \tag{4.19}$$

with the constant $\theta = 1/(2-2^{1/3})$. Better Suzuki-Trotter formula with a higher order of time error can be designed, but they do not improve the accuracy of exponential significantly [77]. However, the Forest-Ruth formula allows us to consider larger step size which essentially helps to reduce the simulation time and to preserve computational resources.

Imaginary-Time Evolution

Imaginary time evolution is required to find out the ground state and the thermal state of the system. The ground state is determined by taking imaginary time evolution for a long time (ideally infinity). The state vector is being normalized after each infinitesimal step of the time evolution. The coefficients of the basis vectors reduce

exponentially during imaginary time evolution. Higher-energy states are being suppressed more, leaving the lowest energy state finally as the ground state of the system. In practice, DMRG code is designed to determine the ground state by imaginary time evolving and normalizing the initial product state iteratively, which is expressed as

$$|\psi_{gr}\rangle = \lim_{\tau\to\infty} \frac{e^{-\tilde{H}\tau}|\psi_P\rangle}{||e^{-\tilde{H}\tau}|\psi_P\rangle||}, \tag{4.20}$$

where $|\psi_P\rangle$ is an initial product state and $\langle\psi_0|\psi_P\rangle = 0$. The implementation is quite straight forward. We evolve the full chain for $\delta\tau$ time step each time and normalize. The algorithm of the imaginary time evolution is slightly different than real time evolution. Unlike higher-order Trotter decomposition, here we use back-forth method. Even though the time evolution for the determination of ground state should continue for infinite time, we terminate the code when we see that the state converges to the ground state and hardly changes anymore. Several convergence criteria can be there to stop the iteration. For instance, one could use the sum of the square of the differences between the λ-coefficients of the two consecutive steps: $\frac{1}{N}\sum_i^N \sum_{\alpha_i}^{\chi} \left(\lambda_{\alpha_i} - \lambda_{\alpha_i}^{[next]}\right)^2$. When the quantity is below a threshold, we consider the convergence is reached.

Back-forth scheme

Higher order Trotter decompositions are often used in real time evolution which is not a good choice for imaginary time evolution for having non-unitary operations on each pair which produces non-orthogonal Schmidt eigenstates. The unitarity of the evolution operator preserves the orthogonality of the sets, which is not happening here. Hence, we sweep the evolution operators across the chain forward and backward direction, with the order $(1,2),(2,3),...,(N-1,N),(N-1,N),(N-2,N-1),...,(1,2)$.

In order to understand the whole scenario, let us start with a two site operation between site n and $n+1$. The non-unitary operation hampers the orthogonality of the state $|\phi_\alpha^{[1..(n-1)]}\rangle$ and $|\phi_\gamma^{[(n+2)..N]}\rangle$. But the SVD ensures orthogonalization of the states $|\phi_\beta^{[1..n]}\rangle$ and $|\phi_\beta^{[(n+1)..N]}\rangle$. In the next step, when we target the alternate sites through Trotter decomposition, we demand orthogonality of the states $|\phi_\alpha^{[1..(n-1)]}\rangle$ and $|\phi_\gamma^{[(n+2)..N]}\rangle$ for the operation on the pairs $(n-2)-(n-1)$ and $(n+2)-(n+3)$, respectively, which is not happening anymore. Hence, instead of choosing alternate sites, we switch to the next pair of sites which is (n+1)-(n+2) to fulfill the requirement of orthogonality of the state $|\phi_\beta^{[(n+1)..N]}\rangle$, which is satisfied from the SVD of the previous operation; and the state $|\phi_\delta^{[1..(n+2)]}\rangle$ which has the orthogonality from the original state, was not changed in the previous operation. This is the reason why we

sweep across the chain in the forward and backward direction while doing imaginary time evolution. Many sets of states become non-orthogonal during the time evolution, but the requirement of orthogonality condition is satisfied for the sets of states that we consider at any point. At the end of the imaginary time evolution, we restore the orthonormality of the states by sweeping across the chain forward and backward with a unitary operator (e.g., the identity) [78].

4.1.4 Estimation of Errors

There are two major error sources in TEBD: Suzuki-Trotter expansion and truncation of the Hilbert space [79].

Trotter Error

In the case of a Trotter approximation of n^{th} order, the error appears of order δt^{n+1}. Taking into account the number of steps $\frac{T}{\delta t}$, the error after the time T is

$$\epsilon_{tr} = \frac{T}{\delta t}\delta t^{n+1} = T\delta t^{n}. \tag{4.21}$$

The actual state $|\tilde{\psi}_{Tr}\rangle$ should be

$$|\tilde{\psi}_{Tr}\rangle = \sqrt{1-{\epsilon_{tr}}^2}|\psi_{Tr}\rangle + \epsilon_{tr}|\psi_{Tr}^{\perp}\rangle, \tag{4.22}$$

where $|\psi_{Tr}\rangle$ is the state obtained after time evolution and $|\psi_{Tr}^{\perp}\rangle$ accounts for the part that is neglected while doing the operation. The total Trotter error scales with time T as

$$\epsilon_{tr}(T) = 1 - |\langle\tilde{\psi_{Tr}}|\psi_{Tr}\rangle|^2 = 1 - 1 + \epsilon_{tr}^2 = \epsilon_{tr}^2. \tag{4.23}$$

Truncation Error

The errors arises with the truncation of the Hilbert space from the decomposition, are twofold. The sum of all discarded eigenvalues of the reduced density matrix, at the bond n is

$$\epsilon_n = \sum_{\alpha=\chi_c}^{\chi} (\lambda_\alpha^{[n]})^2, \tag{4.24}$$

where χ_c is the truncated Schmidt number. Now, at a given bond n, the actual state $|\psi\rangle$ is described by Schmidt decomposition

$$|\psi\rangle = \sqrt{1-\epsilon_n}|\psi_D^{[n]}\rangle + \sqrt{\epsilon_n}|\psi_D^{[n]\perp}\rangle, \tag{4.25}$$

where the truncated state is given by

$$|\psi_D^{[n]}\rangle = \frac{1}{\sqrt{1-\epsilon_n}} \sum_{\alpha_n=1}^{\chi_c} \lambda_{\alpha_n}^{[n]} |\Phi_{\alpha_n}^{[1..n]}\rangle |\Phi_{\alpha_n}^{[n+1..N]}\rangle \tag{4.26}$$

and

$$|\psi_D^{[n]\perp}\rangle = \frac{1}{\sqrt{\epsilon_n}} \sum_{\alpha_n=\chi_c}^{\chi} \lambda_{\alpha_n}^{[n]} |\Phi_{\alpha_n}^{[1..n]}\rangle |\Phi_{\alpha_n}^{[n+1..N]}\rangle \tag{4.27}$$

is the state corresponding to the eigenfunctions of smallest and irrelevant Schmidt coefficients and therefore those are neglected. Also, we see $\langle\psi_D^{[n]\perp}|\psi_D^{[n]}\rangle = 0$ because they are spanned by vectors corresponding to orthogonal spaces. Using the same argument as for the Trotter expansion, the error after the truncation is

$$\epsilon_n = 1 - |\langle\psi|\psi_D^{[n]}\rangle|^2 = \sum_{\alpha=\chi_c}^{\chi} (\lambda_\alpha^{[n]})^2, \tag{4.28}$$

After moving to the next bond, similarly the state gives:

$$|\psi_D^{[n]}\rangle = \sqrt{1-\epsilon_{n+1}}|\psi^{[n+1]}{}_D\rangle + \sqrt{\epsilon_{n+1}}|\psi^{[n+1]\perp}{}_D\rangle. \tag{4.29}$$

After taking truncation on the next bond, the error is

$$\epsilon = 1 - |\langle\psi|\psi_D^{[n+1]}\rangle|^2 = 1 - (1-\epsilon_{n+1})|\langle\psi|\psi_D^{[n]}\rangle|^2 = 1 - (1-\epsilon_{n+1})(1-\epsilon_n) \tag{4.30}$$

and so on. Moving from bond to bond, we determine the total error caused by truncation in the full chain which is given by

$$\epsilon_D = 1 - \prod_{n=1}^{N-1} (1-\epsilon_n). \tag{4.31}$$

4.1.5 Measurement of Correlation Functions

The operator $A^{i_k}_{j_k} B^{i_l}_{j_l}$ acts on the local Hilbert spaces of the sites k and l together to determine the correlation function between the sites. The operators applied on the MPS that determines the correlation function is expressed as

$$\langle\psi^*|A^{i_k}_{j_k} B^{i_l}_{j_l}|\psi\rangle = \sum_{i_1,i_2,...,i_N}^{M} \left(\sum_{\beta_1,.,\beta_{N-1}=0}^{\chi} \lambda^{[1]}_{\beta_1} \Gamma^{[1]i_1}_{\beta_1\beta_2} \lambda^{[2]}_{\beta_2} \Gamma^{[2]i_2}_{\beta_2\beta_3} \cdot ... \cdot \lambda^{[N]}_{\beta_N} \Gamma^{[N]i_N}_{\beta_N\beta_{N+1}} \lambda^{[N+1]}_{\beta_{N+1}} \right)^*$$
$$\times \sum_{\alpha_1,.,\alpha_{N-1}=0}^{\chi} \lambda^{[1]}_{\alpha_1} \Gamma^{[1]i_1}_{\alpha_1\alpha_2} \lambda^{[2]}_{\alpha_2} \Gamma^{[2]i_2}_{\alpha_2\alpha_3} .. \sum_{j_k} A^{i_k}_{j_k} \Gamma^{[k]j_k}_{\alpha_k\alpha_{k+1}} .. \sum_{j_l} B^{i_l}_{j_l} \Gamma^{[l]j_l}_{\alpha_l\alpha_{l+1}} .. \lambda^{[N]}_{\alpha_N} \Gamma^{[N]i_N}_{\alpha_N\alpha_{N+1}} \lambda^{[N+1]}_{\alpha_{N+1}} \tag{4.32}$$

The order of matrix operation in this computation is $N \times M \times \chi^4$. Even though, the operators A_k and B_l acts only on single sites, we can also calculate a higher-order correlation function instantly following the same way with minimum additional computational cost. Reversibly, a single site operator operates on one site only, and hence, the operation is less complicated.

4.2 Preparation of Thermal Bath Using TEBD

In quantum statistical mechanics, the thermal state is considered as a mixed state, which is expressed as an ensemble of pure states. The density matrix of a thermal state (ρ_β) at inverse temperature β with Hamiltonian H is given by $\rho_\beta = \exp(-\beta H)$.

In the previous section we have discussed about TEBD algorithm which is one of the most successful methods to study the strongly correlated one-dimensional (1D) systems. Even though it is designed to study the time evolution and the determination of ground state of a many body systems, quite different methods for the simulations at finite temperatures have been developed, e.g. purification of the density matrix [80, 81]. The combination of real and imaginary time DMRG allows to evaluate the finite-temperature response functions. The method was used successfully to study finite-temperature properties of quantum spin chains [60]. However, the simulation based on matrix purification is often limited due to a subsequent growth of entanglement and the computational costs associated with it.

In order to get rid of this problem, the complementary approach is introduced where one can choose a large number of sample pure states and calculate observables by

taking the average over them [61], instead of purifying the density matrix. The states whose ensemble generate the impact of $\rho_\beta = \exp(-\beta H)$, are *typically* known as minimally entangled typical thermal states (METTS),= and in this chapter we discuss the algorithm and the subsequent theory behind it.

4.2.1 Preparation of METTS with Pure State

Algorithm of minimally entangled typical thermal states

We employ the METTS algorithm, which approximates thermal expectation values of an observable $\langle \hat{O} \rangle_\beta$ by sampling over a large number of pure quantum states that have low entanglement. Overall, these samples which keep physical properties of the system for a given temperature, allows us to make efficient DMRG calculations. The thermal expectation value of an observable is obtained using a set of orthonormal basis $\{|\mathbf{n}\rangle\}$ of classical product states (CPS)

$$|\mathbf{n}\rangle = \bigotimes_i |n_i\rangle, \tag{4.33}$$

where $|n_i\rangle$ are arbitrary orthonormal basis states for lattice site i. The thermal expectation value of the operator is determined as

$$\langle \hat{O} \rangle_\beta = \frac{1}{Z_\beta} \sum_n \langle \mathbf{n}| e^{-\beta H/2} \hat{O} e^{-\beta H/2} |\mathbf{n}\rangle, \tag{4.34}$$

where Z_β is the partition function. The CPS $|\mathbf{n}\rangle$ becomes a matrix product state (MPS) $|\phi_n\rangle$ after the imaginary time evolution with probabilities P_n as

$$|\phi_n\rangle = \frac{1}{\sqrt{P_n}} e^{-\beta H/2} |\mathbf{n}\rangle, \qquad \text{where} \qquad P_n = \langle \mathbf{n}| e^{-\beta H} |\mathbf{n}\rangle. \tag{4.35}$$

Afterwards, the METTS $|\phi_n\rangle$ is collapsed to a new CPS $|n'\rangle$ via projective measurement consists of an arbitrary basis, from which one can subsequently estimate a new METTS $|\phi_{n'}\rangle$ and this process continues to generate a large set of MPS which altogether typically represents a thermal state. Thus, the sampling is obtained efficiently through the generation of a Markov chain of METTS, illustrated in Fig. 4.2; where the thermal average is shown to be determined from a set of imaginary time evolved and normalized MPS states ($|\phi_n\rangle$) with probabilities P_n/Z_β

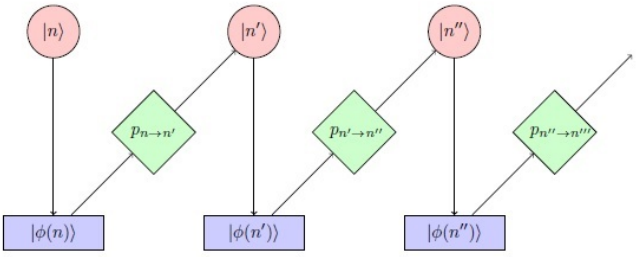

Figure 4.2: Generation of a set of METTS through imaginary time evolution and projective measurement. [Pub.- III] reproduced with permission.

$$\langle \hat{O} \rangle_\beta = \frac{1}{Z_\beta} \sum_n P_n \langle \phi_n | \hat{O} | \phi_n \rangle \rangle \tag{4.36}$$

The computational cost of this process increases when the entanglement between two lattice points increases, and hence, the CPS is the best choice to start with for having the least entanglement. The obtained MPS after imaginary time evolution is minimally entangled and the entanglement entropy of the product states remains reasonably low during real time evolution.

Summarize the algorithm and proof of balance condition

The algorithm that produce a set of METTS that represent a thermal state, can be summarized as:

1. Choose a CPS $|n\rangle$.
2. Compute the MPS $|\phi_n\rangle = \exp(-\beta H/2)|n\rangle P(n)^{-1/2}$ and calculate observables.
3. Collapse a new CPS $|n'\rangle$ from $|\phi_n\rangle$ through projective measurement and return to step 2. A large collection of such MPS exhibits the properties of a thermal state.

The probability of collapsing into a new state $|\mathbf{n}'\rangle$ from the initial product state $|\mathbf{n}\rangle$ is

$$p_{n\to n'} = \frac{1}{P_n} |\langle \mathbf{n}' | e^{-\beta H/2} | \mathbf{n} \rangle|^2. \tag{4.37}$$

Considering an ensemble of all initial CPS $|n\rangle$ with probability distribution P_n/Z_β, we arrive a new CPS $|n'\rangle$ through the time evolution and projective measurement with

probability

$$\begin{aligned}\sum_n \frac{P_n}{Z_\beta} p_{n\to n'} &= \sum_n \frac{P_n}{Z_\beta}\frac{1}{P_n}|\langle \mathbf{n}'|e^{-\beta H/2}|\mathbf{n}\rangle|^2 \\ &= \frac{1}{Z_\beta}\sum_n \langle \mathbf{n}'|e^{-\beta H/2}|\mathbf{n}\rangle\langle \mathbf{n}|e^{-\beta H/2}|\mathbf{n}'\rangle \\ &= \frac{1}{Z_\beta}\langle \mathbf{n}'|e^{-\beta H}|\mathbf{n}'\rangle = \frac{P_{n'}}{Z_\beta}.\end{aligned}$$

Note that the obtained ensemble of all such $|n'\rangle$ has the same original distribution. The transition probabilities follow a detailed balance condition

$$\frac{P_n}{Z_\beta} p_{n\to n'} = \frac{P_{n'}}{Z_\beta} p_{n'\to n}, \tag{4.38}$$

which means the expected distribution of P_n is a fixed point stochastic Markov process. Summarizing the whole process, we conclude by saying that starting from a random CPS and taking imaginary time evolution upto $\beta/2$, one can arrive to an MPS, which is then collapsed to another CPS through a projective measurement with measurement basis. By repeating the same process for few times, we generate a collection METTS, and, by doing the measurement on each METTS, we obtain the running average as the desired output. It is seen that the measurement converges in some point which is considered as our desired output.

4.2.2 Collapse of an MPS to a CPS

In this section, we discuss how to apply the CPS collapsing algorithm to a state $|\phi_n\rangle$ represented as an MPS. During this process, we scan the whole lattice and collapse the MPS of each site to a new CPS. We start by considering the orthogonality center of the MPS at the first site, such that the tensors $\lambda^{[n]}_{\alpha_n}$ and $\Gamma^{[n]j_n}_{\alpha_n\alpha_{n+1}}$ for $n = 2, 3, ...$ are right orthogonal to it. In order to collapse into a new state, first, we compute the expectation values of the projectors $P_1(m)$ on the first site

$$P_1(m) = \sum_{j,k,\alpha_1,\alpha_2} \lambda^{[1]*}_{\alpha_1}\Gamma^{[1]k_1*}_{\alpha_1\alpha_2}\lambda^{[2]*}_{\alpha_2}U(k,m)U^*(j,m)\lambda^{[1]}_{\alpha_1}\Gamma^{[1]j_1}_{\alpha_1\alpha_2}\lambda^{[2]}_{\alpha_2}, \tag{4.39}$$

where U is a random unitary operator that rotates the projector operator in an arbitrary angle. We use the operator U to rotate the orthonormal basis set as well and make it arbitrary to make sure that we are working with a basis set which is not an eigenvector of the Hamiltonian, otherwise the algorithm shrinks down to a trivial

case. The change in the first site forces to update the $\lambda^{[2]}_{\alpha_2}$ tensor for the projective measurement in the next step on site 2. The update goes as

$$\lambda'^{[2]}_{\alpha_2} = \frac{1}{\sqrt{P_1(m)}} \sum_{k_1} U(k_1, m) \Gamma^{[1]k_1}_{\alpha_1\alpha_2}|_{\alpha_1=1} \lambda^{[2]}_{\alpha_2}. \tag{4.40}$$

The new CPS for the site 1 is decided based on the probability $P_1(m)$. The bond dimension of CPS is 1. So, values of $\lambda^{[1]}_{\alpha_1}$ and $\lambda^{[2]}_{\alpha_2}$ vectors go as 1 for the first element and 0 for the rest of the others.

4.3 Mapping of S/B Coupling Model to a Semi-infinite 1D Chain

The theoretical techniques which have been developed over decades and experimented successfully on various two state systems [82, 83], do not provide any satisfactory platform to obtain exact solution in case of a simple, non-trivial model like single two level system (TLS) coupled to a zero temperature bath [84, 85] for having non-linearity, even though nonlinear effects have been encountered formally many times, e.g. micromechanical oscillator [86], Josephson qubits [87], and dielectrics at the limit of single photon excitation energies [88]. As we intend to implement DMRG for open quantum dynamics, one has to map the canonical S/B model to one-dimensional harmonic chain with nearest neighbor interactions. The dynamics of a small subsystem is obtained from the time dynamics of the small part of the chain. In the following section, we discuss about the analytical technique that generates a map between the two models to simulate open quantum system numerically.

4.3.1 System Specification

Here, we present how the multimode environment coupled to a system is transformed into a semi-infinite chain model. The Hamiltonian of the bath for a S/B coupling model given in Eq. (2.8), is expressed in continuous domain as

$$H_B = \int_{-x_{max}}^{x_{max}} \mathrm{d}x g(x) b_x^\dagger b_x, \tag{4.41}$$

where $b_x(b_x^\dagger)$ are the annihilation (creation) operators of a particular mode x of the bath. x_{max} is the hard cutoff limit of the modes. The operators satisfy the bosonic

commutation relation $[b_x, b_y^\dagger] = \delta(x-y)$. $g(x)$ is the frequency of the mode. The coupling Hamiltonian is

$$H_{int} = \int_{-x_{max}}^{x_{max}} \mathrm{d}x h(x) \left(a^\dagger b_x + a b_x^\dagger\right), \tag{4.42}$$

where $a(a^\dagger)$ are the annihilation (creation) operators of the system and $h(x)$ is the coupling strength of each mode, and depending on that we define the measure $\mathrm{d}\mu(x) = h^2(x)\mathrm{d}x$. The dynamics of the system is characterized by a positive function of the energy of the bath, known as spectral density [89]:

$$J(\omega) = \pi h^2[g^{-1}(\omega)]\frac{\mathrm{d}g^{-1}(\omega)}{\mathrm{d}\omega}, \tag{4.43}$$

where $g^{-1}(\omega)$ is the inverse function of ω. As $\mathrm{d}\omega \to 0$, $\frac{\mathrm{d}g^{-1}(\omega)}{\mathrm{d}\omega}$ represents the density of states of the bath. In order to map the S/B coupling model to a semi-infinite chain, we imply a mathematical transformation based on orthogonal polynomials [90]. In Appendix A, we discuss about the definitions and properties of those orthonormal polynomials.

4.3.2 Transformation of the Hamiltonian

The mapping between S/B coupling model is formulated by using a unitary operator which is constructed using orthonormal polynomials. The characteristics of these polynomials were discussed previously. After the transformation of the S/B coupling Hamiltonian, the 1D chain Hamiltonian is expected to be

$$\tilde{H} = H_S + \eta'\left(a^\dagger d_0 + a d_0^\dagger\right) + \lim_{N\to\infty}\left[\sum_{n=0}^{N}\omega_n d_n^\dagger d_n + \sum_{n=0}^{N-1}\eta_n\left(d_n^\dagger d_{n+1} + d_n d_{n+1}^\dagger\right)\right]. \tag{4.44}$$

The transformation is shown with a schematic diagram in Fig. 4.3. $d_n(d_n^\dagger)$ are the annihilation (creation) operators of the chain at site n. ω_n, η' and η are the new parameters which we determine using the recurrence relation of the orthonormal polynomial given in Eq. A.6. The new operators of the lattice sites are obtained by unitary transformation of the old operators for each mode of the bath

$$d_n = \int_{-x_{max}}^{x_{max}} \mathrm{d}x U_n(x) b(x), \tag{4.45}$$

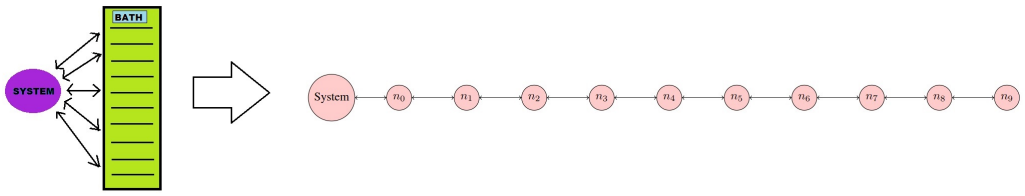

Figure 4.3: Transformation of Hamiltonian from system/bath coupling model to semi infinite chain model. [Pub.- II,III] reproduced with permission.

where

$$U_n(x) = h(x)\tilde{p}_n(x).$$

The inverse transformation is given by

$$b(x) = \sum_n U_n(x)d_n. \tag{4.46}$$

The consideration of wide-band limit approximation (WBLA) makes the real valued coupling coefficient ($h(x)$) independent of the frequency the mode and therefore gives a constant ($h(x) = c_0$). Depending on the type of S/B coupling and the distribution of the modes of the bath, one chooses a suitable orthonormal polynomial for the unitary transformation. For example, in case of an open quantum system where the mode of the bath is continuously distributed, and coupling coefficient is a constant, Legendre polynomial is an essential choice. However, if the mode of the bath is discrete, one should consider Hahn polynomial [90].

Legendre polynomial

In order to make our life easier, we consider such kind of orthogonal polynomials as a structural unit for the construction of unitary operator $U_n(x)$, which has a unit measure. Therefore, the constant associated with the coupling coefficient (c_0) is considered to be absorbed within the system field operator. The frequency of the bath changes linearly with x, giving $\omega = g(x) = g.x$. Essentially, the spectral density function given in Eq. (4.43) becomes

$$J(\omega) = \frac{\pi x_{max}}{\epsilon}\theta(\omega + \epsilon)\theta(\epsilon - \omega). \tag{4.47}$$

$\epsilon = g.x_{max}$ is the extreme cutoff frequency of the mode of the bath. The frequency of the bath mode belongs in the range $\omega \in [-\epsilon, \epsilon]$ and hence we consider a large value

of x_{max} while simulating the open quantum system. The unit measure determines the orthogonality relation as

$$\int_{-x_{max}}^{x_{max}} \mathrm{d}x \tilde{p}_m(x)\tilde{p}_n(x) = \delta_{m,n}. \tag{4.48}$$

Here, we use Legendre polynomial $L_n(y)$ which satisfies the orthonormality criteria in the range of $y \in [-1, 1]$. The orthogonality relation of the Legendre polynomial is given by

$$\int_{-1}^{1} \mathrm{d}y L_n(y)L_m(y) = \delta_{m,n}\frac{2}{2n+1}.$$

As the polynomial is an even function and not normalized, we consider a normalized shifted Legendre polynomial $\tilde{L}_n(x)$ where x is defined in the range $x \in [-x_{max}, x_{max}]$, for the construction of unitary operator which is given by

$$U_n(x) = \sqrt{\frac{(2n+1)}{2x_{max}}} L_n\left[\frac{x}{x_{max}}\right] = \tilde{p}_n(x). \tag{4.49}$$

The unitary operator satisfies the orthonormal relation explained in the Eq. (4.48), and transforms the interaction Hamiltonian to

$$H_{int} = \int_{-x_{max}}^{x_{max}} \mathrm{d}x c_0 \left(a^\dagger b_x + a b_x^\dagger\right) = c_0 \sum_n \int_{-x_{max}}^{x_{max}} \mathrm{d}x U_n(x) \left(a^\dagger d_n + a d_n^\dagger\right).$$

As $L_0(x) = 1$, the zeroth order unitary operator gives $U_0(x) = \sqrt{\frac{1}{2x_{max}}}$. The orthogonality relation $\int_{-x_{max}}^{x_{max}} \mathrm{d}x U_n(x)U_0(x) = \delta_{n,0}$ determines the interaction Hamiltonian as

$$H_{int} = c_0\sqrt{2x_{max}} \left(a^\dagger d_0 + a d_0^\dagger\right). \tag{4.50}$$

We get the value of η' from the above equation, which can also be determined from the expression of spectral density as [91]

$$\eta' = \sqrt{\frac{c_0^2}{\pi}\int_{-x_{max}}^{x_{max}} \mathrm{d}\omega J(\omega)} = c_0\sqrt{2.x_{max}}. \tag{4.51}$$

Using the transformation of $b(x)$ and $b^\dagger(x)$, we determine the Hamiltonian of the bath as

$$H_B = \int_{-x_{max}}^{x_{max}} \mathrm{d}x g(x) b_x^\dagger b_x = g\sum_{m,n}\int_{-x_{max}}^{x_{max}} \mathrm{d}x[x\tilde{p}_n(x)]\tilde{p}_m(x)d_n^\dagger d_m.$$

Inserting the recurrence relation of the orthonormal polynomial provided in the Eq. (A.6) and using the orthonormality among polynomials, we re-express the Hamiltonian of the bath as

$$\begin{aligned} H_B &= g\sum_{m,n}\int_{-x_{max}}^{x_{max}} \mathrm{d}x[x\tilde{p}_n(x)]\tilde{p}_m(x)d_n^\dagger d_m \\ &= g\sum_n\left[\frac{1}{C_n}d_{n+1}^\dagger d_n + \frac{A_n}{C_n}d_n^\dagger d_n + \frac{B_{n+1}}{C_{n+1}}d_n^\dagger d_{n+1}\right] \\ &= g\sum_n\left[\sqrt{\beta_{n+1}}d_{n+1}^\dagger d_n + \alpha_n d_n^\dagger d_n + \sqrt{\beta_{n+1}}d_n^\dagger d_{n+1}\right], \end{aligned} \tag{4.52}$$

which determines coefficients ω_n and η as

$$\eta_n = g\sqrt{\beta_{n+1}} \qquad \text{and} \tag{4.53a}$$

$$\omega_n = g\alpha_n. \tag{4.53b}$$

Now, in order to calculate α_n and β_n, one has to transform the orthogonal polynomial $p_n(x)$ to monic polynomial $\pi_n(x)$ by dividing it by its' leading coefficient, which is

$$f_n = \sqrt{\frac{2n+1}{2.x_{max}}}\frac{(2n)!}{(2.x_{max})^n(n!)^2}.$$

Essentially, β_n is calculated as

$$\beta_n = \frac{\langle \tilde{p}_n, \tilde{p}_n \rangle}{\langle \tilde{p}_{n-1}, \tilde{p}_{n-1} \rangle} \frac{f_{n-1}^2}{f_n^2} = \left(\frac{f_{n-1}}{f_n} \right)^2,$$

which determines η_n as

$$\eta_n = g\sqrt{\beta_{n+1}} = g\left(\frac{f_n}{f_{n+1}} \right) = \epsilon \left(\frac{n+1}{\sqrt{(2n+1)(2n+3)}} \right). \tag{4.54}$$

Similarly, α_n is determined as

$$\begin{aligned} \alpha_n = \frac{\langle x\pi_n, \pi_n \rangle_\mu}{\langle \pi_n, \pi_n \rangle_\mu} = \langle x\tilde{p}_n, \tilde{p}_n \rangle &= \int_{-x_{max}}^{x_{max}} \mathrm{d}x x \frac{(2n+1)}{2.x_{max}} \{L_n \left[\frac{x}{x_{max}} \right]\}^2 \\ &= x_{max} \frac{(2n+1)}{2} \int_{-1}^{1} \mathrm{d}z z \{L_n(z)\}^2 \\ &= 0, \end{aligned}$$

which gives the diagonal elements

$$\omega_n = 0. \tag{4.55}$$

Hahn polynomial

Previously, we mapped a continuous environment to a discrete semi-infinite chain. However, this might not be the case always, especially when a system coupled to a discrete set of oscillators which cannot be determined by a continuous spectral function. This discrete bath can still be transformed into a chain following the same procedure that we have presented previously, the only difference is that one has to use classical discrete orthonormal polynomials instead of continuous ones. Eventually, the transformation relation given in the Eq. (4.45) changes to

$$d_n = \sum_{k=-N}^{N} U_n(k) b_k. \tag{4.56}$$

The inverse transformation would be similar to the Eq. (4.46). The orthogonality relation given in the Eq. (4.48) changes to

$$\sum_{k=-N}^{N} \tilde{p}_m(k) \tilde{p}_n(k) = \delta_{m,n}. \tag{4.57}$$

Here, we use Hahn polynomial $Q_n(k, N)$ which satisfies the orthonormality criteria in the range of $n \in [0, N]$ [92]. As the polynomial is an even function and not normalized, we consider a normalized shifted Hahn polynomial by rescaling it and multiplying by a normalization factor. The orthogonality relation of the Hahn polynomial is given by

$$\sum_{k=-N}^{N} \tilde{Q}_m(k, N)\tilde{Q}_n(k, N) = \delta_{m,n}\rho_n^2, \tag{4.58}$$

where $\tilde{Q}_n(k, N) = Q_n(2k - N, N)$ is the shifted Hahn polynomial and ρ is the normalization coefficient which is expressed by

$$\rho_n = (-1)^n(N!)\sqrt{\frac{(2n+1)}{(N+n+1)!(N-n)!}}. \tag{4.59}$$

Using the orthogonality relation given in the Eq. (4.58), one can show that the new modes $d_n^\dagger$ and d_n obey the same bosonic commutation relation, similar to the original modes. The spectral density of the discrete bath can be deduced from the Eq. (4.43) as

$$J_k = \pi g_k^2 = \pi\theta(N - k)\theta(N + k), \tag{4.60}$$

which determines the coefficient η':

$$\eta' = c_0\sqrt{\frac{1}{\pi D}\sum_{k=-N}^{N} J_k} = c_0\sqrt{2N}. \tag{4.61}$$

Inserting the transformation of b_k and $b_k^\dagger$ we re-express the Hamiltonian of the bath as

$$\begin{aligned} H_B &= \sum_{-N}^{N} \omega_k b_k^\dagger b_k = \sum_{m,n}\sum_{k} k\frac{\delta\omega_k}{\delta k}\tilde{p}_m(k)\tilde{p}_m(k)d_m^\dagger d_n \\ &= \sum_{m,n}\sum_{k}(k/D)\tilde{Q}_m(k, N)\tilde{Q}_n(k, N)\rho_m^{-1}\rho_n^{-1}d_m^\dagger d_n. \end{aligned} \tag{4.62}$$

The recurrence relation of the Hahn orthogonal polynomial is given by

$$-\frac{1}{2}(k + N)\tilde{Q}_n(k, N) = \left[A_n\tilde{Q}_{n+1}(k, N) - (A_n + C_n)\tilde{Q}_n(k, N) + C_n\tilde{Q}_{n-1}(k, N)\right], \tag{4.63}$$

where

$$A_n = \frac{(n+1)(N-n)}{2(2n+1)} \qquad \text{and} \tag{4.64a}$$

$$C_n = \frac{(n+N+1)n}{2(2n+1)}. \tag{4.64b}$$

Using the recurrence relation and the orthogonality of the Hahn polynomial, one can rewrite the Hamiltonian of the reservoir given in Eq. (4.62) as

$$H_B = \frac{1}{D}\sum_n \left[-2A_n\rho_n^{-1}\rho_{n+1}d_n^\dagger d_{n+1} + (A_n + C_n - N)d_n^\dagger d_n - 2C_{n+1}\rho_{n+1}^{-1}\rho_n d_{n+1}^\dagger d_n\right]. \tag{4.65}$$

Using the expression of A_n, C_n and ρ_n, we determine the coefficients ω_n and η_n as

$$\eta_n = 1/D\sqrt{(N-n)(N+n+2)}\left(\frac{n+1}{\sqrt{(2n+1)(2n+3)}}\right) \tag{4.66}$$

$$\omega_n = 0. \tag{4.67}$$

It is not possible realistically to accept the semi-infinite chain ($N \to \infty$) for numerical simulation, and so we truncate the length of the chain in some point, which causes recurrence in the time dynamics. We will explore this phenomenon while analyzing the results of numerical simulation. However, the difference in the hopping coefficients (η_n) for the Legendre and Hahn does not create a serious problem other than the dispersion relation. The dispersion relation of the Hahn polynomial is linear as expected, but not always in the case of Legendre polynomials. Even though it shows linearity in the central region, towards the edge of cutoff frequency it exhibits nonlinearity, which is demonstrated in Fig. 4.4.

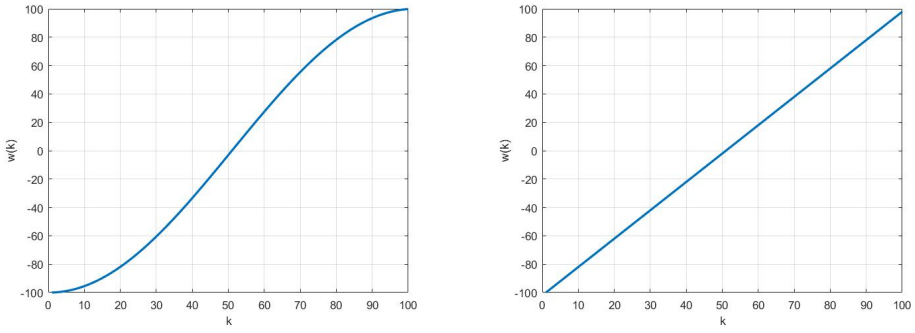

(a) (b)

Figure 4.4: The dispersion relation of the chain constructed by (a)Legendre and (b)Hahn polynomials.

5 Numerical Simulation of Open Quantum Systems

Here, we use the TEBD numerical scheme introduced in the previous section to investigate simple linear S/B coupling and to study the consequences induced by modeling and the numerical parameters. In order to check the applicability this algorithm, we first simulate the dissipative dynamics of an open quantum system and then introduce a thermal bath to study the thermalization dynamics of the system. Both the cases, we have chosen a simple S/B coupling model given in Sec. 2.2.1, with the generic function $F(a, a^\dagger) = a$. The interaction Hamiltonian in Eq. (2.16) becomes $H_{int} = \sum_{\mathrm{k}} c_0(a^\dagger b_{\mathrm{k}} + a b_{\mathrm{k}}^\dagger)$, where c_0 is the coupling strength.

5.1 Free Dissipative Systems (T=0)

We start by assuming one photon kept initially in the system leaving bath completely empty at zero temperature. The transformation of the continuous modes of the bath to the discrete chain is done using Legendre polynomial given in the Sec. 4.3.2. The model is chosen to study how the system population decays over time in the presence of the empty bath. Transforming the open quantum system to 1D chain system we see that the first site is populated by one quantum, all other sites remaining empty. The dissipative dynamics of the system population is estimated analytically from Eq. (2.40), and numerically through real time evolution of the full chain.

We plotted the population dynamics of the system in Fig. 5.1, evaluated in two ways; analytically from QLE and numerically by TEBD, to compare them. In the system population of the numerical result, we see an increment after a certain time, which is caused due to the fact that the particle reflects from the end of the chain. The finite size effect of the chain is discussed explicitly later in the appendix. However, the population plot of the full chain exhibits the reflection of the particle, which is given in the insets of Fig. 5.1. Afterwards, we fit the curve and estimate the rate of dissipation from the numerical data and compare with analytics.

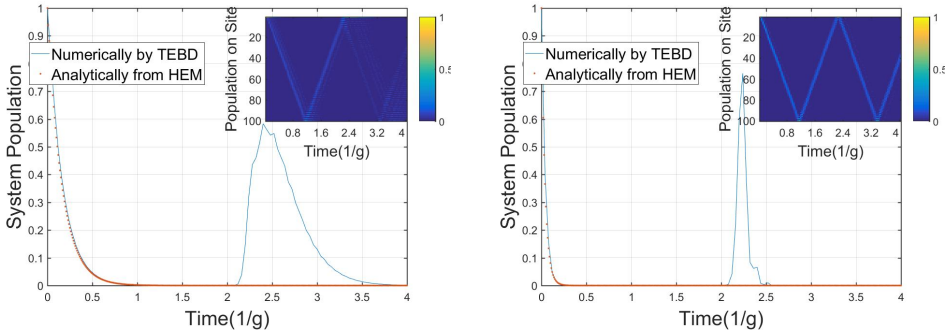

(a) (b)

Figure 5.1: Plot of system population determined numerically by TEBD and analytically from the solution of QLE for different coupling constant $(a)c_0 = 1$, $(b)c_0 = 2$. The parameters for TEBD simulation are given as: cutoff frequency $\epsilon = 100[g]$ (g is the inverse of density of states), number of sites for the bath $N = 101$, Schmidt number $(\chi) = 15$, size of local Hilbert space $(M) = 4$, time step $\delta t = 10^{-2}g^{-1}$. In the inset the image plot the population of the sites shows how the recurrence is occurring from the boundary.

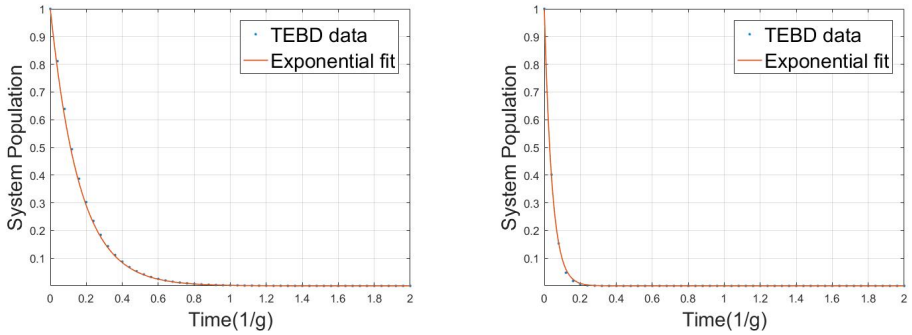

(a) (b)

Figure 5.2: Plot of system population determined by TEBD and an exponential fit of the data for the different coupling constant $(a)c_0 = 1$, $(b)c_0 = 2$. The parameters for TEBD simulation are same with Fig. 5.1

5.1.1 Curve Fit and Estimation

Here, we fit the TEBD numerical data with the best possible exponential curve ($a * \exp[-bt]$) using least absolute residuals (LAR) method determined by Levenberg-Marquardt algorithm [93] to estimate the rate of dissipation. In order to compare the analytics and numerics, one must ignore the rise-up of the system population due to the recurrence of particle from the end. The system population determined by TEBD and its fitted curve both are plotted in the Fig. 5.2. It is to be noted that the numerically determined decay rate is little less than the analytically determined decay rate, which happens due to the fact that the time error introduced from the Suzuki-Trotter decomposition, which is discussed in the Appendix B.

5.2 Thermal Bath and Evolution of Open Quantum System (for Simple S/B Coupling)

We study the time dynamics and the steady-state behavior of the system in the presence of a thermal bath for a simple S/B coupling model. The dynamics of the system field is described by QLE given in Eq. (2.32). The model is similar to the model chosen in Sec. 5.1, the only difference is that a thermal bath is chosen this time instead of an empty bath. We employ the numerical model for the thermalization dynamics of open quantum systems for the first time, which includes generating the thermal bath using minimally entangled typical thermal state algorithm explained explicitly in Sec. 4.2 and couple the thermal bath to an empty system to observe its evolution. In this case, Hahn polynomial is preferred over Legendre polynomial for the transformation of the system bath coupling model to 1D chain model for having linear dispersion relation which is shown in Fig. 4.4. The nonlinear dispersive property of the Legendre polynomial introduces unwanted error while determining the population spectrum of the bath. Also, we consider a realistic picture where the resonating frequency of the system (ω_c) is much larger than the cutoff window (ϵ) (the lower cutoff $\omega_c - \epsilon > 0$). The idea of such kind of modeling has been introduced due to the fact that few modes of the bath around the resonating mode of the system are coupled. The analytical estimation of the dynamics of the system population is given in the following section.

5.2.1 Analytics of System Dynamics in Presence of Thermal Bath

Integrating QLE of a simple S/B coupling model given in the Eq. 2.32, we get the time dynamics of the field operator of the system as

$$a(t) = -i\sqrt{\frac{\gamma}{2\pi D}}\sum_k \frac{b_k(t_0)}{-i(\omega_k-\omega_c)+\frac{\gamma}{2}}\{e^{-i\omega_k(t-t_0)} - e^{-(i\omega_c+\gamma/2)(t-t_0)}\}. \tag{5.1}$$

This determines the population of the system, which is given by

$$\langle a^\dagger a\rangle(t) = \frac{1}{2\pi D}\sum_k |\frac{\sqrt{\gamma}}{(\frac{\gamma}{2}-i(\omega_k-\omega_c))}\left[e^{-i(\omega_k-\omega_c)(t-t_0)} - e^{-\frac{\gamma}{2}(t-t_0)}\right]|^2\langle b_k^\dagger(t_0)b_k(t_0)\rangle \tag{5.2}$$

The initial thermal population distribution of the bath is

$$\langle b_k^\dagger(t_0)b_k(t_0)\rangle = \frac{1}{e^{\beta\omega_k}-1}, \qquad \text{when } k\in[-N,N]. \tag{5.3}$$

The thermal population of the system given in the Eq. (5.2) is given by

$$\langle a^\dagger a\rangle(t) = \sum_{\omega_c-\epsilon}^{\omega_c+\epsilon} AI_k + BJ_k, \tag{5.4}$$

where

$$I_k = \frac{\gamma/2\pi D}{[(\omega_k-\omega_c)^2+(\frac{\gamma^2}{4})]}\frac{1}{[e^{\beta\omega_k}-1]} \tag{5.5a}$$

$$J_k = \frac{(\gamma/2\pi D)\cos((\omega_k-\omega_c)(t-t_0))}{[(\omega_k-\omega_c)^2+(\frac{\gamma^2}{4})]}\frac{1}{[e^{\beta\omega_k}-1]} \tag{5.5b}$$

and

$$A = (1+e^{-\gamma(t-t_0)}) \tag{5.6a}$$

$$B = -2e^{-\gamma(t-t_0)/2}. \tag{5.6b}$$

We see that the time dynamics of the system is dependent on three parameters: the temperature, rate of dissipation and the cutoff frequency. In the following section, we

discuss how these parameters effect on the modeling and the steady-state behavior of the thermal bath coupled system.

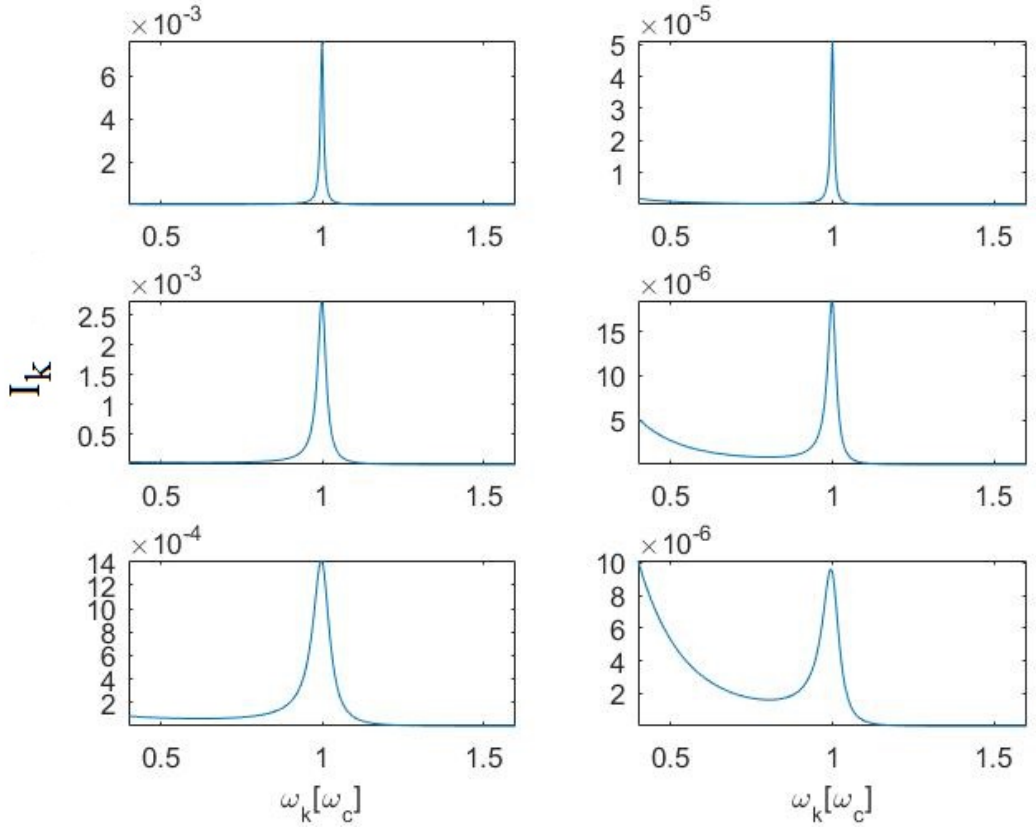

Figure 5.3: Plot of the function I_k for different temperature and coupling between the system and environment. The temperature is fixed for all plots in columns. $\beta = 5, 10[1/\omega_c]$ for the first and second column respectively, and the dissipation rate changes over rows. $\gamma = 0.0113, 0.0314, 0.0616\omega_c$ for the first, second and third row respectively. [Pub.- III] reproduced with permission.

Modeling constraint of a thermal bath coupled system

- *Cutoff frequency with temperature:*

  As the coefficient B goes away when we reach steady state, the system population is determined by the function I_k given in Eq. (5.5a). According to the system/bath formalism, the system population dynamics is dependent on few modes of the bath around the resonating mode of the system, and hence, one should consider the cutoff frequency (ϵ) in an way so that it can marginalize the the contribution of bath modes those are far away from the system mode. The idea behind the fact is the impact of the modes of the bath whose frequencies

are far away from the frequency of the mode of the system, have a minimum impact in the dynamics and the steady state of the system. Therefore, the function I_k should converge when the frequency (ω_k) goes far away from the cavity resonance frequency (ω_c). However, Fig. 5.3 shows that despite having a peak of the function I_k at resonating frequency of the system, the function rises up again for much lower frequency of the system mode ($\omega_k << \omega_c$), which is caused due to the fact that the exponential thermal population distribution function of the bath ($\frac{1}{[e^{\beta\omega_k}-1]}$) dominates over the Lorentzian function $\left(\frac{\gamma/2\pi D}{[(\omega_k-\omega_c)^2+(\frac{\gamma^2}{4})]}\right)$. In case of a lower temperature bath, the rising up occurs faster than that of a high temperature. One can bypass such kind of situations by reducing ϵ, but that rises up the ratio between γ and ϵ, which is the next topic of discussion. However, the thermal population always remains zero for all modes in a zero temperature bath. Hence, the system is not effected by the cutoff frequency while relaxing to the ground state.

- *Dissipation rate and cutoff frequency:*

  The model of open quantum system assumes that the S/B coupling is weak so that the second-order perturbation is a good approximation to study the dynamics, which makes the rate of dissipation to be much lower than the cutoff limit ($\gamma << \epsilon$), ensuring the Lorentzian function $\left(\frac{\gamma/2\pi D}{[(\omega_k-\omega_c)^2+(\frac{\gamma^2}{4})]}\right)$ to act like a delta function around ω_c. The reduction of the rate of dissipation makes the Lorentzian function closer to the delta function, and therefore it gives a more accurate result.

  Fig. 5.3 also plots the function I_k for different decay rates of the system, which shows that in case of low temperature bath, smaller values of decay rate are more demands for the translation of the analytics into the numerics. But in that case the system demands more time to reach the steady state. Therefore, it might not reach steady state sometime before the particle reflects back from the boundary. The recurrence time can be raised up by increasing the density of states, but some other constrains comes into the picture, as discussed at the end of this section.

  As the Lorentzian function becomes a delta function for a given condition $\gamma << \epsilon$, the steady-state population of the system is approximated to

$$\langle a^\dagger a\rangle(\infty) = \frac{1}{e^{\beta\omega_c}-1}, \tag{5.7}$$

  which is the thermal population of the bath corresponding to the mode of the system.

The numerical parameters have a substantial impact in the generation of the thermal

bath, and in the following part we investigate how the quality of simulation changes with the variation of those parameters, which is helpful for the optimization of numerics.

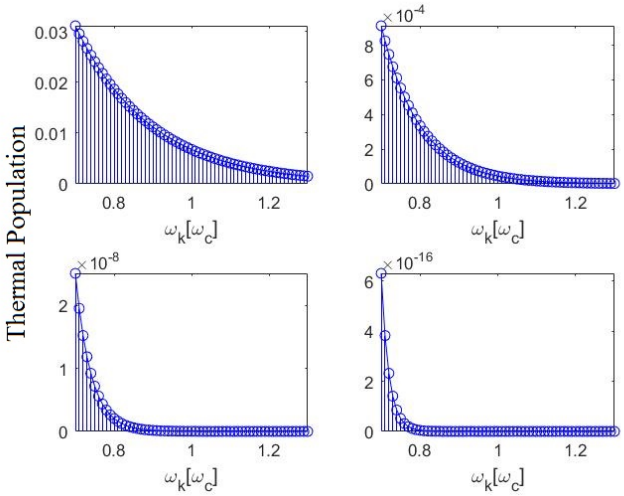

Figure 5.4: Population spectra for different temperature ($\beta = 5, 10, 25, 50[1/\omega_c]$). [Pub.- III] reproduced with permission.

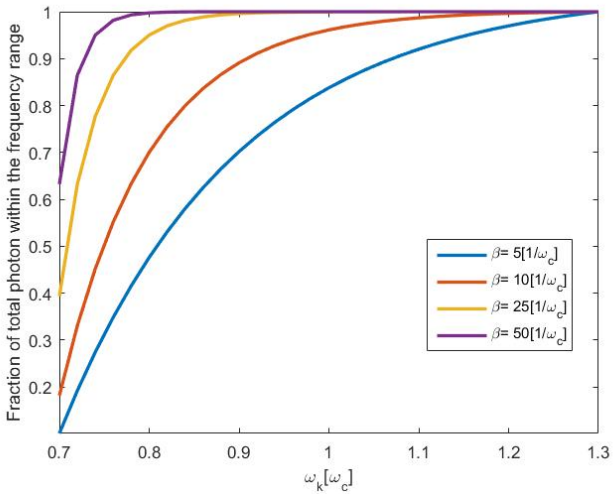

Figure 5.5: Cumulative probability distribution of photon occupation for different temperature ($\beta = 5, 10, 25, 50[1/\omega_c]$). [Pub.- III] reproduced with permission.

5.2.2 Generation of Thermal Bath Using TEBD

The quality of thermal state generated by METTS algorithm is dependent on two crucial parameters: temperature and the number of samples. Here, we discuss how

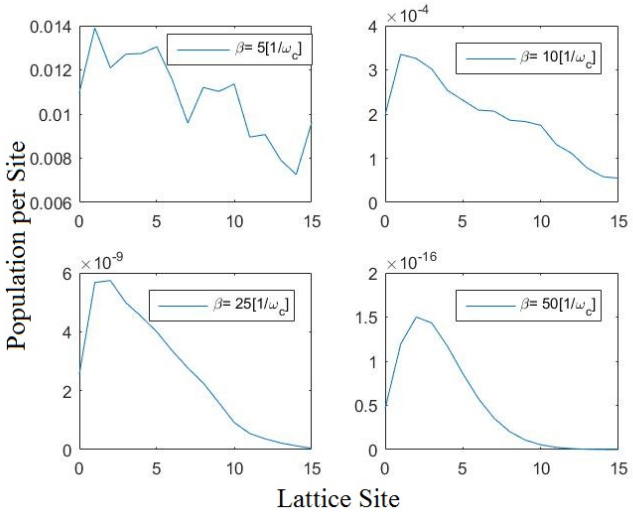

Figure 5.6: Population variation in the lattice sites for different temperature ($\beta = 5, 10, 25, 50[1/\omega_c]$). Frequency range of the bath $\omega_k \in [0.7, 1.3]\omega_c$. Number of METTS samples = 50. [Pub.- III] reproduced with permission.

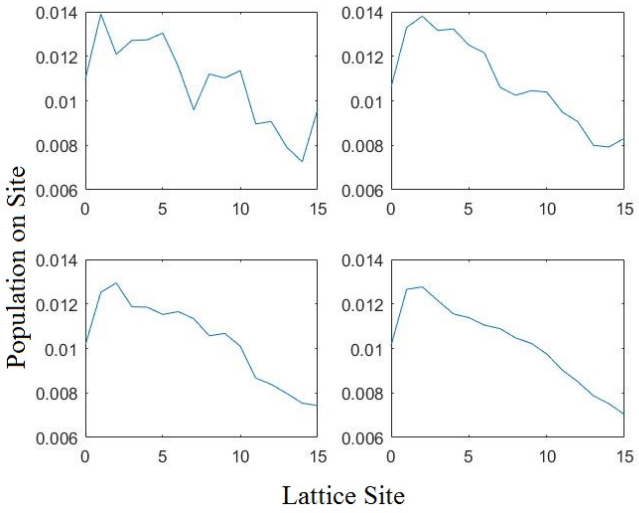

Figure 5.7: Population spectrum in lattice with the increment of number of METTS samples (50, 100, 500, 1000), for a fixed temperature ($\beta = 5[1/\omega_c]$). Frequency the bath belongs to the range $\omega_k \in [0.7, 1.3]\omega_c$. [Pub.- III] reproduced with permission.

the simulation is affected by these parameters.

Change of Temperature

We plot the frequency spectrum of thermal population of the bath in Fig. 5.4, where we see that as the thermal population reduces rapidly at lower temperature, less number of modes are needed to be considered. This is also hinted by the Fig. 5.5, where it is seen that in the case of low-temperature bath, the cumulative probability saturates faster, and therefore the requirement of number of METTS samples goes down. As a result, in Fig. 5.6, we see that the population distribution becomes smooth when we reduce the temperature keeping number of METTS fixed, which indicates a better quality of generation of thermal state. The comparison between analytical and numerical thermal population are given in Table. 5.1.

Even though the METTS algorithm performs better at low temperature, however, the overall thermal population goes down so significantly that after certain range the number looses reliability for numerical simulation. Hence, one can conclude by saying that the preparation of the bath through imaginary time evolution is quite promising to work with, but one has to compromise between the quality of preparation and the number of photons.

Table 5.1: Population of a thermal bath for different temperature. Analytical and numerical values are compared here for the frequency range $\omega_k \in [0.7, 1.3]\omega_c$. The number of METTS samples is kept fixed at 50 for all cases. [Pub.- III] reproduced with permission.

$\beta[1/\omega_c]$	Exact population	TEBD prepared population
5	0.1626	0.1730
10	0.0028	0.0030
25	3.9723×10^{-8}	3.9677×10^{-8}
50	7.2920×10^{-16}	7.9524×10^{-16}

Number of Samples

A thermal state at higher temperature is always preferable in order to obtain population at a significant level, which leads us to consider a large number of METTS samples when we do real time evolution. Fig. 5.7 shows an improvement of the quality of the preparation of the bath with the increment of the number of METTS samples, which is hinted by the improvement of the smoothness of the plot defining a significant pattern in the population distribution. However, the increment of the number of samples also costs computational time and resources.

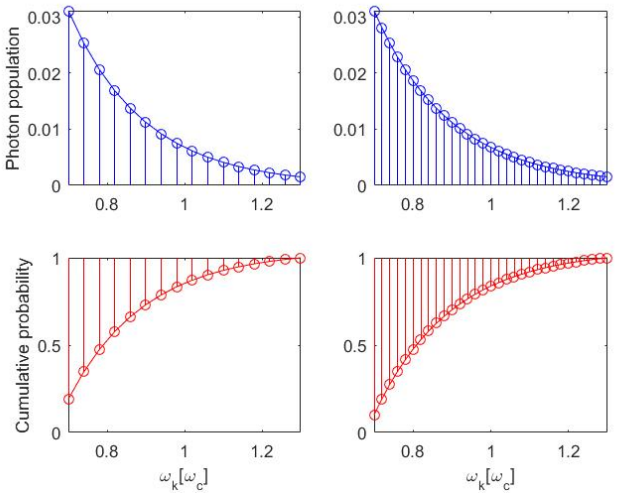

Figure 5.8: Variation in the number of modes in population spectra and cumulative probability distribution with the variation of density of state (DOS=25,50 $[1/\omega_c]$ respectively for first and second column). The temperature is fixed for both cases ($\beta = 5[1/\omega_c]$). [Pub.- III] reproduced with permission.

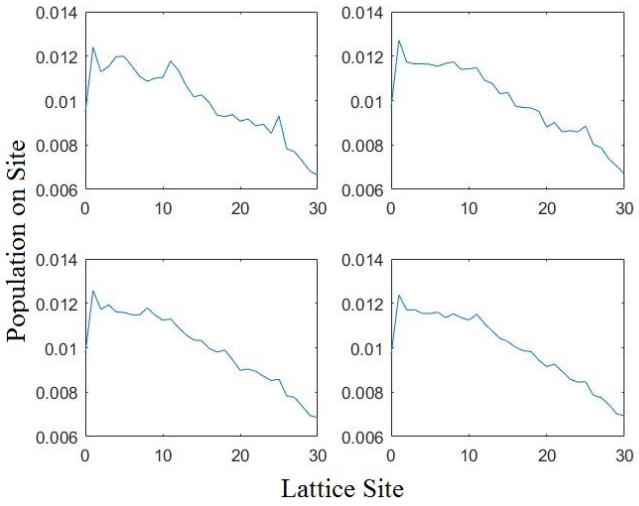

Figure 5.9: Population spectrum in lattice with the increment of number of METTS samples (500, 1000, 1500, 2500), for a fixed temperature ($\beta = 5[1/\omega_c]$). Frequency the bath belongs to the range $\omega_k \in [0.7, 1.3]\omega_c$. The density of states is fixed as $50[1/\omega_c]$. [Pub.- III] reproduced with permission.

Change of Density of States

The increment of density of states (DOS) increases the recurrence time, which gives the system more time for relaxation to reach the steady state. In case of weak coupling

between system and environment, more relaxation time is required, and therefore higher DOS is a better choice. The increment of DOS also increases the number of modes, which can be justified from the comparative study given in Fig. 5.8. Therefore, more number of METTS samples are required to represent such kind of thermal state, which comes out as a disadvantage. Another disadvantage of the increment of DOS is the increment of the requirement of the number of lattice sites, which causes more simulation time and memory space.

We plot the population per site for a fixed temperature ($\beta = 5[1/\omega_c]$) and a fixed range of cutoff frequency ($\omega_k \in [0.7, 1.3]\omega_c$) in Fig. 5.9 where we doubled the DOS compared to the Fig. 5.7. The figure represents how the population per site in the bath changes when we change of number of METTS samples. We see that the more number of METTS samples is required to represent a bath of higher density of state. The increase of DOS of the bath increases the total population, as seen from the Table. 5.2.

Table 5.2: Population of a thermal bath for different density of state. Analytical and numerical values are compared here for the frequency range $\omega_k \in [0.7, 1.3]\omega_c$ and temperature $\beta = 5[1/\omega_c]$. The number of METTS samples is kept fixed at 1000 for all cases. [Pub.- III] reproduced with permission.

DOS $[1/\omega_c]$	Exact population of bath	Population of TEBD prepared bath
25	0.1626	0.1630
50	0.3082	0.3088

5.2.3 Real Time Propagation of System Coupled to Thermal Bath

In this section, we evolve a system which was in ground state initially and coupled to a thermal bath of inverse temperature $\beta = 5[1/\omega_c]$. In Fig. 5.10, the time dynamics of the system population for different cutoff frequencies and coupling strength is shown, where the system population increases slowly in the case of lower values of dissipation constant. The recurrence time of the system is $150[1/\omega_c]$ and hence the plot is not given beyond that. The oscillation in the system population is gifted by the left tail of the Fig. 5.3 and it can be explained analytically from the Eq. (5.4). The higher value of γ also introduces more error in terms of oscillation to the dynamics of the system population. We see the steady state population of the system is comparable to the population of the bath at the resonating frequency of the system (ω_c), which is indicated by the Eq. (5.7) and marked by the black discrete line in Fig. 5.10. It shows that the numerical result is synchronous to the analytical value and both of them merge with the expected result when the system evolves for longer time.

Time evolution with higher cutoff frequency

The time evolution of the population of the system is also determined with the variation of the cutoff frequency of the bath. As anticipated by the Eq. (5.4), the extension of the lower cutoff frequency contributes more oscillation to the dynamics of the system population, which is visible when we compare between Fig. 5.10(a) and (b). For a fixed density of state, the increment of the cutoff frequency essentially demands a longer chain for the simulation, and hence we had to increase the length of the chain for the Fig. 5.10(b). Even though that longer chain demands more number of METTS samples for the preparation of a thermal state, we kept the number fixed for all simulations. Hence, for a fixed number of samples, the quality of the simulation is expected to be poor in case of a bath with higher cutoff frequency, which is also realized by comparing between Fig. 5.10(a) and (b). The quality of the simulation has been identified by looking at the smoothness of the plot which defines a significant pattern comparable with the analytics.

Time Evolution with Higher DOS of Bath

Both in Fig. 5.10(a) and (b), the system is unable to reach steady state due to slow decay rate (especially for $\gamma = 0.0113\omega_c$). Hence, we raised the recurrence time up by increasing the density of states (DOS) in Fig. 5.10(c) which ensures sufficient freedom to relax to the steady state for the system.

5.2.4 Time Evolution of Quadrature Fluctuations

The numerical technique moreover provides a promising platform for the investigation of the dynamics of open quantum systems. Here, real-time dynamics of the quadrature fluctuations is plotted in Fig. 5.11 comparing with its analytics, to investigate the applicability of the method in the physics of quantum Brownian motion. The arbitrary quadrature is defined as $X_\theta(t) = e^{i\theta}c(t) + e^{-i\theta}c^\dagger(t)$. We see the quadrature fluctuation becomes phase (θ) independent ($\delta X_\theta(t) = \sqrt{1 + 2n(t)}$) due to the fact that $\langle d_k(0)\rangle = \langle d_k^\dagger(0)\rangle = \langle d_k^2(0)\rangle = \langle {d_k^\dagger}^2(0)\rangle = 0$, and its time dynamics gives similar pattern to the population dynamics.

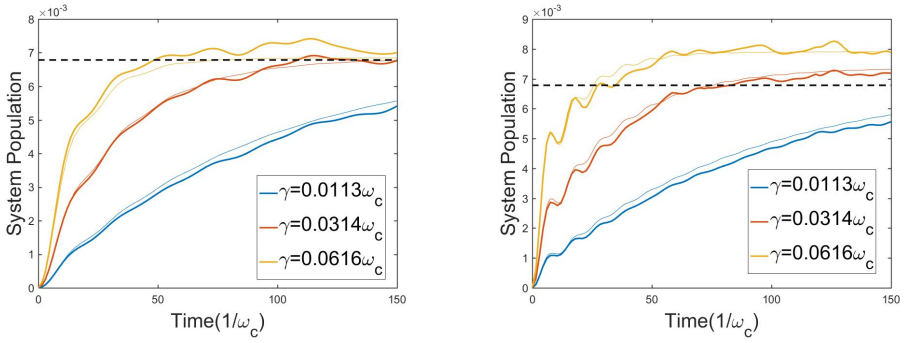

(a) (b)

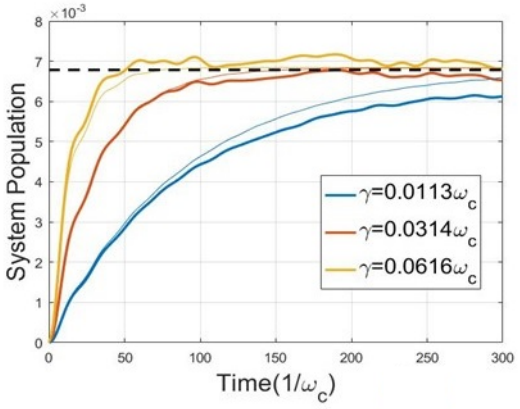

(c)

Figure 5.10: (a,b) Plot of the time evolution of the system population for different cutoff frequency: (a)$\epsilon = 0.3\omega_c$ is and (b)$\epsilon = 0.6\omega_c$. The length of the chain of the bath is 16 and 31, respectively, keeping the DOS fixed $DOS = 25[1/\omega_c]$. (c) Plot of the time evolution of the system population increasing the density of state $DOS = 50[1/\omega_c]$. The length of the chain of the bath is 31, and the cutoff frequency is ($\epsilon = 0.3\omega_c$) . The temperature ($\beta = 5[1/\omega_c]$) and number of METTS samples (4000) are kept fixed in all cases. Thick lines corresponds to the TEBD numerical result and the thin lines represent analytical results obtained from the Eq. 5.4. The black dashed line stands for the thermal population corresponding to the mode of the system expressed in Eq. 5.7. [Pub.- III] reproduced with permission.

.

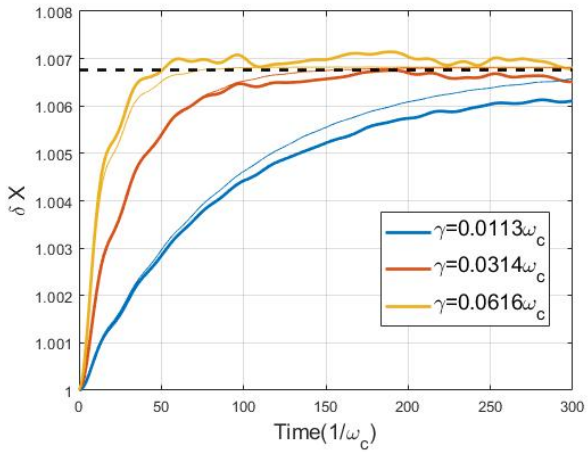

Figure 5.11: Plot of the time evolution of the quadrature fluctuation for different rate of dissipation. All other parameters are kept same with Fig. 5.10(c). Thick lines correspond to the TEBD numerical result and the thin lines represent their corresponding analytics. The black dashed line stands for the quadrature fluctuation corresponding to the mode of the system at same temperature. [Pub.- III] reproduced with permission.

5.3 Conclusion

We used the transformed 1D chain model of open quantum systems to study dissipation and thermalization dynamics of that open quantum system. We see the recurrence time of the real time evolution raises up linearly when the DOS increases. Also, it is seen that even though the METTS algorithm exhibits better performance at lower temperature, the overall model demands the thermal state to be prepared at higher temperature to get thermal population up to a significant level, which helps to overcome unwanted error in the system population dynamics, which is contributed by the lower limit of cutoff frequency. Hence, we consider more METTS samples which costs more computation resources. In conclusion, we say that the thermal bath generated numerically is satisfactory to work with, but the quality of the result should be compromised with computation resources. The numerical scheme could be a useful tool in the determination of the exact solution in case of nonlinear S/B coupling [94], single photon optomechanics [38, 39], and analyzing non-classical dynamics of nonlinear systems [95]. Also, the technique can be useful for the critical behaviors and non-Markovian dynamics spin-Bosson coupling models [63, 82–84].

6 Kerr Nonlinear Systems

The Kerr effect was discovered by John Kerr in 1875 [96], which shows quadratic electro-optic (QEO) effect and is seen in almost all materials. We generally determine the steady state solution of the Kerr nonlinear system in two different ways: semiclassically where we approximate the state of the system to a nearest coherent state, and quantum-mechanically, where the exact solution is estimated from the master equation of the density matrix of the system. The semicalssical estimation of dispersive and absorptive bistability both were derived from the Heisenberg equation of motion [97, 98]. However, the quantum-mechanical solution for absorptive [99] and dissipative cases [100] were determined by mapping master equation to the Fokker plank equation. Here, we aim to present both full quantum-mechanical and semiclassical calculations of the dispersive optical bistability. Afterwards, we intend to determine the dynamical behavior of Kerr nonlinear system. One way of approaching analytically could be applying the linearized approximation, where we linearize the quantum fluctuation over nonlinear steady-state field amplitude. The method exhibits accuracy when the impact of nonlineary is negligible, which means the steady state field of the system changes linearly with the change of the driving field. The linearized model fails when we increase the strength of the driving pump. In that situation, no such analytical model is useful to extract out information from the system. Therefore, we introduce TEND numerical model for the investigation of the transient and steady state behavior of the Kerr nonlinear system.

6.1 Hamiltonian Formulation

The Kerr effect exhibits distinction from from the Pockels effect (linear electro-optic effect) for having a change of induced refractive index proportional to the square of the electric field. The difference in index of refraction (Δn) is given by

$$\Delta n = \lambda K \mathcal{E}^2, \tag{6.1}$$

where λ is the wavelength of the light, K is the Kerr constant, and $\mathcal{E}$ is the strength of the internal electric field. For a general nonlinear model, the electric polarization field $\mathcal{P}$ changes to the electric field $\mathcal{E}$ according to

$$\mathcal{P} = \chi^{(1)} : \mathcal{E} + \chi^{(2)} : \mathcal{E}\mathcal{E} + \chi^{(3)} : \mathcal{E}\mathcal{E}\mathcal{E} + \cdots , \tag{6.2}$$

where $\chi^{(n)}$ is the $(n+1)$th rank of susceptibility tensor. In a Coulomb gauge the vector potential is determined from the equations

$$\mathcal{E} = -\frac{\partial \mathbf{A}}{\partial t} \tag{6.3a}$$

$$\mathcal{B} = \nabla \times \mathbf{A} \qquad \text{and} \tag{6.3b}$$

$$\nabla.\mathbf{A} = 0. \tag{6.3c}$$

Using Maxwell's equation $\nabla \times \mathcal{B} = \frac{1}{c^2}\frac{\partial \mathcal{E}}{\partial t}$(considering no displacement current), and vector identity $\nabla \times \nabla \times \mathbf{A} = \nabla(\nabla.\mathbf{A}) - \nabla^2\mathbf{A}$, one can find the wave equation for the vector potential $(\mathbf{A}(r,t))$ as

$$\nabla^2\mathbf{A} = \frac{1}{c^2}\frac{\partial^2 \mathbf{A}}{\partial t^2}. \tag{6.4}$$

The solution of the differential equation allows us to express the vector potential in the form of field operators as

$$\mathbf{A} = i\left(\frac{1}{2\omega_S \epsilon_0}\right)^{1/2}\left(a\mathbf{u}(r) - a^\dagger \mathbf{u}^*(r)\right), \tag{6.5}$$

where ω_S is the frequency of the system mode and the mode function $\mathbf{u}$ is defined to satisfy

$$\int_V \mathbf{u}(r)\mathbf{u}^*(r)\mathrm{d}^3\mathbf{r} = 1.$$

From here, one can deduce the corresponding electric and magnetic field by solving the differential equations given in the Eq. (6.3) as

$$\mathcal{E} = i\left(\frac{\omega_S}{2\epsilon_0}\right)^{1/2}\left(a\mathbf{u}(r) - a^\dagger \mathbf{u}^*(r)\right) \qquad \text{and} \tag{6.6a}$$

$$\mathcal{B} = i\left(\frac{\omega_S \mu_0}{2}\right)^{1/2}\left(a\mathbf{u}(r) - a^\dagger \mathbf{u}^*(r)\right) \tag{6.6b}$$

The Hamiltonian of of the system is determined by

$$H_S = \int \mathrm{d}r \left(\frac{\mathcal{B}^2}{2\mu_0} + \epsilon_0 \mathcal{E} \left[\frac{1}{2}\chi^{(1)} : \mathcal{E} + \frac{1}{3}\chi^{(2)} : \mathcal{E}\mathcal{E} + \frac{1}{4}\chi^{(3)} : \mathcal{E}\mathcal{E}\mathcal{E} + \cdots \right] \right). \tag{6.7}$$

In case of a Kerr nonlinear system the nonlinearity exhibits up to third order. From the expression of electric and magnetic field given in Eq. (6.6), one can obtain the anharmonicity parameter as

$$\chi" = (\frac{3\hbar\omega_S^2}{8\epsilon_0^2}) \int_V \chi^{(3)}(\mathbf{r}) |\mathbf{u}(r)|^4 \mathrm{d}^3\mathbf{r} \tag{6.8}$$

Essentially, the Hamiltonian becomes

$$H_S = \omega_S a^\dagger a + \chi'' {a^\dagger}^2 a^2 - i(a^\dagger E e^{-i\omega_L t} - a E^* e^{i\omega_L t}). \tag{6.9}$$

The last term of the right hand side is the coupling Hamiltonian, which represents system coupled to a large number of bosonic modes of the reservoir. Eventually, E is the amplitude of an external classical electric field, which is driving the system with an oscillation frequency ω_L. The field is given by $\vec{E}(t) = \vec{E} e^{-i\omega_L t} + \vec{E}^* e^{i\omega_L t}$.

6.2 Quantum Fluctuations via the Fokker-Planck equation

The equation of motion of the density operator (ρ_S) of the system is obtained from the Master equation given by Eq. (2.12) [8, 13],

$$\begin{aligned} \dot{\rho}_S = -i\Delta[a^\dagger a, \rho_S] - i\chi''[{a^\dagger}^2 a^2, \rho_S] \\ -([a^\dagger, \rho_S]E - [a, \rho_S]E^*) \\ -\frac{\gamma}{2}[(N+1)(a^\dagger a \rho_S + \rho_S a^\dagger a - 2a\rho_S a^\dagger) \\ +N(aa^\dagger \rho_S + \rho_S aa^\dagger - 2a^\dagger \rho_S a), \end{aligned} \tag{6.10}$$

where N is the thermal population of the thermal reservoir. Now, suppose that the observer switches to the frame of the driving field and observes the oscillation of the cavity mode modifies as $a_{orig} = e^{-i\omega_L t} a_{here}$. Hence, the detuned cavity frequency

becomes $\Delta = \omega_S - \omega_L$ (see Appendix A). γ is the decay rate of the internal field of the system, which comes from the coupling to the environment. The terms of the top row correspond to isolated time evolution of the system, the second row stands for the fluctuation due to external noise interference caused by the bath, and the last two rows represent dissipation of the system.

In the next step, we determine the Fokker-Planck equation of the corresponding master equation, which represents the time evolution of the quasiprobability distribution function [100]. As the Fokker-Planck equation does not have a generalized solution, we adopt a non-diagonal generalized P-representation which expresses the density matrix of the system in a spectrum of coherent basic state

$$\rho_S = \int P(\alpha,\beta)\frac{|\alpha\rangle\langle\beta^*|}{\langle\beta^*|\alpha\rangle}\mathrm{d}\alpha\mathrm{d}\beta, \tag{6.11}$$

where α, β are the amplitude of coherent states. $P(\alpha,\beta)$ is the P-function, which represents the probability of the density operator corresponds to coherent states of amplitude α and β.

6.2.1 Mapping of Master Equation to the Fokker-Planck Equation

The mapping of operators acting on the density matrix is (see Appendix A)

$$\begin{aligned} a\rho &\to \alpha P(\alpha,\beta) & a^\dagger\rho &\to (\beta - \frac{\partial}{\partial\alpha})P(\alpha,\beta) \\ \rho a^\dagger &\to \beta P(\alpha,\beta) & \rho a &\to (\alpha - \frac{\partial}{\partial\beta})P(\alpha,\beta). \end{aligned} \tag{6.12}$$

In this stage we try to get the P representation on the RHS and LHS of the Eq. 6.10. The P representation of the LHS of the Eq. 6.10 is $\frac{d}{dt}P(\alpha,\beta)$. Using the relations given in the Eq. 6.12 one can map the RHS of the Eq. 6.10 as

$$\begin{aligned} -i\Delta(a^\dagger a\rho_S - \rho_S a^\dagger a) \to -i\Delta\left[(\beta - \frac{\partial}{\partial\alpha})\alpha - (\alpha - \frac{\partial}{\partial\beta})\beta\right]P(\alpha,\beta) \\ = i\Delta\left[\frac{\partial}{\partial\alpha}\alpha - \frac{\partial}{\partial\beta}\beta\right]P(\alpha,\beta) \end{aligned}$$

$$-i\chi''\left[a^{\dagger 2}a^2\rho_S-\rho_S a^{\dagger 2}a^2\right]\rightarrow -i\chi\left[(\beta-\frac{\partial}{\partial\alpha})^2\alpha^2-(\alpha-\frac{\partial}{\partial\beta})^2\beta^2\right]P(\alpha,\beta)$$
$$=i\chi\left[\frac{\partial}{\partial\alpha}2\alpha^2\beta-\frac{\partial^2}{\partial\alpha^2}\alpha^2-\frac{\partial}{\partial\beta}2\beta^2\alpha+\frac{\partial^2}{\partial\beta^2}\beta^2\right]P(\alpha,\beta)$$

$$-(Ea^\dagger-E^*a)\rho_S+\rho_S(Ea^\dagger-E^*a)\rightarrow[-E(\beta-\frac{\partial}{\partial\alpha})+E^*\alpha+\beta E-(\alpha-\frac{\partial}{\partial\beta})E^*]P(\alpha,\beta)$$
$$=[\frac{\partial}{\partial\alpha}E+\frac{\partial}{\partial\beta}E^*]P(\alpha,\beta)$$

$$-\frac{\gamma}{2}(N+1)(a^\dagger a\rho_S+\rho_S a^\dagger a-2a\rho_S a^\dagger)\rightarrow$$
$$-\frac{\gamma}{2}(N+1)\left[(\beta-\frac{\partial}{\partial\alpha})\alpha+(\alpha-\frac{\partial}{\partial\beta})\beta-2\alpha\beta\right]P(\alpha,\beta)$$
$$=\frac{\gamma}{2}(N+1)\left[\frac{\partial}{\partial\alpha}\alpha+\frac{\partial}{\partial\beta}\beta\right]P(\alpha,\beta)$$

$$-\frac{\gamma}{2}N(aa^\dagger\rho_S+\rho_S aa^\dagger-2a^\dagger\rho_S a)\rightarrow$$
$$-\frac{\gamma}{2}N\left[(\beta-\frac{\partial}{\partial\alpha})\alpha+(\alpha-\frac{\partial}{\partial\beta})\beta-(\alpha-\frac{\partial}{\partial\beta})(\beta-\frac{\partial}{\partial\alpha})-(\beta-\frac{\partial}{\partial\alpha})(\alpha-\frac{\partial}{\partial\beta})\right]P(\alpha,\beta)$$
$$=-\frac{\gamma}{2}N\left[\frac{\partial}{\partial\alpha}\alpha+\frac{\partial}{\partial\beta}\beta-2\frac{\partial^2}{\partial\alpha\partial\beta}\right]P(\alpha,\beta).$$

Equating the P representation of the LHS and RHS one obtains

$$\frac{d}{dt}P(\alpha,\beta)=\Big[\frac{\partial}{\partial\alpha}(i\Delta\alpha+2i\chi''\alpha^2\beta+E+\frac{\gamma}{2}\alpha)+\frac{\partial}{\partial\beta}(-i\Delta\beta-i\chi''2\beta^2\alpha+E^*+\frac{\gamma}{2}\beta)$$
$$+\frac{\partial^2}{\partial\alpha^2}(-i\chi''\alpha^2)+\frac{\partial^2}{\partial\beta^2}(i\chi''\beta^2)+\frac{\partial^2}{\partial\alpha\partial\beta}(\gamma N)\Big]P(\alpha,\beta). \tag{6.13}$$

Note that the partial differential equation is describing the time evolution of the quasiprobability distribution of a state of a system under the influence of random forces, and this is why it is called quantum Fokker-Planck equation of the open quantum system. One can remind the parallel picture of the classical Fokker-Planck equation which is discussed explicitly in Appendix A. Eq. (6.13) can be represented in the form of a matrix equation as

$$\frac{d}{dt}P(\alpha,\beta)=\sum_{i=1,2}\frac{\partial}{\partial\xi_i}\left[-A_i(\xi)+\frac{1}{2}\sum_{j=1,2}\frac{\partial}{\partial\xi_j}B_{i,j}(\xi)\right]P(\xi), \tag{6.14}$$

where $\xi_1 = \alpha$ and $\xi_2 = \beta$. The quantities A and B are defined as

$$A = -\begin{pmatrix} i\Delta\alpha + 2i\chi''\alpha^2\beta + E + \frac{\gamma}{2}\alpha \\ -i\Delta\beta - i\chi''2\beta^2\alpha + E^* + \frac{\gamma}{2}\beta \end{pmatrix} \quad \text{and} \tag{6.15a}$$

$$B = 2\begin{pmatrix} -i\chi''\alpha^2 & \frac{\gamma}{2}N \\ \frac{\gamma}{2}N & i\chi''\beta^2 \end{pmatrix}. \tag{6.15b}$$

6.2.2 Potential Condition for Steady State Solution

The steady state situation of the system is considered when the system relaxes after the occurrence of all possible transition, i.e. time evolved state after a long time. As the system does not change in this situation one can simply consider that the left-hand side of the Eq. (6.14) is zero, and arrives at the condition

$$\sum_{i=1,2} \frac{\partial}{\partial \xi_i} \left[-A_i(\xi) + \frac{1}{2} \sum_{j=1,2} \frac{\partial}{\partial \xi_j} B_{i,j}(\xi) \right] P(\xi) = 0. \tag{6.16}$$

The situation holds in case of even more simplified condition

$$A_i(\xi)P(\xi) = \frac{1}{2}\frac{\partial}{\partial \xi_j} B_{i,j}(\xi)P(\xi), \tag{6.17}$$

which implies

$$B_{i,j}\frac{\partial \ln P}{\partial \xi_j} = 2A_i - \frac{\partial B_{i,j}}{\partial \xi_j}. \tag{6.18}$$

Considering $P(\xi) = \exp(-\phi(\xi))$, one arrives at

$$-\frac{\partial \phi(\xi)}{\partial \xi_j} = (B^{-1}_{i,j}) \left(2A_i - \frac{\partial B_{i,j}}{\partial \xi_j} \right) \equiv F_j(\xi). \tag{6.19}$$

If we consider F_i as the generalized force, $\phi(\xi)$ must be corresponding potential. In order to integrate the differential equation the following condition has to be satisfied

$$-\frac{\partial^2 \phi(\xi)}{\partial \xi_j \partial \xi_i} = \frac{\partial F_j(\xi)}{\partial \xi_i} = \frac{\partial F_i(\xi)}{\partial \xi_j} = -\frac{\partial^2 \phi(\xi)}{\partial \xi_i \partial \xi_j}. \tag{6.20}$$

The condition indicates that the multivariate integral is independent of the path of integration. In the case of one dimensional case, the potential condition is always

satisfied. The turning point of the potential appears when the following condition is satisfied

$$2A_i = \sum_j \frac{\partial B_{i,j}}{\partial \xi_j}. \tag{6.21}$$

Such a case, where the diffusion matrix is diagonal and constant ($B_{i,j} = W\delta_{i,j}$), the differential equation becomes

$$-\frac{\delta\phi}{\delta\xi_i} = \frac{2A_i}{W}. \tag{6.22}$$

Hence, one can say that the turning point is a deterministic condition, i.e. where the steady-state solutions are obtainable.

6.2.3 Correlation Function

The diffusion matrix given in Eq. (6.15b) is neither diagonal nor constant. So, the formula given in the Eq. (6.22) is not useful for the determination of the correlation functions. Hence, we determine the generalized force $F(\xi)$ given in the Eq. (6.19), which is given by

$$\begin{aligned}
F_1(\xi) = (B_{1,1}^{-1})\left(2A_1 - \frac{\partial B_{1,1}}{\partial\alpha}\right) &= (-i\chi''\alpha^2)^{-1}(-i\Delta\alpha - 2i\chi''\alpha^2\beta - E - \frac{\gamma}{2}\alpha + 2i\chi''\alpha) \\
&= \left(\frac{\Delta}{\chi''\alpha} + 2\beta + \frac{E}{i\chi''\alpha^2} + \frac{\gamma}{2i\chi''\alpha} - \frac{2}{\alpha}\right) \\
F_2(\xi) = (B_{2,2}^{-1})\left(2A_2 - \frac{\partial B_{2,2}}{\partial\beta}\right) &= (i\chi''\beta^2)^{-1}(i\Delta\beta + 2i\chi''\beta^2\alpha - E^* - \frac{\gamma}{2}\beta - 2i\chi''\beta) \\
&= \left(\frac{\Delta}{\chi''\beta} + 2\alpha - \frac{E^*}{i\chi''\beta^2} - \frac{\gamma}{2i\chi''\beta} - \frac{2}{\beta}\right).
\end{aligned} \tag{6.23}$$

One can check whether the condition of integratability given in Eq. (6.20), is satisfying in this case ($\frac{\partial F_1}{\partial\beta} = 2 = \frac{\partial F_2}{\partial\alpha}$). Now, in order to get the expression of $P(\alpha,\beta)$, we determine the potential by integrating the generalized force term over two different independent paths $0,0 \to \alpha,0$ and $\alpha,0 \to \alpha,\beta$

$$\begin{aligned}
P(\alpha,\beta) &= \exp\left[\int_{\alpha,0}^{\alpha,\beta}\int_{0,0}^{\alpha,0}(F_1\mathrm{d}\alpha + F_2\mathrm{d}\beta)\right] \\
&= \exp\left[(\frac{\Delta}{\chi''} + \frac{\gamma}{2i\chi''} - 2)\ln\alpha + \frac{E}{i\chi''\alpha} + 2\beta\alpha + (\frac{\Delta}{\chi''} - \frac{\gamma}{2i\chi''} - 2)\ln\beta - \frac{E^*}{i\chi''\beta}\right] \\
&= \alpha^{[\frac{\Delta}{\chi''} + \frac{\gamma}{2i\chi''} - 2]}\beta^{[\frac{\Delta}{\chi''} - \frac{\gamma}{2i\chi''} - 2]}\exp\left(2\alpha\beta - \frac{E}{i\chi''\alpha} + \frac{E^*}{i\chi''\beta}\right).
\end{aligned} \tag{6.24}$$

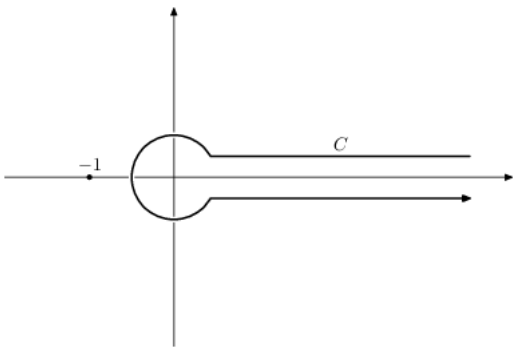

Figure 6.1: Hankel contour starts at $+\infty$ at real axis goes towards 0 and encircles 0 in a counter clockwise direction and returns back to $+\infty$.

Clearly, the function diverges in the usual complex integration domain. This says the P representation does not exist in a steady-state until it becomes a determinable special function. To determine the moments, one has to accept that the P function is given in the complex domain. We have exposed the domain of integration in the latter section. However, if the driving field E is real $E = E^* = E_0$, the normalization integral can be written as

$$I(p,q) = \int_c \sum_n \frac{2^n}{n!} x^{-p-n} y^{-q-n} \exp\left[-\frac{E_0}{i\chi''}(x-y)\right] \mathrm{d}x\mathrm{d}y, \tag{6.25}$$

where $p = [\frac{\Delta}{\chi''} + \frac{\gamma}{2i\chi''}], q = [\frac{\Delta}{\chi''} - \frac{\gamma}{2i\chi''}]$ and $x = \frac{1}{\alpha}$ and $y = \frac{1}{\beta}$. The integral is determinable in terms of a sum of "Gamma" function integrals. The reciprocal of the "Gamma" function is defined as

$$[\Gamma(t)]^{-1} = \left(\frac{1}{2\pi i}\right) \oint_H (-w)^{-t} \exp(-w)\mathrm{d}w. \tag{6.26}$$

Here, the variable w is defined along the Hankel contour which starts at $+\infty$ at the real axis, goes towards the origin and encirculating the origin in a counterclockwise direction returns back to $+\infty$ through another sheet. The contour is shown in the Fig. 6.1. In this case, The branch point is located at origin, and the branch cut is defined along the positive real axis. Using the above expression, one can express the integral $I(p,q)$ as

$$I(p,q) = -4\pi^2 \sum_n \frac{2^n (-1)^{q+n-1} (-E_0/i\chi'')^{p+q+2(n-1)}}{n!\Gamma(p+n)\Gamma(q+n)}. \tag{6.27}$$

This is a transcendental series, which can be written in terms of well defined generalized ${}_0F_2$ hypergeometric series

$$F\Big([],[p,q],z\Big)=\sum_n \frac{z^n\Gamma(p)\Gamma(q)}{n!\Gamma(p+n)\Gamma(q+n)}. \tag{6.28}$$

Introducing the above expression, finally we express the normalization integral as

$$I(p,q)=\left(\frac{4\pi^2(-1)^p[E_0/i\chi'']^{p+q-2}}{\Gamma(p)\Gamma(q)}F\big([],[p,q],2[E_0/i\chi'']^2\big)\right). \tag{6.29}$$

As the generalized P representation is a normally ordered representation, the normal order averages of the operator moments can be calculated as

$$\langle(a^\dagger)^m(a)^n\rangle=\int P(\alpha,\beta)\beta^m\alpha^n\mathrm{d}\alpha\mathrm{d}\beta. \tag{6.30}$$

In order to get observables, one has to calculate the moments and divide it by normalization factor. In this case, we see the moments are the same function as the normalization factor, but with a replacement of (p,q) by $(p+n,q+m)$. Essentially, we get the moment calculating generalized function as

$$G^{(m,n)}=\langle(a^\dagger)^m(a)^n\rangle=\left(\frac{(-1)^n[E_0/i\chi'']^{(m+n)}\Gamma(p)\Gamma(q)F\big([],[p+n,q+m],2[E_0/\chi'']^2\big)}{\Gamma(p+n)\Gamma(q+m)F\big([],[p,q],2[E_0/\chi'']^2\big)}\right). \tag{6.31}$$

We calculate the mean of coherent field amplitude $\langle a\rangle$ and the second order correlation function $g^2(0)$ from the Eq. (6.31) as

$$\langle a\rangle=\left(\frac{[E_0/i\chi'']F\big([],[p+1,q],2[E_0/\chi'']^2\big)}{pF\big([],[p,q],2[E_0/\chi'']^2\big)}\right) \tag{6.32a}$$

$$g^2(0)=\frac{\langle(a^\dagger)^2a^2\rangle}{\langle a^\dagger a\rangle^2}=\left(\frac{pqF\big([],[p,q],2[E_0/\chi'']^2\big)F\big([],[p+2,q+2],2[E_0/\chi'']^2\big)}{(p+1)(q+1)[F\big([],[p+1,q+1],2[E_0/\chi'']^2\big)]^2}\right). \tag{6.32b}$$

6.3 Coherent State Approach

The equation of motion of the system field operators can be obtained from the quantum Langevin equation

$$\begin{aligned}\dot{a} &= -i\Delta a - 2i\chi'' a^\dagger a^2 - E - \frac{\gamma}{2}a \\ \dot{a}^\dagger &= i\Delta a^\dagger + 2i\chi'' {a^\dagger}^2 a - E^* - \frac{\gamma}{2}a^\dagger.\end{aligned} \tag{6.33}$$

Now, we replace the field operators by the coherent field amplitude ($\alpha \equiv \langle a \rangle$) of the system. When the system relaxes down to a steady state situation, we get the solutions following from the above equation

$$|E|^2 = |\alpha|^2 \left((\Delta + 2\chi''|\alpha|^2)^2 + \frac{\gamma^2}{4} \right). \tag{6.34}$$

The turning points are those points where $|E|$ holds its extreme values,

$$\frac{d|E|^2}{d|\alpha|} = 2|\alpha| \left(\Delta^2 + 8\Delta\chi''|\alpha|^2 + 12{\chi''}^2|\alpha|^4 + \frac{\gamma^2}{4} \right) = 0 \tag{6.35}$$

This yields the turning points

$$|\alpha|_s^2 = \frac{1}{6\chi''} \left(-2\Delta \pm \sqrt{\Delta^2 - 3\frac{\gamma^2}{4}} \right). \tag{6.36}$$

To investigate the regions of stability, we introduce a linearized analysis about the steady state by considering a small fluctuations about the steady state

$$\alpha(t) = \alpha_0 + a(t).$$

The first orders of the fluctuations leads to get the equation

$$\begin{bmatrix} \dot{a} \\ \dot{a}^\dagger \end{bmatrix} = -\mathbf{A} \begin{bmatrix} a \\ a^\dagger \end{bmatrix}, \tag{6.37}$$

where

$$\mathbf{A} = \begin{bmatrix} 4i\chi''|\alpha|^2 + \frac{\gamma}{2} + i\Delta & 2i\chi''\alpha^2 \\ -2i\chi''\alpha^{*2} & -4i\chi''|\alpha|^2 + \frac{\gamma}{2} - i\Delta. \end{bmatrix}$$

Now, according to the Routh-Hurwitz stability criterion, the roots of the characteristic polynomial of a linear system must have negative real parts, which yields to determine

$$\begin{aligned} \mathrm{Tr}\{\mathbf{A}\} &= \gamma > 0 \\ \mathrm{Det}\{\mathbf{A}\} &= \frac{\gamma^2}{4} + \Delta + 8\chi''\Delta|\alpha|^2 + 12\chi''^2|\alpha|^4 > 0. \end{aligned} \tag{6.38}$$

One can notice that $\mathrm{Det}\{\mathbf{A}\} = \frac{d(|E|^2)}{d(|\alpha|^2)}$. Hence, $\mathrm{Det}\{\mathbf{A}\} = 0$ is equivalent to finding a turning point and those are soft-mode instabilities. One can verify that for $|\alpha| < |\alpha|_s$ or $|\alpha| > |\alpha|_s$ the Hurwitz criterion gives stable eigenvalues. Typically, $|\alpha|_s$ is a real positive quantity and hence the Eq. (6.38) bounds the domain $\Delta < 0$ and $|\Delta| > 3\frac{\gamma^2}{4}$ to see the turning point.

6.4 Results

In order to justify the applicability of the numerical model, we compare the analytics and numerics by plotting the steady state system field and the second-order correlation function of the Kerr nonlinear system. The analytics is given explicitly in Eqs. (6.32) and (6.37), and the numerics is determined based on the Hamiltonian given in the Eq. (6.9), in two different methods: TEBD algorithm and the time propagation of Heisenberg equation of motion by solving the differential equation given in Eq. (6.33) using Euler's method. Initially, the bath is at zero temperature, and the transformation of the continuous modes of the bath to the discrete chain is done using Legendre polynomial given in the Sec. 4.3.2.

6.4.1 Steady-State Situation

In Fig. 6.2 (a), we have plotted the stationary value of the field of the system and the second-order correlation function determined analytically and numerically. We see the TEBD determined numerical values follow the quantum mechanical exact analytical solution obtained by solving the Fokker-Plank equation of the EOM of the density matrix, which is expressed in Eq. (6.32). It is also noticeable that there is a difference between the analytics and numerics, which is more visible in the transition region,

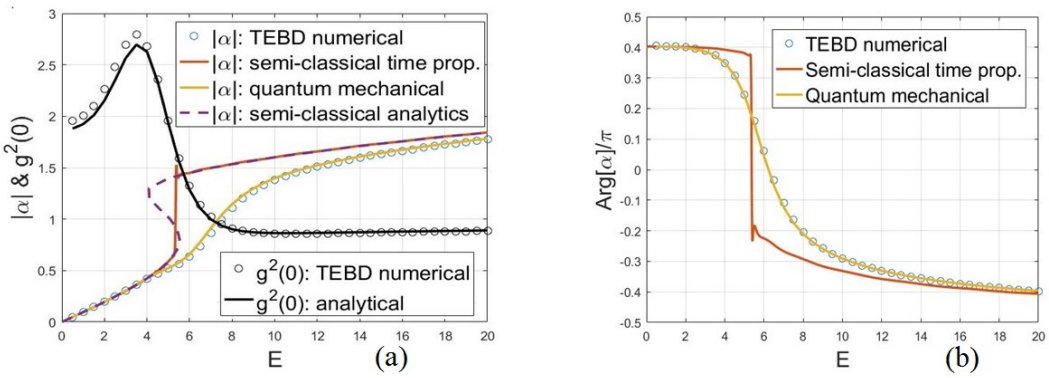

Figure 6.2: (a) Steady state field amplitude and second order correlation function, (b) phase plotted for $\Delta = -10, \chi" = 3, \gamma = 6.3$ with the variation of driving field amplitude. All quantities are in the units of g and the TEBD simulation parameters: $N = 50, \chi = 25, M = 15, \delta t = 10^{-2}g^{-1}$.. [Pub.- II] reproduced with permission.

caused by the fact that the TEBD numerics suffers time error due to Suzuki-Trotter decomposition. The semi-classically obtained analytical solution given in the Eq. (6.34) is also plotted in this figure, which determines the branch values and the transition region. The difference between semiclassical and quantum-mechanical solution is that the first solution exhibits bistability, whereas the second one does not. In the plot of $g^2(0)$ the peak indicates the raising-up of the fluctuations around the transition point. This happens because of the superposition of two coherent states around the transition region. Due to the fact that the coherent states are not mutually orthogonal, the state loses its classical nature, creating a non classical state. One can also visualize the turning points of the semi-classical solution from the Eq. (6.36). Comparing with the classical bistability, it is seen that the major shift in the simulation of the quantum dynamics occurs around the classically determined transition region. It is also to be noted that the numerical time propagation of the QLE obtained through Euler's method follows the analytically estimated semi-classical solution; where the transition occurs in between the boundary of analytically predicted region. The phase angle is also plotted in the Fig. 6.2 (b). As anticipated, the semi-classically and numerically determined value initially follows the lower branch and jumps to the upper branch in the interval of the transition region, whereas the TEBD determined value follows the quantum-mechanical exact solution which has a gradual change towards the upper branch.

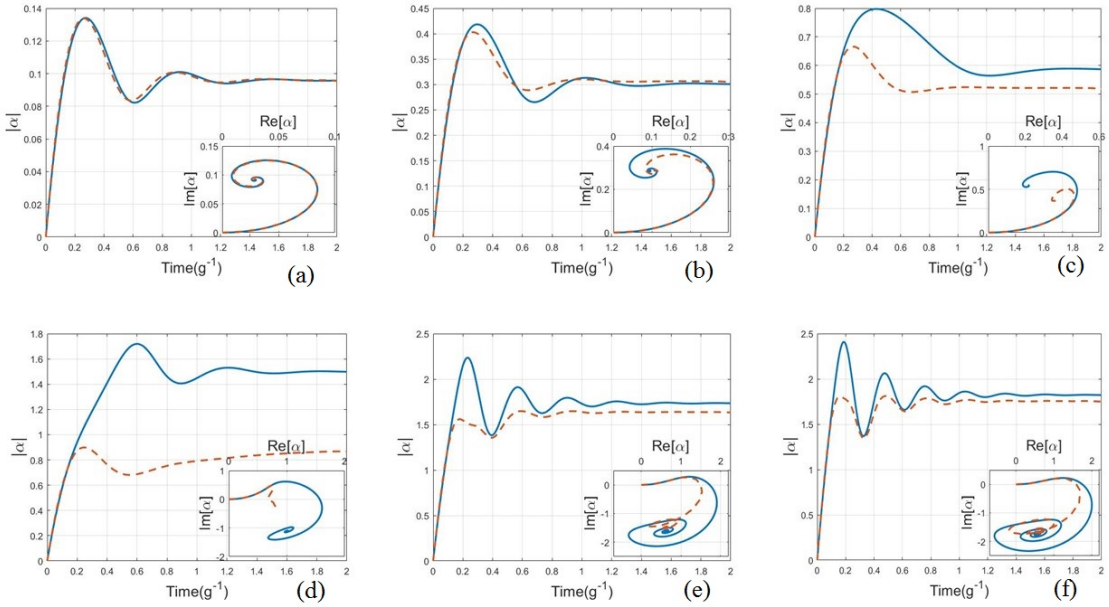

Figure 6.3: Time dynamics of the system field with the variation of driving field amplitude ((a)1, (b)3, (c)5, (d)7, (e)15, (f)19). The blue solid line and the red dashed lines correspond to the time propagation using Euler's method and TEBD numerical method, respectively. In inset we plot the trajectory of the system field, along with the phase. All other parameters remain same with Fig. 6.2. [Pub.- II] reproduced with permission.

6.4.2 Time Dynamics of System Field

The time dynamics of system field, plotted in Fig. 6.3, is determined numerically using two different methods. It is seen from the plot that the field stabilizes after suffering initial oscillation. The frequency of the oscillation decreases while increasing the strength of the driving pump when the system is in lower branch, but increases when it switches to upper branch. The reason behind the difference in two different methods is the fact that the semi-classical Euler's method gives the coherent field of the system which belongs to one among two branches, whereas the TEBD determined result keeps the superposition of both the branches while determining the time dynamics. The difference is more visible in the extreme transition region (Fig. 6.3(c) and (d)). Also, the interesting phenomenon is seen in the plot of the time evolution of the amplitude and the phase of the field of the system together which is given in insets, where we see that the system reaches two different steady states following completely opposite trajectories. The lower branch follows anticlockwise trajectory (Fig. 6.3(a), (b) and (c)) whereas the upper branch follows clockwise (Fig. 6.3(d), (e) and (f)). However, in the transition region we don't find any particular pattern due

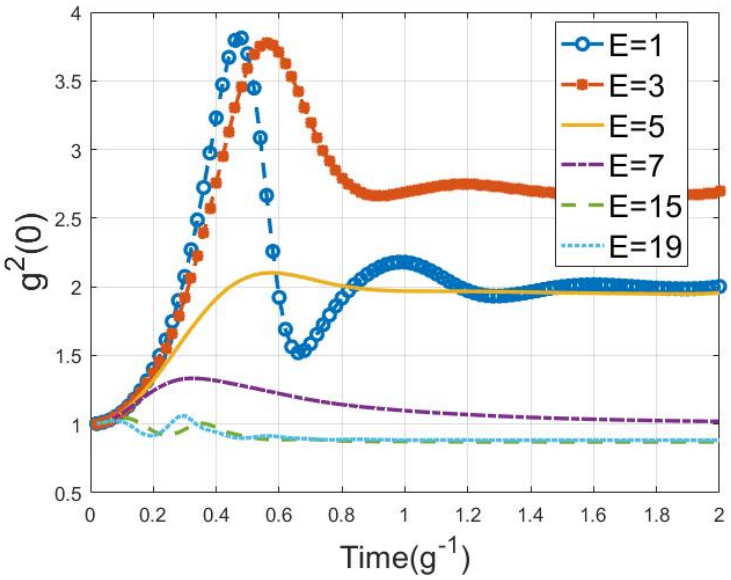

Figure 6.4: Plot of the second order correlation function with the variation of the driving field. All other parameters remain same with Fig. 6.2. [Pub.- II] reproduced with permission.

to the superposition of two coherent fields.

6.4.3 Second Order Correlation Function

Time evolution of the second order correlation function are plotted using TEBD algorithm in Fig. 6.4 where the correlation function moreover gives unit value towards a stable classical branch. Anticipating that, we see the time evolution of $g^2(0)$ deviates much from unit value around the transition region, which is caused by the superposition of two coherent states. This indicates that the evolution of the system goes through nonclassical states.

6.5 Conclusion

Analyzing of the steady state of the system, we observe that the TEBD numerical result follows the quantum mechanical exact solution and the time propagation of the system field by Euler's method obeys the semi-classical solution of the Heisenberg equation of motion. It is observed from the time dynamics of the Kerr system that the semi-classical Euler's method gives the coherent field of the system among two

possibilities, whereas TEBD numerical result determines superposition of them. The consequence is visualized in terms of a significant difference while determining system field using two different methods, which certainly increases around the classical transition region. Also, we see that TEBD determined $g^2(0)$ does not show its dynamics evolve as unit valued, especially when it is around the transition region, and indicating a non-classical state which is caused by the superposition of two coherent states.

7 Summary

In this thesis, a theoretical and numerical model has been presented to study the time evolution of open quantum systems aiming to be applied in a different types of systems. In particular, the methods have been designed targeting to be used in nonlinear systems and to study thermalization of open quantum systems.

In chapter 2, we have explained the theoretical tools used to study the dynamics of open quantum systems. These tools include quantum Langevin equation and master equation, and, in this section, we have given a detailed derivation of those equations, established a connection between them and their classical counterparts. The decoherence and dephasing dynamics for different types of S/B coupling are also included within this framework.

The chapter 3 presents an application of the theoretical modeling of an open quantum system, where we reported the way of deducing nonlinear QLEs from a nonlinear S/B coupling Hamiltonian. Overall, we have shown here how an effective nonlinear S/B coupling can be modified in the presence of impurities modeled as TLSs. For the small values of external field, we see the steady state system field does not change much from the steady state field obtained in the absence of nonlinear dissipation, but for the stronger external field the deviation becomes substantial from the solution of linear system. It is also seen that the fluctuation spectrum of the system shows dependency on phase angle.

In chapter 4, we have introduced a time-evolving block decimation algorithm for the numerical simulation of an open quantum system. The chapter starts with a description of the algorithm, explaining real and imaginary time evolution of one-dimensional many-body systems. We also explain another algorithm that describes the preparation of a minimally entangled typical thermal state, which is required to generate a thermal bath to study the thermalization of an open quantum system. In the end, we provide a mapping of the system-reservoir model to a semi-infinite discrete chain with nearest-neighbour interactions using orthogonal polynomials.

In chapter 5, we have presented the results of numerical simulation open quantum systems using TEBD algorithm and the comparison with analytics. We start with evolving a simple model of a free dissipating open quantum system where one quantum of boson dissipates freely in an empty bath. Both the numerical and analytical estimation presents a similar rate of dissipation of the system population. Afterward,

we present the numerical simulation of the thermalization of an open quantum system and compared it with analytical estimation. The results show that even though the METTS algorithm performs better at a lower temperature, we prefer to generate a higher temperature thermal bath to obtain the population to a significant threshold level. The another reason is to avoid unwanted error in the dynamical behavior of the system population which comes from the lower cutoff frequency limit. Hence, one must consider a large number of METTS samples which costs more computation resources, and therefore appears as a disadvantage.

Finally in chapter 6, we have studied the coherent driven Kerr nonlinear system discussing comparatively theoretical and numerical estimations of steady state behavior. The analytical method includes semi-classical solution of the Heisenberg equation of motion and quantum mechanical exact solution obtained by mapping the equation of motion of the density matrix of the system to a Fokker-Plank equation. The numerical approach not only includes TEBD algorithm, but also the time propagation of the system field by solving semi classical equation using Euler's method. It is observed that TEBD numerical result obeys quantum mechanical exact solution, whereas the time propagation using Euler's method follows the semi-classical analytical solution of the Heisenberg equation of motion. It is also seen that the semi-classical Euler's method estimates a coherent field of the system which is one among two solutions, but TEBD determined numerical result keeps the superposition of both of them. As a consequence, the TEBD obtained dynamics exhibits generation of non-classical states while evolving the Kerr nonlinear systems.

Appendix A:
Theoretical Appendix

Orthonormal Polynomials

Let us define an orthogonal polynomial $p_n(x)$ of degree n, which belongs to a space $p_n(x) \in \mathbb{P}$ with real coefficients, as

$$p_n(x) = \sum_{i=0}^{n} a_i x^i, \tag{A.1}$$

where $a_i \in \mathbb{R}$ and x is real (as it corresponds to the mode of the system). One can extend it to complex, but real coefficients are good enough in this formulation. For a positive nondecreasing and differentiable measure $\mathrm{d}\mu(x)$ defined in a finite interval $[a, b]$, all moments have finite value:

$$\int_a^b \mathrm{d}\mu(x) x^r < \infty, \;\; r = 0, 1, 2, ...$$

The inner product of any two polynomials $(p(x), q(x) \in \mathbb{P})$ is defined as

$$\langle p(x), q(x) \rangle_\mu = \int_a^b \mathrm{d}\mu(x) p(x) q(x), \;\; r = 0, 1, 2, ... ,$$

which yields the the Cauchy-Schwarz's inequality

$$|\langle p, q \rangle_\mu| \leq ||p||_\mu ||q||_\mu,$$

where norm of a polynomial $(||p||_\mu)$ is given by

$$||p||_\mu = \sqrt{\langle p(x), p(x) \rangle_\mu} > 0,$$

Orthogonal polynomial $p_n(x)$ satisfies the orthogonality relation

$$\langle p_m(x), p_n(x) \rangle_\mu = \int_a^b \mathrm{d}\mu(x) p_m(x) p_n(x) = \delta_{m,n},$$

The polynomial p_n is called monic if the leading coefficient $a_n = 1$. Then, it is denoted as $\pi_n(x)$. Any polynomial can be made monic, by dividing it by its leading coefficient. The orthogonality relation changes to

$$\langle \pi_n(x), \pi_m(x) \rangle_\mu = ||\pi_n||^2_\mu \delta_{m,n}. \tag{A.2}$$

The monic non-orthogonal polynomial can be recovered to an orthonormal polynomial as $p_n(x) = \pi_n(x)/||\pi_n||$. For a nonzero measure $\mathrm{d}\mu$, the monic polynomials are constructed by *Gram-Schmidt algorithm*:

$$\pi_k(x) = m_k(x) - \sum_{n=0}^{k-1} \left(\frac{\langle m_k, \pi_n \rangle_\mu}{\langle \pi_n, \pi_n \rangle_\mu} \right) \pi_n, \tag{A.3}$$

where $m_k(x) = x^k$ and $\pi_0 = 1$. One can check the orthogonality relation given in Eq. (A.2) recursively, from the structure given in the Eq.(A.3) as

$$\langle \pi_k, \pi_l \rangle_{k\rangle l} = \langle m_k, \pi_l \rangle - \sum_{n=0}^{k-1} \left(\frac{\langle m_k, \pi_n \rangle_\mu}{\langle \pi_n, \pi_n \rangle_\mu} \right) \langle \pi_n, \pi_l \rangle = \langle m_k, \pi_l \rangle - \left(\frac{\langle m_k, \pi_l \rangle_\mu}{\langle \pi_l, \pi_l \rangle_\mu} \right) \langle \pi_l, \pi_l \rangle = 0.$$

Hereafter, we deduce a useful recurrence relation for the monic polynomials from the Gram-Schmidt algorithm given in the Eq. (A.3), as

$$\pi_{n+1} = (x - \alpha_n)\pi_n(x) - \beta_n \pi_{n-1}(x), \quad n = 0, 1, 2, 3, \ldots, \tag{A.4}$$

where $\pi_{-1} \equiv 0$ and the recurrence coefficients are

$$\alpha_n = \frac{\langle x\pi_n, \pi_n \rangle_\mu}{\langle \pi_n, \pi_n \rangle_\mu} \qquad \text{and} \tag{A.5a}$$

$$\beta_n = \frac{\langle \pi_n, \pi_n \rangle_\mu}{\langle \pi_{n-1}, \pi_{n-1} \rangle_\mu} \tag{A.5b}$$

The corresponding recurrence relation for the non-monic orthogonal polynomial is

$$\tilde{p}_{n+1}(x) = (xC_k - A_k)\tilde{p}_n(x) - B_n \tilde{p}_{n-1}, \qquad n = 0, 1, 2, 3, \ldots \tag{A.6}$$

with $p_{-1} \equiv 0$. The coefficients of both recurrence relations are given by

$$A_n = \frac{\alpha_n}{\sqrt{\beta_{n+1}}}, \tag{A.7a}$$

$$B_n = \frac{\sqrt{\beta_n}}{\sqrt{\beta_{n+1}}} \qquad \text{and} \tag{A.7b}$$

$$C_n = \frac{1}{\sqrt{\beta_{n+1}}}. \tag{A.7c}$$

The orthonormal polynomials are used in the following section for the transformation of the S/B model to 1D semi-infinite chain model.

Transformation of Hamiltonian to a Rotating Frame

We start with considering the total Hamiltonian H_S and the wave function $|\Psi_S(t)\rangle$ at time t describes a system in the Schrödinger picture. The equation of motion of the wave function gives

$$i\frac{\partial|\Psi_S\rangle}{\partial t} = H_S|\Psi_S\rangle. \tag{A.8}$$

Now, suppose that the Hamiltonian contains two different parts

$$H_S = H_{0,S} + H_{1,S}, \tag{A.9}$$

which are provided by two different sources and therefore do not commute. Assume that $H_{1,S}$ is the external source and $H_{0,S}$ is contributed by the internal field. In this case one can represent the wave function in the interaction picture as

$$|\Psi_I\rangle = U^\dagger|\Psi_S\rangle, \tag{A.10}$$

where the unitary operator $U = \exp(-iH_{1,S}t)$. We now find the corresponding trans-

formed Hamiltonian $\tilde{H}$ from the Schrödinger equation of motion as

$$\begin{aligned} i\frac{\partial|\Psi_I\rangle}{\partial t} &= i\frac{\partial U^\dagger|\Psi_S\rangle}{\partial t} = iU^\dagger\frac{\partial|\Psi_S\rangle}{\partial t} + i\frac{\partial U^\dagger}{\partial t}|\Psi_S\rangle \\ &= U^\dagger H_S|\Psi_S\rangle - H_{1,S}U^\dagger|\Psi_S\rangle \\ &= \left(U^\dagger H_S U - H_{1,S}\right)U^\dagger|\Psi_S\rangle \\ &= \left(U^\dagger H_S U - H_{1,S}\right)|\Psi_I\rangle \end{aligned} \tag{A.11}$$

Therefore $\tilde{H} = \left(U^\dagger H_S U - H_{1,S}\right)$. Clearly, $U^\dagger$ does not commute with H_S and hence, we see a frequency shift while considering the system Hamiltonian.

Coherent Representation of Density Matrix

A master equation can be transformed to a c-number equation using Glauber-Sudarshan P representation of the density matrix. It is required to establish the relation between the operators and the corresponding c-number. For that, we represent the density matrix in coherent basis. Typically, a coherent state is represented on the basis of Fock states, as

$$|\alpha\rangle = e^{-\frac{|\alpha|^2}{2}}\sum_{n=0}^{\infty}\frac{\alpha^n}{\sqrt{n!}}|n\rangle = e^{-\frac{|\alpha|^2}{2}}e^{\alpha\hat{a}^\dagger}|0\rangle. \tag{A.12}$$

The operators, on the coherent state gives

$$a|\alpha\rangle = \alpha|\alpha\rangle \tag{A.13a}$$

$$\langle\alpha|a^\dagger = \alpha^*\langle\alpha|. \tag{A.13b}$$

In order to derive other relations we use Bargmann state ($||\alpha\rangle$), which is defined by

$$||\alpha\rangle = e^{\frac{|\alpha|^2}{2}}|\alpha\rangle = \sum_{n=0}^{\infty}\frac{\alpha^n}{\sqrt{n!}}|n\rangle, \tag{A.14}$$

so that

$$a^\dagger||\alpha\rangle = \sum_{n=0}^{\infty}\frac{\alpha^n}{\sqrt{n!}}\sqrt{n+1}|n+1\rangle = \frac{\partial}{\partial\alpha}||\alpha\rangle. \tag{A.15}$$

Similarly,

$$\langle\alpha||a = \frac{\partial}{\partial\alpha^*}\langle\alpha||. \tag{A.16}$$

The P-representation of the density matrix is given by

$$\rho = \int \mathrm{d}\alpha\mathrm{d}\beta^* \frac{||\alpha\rangle\langle\beta||}{\langle\beta|\alpha\rangle} e^{-\frac{(|\alpha|^2+|\beta|^2)}{2}} P(\alpha,\beta^*) = \int \mathrm{d}\alpha\mathrm{d}\beta^* ||\alpha\rangle\langle\beta|| e^{-\alpha\beta^*} P(\alpha,\beta^*). \tag{A.17}$$

Therefore, the operators on the density matrix give

$$\begin{aligned} a^\dagger\rho \quad &= \int \mathrm{d}\alpha\mathrm{d}\beta^* \left(\frac{\partial}{\partial\alpha}||\alpha\rangle\langle\beta||\right) e^{-\alpha\beta^*} P(\alpha,\beta^*) \\ &= \int \mathrm{d}\alpha\mathrm{d}\beta^* ||\alpha\rangle\langle\beta|| e^{-\alpha\beta^*} \left(\beta^* - \frac{\partial}{\partial\alpha}\right) P(\alpha,\beta^*), \end{aligned} \tag{A.18}$$

and

$$\rho a = \int \mathrm{d}\alpha\mathrm{d}\beta^* ||\alpha\rangle\langle\beta|| e^{-\alpha\beta^*} \left(\alpha - \frac{\partial}{\partial\beta^*}\right) P(\alpha,\beta^*). \tag{A.19}$$

Fokker-Planck Equation

The time evolution of the probability distribution of the velocity of a particle which is in Brownian motion under the influence of random forces, is treated by the Fokker-Planck equation. We formulate the equation in terms of the evolution of the conditional probabilities for a stationary random process. We also assume that the evolution goes through a Markov process where the future probabilities are determined by the most recently known value, not on the previous history. Therefore, the conditional probability is given by

$$P_n(y_1,t_1;y_2,t_2;...|y_n,t_n)dy_n = P_2(y_{n-1},t_{n-1}|y_n,t_n)dy_n \tag{A.20}$$

that lies between y_n and $y_n + dy_n$ at time t_n (where $t_1 < t_2 < t_3... < t_n$). The probability distributions p_n and the conditional probabilities P_n are related through

$$p_n(y_1,t_1;...;y_n,t_n) = p_{n-1}(y_1,t_1;...;y_{n-1},t_{n-1}) \times P_n(y_1,t_1;...;y_{n-1},t_{n-1}|y_n,t_n). \tag{A.21}$$

According to general probability theory, the two point conditional probability distribution satisfies Chapman-Kolmogorov equation, and, if the process is Markovian, the equation reduces to the Smoluchowski equation

$$P_2(y_1, t_1|y_3, t_3) = \int_{-\infty}^{\infty} dy_2 P_2(y_1, t_1|y_2, t_2) P_2(y_2, t_2|y_3, t_3). \tag{A.22}$$

Writing in terms of $P_2(y_0|y, t)$ where y_0 and y are the starting and ending point at time t, respectively, the Fokker-Planck equation is

$$\frac{\partial}{\partial t} P_2 = -\frac{\partial}{\partial y}[A(y)P_2] + \frac{1}{2}\frac{\partial^2}{\partial y^2}[B(y)P_2], \tag{A.23}$$

where

$$A(y) = \lim_{\delta t \to 0} \int_{-\infty}^{\infty} dy'(y' - y) P_2(y|y', \delta t) \qquad \text{and} \tag{A.24a}$$

$$B(y) = \lim_{\delta t \to 0} \int_{-\infty}^{\infty} dy'(y' - y)^2 P_2(y|y', \delta t) \tag{A.24b}$$

are the rate of growth of the mean and standard deviation, respectively. The equation can be solved with the initial conditions $P_2(y_0|y, 0) = \delta(y - y_0)$. The first term is a drift and the second to a diffusion of the distribution corresponding to a systematic bias and a residual average effect of negative and positive jumps, respectively.

Derivation

Considering $y_1 \to y_0, y_3 \to y, y_2 \to y - \eta$ and $t_2 - t_1 \to t, t_3 - t_2 \to \tau$, we express the Eq. (A.22) as

$$P_2(y_0|y, t + \tau) = \int_{-\infty}^{\infty} d\eta P_2(y_0|y - \eta, t) P_2(y - \eta|y, \tau), \tag{A.25}$$

where τ is a small time increment. Now, expanding the left hand side in a Taylor series of τ, and keeping upto the first order, we obtain

$$P_2(y_0|y, t + \tau) = P_2(y_0|y, t) + \frac{\partial P_2(y_0|y, t)}{\partial t}\tau \tag{A.26}$$

Now expanding $P_2(y_0|y - \eta, t)P_2(y - \eta|y, \tau)$ of the right hand side of the Eq. (A.25), we write

$$P_2(y_0|y-\eta,t)P_2(y-\eta|y,\tau) = \sum_{n=0}^{\infty} \frac{(-1)^n}{n!}\eta^n \frac{\partial^n}{\partial y^n} P_2(y_0|y-\eta,t)P_2(y-\eta|y,\tau), \quad \text{(A.27)}$$

Comparing with Eq. (A.26), we get

$$\frac{\partial P_2(y_0|y,t)}{\partial t} = \sum_{n=1}^{\infty} \frac{(-1)^n}{n!} \lim_{\tau\to 0} \frac{1}{\tau} \int_{-\infty}^{\infty} d\eta \eta^n \frac{\partial^n}{\partial y^n} P_2(y_0|y-\eta,t)P_2(y-\eta|y,\tau) \quad \text{(A.28)}$$

The evolution of the random process is conducted by small changes, and therefore, only first two moments $n = 1, 2$ of P_2 contribute, not higher moments increasing with τ^p (where $p > 1$) as $\tau \to 0$.

Appendix B:
Numerical Appendix

Free Dissipative Open Quantum Systems (T=0)

Here, we investigate about the simulation errors of the free dissipative system mentioned in the Sec. 5.1. This study will be useful to optimize the parameters in order to do the simulation efficiently compromising with the resources and a minimum amount of error. The errors appear in this numerical simulation in two ways: modeling error and numerical error. The first type of error comes from the canonical transformation of S/B coupling to 1D chain model and the second type is introduced due to the limitation of TEBD algorithm.

Modeling Error

In practice, we opt a model where the chain is having a finite length due to finite number of modes of the bath (Sec. 4.3.2), which introduces modeling error. Here, we investigate how the recurrence time changes when the modeling parameters change, and estimate the time of the first recurrence of the particle which is shown in Fig. 5.1.

- *Length of the chain:* In Fig. B.1a, we see a linear increment in the recurrence time when the length of the chain increases, which causes because of the reduction of the group velocity for photon while increasing of the number of sites. The group velocity is defined by $v_g = \frac{\delta\omega}{\delta k_N}$, where ω is the frequency, and k_N is the wavenumber determined by the number of lattice sites ($k_N \propto N$).
- *Cut-off frequency:* Fig. B.1b shows that recurrence time decreases with the increment of the cutoff frequency. This happens due to the fact that the increment of the cutoff frequency increases the group velocity, causing the phonon traveling faster in the lattice.

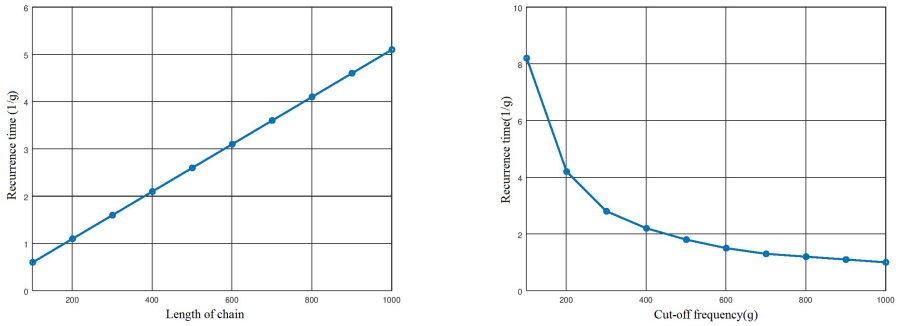

(a) (b)

Figure B.1: Variation of first recurrence time with the change of (a) the length of chain (for fixed x_{max}= 400) and (b) cut-off frequency (for fixed length of chain N= 400). g is the inverse of the density of states.

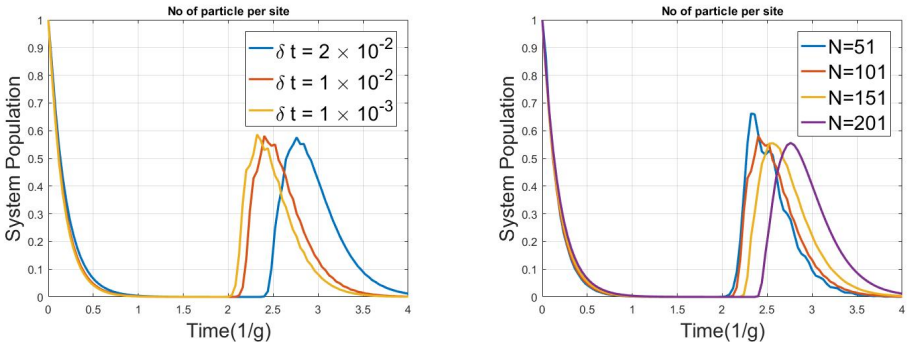

(a) (b)

Figure B.2: (a) Plot of time evolution of a free dissipative system for different time steps. Other parameters: $x_{max} = 100, N = 101, M = 4, \chi = 15, c_0 = 1$
(b) Plot of time evolution of a free dissipative system for different length of the chain. The cutoff frequency changes from 50 to 200g, as the density of states is kept fixed) . Other parameters: $\delta t = 1 \times 10^{-2} g^{-1}, M = 4, \chi = 15, c_0 = 1$

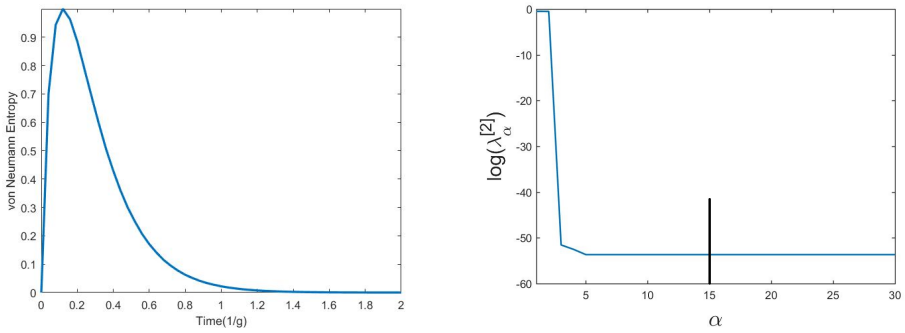

(a) (b)

Figure B.3: (a) Plot of the time evolution of the von Neumann entropy of the first site. Other parameters: $x_{max} = 100, N = 101, M = 4, \chi = 15, c_0 = 1$.
(b) Plot of the eigenvalues of the reduced density matrix (in logarithmic scale) when the entanglement is maximized. The black line shows the truncation point.

Numerical Error

As we discussed earlier in Sec. 4.1.4, there are two major error sources present in TEBD algorithm; they are time error and truncation error of the Hilbert space.

- *Suzuki-Trotter error:* The Suzuki-Trotter error in real time evolution concentrates in the overall phase and causes the time error (Sec. 4.1.4). Fig. B.2a, demonstrates an improvement of accuracy of the simulation while reducing time step which can be justified by Eq. (4.21). The error also increases while increasing the size of the system, which is indicated from the Eq. (4.31). Fig. B.2b justifies the phenomenon by exhibiting the increment of the time error with the length of the chain despite of the fact that the cutoff frequency increases proportionally. In this simulation, we increase the cutoff limit proportionally while increasing the length of the chain keeping the density of states is kept fixed.

- *Truncation error:* Here, we deal with only one photon which was located initially at the first site. Hence, the choice of the size of local Hilbert space is sufficient to represent a complete set. However, the truncation on the Schmidt spectrum (Sec. 4.1.4) could be an issue. To estimate a reasonable size of the Schmidt number, we plot the von Neumann entropy (given in Eq. (4.11)) associated with the entanglement between the system and the first site in Fig. B.3a. As the evolution of the state starts from a product state, the von Neumann entropy was zero at the beginning. The quantity increases initially and reaches to the maximum value, and then reduces with time.

  We estimate the Schmidt number when the entanglement is maximized. The Schmidt number should be chosen in such a way that the contribution of the

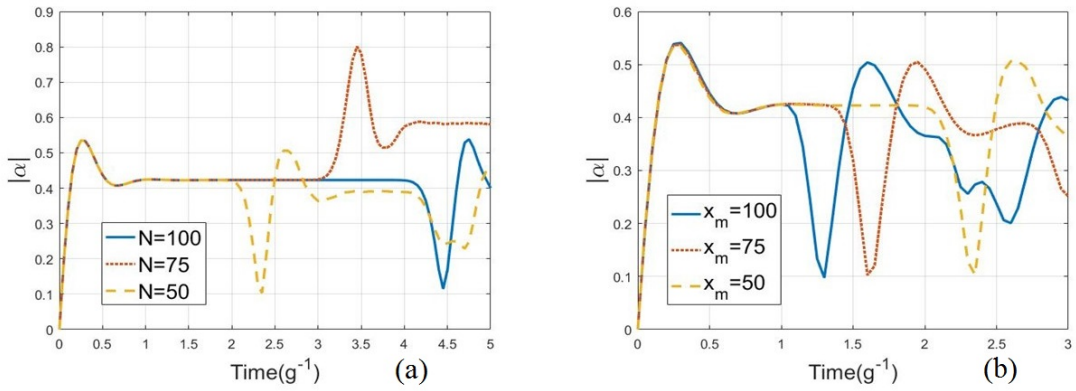

Figure B.4: Variation of recurrence time with the variation of (a) number of sites, (b) cutoff frequency. $E = 4$ and all other parameters remain same with Fig. 6.2. [Pub.-II] reproduced with permission.

eigenvalues after truncation is negligible when we compare with the accepted Schmidt spectrum (difference is in the order of magnitude). In Fig. B.3b we plotted the eigenvalues of the reduced density matrices in logarithmic scale when the entanglement is maximum between the system and the first site of the chain. The truncation is shown by the black line which shows that the choice of Schmidt number is reasonable in this case.

Kerr Nonlinear System (T=0)

The modeling and numerical error in the simulation of Kerr nonlinear system are discussed below.

Modeling Error

- *Length of the chain:* It is seen from the Fig. B.4(a) that the recurrence time increases with the increment of the length of the chain, which happens due to the fact that the increment of the number of sites reduces the group velocity for the particle to travel.
- *Cut off frequency:* The increment of the cutoff frequency increases the group velocity, which ensures the particle to travel faster in the lattice. This causes the reduction of the recurrence time which is visible in the Fig. B.4(b).

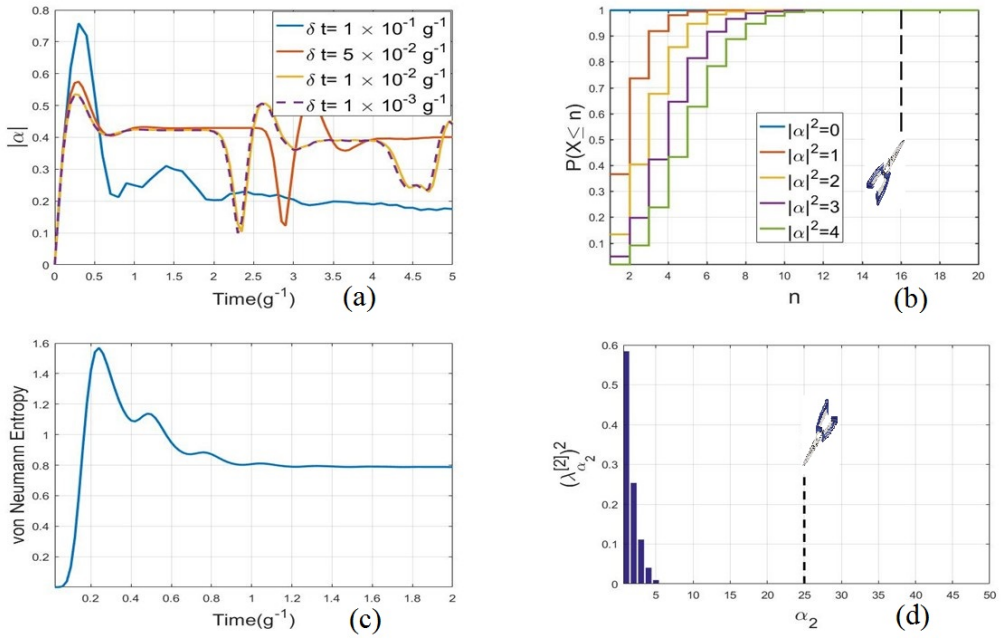

Figure B.5: (a) Time evolution of the system field with the variation of step size in TEBD simulation. (b) Plot of cumulative probability of a regular Poisson distribution for different mean values. The black line shows the truncation point in the Hilbert space. (c) Plot of the time evolution of the von Neumann entropy of the first site. (d) Plot of the eigenvalues of the reduced density matrix when the entanglement is maximized, and the black line shows the truncation point. For (a) $E = 4$ and (c,d) $E = 20$, and all other parameters remain same with Fig. 6.2. [Pub.- II] reproduced with permission.

Numerical Error

- *Suzuki-Trotter error:* From Fig. B.5(a), we see an improvement in the accuracy of the simulation with the reduction time step. The curves approach each other as time step decreases, and beyond the time step $10^{-2}g^{-1}$, any substantial improvement is not visible in the plot of system field.

- *Truncation error:* The *reasonable size* of Hilbert space is expected to be a size which is capable of expressing the field of the system with a negligible amount of error. The Poisson probability distribution of the coherent field generated in the system demands an infinite local Hilbert space to make the set complete, which is practically not possible. The occupation probability of boson of this coherent field ($|n\rangle$) is distributed in Fock basis according to $|\langle n|\alpha\rangle|^2 = \frac{1}{n!}(|\alpha|^{2n}e^{-|\alpha|^2})$. In Fig. B.5(b), we have shown the cumulative probability distribution estimates the reasonable size of local Hilbert space, accepting accuracy upto a significant extent.

  Afterwards, the von Neumann entropy is plotted in Fig. B.5(c) for the estimation of the reasonable size of the Schmidt number. The quantity is associated to the entanglement between the system and the first site ($S = -\sum_{\alpha_2}(\lambda^{[2]}_{\alpha_2})^2 \log_2(\lambda^{[2]}_{\alpha_2})^2$). It is seen to be zero at the beginning due to the fact that the evolution starts from a product state. It increases initially and reaches to the maximum value, and after that reduces with time.

  We estimate the Schmidt number for maximal entanglement between first two sites. The Schmidt number should be chosen in such a way that the eigenvalues after truncation contribute so less that they can easily be neglected. The eigenvalues of the reduced density matrices are plotted in Fig. B.5(d), and the truncation line confirms the choice of Schmidt number to be reasonable here.

References

[1] V. Gorini, A. Kossakowski, and E. C. G. Sudarshan. Completely positive dynamical semigroups of n level systems. *Journal of Mathematical Physics*, 17(5):821, 1976.

[2] G. Lindblad. On the generators of quantum dynamical semigroups. *Communications in Mathematical Physics*, 48(2):119, 1976.

[3] A. A. Markov. The theory of algorithms. *Trudy Mat. Inst. Steklov.*, 42(Acad. Sci. USSR, Moscow–Leningrad):3, 1954.

[4] A. D. Fokker. Die mittlere energie rotierender elektrischer dipole im strahlungsfeld. *Annalen der Physik*, 348(5):810, 1914.

[5] M. Planck. über einen satz der statistischen dynamik und seine erweiterung in der quantentheorie. *Sitzungsberichte der Preussischen Akademie der Wissenschaften zu Berlin*, 24:324, 1917.

[6] A. Kolmogoroff. Über die analytischen methoden in der wahrscheinlichkeitsrechnung. *Mathematische Annalen*, 104(1):415, 1931.

[7] N. N. Bogoliubov and N. M. Krylov. Fokker-planck equations generated in perturbation theory by a method based on the spectral properties of a perturbed hamiltonian. *Zapiski Kafedry Fiziki Akademii Nauk Ukrainian SSR*, 4:81, 1939.

[8] D. F. Walls and G. J. Milburn. *Quantum Optics*. Springer Study Edition. Springer-Verlag Berlin Heidelberg, 1 edition, 1994.

[9] H. M. Wiseman amd G. J. Milburn. *Quantum Measurement and Control*. Cambridge University Press, 1 edition, 2009.

[10] W. Heisenberg. Über quantentheoretische umdeutung kinematischer und mechanischer beziehungen. *Zeitschrift für Physik*, 33(1):879, 1925.

[11] C. Gardiner and P. Zoller. *Quantum noise: A Handbook of Markovian and Non-Markovian Quantum Stochastic Methods with Applications to Quantum Optics*. Springer series in synergetics. Springer, 2nd enlarged ed edition, 2004.

[12] D. S. Lemons and A. Gythiel. Paul langevins 1908 paper on the theory of brownian motion [sur la théorie du mouvement brownien, c. r. acad. sci. (paris) 146, 530-533 (1908)]. *American Journal of Physics*, 65(11):1079, 1997.

[13] C. W. Gardiner and M. J. Collett. Input and output in damped quantum systems: Quantum stochastic differential equations and the master equation. *Phys. Rev. A*, 31:3761, 1985.

[14] G. W. Ford, J. T. Lewis, and R. F. O'Connell. Quantum langevin equation. *Phys. Rev. A*, 37:4419, 1988.

[15] A. Rivas and S. F. Huelga. *Open Quantum Systems*. Springer, Berlin, Heidelberg, 2nd edition, 2012.

[16] N Gisin and I C Percival. The quantum-state diffusion model applied to open systems. *Journal of Physics A: Mathematical and General*, 25(21):5677, 1992.

[17] O. Oreshkov, D. A. Lidar, and T. A. Brun. Operator quantum error correction for continuous dynamics. *Phys. Rev. A*, 78:022333, 2008.

[18] R. S. Ingarden. Quantum information theory. *Reports on Mathematical Physics*, 10(1):43, 1976.

[19] T. J. Hollowood and J. I. McDonald. Decoherence, discord, and the quantum master equation for cosmological perturbations. *Phys. Rev. D*, 95:103521, 2017.

[20] D. Boyanovsky. Effective field theory during inflation: Reduced density matrix and its quantum master equation. *Phys. Rev. D*, 92:023527, 2015.

[21] Charles H. Bennett and David P. DiVincenzo. Quantum information and computation. *Nature*, 404(247), 2000.

[22] B. Bylicka, D. Chruściński, and S. Maniscalco. Non-markovianity and reservoir memory of quantum channels: a quantum information theory perspective. *Scientific Reports*, 4(5720), 2014.

[23] A. S. Holevo. Bounds for the quantity of information transmitted by a quantum communication channel. *Probl. Peredachi Inf.*, 9(3–11), 1973.

[24] D. Boyanovsky. Effective field theory during inflation. ii. stochastic dynamics and power spectrum suppression. *Phys. Rev. D*, 93:043501, 2016.

[25] S. Shandera, N. Agarwal, and A. Kamal. Open quantum cosmological system. *Phys. Rev. D*, 98:083535, 2018.

[26] J. Martin and V. Vennin. Non gaussianities from quantum decoherence during inflation. *Journal of Cosmology and Astroparticle Physics*, 2018(06):037, 2018.

[27] J. Martin and V. Vennin. Observational constraints on quantum decoherence during inflation. *Journal of Cosmology and Astroparticle Physics*, 2018(05):063, 2018.

[28] E. Nelson. Quantum decoherence during inflation from gravitational nonlinearities. *Journal of Cosmology and Astroparticle Physics*, 2016(03):022, 2016.

[29] C. P. Burgess, R. Holman, G. Tasinato, and M. Williams. Eft beyond the horizon: stochastic inflation and how primordial quantum fluctuations go classical. *Journal of High Energy Physics*, 2015(3):90, 2015.

[30] F. C. Lombardo and G. J. Turiaci. Dynamics of an acoustic black hole as an open quantum system. *Phys. Rev. D*, 87:084028, 2013.

[31] H. Yu and J. Zhang. Understanding hawking radiation in the framework of open quantum systems. *Phys. Rev. D*, 77:024031, 2008.

[32] S. Diehl, A. Micheli, A. Kantian, B. Kraus, H. P. Büchler, and P. Zoller. Quantum states and phases in driven open quantum systems with cold atoms. *Nature Physics*, 4(878), 2008.

[33] A. Kumar, T. Y. Wu, F. Giraldo, and D. S. Weiss. Sorting ultracold atoms in a three-dimensional optical lattice in a realization of maxwells demon. *Nature*, 561(83), 2018.

[34] W. Zwerger. Mott-hubbard transition of cold atoms in optical lattices. *Journal of Optics B: Quantum and Semiclassical Optics*, 5(2):S9, 2003.

[35] C. Ospelkaus, U. Warring, Y. Colombe, K. R. Brown, J. M. Amini, D. Leibfried, and D. J. Wineland. Microwave quantum logic gates for trapped ions. *Nature*, 476:181, 2011.

[36] J. T. Barreiro, M. Müller, P. Schindler, D. Nigg, T. Monz, M. Chwalla, M. Hennrich, C. F. Roos, P. Zoller, and R. Blatt. An open-system quantum simulator with trapped ions. *Nature*, 470:486, 2011. Article.

[37] J. F. Poyatos, J. I. Cirac, and P. Zoller. Quantum reservoir engineering with laser cooled trapped ions. *Phys. Rev. Lett.*, 77:4728, 1996.

[38] A. Nunnenkamp, K. Børkje, and S. M. Girvin. Single-photon optomechanics. *Phys. Rev. Lett.*, 107:063602, 2011.

[39] J.-M. Pirkkalainen, E. Damskägg, M. Brandt, F. Massel, and M. A. Sillanpää. Squeezing of quantum noise of motion in a micromechanical resonator. *Phys. Rev. Lett.*, 115:243601, 2015.

[40] P. Rabl, P. Cappellaro, M. V. Gurudev Dutt, L. Jiang, J. R. Maze, and M. D. Lukin. Strong magnetic coupling between an electronic spin qubit and a mechanical resonator. *Phys. Rev. B*, 79:041302, 2009.

[41] A. Pályi, P. R. Struck, M. Rudner, K. Flensberg, and G. Burkard. Spin-orbit-induced strong coupling of a single spin to a nanomechanical resonator. *Phys. Rev. Lett.*, 108:206811, 2012.

[42] P. Treutlein, D. Hunger, S. Camerer, T. W. Hänsch, and J. Reichel. Bose-einstein condensate coupled to a nanomechanical resonator on an atom chip. *Phys. Rev. Lett.*, 99:140403, 2007.

[43] S. K. Steinke, S. Singh, M. E. Tasgin, P. Meystre, K. C. Schwab, and M. Vengalattore. Quantum-measurement backaction from a bose-einstein condensate coupled to a mechanical oscillator. *Phys. Rev. A*, 84:023841, 2011.

[44] N. Lo Gullo, Th. Busch, G. M. Palma, and M. Paternostro. Probing mechanical quantum coherence with an ultracold-atom meter. *Phys. Rev. A*, 84:063815, 2011.

[45] S. Hong, M. S. Grinolds, P. Maletinsky, R. L. Walsworth, M. D. Lukin, and A. Yacoby. Coherent, mechanical control of a single electronic spin. *Nano Letters*, 12(3920), 2012.

[46] D. Rugar, R. Budakian, H. J. Mamin, and B. W. Chui. Single spin detection by magnetic resonance force microscopy. *Nature*, 430(329), 2004.

[47] O. Arcizet, V. Jacques, A. Siria, P. Poncharal, P. Vincent, and S. Seidelin. A single nitrogen-vacancy defect coupled to a nanomechanical oscillator. *Nature Physics*, 7(879), 2011.

[48] Shimon Kolkowitz, Ania C. Bleszynski Jayich, Quirin P. Unterreithmeier, Steven D. Bennett, Peter Rabl, J. G. E. Harris, and Mikhail D. Lukin. Coherent sensing of a mechanical resonator with a single-spin qubit. *Science*, 335(6076):1603, 2012.

[49] S D Bennett, S Kolkowitz, Q P Unterreithmeier, P Rabl, A C Bleszynski Jayich, J G E Harris, and M D Lukin. Measuring mechanical motion with a single spin. *New Journal of Physics*, 14(12):125004, 2012.

[50] A. M. Ferrenberg and R. H. Swendsen. New monte carlo technique for studying phase transitions. *Phys. Rev. Lett.*, 61:2635, 1988.

[51] S. Sorella and E. Tosatti. Semi-metal-insulator transition of the hubbard model in the honeycomb lattice. *EPL (Europhysics Letters)*, 19(8):699, 1992.

[52] J. K. Freericks and H. Monien. Strong-coupling expansions for the pure and disordered bose-hubbard model. *Phys. Rev. B*, 53:2691, 1996.

[53] J. K. Freericks and H. Monien. Phase diagram of the bose-hubbard model. *EPL (Europhysics Letters)*, 26(7):545, 1994.

[54] A. Juozapavičius, S. Caprara, and A. Rosengren. Quantum ising model in a transverse random field: A density-matrix renormalization-group analysis. *Phys. Rev. B*, 56:11097, 1997.

[55] M. L. Wall and L. D. Carr. Out-of-equilibrium dynamics with matrix product states. *New Journal of Physics*, 14(12):125015, 2012.

[56] A. M. Läuchli and C. Kollath. Spreading of correlations and entanglement after a quench in the one-dimensional bose-hubbard model. *Journal of Statistical Mechanics: Theory and Experiment*, 2008(05):P05018, 2008.

[57] R. Arita, K. Kuroki, H. Aoki, and M. Fabrizio. Density-matrix renormalization-group study of the spin gap in a one-dimensional hubbard model: Effect of the distant transfer and exchange coupling. *Phys. Rev. B*, 57:10324, 1998.

[58] A. Mielke. Ferromagnetism in the hubbard model and hund's rule. *Physics Letters A*, 174(5):443, 1993.

[59] S. R. White. Density matrix formulation for quantum renormalization groups. *Phys. Rev. Lett.*, 69:2863, 1992.

[60] A. E. Feiguin and S. R. White. Finite-temperature density matrix renormalization using an enlarged hilbert space. *Phys. Rev. B*, 72:220401, 2005.

[61] E. M. Stoudenmire and S. R. White. Minimally entangled typical thermal state algorithms. *New Journal of Physics*, 12(5):055026, 2010.

[62] G. Vidal. Efficient classical simulation of slightly entangled quantum computations. *Phys. Rev. Lett.*, 91:147902, 2003.

[63] H. P. Breuer, E. M. Laine, J. Piilo, and B. Vacchini. Colloquium: Non-markovian dynamics in open quantum systems. *Rev. Mod. Phys.*, 88:021002, 2016.

[64] J. Preskill. Lecture notes for ph219/cs219: Foundations ii: Measurement and evolution, 2015.

[65] H. J. Kreuzer. *Nonequilibrium thermodynamics and its statistical foundations.* Monographs on the Physics and Chemistry of Materials. Oxford University Press, USA, 1984.

[66] P. Myöhänen, A. Stan, G. Stefanucci, and R. van Leeuwen. Kadanoff-baym approach to quantum transport through interacting nanoscale systems: From the transient to the steady-state regime. *Phys. Rev. B*, 80:115107, 2009.

[67] A. Ishizaki, T. R. Calhoun, G. S. Schlau-Cohen, and G. R. Fleming. Quantum coherence and its interplay with protein environments in photosynthetic electronic energy transfer. *Phys. Chem. Chem. Phys.*, 12:7319, 2010.

[68] M. J. Leskinen, O. H. T. Nummi, F. Massel, and P. Törmä. Fermi-polaron-like effects in a one-dimensional (1d) optical lattice. *New Journal of Physics*, 12(7):073044, 2010.

[69] M. D. LaHaye, J. Suh, P. M. Echternach, K. C. Schwab, and M. L. Roukes. Nanomechanical measurements of a superconducting qubit. *Nature*, 459(960-4), 2009.

[70] A. D. O'Connell, M. Hofheinz, M. Ansmann, Radoslaw C. Bialczak, M. Lenander, Erik Lucero, M. Neeley, D. Sank, H. Wang, M. Weides, J. Wenner, John M. Martinis, and A. N. Cleland. Quantum ground state and single-phonon control of a mechanical resonator. *Nature*, 464(697), 2010.

[71] A. D. Armour, M. P. Blencowe, and K. C. Schwab. Entanglement and decoherence of a micromechanical resonator via coupling to a cooper-pair box. *Phys. Rev. Lett.*, 88:148301, 2002.

[72] B. Trendelkamp-Schroer, J. Helm, and W. T. Strunz. Environment-assisted error correction of single-qubit phase damping. *Phys. Rev. A*, 84:062314, 2011.

[73] M. A. Cazalilla and J. B. Marston. Time-dependent density-matrix renormalization group: A systematic method for the study of quantum many-body out-of-equilibrium systems. *Phys. Rev. Lett.*, 88:256403, 2002.

[74] H. N. Phien, I. P. McCulloch, and G. Vidal. Fast convergence of imaginary time evolution tensor network algorithms by recycling the environment. *Phys. Rev. B*, 91:115137, 2015.

[75] M. Zwolak and G. Vidal. Mixed-state dynamics in one-dimensional quantum lattice systems: A time-dependent superoperator renormalization algorithm. *Phys. Rev. Lett.*, 93:207205, 2004.

[76] U. Schollwöck. The density-matrix renormalization group in the age of matrix product states. *Annals of Physics*, 326(1):96, 2011. January 2011 Special Issue.

[77] I.P. Omelyan, I.M. Mryglod, and R. Folk. Optimized forest-ruth and suzuki-like algorithms for integration of motion in many-body systems. *Computer Physics Communications*, 146(2):188, 2002.

[78] A. J. Daley. *Manipulation and Simulation of Cold Atoms in Optical Lattices.* Doctoral Dissertation. Leopold-Franzens-Universität Innsbruck, 2005.

[79] N. Hatano and M. Suzuki. *Finding Exponential Product Formulas of Higher Orders.* Springer Berlin Heidelberg, Berlin, Heidelberg, 2005.

[80] A. Uhlmann. The transition probability in the state space of a $*-$algebra. *Reports on Mathematical Physics*, 9(2):273, 1976.

[81] A. Uhlmann. Parallel transport and quantum holonomy along density operators. *Reports on Mathematical Physics*, 24(2):229, 1986.

[82] A. J. Leggett, S. Chakravarty, A. T. Dorsey, Matthew P. A. Fisher, Anupam Garg, and W. Zwerger. Dynamics of the dissipative two-state system. *Rev. Mod. Phys.*, 59:1, 1987.

[83] H. Spohn. Ground state(s) of the spin-boson hamiltonian. *Comm. Math. Phys.*, 123(2):277, 1989.

[84] S. K. Kehrein and A. Mielke. On the spin-boson model with a sub-ohmic bath. *Physics Letters A*, 219(5):313, 1996.

[85] A. Chin and M. Turlakov. Coherent-incoherent transition in the sub-ohmic spin-boson model. *Phys. Rev. B*, 73:075311, 2006.

[86] S. Zaitsev, O. Shtempluck, E. Buks, and O. Gottlieb. Nonlinear damping in a micromechanical oscillator. *Nonlinear Dynamics*, 67(1):859, 2012.

[87] J. M. Martinis, K. B. Cooper, R. McDermott, M. Steffen, M. Ansmann, K. D. Osborn, K. Cicak, S. Oh, D. P. Pappas, R. W. Simmonds, and C. C. Yu. Decoherence in josephson qubits from dielectric loss. *Phys. Rev. Lett.*, 95:210503, 2005.

[88] A. D. O'Connell, M. Ansmann, R. C. Bialczak, M. Hofheinz, N. Katz, E. Lucero, C. McKenney, M. Neeley, H. Wang, E. M. Weig, A. N. Cleland, and J. M. Martinis. Microwave dielectric loss at single photon energies and millikelvin temperatures. *Applied Physics Letters*, 92(11):112903, 2008.

[89] R. Bulla, H. J. Lee, N. H. Tong, and M. Vojta. Numerical renormalization group for quantum impurities in a bosonic bath. *Phys. Rev. B*, 71:045122, 2005.

[90] A. W. Chin, Á. Rivas, S. F. Huelga, and M. B. Plenio. Exact mapping between system-reservoir quantum models and semi-infinite discrete chains using orthogonal polynomials. *Journal of Mathematical Physics*, 51(9):092109, 2010.

[91] R. Bulla, H. J. Lee, N. H. Tong, and M. Vojta. Numerical renormalization group for quantum impurities in a bosonic bath. *Phys. Rev. B*, 71:045122, 2005.

[92] R. Koekoek and R. F. Swarttouw. The askey-scheme of hypergeometric orthogonal polynomials and its q-analogue, 1998.

[93] K. Levenberg. A method for the solution of certain non-linear problems in least squares. *Quarterly of Applied Mathematics*, 2(2):164, 1944.

[94] J. Manninen, S. Agasti, and F. Massel. Nonlinear quantum langevin equations for bosonic modes in solid-state systems. *Phys. Rev. A*, 96:063830, 2017.

[95] S. Agasti. Numerical simulation of kerr nonlinear systems; analyzing non-classical dynamics. *Journal of Physics Communications*, 3(10):105004, 2019.

[96] J. Kerr. Xl. a new relation between electricity and light: Dielectrified media birefringent. *The London, Edinburgh, and Dublin Philosophical Magazine and Journal of Science*, 50(332):337, 1875.

[97] S. L. McCall. Instabilities in continuous-wave light propagation in absorbing media. *Phys. Rev. A*, 9:1515, 1974.

[98] G. P. Agrawal and H. J. Carmichael. Optical bistability through nonlinear dispersion and absorption. *Phys. Rev. A*, 19:2074, 1979.

[99] H. J. Carmichael and D. F. Walls. Hysteresis in the spectrum for cooperative resonance fluorescence. *Journal of Physics B: Atomic and Molecular Physics*, 10(18):L685, 1977.

[100] P. D. Drummond and D. F. Walls. Quantum theory of optical bistability. i. nonlinear polarisability model. *Journal of Physics A: Mathematical and General*, 13(2):725, 1980.

ORIGINAL PAPERS

I

NONLINEAR QUANTUM LANGEVIN EQUATIONS FOR BOSONIC MODES IN SOLID-STATE SYSTEMS

by

Manninen, Juuso; Agasti, Souvik; Massel, Francesco (2017)

Physical Review A, 96 (6), 063830

https://doi.org/10.1103/PhysRevA.96.063830

PHYSICAL REVIEW A **96**, 063830 (2017)

Nonlinear quantum Langevin equations for bosonic modes in solid-state systems

Juuso Manninen
Department of Applied Physics, Low Temperature Laboratory, Aalto University, P.O. Box 15100, FI-00076 AALTO, Finland and Department of Physics and Nanoscience Center, University of Jyvaskyla, P.O. Box 35 (YFL), FI-40014 University of Jyvaskyla, Finland

Souvik Agasti and Francesco Massel*
Department of Physics and Nanoscience Center, University of Jyvaskyla, P.O. Box 35 (YFL), FI-40014 University of Jyvaskyla, Finland
(Received 18 September 2017; published 20 December 2017)

Based on the experimental evidence that impurities contribute to the dissipation properties of solid-state open quantum systems, we provide here a description in terms of nonlinear quantum Langevin equations of the role played by two-level systems in the dynamics of a bosonic degree of freedom. Our starting point is represented by the description of the system-environment coupling in terms of coupling to two separate reservoirs, modeling the interaction with external bosonic modes and two-level systems, respectively. Furthermore, we show how this model represents a specific example of a class of open quantum systems that can be described by nonlinear quantum Langevin equations. Our analysis offers a potential explanation of the parametric effects recently observed in circuit-QED cavity optomechanics experiments.

DOI: 10.1103/PhysRevA.96.063830

I. INTRODUCTION

The dynamics of open quantum systems, i.e., quantum systems that can be described as separate entities from their surrounding environment while being somehow coupled to it, is arguably one of the most fundamental problems in quantum mechanics, encompassing concepts such as the *measurement paradox* [1] and the boundary between quantum and classical physics [2]. On general grounds, the interaction between a quantum system and its environment represents an important aspect of the physics of condensed matter and complex systems, which has been the focus of extensive analysis [3–5], with repercussions in contexts ranging from the energy transport in photosynthetic complexes [6] to the physics of ultracold gases [7–9].

In the description of these systems, the inclusion of the role played by coupling to an external environment is necessary, if only because the system has to be coupled to an external measurement apparatus which, from the quantum-dynamical perspective of the system, represents a source of noise and dissipation. At the same time the manipulation of open quantum systems has recently led to the possibility of preparing and detecting quantum states of matter and radiation [10,11], paving the way for the definition of a new paradigm of *quantum technology*, which represents an important field for applications ranging from secure (quantum) communication [12] to sensing of electromagnetic fields [13] and to the detection of gravitational waves [14]. This prospect of technological application of quantum mechanics is rooted in the relatively recent development of fabrication techniques at the nanoscale, in particular, nanomechanical resonators, superconducting qubits, and, more in general, circuit quantum electrodynamics (QED) setups [15–18], where the characteristic scales involved in the dynamics of these systems naturally lead to the study of the quantum properties in the presence of coupling to an environment.

Within this framework, it has recently been observed that this coupling can represent an important resource leading to the notion of *reservoir engineering* [19]. This concept corresponds to the idea that, by manipulating the properties of the environment coupled to a given quantum system or even the nature of the system-environment coupling itself, it is possible to generate specific (quantum) states for the system. Prominent examples are represented by the recent achievements in the field of cavity optomechanics, where ground-state cooling [20] and squeezing below the standard quantum limit (SQL) [21–23], along with nearly quantum limited amplification [24,25] and nonreciprocal photon transmission [26], have been achieved by introducing a specific (Gaussian) state for the reservoir. While these examples correspond to inducing a specific state for the system by manipulating the state of the reservoir, in Refs. [27] and [28] it is shown that by designing a specific nonlinear coupling between system and environment, it is possible to protect certain quantum states (cat states) against decoherence.

If the coupling between the system and the environment is described by a linear Hamiltonian, the effects of noise and dissipation on the dynamics of the system can be described in terms of linear quantum Langevin equations (QLEs) [11]. These equations represent an extension to the quantum regime of the classical Langevin equations and, in analogy to their classical counterpart, include in the description of the dynamics of the system the role played by the environment, including dissipative and noise effects. However, the case of a linear system-environment coupling is not the most general situation that can arise. For instance, for nanomechanical resonators [29–33] and for circuit-QED setups [34–39], the experimental evidence of nonlinear phenomena related to the coupling between system and environment has emerged and, more importantly for our analysis, the relevance of impurities in this phenomenon has been discussed. For both setups, it has been shown (see, e.g., [29,34]) that the impurities naturally arising in the material composing the devices, its supports, and/or substrate represent a source of dissipation. These defects can be modeled in terms of two-level systems (TLSs).

*francesco.p.massel@jyu.fi

The reason behind the possibility of modeling impurities in these terms is represented by the fact that each impurity can be construed as quantum systems which exhibit two local energy minima. For instance, as a charged impurity that can hop between two defects in the crystal structure, or a dangling bond with two possible configurations.

More specifically, these TLSs exist primarily due to the disordered potential landscape of amorphous materials, e.g., in surface oxides of thin-film circuit electrodes [38], in the tunnel barrier of Josephson junctions [34], and at disordered interfaces [40,41], coupling with the bosonic degrees of freedom of the system, either through a purely electromagnetic interaction (optical and circuit-QED setups) or a phononic one in the context of nanomechanical systems [42].

II. MODEL

In this article we show under what conditions, considering a nonlinear coupling between system and a bath of TLSs, it is possible to derive a nonlinear QLE for the dynamics of the degrees of freedom of the system, having in mind a circuit-QED setup. In addition, we show how the nonlinear QLEs derived here can represent an explanation to some of the phenomena recently observed in the context of microwave quantum optomechanics [22].

The starting point for our analysis is represented by a bosonic system ($\mathcal{S}$) coupled to an environment ($\mathcal{E}$). The total Hamiltonian of the bipartite system ($\mathcal{S}+\mathcal{E}$) is given by

$$H = H_{\mathcal{S}} + H_{\mathcal{E}} + H_{\mathcal{S}-\mathcal{E}}, \tag{1}$$

where $H_{\mathcal{S}} = H_{\mathcal{S}}(c,c^\dagger)$ is the Hamiltonian of the isolated system, exhibiting a generic dependence on the annihilation (creation) operators c ($c^\dagger$) associated with the system, and $H_{\mathcal{E}}$ is the Hamiltonian for the bath.

We assume here that the environment Hamiltonian can be decomposed into two terms, $H_{\mathcal{E}}^{\mathrm{B}} = \sum_{\mathrm{k}} \omega_{\mathrm{k}} b_{\mathrm{k}}^\dagger b_{\mathrm{k}}$ and $H_{\mathcal{E}}^{\mathrm{TLS}}$, corresponding to a bath of free bosonic modes and to a bath of TLSs, respectively (see Fig. 1). The bosonic bath describes, for instance, the modes of the electromagnetic field of the environment. In our analysis we assume that these

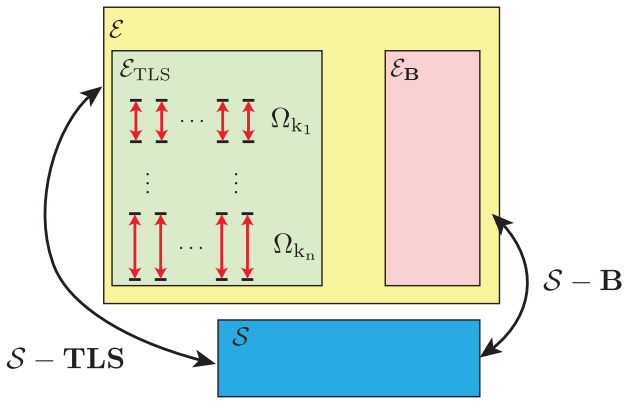

FIG. 1. Cartoon picture of the setup. The system $\mathcal{S}$ is coupled to an environment $\mathcal{E}$, which is constituted by a bosonic bath $\mathcal{E}_{\mathrm{B}}$ and a bath of TLSs $\mathcal{E}_{\mathrm{TLS}}$. The coupling between the two baths and the system is mediated by the Hamiltonians $H_{\mathcal{S}-\mathrm{B}}$ and $H_{\mathcal{S}-\mathrm{TLS}}$, respectively.

modes, while being associated with the noise properties and dissipation of the system, encompass also the external coherent fields driving the system whose properties are encoded in the state of the bath for the modes b_{k} (see, e.g., [11]). Our choice is equivalent to considering a coherent driving term for the system Hamiltonian and a purely thermal bath.

In this scenario, we describe the coupling between these modes and the degrees of freedom of the system by the following Hamiltonian:

$$H_{\mathcal{S}-\mathrm{B}} = \sum_k g_{\mathrm{k}}^{\mathrm{B}} (c^\dagger b_{\mathrm{k}} + c b_{\mathrm{k}}^\dagger). \tag{2}$$

In addition, we model the bath of TLSs as a collection of spins $\mathbf{J}_{\mathrm{k}}$. In this scenario we have that $H_{\mathcal{E}}^{\mathrm{TLS}} = \sum_k \Omega_{\mathrm{k}} J_z^{\mathrm{k}}$. This choice for the modeling of TLSs corresponds to the idea that, for each Ω_{k} multiple TLSs are present that collectively couple with the system $\mathcal{S}$. While for $\Omega_{\mathrm{k}} \simeq \omega_{\mathrm{S}}$, where ω_{S} corresponds to a characteristic frequency for the system, the presence of impurities leads to a renormalization of the linewidth associated with the linear response of the system induced by the coupling given in Eq. (2) (see Appendix D); for $\Omega_{\mathrm{k}} \simeq n\,\omega_{\mathrm{S}}$, nonlinear contributions appear. In our analysis, also in light of the recent investigations concerning the relevance of two-photon emission processes by TLSs [43,44] when coupled to bosonic modes, we consider the case $n = 2$, representing the lowest-order approximation beyond linear coupling. This assumption appears to be compatible with the usual experimental conditions encountered in the context of circuit QED, where microwave cavities operate at frequencies corresponding to few GHz [15,16,45] while the energy separation of a TLS relevant for the physics of either of these systems is of the order of 10 GHz [45,46]. In this case, it is possible to write the system-TLS coupling Hamiltonian as

$$H_{\mathcal{S}-\mathrm{TLS}} = \sum_{\mathrm{k}} g_{\mathrm{k}}^{\mathrm{TLS}} (J_+^{\mathrm{k}} c^2 + J_-^{\mathrm{k}} c^{\dagger 2}). \tag{3}$$

If we assume that $|\mathbf{J}_{\mathrm{k}}| \gg 1$, corresponding to the idea that for each value of k multiple TLSs couple to the system $\mathcal{S}$, by resorting to the Holstein-Primakoff (HP) realization of spin operators in terms of bosonic modes, we can replace the spin operators with bosonic ones. This mapping can be performed in two different ways, corresponding to complementary experimental conditions (see Appendix A). If it is assumed that the TLSs mostly reside in their ground state, we have that $J_3^{\mathrm{k}} \simeq -j_{\mathrm{k}}$, where j_{k} is the index of the representation associated with the spin $\mathbf{J}_{\mathrm{k}}$ and the HP mapping reads $J_3^{\mathrm{k}} \to d_{\mathrm{k}}^\dagger d_{\mathrm{k}} - j_{\mathrm{k}}$, $J_-^{\mathrm{k}} \to d_{\mathrm{k}}$, $J_+^{\mathrm{k}} \to d_{\mathrm{k}}^\dagger$. In this case, the coupling between the system and the TLS bath can be approximated by

$$H_{\mathcal{S}-\mathrm{HP}_-} = \sum_{\mathrm{k}} g_{\mathrm{k}}^{\mathrm{HP}} (d_{\mathrm{k}}^\dagger c^2 + d_{\mathrm{k}} c^{\dagger 2}), \tag{4}$$

with $g_{\mathrm{k}}^{\mathrm{HP}} = \sqrt{2 j_{\mathrm{k}}}\, g_{\mathrm{k}}^{\mathrm{TLS}}$. On the other hand, if the TLSs mainly reside in their excited state ($J_3^{\mathrm{k}} \simeq +j_{\mathrm{k}}$) the mapping can be written as $J_3^{\mathrm{k}} \to j_{\mathrm{k}} - d_{\mathrm{k}}^\dagger d_{\mathrm{k}}$, $J_-^{\mathrm{k}} \to d_{\mathrm{k}}^\dagger$, $J_+^{\mathrm{k}} \to d_{\mathrm{k}}$, leading to the following approximation for $H_{\mathcal{S}-\mathrm{TLS}}$:

$$H_{\mathcal{S}-\mathrm{HP}_+} = \sum_{\mathrm{k}} g_{\mathrm{k}}^{\mathrm{TLS}} (d_{\mathrm{k}} c^2 + d_{\mathrm{k}}^\dagger c^{\dagger 2}). \tag{5}$$

These two different forms of the HP mapping correspond to two different physical situations. In the former case, the TLSs prevalently reside in their ground state, corresponding to the idea that the impurities mainly reside in their ground state, implying a low-temperature regime. In this case, the bosonic excitations described by the operators d_k represent (weak) excitations around the ground state. On the other hand, the latter case corresponds to the situation in which the highest excited (metastable) state of the TLSs is weakly (de-)excited, corresponding, for instance, to the case in which an external drive induces excitations in the TLSs bath, leading to a possible interpretation of the linewidth narrowing observed in circuit-QED setups under strong driving conditions [35] in terms of nonlinear QLEs associated with the saturation of the TLSs. In this picture, the external drive effectively heats the impurities to their excited state, inducing the population inversion for the ensemble of TLSs and a consequent saturation, justifying the HP_+ transformation in terms of (weak) deexcitations of the highest excited state.

As we show in Appendix B, it is possible to derive QLEs for the system, provided that the environment Hamiltonian is described by a set of bosonic operators coupled linearly to the system degrees of freedom. It is important to note that the requirement of linearity concerning the system-environment Hamiltonian is limited to the bath degrees of freedom, meaning that its most general form can be expressed as

$$H_{\mathcal{S}-\mathcal{E}} = \sum_k g_k[F^\dagger(c,c^\dagger)e_k + F(c,c^\dagger)e_k^\dagger], \tag{6}$$

where e_k and $e_k^\dagger$ represent generic bosonic operators associated with the environment degrees of freedom. The form the system-environment coupling represents a sufficient condition for the derivation of a nonlinear QLE, along with the assumption that the modes of the bath are noninteracting. In other terms, it is necessary to assume a linear dependence of the coupling Hamiltonian on the environmental degrees of freedom, since in order to derive the QLEs for the system, the solution of the Heisenberg equation of motion for the environment degrees of freedom has to assume a specific form in which the contribution of the system and the environment operators can be represented as two separate additive terms (see Appendix B).

III. EQUATIONS OF MOTION

It is clear that since the form of $H_{\mathcal{S}-\mathrm{B}}$ and $H_{\mathcal{S}-\mathrm{HP}_\pm}$ can be expressed in the form given by Eq. (6), with $F(c,c^\dagger)$ given by c, c^2, and $c^{\dagger 2}$, and with $e_k = b_k$ and $e_k = d_k$ for $\mathcal{S}-\mathrm{B}$, $\mathcal{S}-\mathrm{HP}_-$, and $\mathcal{S}-\mathrm{HP}_+$, respectively, we can write the dynamics of the system in terms of a (nonlinear) QLE as

$$\dot{c} = -i[c,H_S] - \left(\frac{\kappa}{2} + \kappa_N c^\dagger c\right)c + \sqrt{\kappa}c_{\mathrm{in}} + 2\sqrt{\kappa_N}c^\dagger c_{\mathrm{in}}^{\mathrm{TLS}}, \tag{7a}$$

$$\dot{c} = -i[c,H_S] - \left(\frac{\kappa}{2} - \kappa_N c^\dagger c\right)c + \sqrt{\kappa}c_{\mathrm{in}} + 2\sqrt{\kappa_N}c^\dagger c_{\mathrm{in}}^{\mathrm{TLS}^\dagger}. \tag{7b}$$

Equations (7a) and (7b), obtained considering the system-environment coupling given by $H_{\mathcal{S}-\mathrm{HP}_-}$ and $H_{\mathcal{S}-\mathrm{HP}_+}$, respectively, are the main result of our analysis. The presence of a TLS bath leads to the appearance of nonlinear dissipative terms ($\pm\kappa_N c^\dagger c\, c$) and to purely imaginary parametric noise terms ($2\sqrt{\kappa_N}c^\dagger c_{\mathrm{in}}^{\mathrm{TLS}(\dagger)}$). We stress here that these terms are the direct result of the modeling of the bath in terms of two separate environments ($H_{\mathcal{S}-\mathrm{B}}$ and $H_S - \mathrm{HP}_\pm$) and do not represent an *ad hoc* modification of the linear QLEs that can be derived in the absence of coupling to TLSs. In particular, while the nonlinear dissipation term possibly represents a natural extension to the nonlinear regime of linear QLEs, the parametric noise term is a nontrivial contribution associated with the presence of the TLS bath.

In addition, we observe here that, analogously to their linear counterpart, Eqs. (7a) and (7b) are time local, i.e., the dynamics is Markovian. As detailed in Appendix B, this property is related to the assumption that within the range of frequencies of interest, the coupling strength between system and environment is independent of the mode considered (wide-band-limit approximation) [47].

If we further consider a pump probe representative of a circuit-QED setup (e.g., a circuit optomechanical experiment), we can assume that the dynamics given by Eq. (7) is linearized around a strong coherent tone:

$$\alpha_p = \alpha_{\mathrm{in}}\exp[-i\omega_p t].$$

The frequency ω_p is detuned by $\Delta = \omega_p - \omega_c$ from the cavity resonant frequency. As a result of the linearization scheme, we have that the amplitude of the cavity field oscillating at ω_p is given by the solution of a nonlinear algebraic equation. In Fig. 2 we have plotted the stationary value of the cavity field for the two choices of the HP mapping ($\mathrm{HP}_\pm$). As expected, for small values of the driving field α_{in}, the stationary solution corresponds to the solution in the absence of nonlinear dissipation. However, for larger values of α_{in} the stationary solution substantially deviates from the solution of the linear system, with, for the parameters discussed here, a negligible difference between $\mathrm{HP}_\pm$ cases.

Furthermore, the (first-order) dynamics of the fluctuations $c = \alpha + a$ around the stationary value induced by the pump (in a frame rotating at ω_p) is given by

$$\dot{a} = \left[i\Delta - \left(\frac{\kappa}{2} + 2\kappa_N|\alpha|^2\right)\right]a - \kappa_N\alpha^2 a^\dagger + \sqrt{\kappa}a_{\mathrm{in}} + 2\sqrt{\kappa_N}\alpha^* a_{\mathrm{in}}^{\mathrm{TLS}}, \tag{8a}$$

$$\dot{a} = \left[i\Delta - \left(\frac{\kappa}{2} - 2\kappa_N|\alpha|^2\right)\right]a + \kappa_N\alpha^2 a^\dagger + \sqrt{\kappa}a_{\mathrm{in}} + 2\sqrt{\kappa_N}\alpha^* a_{\mathrm{in}}^{\mathrm{TLS}^\dagger}, \tag{8b}$$

the HP_- and HP_+ case, respectively (see Appendix C). It is possible to see that Eqs. (8a) and (8b) include a purely imaginary parametric term on top of a nonlinear dissipation term, implying linewidth broadening or narrowing, depending on the state of the TLSs bath. Recently, in Ref. [22] a term of the same form was introduced as an *ad hoc* parameter in order to match the experimental results of a cavity optomechanical

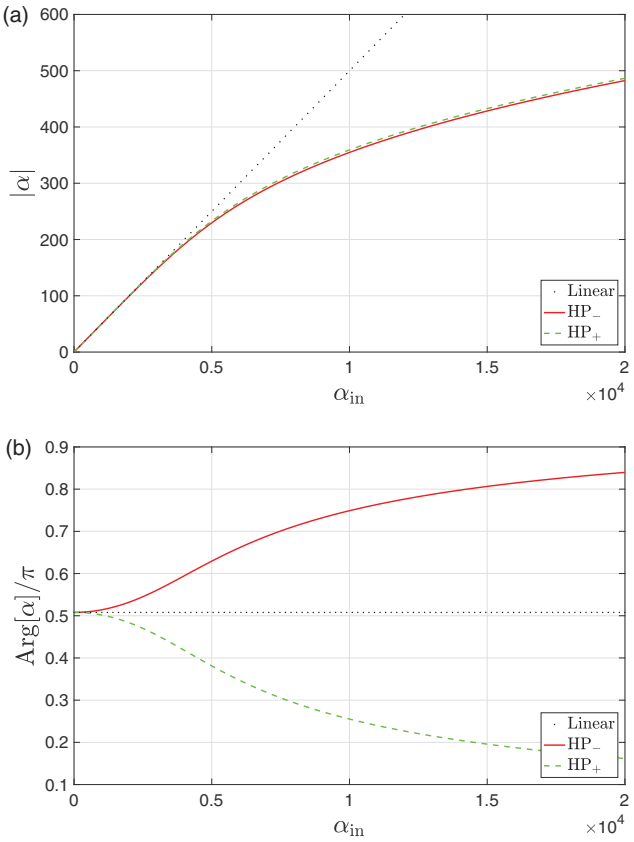

FIG. 2. Amplitude (a) and phase (b) for the stationary value (in a frame rotating at ω_p, see text) of the cavity field α in the presence of a driving α_{in}. Parameters: $\kappa_N = 1.5\times10^{-4}$, $\Delta = 20$ (all quantities expressed in units of κ).

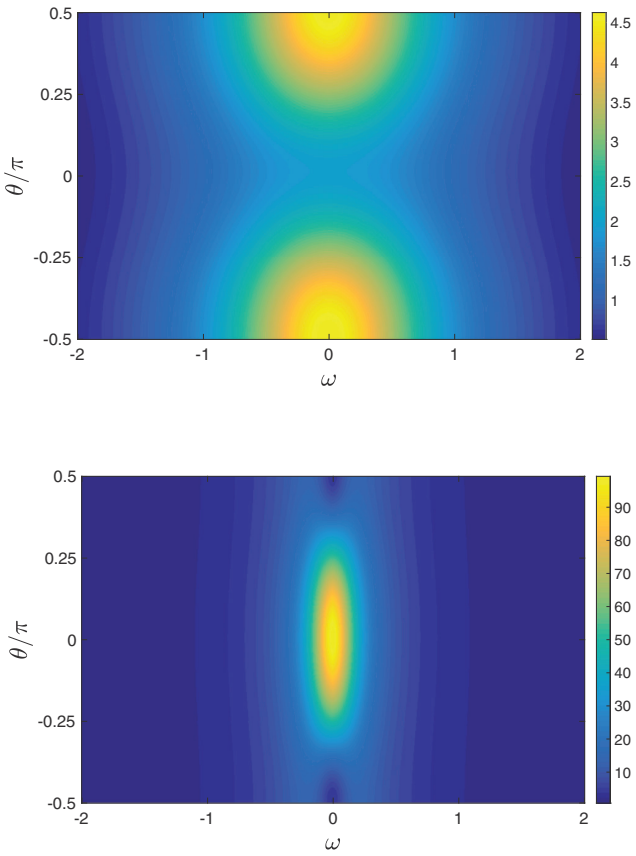

FIG. 3. Noise spectrum for the cavity field in the presence of an external drive $\alpha_{in} = 700$, for (a) HP$_-$ and (b) HP$_+$ for $\langle a_{in}^{\dagger} a_{in}\rangle = \langle a_{in}^{TLS\dagger} a_{in}^{TLS}\rangle = 1$ (all other parameters as in Fig. 2).

experiment aimed at establishing squeezing below the SQL of a nanomechanical resonator.

Our description, therefore provides a potential explanation of such parametric effects in terms of nonlinear dissipation phenomena associated with the nonlinear coupling to a bath of TLSs. In order to characterize the effect induced by the presence of the nonlinear coupling to TLSs, we evaluate the fluctuation spectrum of the cavity field $S_\omega^\theta = 1/2\langle\{X_\omega^\theta, X_{-\omega}^\theta\}\rangle$, with $X_\omega^\theta = 1/\sqrt{2}(a_{-\omega}^{\dagger} e^{i\theta} + a_\omega e^{-i\theta})$, assuming thermal fluctuations both for the bosonic and the TLS bath. As hinted by the structure of Eqs. (8a) and (8b), the presence of a parametric term induces squeezing, which can be experimentally observed by homodyne detection of the output field, in the cavity spectrum for both cases, as seen in Fig. 3, where the cavity fluctuation spectrum exhibits a clear dependence on the phase θ.

IV. CONCLUSIONS

We have reported here how it is possible to deduce nonlinear QLEs for the dynamics of an open quantum system from a nonlinear system-environment coupling Hamiltonian. Moreover, we have discussed how an effective nonlinear system-environment coupling can emerge in the presence of impurities modeled as TLSs. Ultimately, we have shown that the TLS-induced nonlinearities can represent a potential explanation for the imaginary parametric terms reported in Ref. [22].

ACKNOWLEDGMENT

This work was supported by the Academy of Finland (Contract No. 275245) and the European Research Council (Grant No. 670743).

APPENDIX A: HOLSTEIN-PRIMAKOFF TRANSFORMATION

We discuss here the Holstein-Primakoff realization allowing us to replace the spin operators J_z, $J_\pm$ obeying the usual SU(2) commutation relations

$$\left[J_z^k, J_\pm^k\right] = \pm J_\pm^k, \quad [J_+^k, J_-^k] = 2J_z^k, \tag{A1}$$

with bosonic operators d_k, $d_k^\dagger$, for which

$$[d_k, d_k^\dagger] = 1. \tag{A2}$$

As discussed in the main text, in order to map the spin operators obeying Eq. (A1) with the bosonic operators d_k, $d_k^\dagger$, we have two possibilities, depending on the physical situation we want to describe. If we assume that $J_z^k \simeq -j_k$, this choice is indicated in the main text as HP$_-$, we can consider the

following transformation:

$$J_z^{\mathrm{k}} = \hat{n}_{\mathrm{k}} - j_{\mathrm{k}}, \quad J_+^{\mathrm{k}} = d_{\mathrm{k}}^\dagger \sqrt{2j_{\mathrm{k}} - \hat{n}_{\mathrm{k}}}, \quad J_-^{\mathrm{k}} = \sqrt{2j_{\mathrm{k}} - \hat{n}_{\mathrm{k}}}\, d_{\mathrm{k}}, \tag{A3}$$

where $\hat{n}_{\mathrm{k}} = d_{\mathrm{k}}^\dagger d_{\mathrm{k}}$. The operators J_z^{k}, $J_\pm^{\mathrm{k}}$ can be shown to fulfill the SU(2) commutation relations

$$\left[J_z^{\mathrm{k}}, J_+^{\mathrm{k}}\right] = [\hat{n}_{\mathrm{k}}, d_{\mathrm{k}}^\dagger]\sqrt{2j_{\mathrm{k}} - \hat{n}_{\mathrm{k}}} = J_+^{\mathrm{k}},$$

$$\left[J_z^{\mathrm{k}}, J_-^{\mathrm{k}}\right] = \sqrt{2j_{\mathrm{k}} - \hat{n}_{\mathrm{k}}}[\hat{n}_{\mathrm{k}}, d_{\mathrm{k}}] = -J_-^{\mathrm{k}}, \tag{A4a}$$

$$\begin{aligned}[J_+^{\mathrm{k}}, J_-^{\mathrm{k}}] &= d_{\mathrm{k}}^\dagger(\sqrt{2j_{\mathrm{k}} - \hat{n}_{\mathrm{k}}})^2 d_{\mathrm{k}} - \sqrt{2j_{\mathrm{k}} - \hat{n}_{\mathrm{k}}}\,\hat{n}_{\mathrm{k}}\sqrt{2j_{\mathrm{k}} - \hat{n}_{\mathrm{k}}} \\ &= \hat{n}_{\mathrm{k}}\left(2j_{\mathrm{k}} - \hat{n}_{\mathrm{k}} + 1\right) - 2j_{\mathrm{k}} + \hat{n}_{\mathrm{k}} - \hat{n}_{\mathrm{k}}(2j_{\mathrm{k}} - \hat{n}_{\mathrm{k}}) = 2J_z^{\mathrm{k}}.\end{aligned} \tag{A4b}$$

In the limit $j_{\mathrm{k}} \to \infty$, we have that

$$\frac{J_+^{\mathrm{k}}}{\sqrt{2j_{\mathrm{k}}}} = d_{\mathrm{k}}^\dagger \sqrt{\frac{2j_{\mathrm{k}} - \hat{n}_{\mathrm{k}}}{2j_{\mathrm{k}}}} = d_{\mathrm{k}}^\dagger\left(1 - \frac{\hat{n}_{\mathrm{k}}}{4j_{\mathrm{k}}} + \cdots\right) \simeq d_{\mathrm{k}}^\dagger,$$

$$\frac{J_-^{\mathrm{k}}}{\sqrt{2j_{\mathrm{k}}}} \simeq d_{\mathrm{k}}, \quad \frac{J_z^{\mathrm{k}}}{j_{\mathrm{k}}} = \frac{\hat{n}_{\mathrm{k}}}{j_{\mathrm{k}}} - 1 \simeq -1. \tag{A5}$$

Therefore the bosonic excitations described by d_{k} and $d_{\mathrm{k}}^\dagger$ correspond to (small) excitations around the $J_z^{\mathrm{k}} = -j_{\mathrm{k}}$ state. Conversely, we can write

$$J_z^{\mathrm{k}} = j_{\mathrm{k}} - \hat{n}_{\mathrm{k}}, \quad J_-^{\mathrm{k}} = d_{\mathrm{k}}^\dagger \sqrt{2j_{\mathrm{k}} - \hat{n}_{\mathrm{k}}}, \quad J_+^{\mathrm{k}} = \sqrt{2j_{\mathrm{k}} - \hat{n}_{\mathrm{k}}}\, d_{\mathrm{k}}, \tag{A6}$$

so that when $j_{\mathrm{k}} \to \infty$,

$$\frac{J_+^{\mathrm{k}}}{\sqrt{2j_{\mathrm{k}}}} \simeq d_{\mathrm{k}}, \quad \frac{J_-^{\mathrm{k}}}{\sqrt{2j_{\mathrm{k}}}} \simeq d_{\mathrm{k}}^\dagger, \quad \frac{J_z^{\mathrm{k}}}{j_{\mathrm{k}}} = 1 - \frac{\hat{n}_{\mathrm{k}}}{j_{\mathrm{k}}} \simeq 1, \tag{A7}$$

which correspond to the description of small fluctuations around the $J_z^{\mathrm{k}} = j$ state, indicated as HP_+ in main text.

APPENDIX B: QLE FOR $F(c,c^\dagger)$

We discuss here the form of the QLEs generated by a model for which, following the notation introduced in Eq. (1) of the main text, $H_{\mathcal{S}}$ is left unspecified. The environment is given by a set of noninteracting bosonic modes described by $H_{\mathcal{E}} = \sum_{\mathrm{k}} \omega_{\mathrm{k}} e_{\mathrm{k}}^\dagger e_{\mathrm{k}}$, where e_{k} ($e_{\mathrm{k}}^\dagger$) are the annihilation (creation) operators associated with mode k and the system-environment coupling is given by the following Hamiltonian:

$$H_{\mathcal{S}-\mathcal{E}} = \sum_{\mathrm{k}} g_{\mathrm{k}}[F(c,c^\dagger)e_{\mathrm{k}}^\dagger + F^\dagger(c,c^\dagger)e_{\mathrm{k}}], \tag{B1}$$

where $F(c,c^\dagger)$ is a generic function of the creation and annihilation operators of the system. Since $H_{\mathcal{S}-\mathcal{E}}$ is a linear operator with respect to the degrees of freedom of the bath and $e_{\mathrm{k}}^{(\dagger)}$ commutes with $H_{\mathcal{S}}$, we can follow the same strategy employed for the derivation of the linear QLEs [11] and write the equations of motion (EOM) for the bath field operators in the Heisenberg picture as

$$\dot{e}_{\mathrm{k}}(t) = -i\omega_{\mathrm{k}} e_{\mathrm{k}}(t) - i g_{\mathrm{k}} F(c,c^\dagger). \tag{B2}$$

Similarly, the EOM for the system can be written as

$$\dot{c}(t) = i[H_{\mathcal{S}}, c(t)] + i\sum_{\mathrm{k}} g_{\mathrm{k}}([F,c]e_{\mathrm{k}}^\dagger + [F^\dagger, c]e_{\mathrm{k}}). \tag{B3}$$

Equation (B2) can be solved in terms of an initial condition t_0, yielding

$$e_{\mathrm{k}}(t) = e^{-i\omega_{\mathrm{k}}(t-t_0)} e_{\mathrm{k}}(t_0) - i g_{\mathrm{k}} \int_{t_0}^{t} e^{-i\omega_{\mathrm{k}}(t-t')} F[c(t'), c^\dagger(t')]\, dt'. \tag{B4}$$

By substituting Eq. (B4) and its Hermitian conjugate into Eq. (B3) we obtain

$$\begin{aligned}\dot{c}(t) = i[H_{\mathcal{S}}, c(t)] + i\sum_{\mathrm{k}} g_{\mathrm{k}}\Bigg\{&[F,c]\left[e^{i\omega_{\mathrm{k}}(t-t_0)} e_{\mathrm{k}}^\dagger(t_0) + i g_{\mathrm{k}} \int_{t_0}^{t} e^{i\omega_{\mathrm{k}}(t-t')} F^\dagger(t')\, dt'\right] \\ &+ [F^\dagger, c]\left[e^{-i\omega_{\mathrm{k}}(t-t_0)} e_{\mathrm{k}}(t_0) - i g_{\mathrm{k}} \int_{t_0}^{t} e^{-i\omega_{\mathrm{k}}(t-t')} F(t')\, dt'\right]\Bigg\}.\end{aligned} \tag{B5}$$

Like for the purely linear case, we introduce the density of states $D = \partial \mathrm{k}/\partial\omega_{\mathrm{k}}$ (supposing a continuum of states for the bath) and assume that, in the relevant frequency regime, g_{k} does not depend on the mode index k. If we define

$$g_{\mathrm{k}} = \sqrt{\frac{\kappa}{2\pi D}}, \tag{B6}$$

where κ is the mode-independent constant, we can write Eq. (B5) as

$$\begin{aligned}\dot{c}(t) &= i[H_{\mathcal{S}}, c(t)] + i\sum_{\mathrm{k}} \sqrt{\frac{\kappa}{2\pi D}}\Bigg\{[F,c]\left(e^{i\omega_{\mathrm{k}}(t-t_0)} e_{\mathrm{k}}^\dagger(t_0) + i\sqrt{\frac{\kappa}{2\pi D}} \int_{t_0}^{t} e^{i\omega_{\mathrm{k}}(t-t')} F^\dagger(t')\, dt'\right) \\ &\quad + [F^\dagger, c]\left(e^{-i\omega_{\mathrm{k}}(t-t_0)} e_{\mathrm{k}}(t_0) - i\sqrt{\frac{\kappa}{2\pi D}} \int_{t_0}^{t} e^{-i\omega_{\mathrm{k}}(t-t')} F(t')\, dt'\right)\Bigg\} \\ &= i[H_{\mathcal{S}}, c(t)] + \sqrt{\kappa}\left\{[F,c]\left(-c_{\mathrm{in}}^\dagger(t) - \frac{\sqrt{\kappa}}{2} F^\dagger(t)\right) + [F^\dagger, c]\left(-c_{\mathrm{in}}(t) + \frac{\sqrt{\kappa}}{2} F(t)\right)\right\},\end{aligned} \tag{B7}$$

where we have defined $c_{\rm in}(t)$ as

$$c_{\rm in}(t) = -\frac{i}{\sqrt{2\pi D}}\sum_k e^{-i\omega_k(t-t_0)}e_k(t_0). \tag{B8}$$

The definition introduced in Eq. (B6) corresponds to what in the context of electronic transport is defined as "a wide-band-limit approximation" and, allowing us to write the QLE given in Eq. (B7) in time-local form, can be considered equivalent to the Markov approximation [47].

Let us focus on the case, discussed in the text, of two separate baths: a bosonic bath with operators $b_{\rm k}$ and a bath of TLSs with HP-transformed modes $d_{\rm k}$. We define two functions $F_{\rm b}$ and $F_{\rm TLS}$ of the system operators that couple to the bosonic and TLS baths, respectively. The QLE (B7) then reads

$$\begin{aligned}\dot{c}(t) = i[H_S,c(t)] &+ \sqrt{\kappa}\left\{[F_{\rm b},c]\left(-c_{\rm in}^\dagger - \frac{\sqrt{\kappa}}{2}F_{\rm b}^\dagger\right) + [F_{\rm b}^\dagger,c]\left(-c_{\rm in} + \frac{\sqrt{\kappa}}{2}F_{\rm b}\right)\right\}\\ &+ \sqrt{\kappa_{\rm N}}\left\{[F_{\rm TLS},c]\left(-c_{\rm in}^{\rm TLS\dagger} - \frac{\sqrt{\kappa_{\rm N}}}{2}F_{\rm TLS}^\dagger\right) + [F_{\rm TLS}^\dagger,c]\left(-c_{\rm in}^{\rm TLS} + \frac{\sqrt{\kappa_{\rm N}}}{2}F_{\rm TLS}\right)\right\}.\end{aligned} \tag{B9}$$

Assuming a linear coupling between the system and the bosonic bath and choosing the HP$_-$ mapping for the TLSs, one obtains $F_{\rm b} = c$ and $F_{\rm TLS} = c^2$. Substituting these into Eq. (B9) gives

$$\dot{c} = i[H_S,c(t)] - \left(\frac{\kappa}{2} + \kappa_{\rm N}c^\dagger c\right)c + \sqrt{\kappa}c_{\rm in} + 2\sqrt{\kappa_{\rm N}}c^\dagger c_{\rm in}^{\rm TLS}, \tag{B10}$$

which corresponds to Eq. (7a) of the main text. On the contrary, if the HP$_+$ mapping is chosen, one obtains Eq. (7b) with $F_{\rm TLS} = c^{\dagger 2}$.

APPENDIX C: LINEARIZATION OF THE QUANTUM LANGEVIN EQUATIONS

Here we outline the linearization strategy that allows us, in the presence of a strong coherent tone $\alpha_{\rm p} = \alpha_{\rm in}e^{-i\omega_{\rm p}t}$, to recast Eqs. (7b) of the main text in terms of equations describing the stationary state (in a frame rotating at $\omega_{\rm p}$) and the fluctuations around this stationary state, given by Eqs. (8a) and (8b) of the main text.

Focusing on Eq. (7a),

$$\dot{c} = -i[c,H_S] - \left(\frac{\kappa}{2} + \kappa_N c^\dagger c\right)c + \sqrt{\kappa}c_{\rm in} + 2\sqrt{\kappa_N}c^\dagger c_{\rm in}^{\rm TLS}. \tag{C1}$$

In the presence of a strong coherent pump $\alpha_{\rm p} = \alpha_{\rm in}e^{-i\omega_{\rm p}t}$, we seek a solution of the form $c = \alpha + a$,

$$\begin{aligned}-i\omega_{\rm p}\alpha + \dot{a} = -i\omega_{\rm c}(\alpha + a) &- \left[\frac{\kappa}{2} + \kappa_N(\alpha^* + a^\dagger)(\alpha + a)\right]\\ &\times(\alpha + a) + \sqrt{\kappa}(\alpha_{\rm in} + a_{\rm in})\\ &+ 2\sqrt{\kappa_N}(\alpha^* + a^\dagger)a_{\rm in}^{\rm TLS},\end{aligned} \tag{C2}$$

where without loss of generality, we have assumed that $H_S = \omega_{\rm c}c^\dagger c$.

Neglecting the fluctuation terms, we obtain the equation for the steady-state solution

$$0 = i\Delta\alpha - \frac{\kappa}{2}\alpha - \kappa_N\alpha|\alpha|^2 + \sqrt{\kappa}\alpha_{\rm in}, \tag{C3}$$

where $\Delta = \omega_{\rm p} - \omega_{\rm c}$. From Eq. (C2) the equation for the fluctuation around the steady-state solution value of α given above is thus expressed as

$$\begin{aligned}\dot{a} = &\left[i\Delta - \left(\frac{\kappa}{2} + 2\kappa_N|\alpha|^2\right)\right]a - \kappa_N\alpha^2a^\dagger + \sqrt{\kappa}a_{\rm in}\\ &+ 2\sqrt{\kappa_N}\alpha^*a_{\rm in}^{\rm TLS}.\end{aligned} \tag{C4}$$

With a similar procedure one can also show that Eq. (7b) leads to Eq. (8b). Notice that the nonlinear dissipative terms $\mp 2\kappa_N|\alpha|^2a$ in Eqs. (8a) and (8b) lead to the broadening or narrowing of the linewidth associated with the linearized response of the cavity field fluctuations, respectively (see Fig. 4).

APPENDIX D: FLUCTUATION SPECTRUM OF THE NONLINEAR MODEL

Assuming that, in addition to the strong coherent tone, the dynamics of the system is affected by thermal fluctuations of both the bosonic and the TLS baths degrees of freedom,

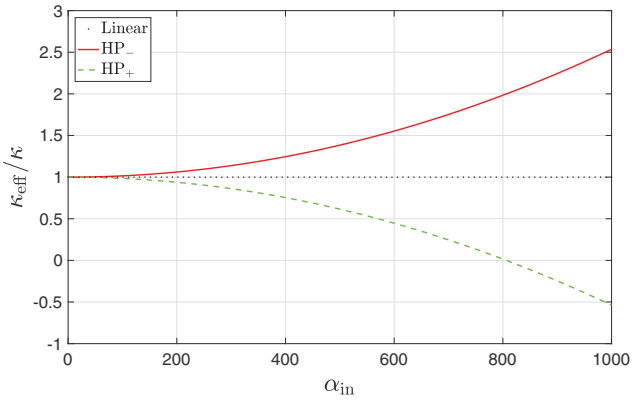

FIG. 4. The total effective dissipation of the linearized models Eq. (8a) (solid red) and Eq. (8b) (dashed green) that correspond to the cases where the majority of the TLSs are in the ground state and excited state, respectively. They are compared to the case of pure linear dissipation (black dots). Here we assume the system to be a simple cavity with $H_S = \omega_{\rm c}c^\dagger c$. In units of κ, the parameters are $\Delta = \omega_{\rm p} - \omega_{\rm c} = 20$ and $\kappa_N = 1.5\times10^{-4}$.

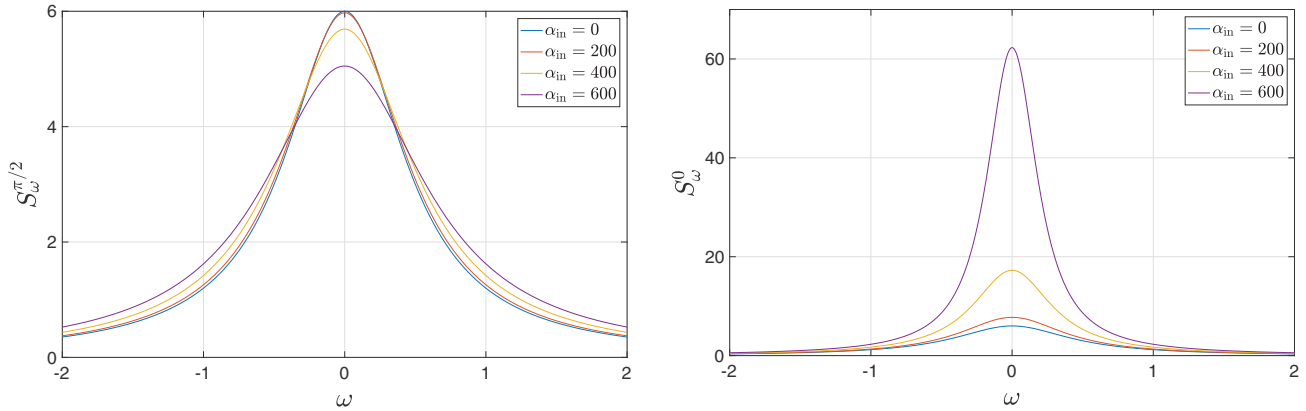

FIG. 5. The cavity spectra related to the Holstein-Primakoff couplings (a) HP_- and (b) HP_+ for the largest uncertainty quadrature ($\theta = \pi/2$ and $\theta = 0$, respectively). In (a) the linewidth widens as $\alpha_{\rm in}$ becomes larger (larger values of $\alpha_{\rm in}$ correspond to smaller values of the maximum at $\omega = 0$), whereas in (b) the linewidth becomes narrower (larger values of $\alpha_{\rm in}$ correspond to larger values of the maximum at $\omega = 0$). Here the thermal populations of the bosonic and TLS baths are $n_{\rm th} = n_{\rm th}^{\rm TLS} = 1$, and in the units of κ, the other parameters are $\Delta = 20$ and $\kappa_N = 1.5\times10^{-4}$.

we evaluate here the spectrum of these fluctuations focusing on the HP_- case (an analogous derivation holds for the HP_+ mapping). The fluctuation spectrum

$$S_\omega^\theta = \tfrac{1}{2}\langle\{X_\omega^\theta, X_{-\omega}^\theta\}\rangle, \tag{D1}$$

with $X_\omega^\theta = 1/\sqrt{2}(a_{-\omega}^\dagger e^{i\theta} + a_\omega e^{-i\theta})$, can be obtained by Fourier transforming the QLE given by Eq. (8a) and its Hermitian conjugate

$$\left[-i(\omega+\Delta) + \frac{\kappa}{2} + 2\kappa_N|\alpha|^2\right]a_\omega + \kappa_N\alpha^2 a_{-\omega}^\dagger = \sqrt{\kappa}a_{{\rm in},\omega} + 2\sqrt{\kappa_N}\alpha^* a_{{\rm in},\omega}^{\rm TLS}, \tag{D2a}$$

$$\left[-i(\omega-\Delta) + \frac{\kappa}{2} + 2\kappa_N|\alpha|^2\right]a_{-\omega}^\dagger + \kappa_N\alpha^{*2} a_\omega = \sqrt{\kappa}a_{{\rm in},-\omega}^\dagger + 2\sqrt{\kappa_N}\alpha a_{{\rm in},-\omega}^{\rm TLS\dagger}, \tag{D2b}$$

with the usual convention for the Fourier transform, according to which $a_t \overset{\rm FT}{\longmapsto} a_\omega$ and $a_t^\dagger \overset{\rm FT}{\longmapsto} a_{-\omega}^\dagger$.

Defining

$$A = -i(\omega+\Delta) + \frac{\kappa}{2} + 2\kappa_N|\alpha|^2, \tag{D3a}$$

$$B = \kappa_N\alpha^2, \tag{D3b}$$

$$C = -i(\omega-\Delta) + \frac{\kappa}{2} + 2\kappa_N|\alpha|^2, \tag{D3c}$$

the QLE for the system can be expressed as

$$\begin{pmatrix} a_\omega \\ a_{-\omega}^\dagger \end{pmatrix} = \frac{1}{AC-|B|^2}\begin{pmatrix} C & -B \\ -B^* & A \end{pmatrix} \times \begin{pmatrix} \sqrt{\kappa}a_{{\rm in},\omega} + 2\sqrt{\kappa_N}\alpha^* a_{{\rm in},\omega}^{\rm TLS} \\ \sqrt{\kappa}a_{{\rm in},-\omega}^\dagger + 2\sqrt{\kappa_N}\alpha a_{{\rm in},-\omega}^{\rm TLS\dagger} \end{pmatrix}, \tag{D4}$$

and

$$a_\omega = \chi_d(\omega)a_{{\rm in},\omega} + \chi_{\rm x}(\omega)a_{{\rm in},-\omega}^\dagger + \chi_d^{\rm TLS}(\omega)a_{{\rm in},\omega}^{\rm TLS} + \chi_{\rm x}^{\rm TLS}(\omega)a_{{\rm in},-\omega}^{\rm TLS\dagger}, \tag{D5a}$$

$$a_{-\omega}^\dagger = \chi_{\rm x}^*(-\omega)a_{{\rm in},\omega} + \chi_d^*(-\omega)a_{{\rm in},-\omega}^\dagger + \chi_{\rm x}^{\rm TLS*}(-\omega)a_{{\rm in},\omega}^{\rm TLS} + \chi_d^{\rm TLS*}(-\omega)a_{{\rm in},-\omega}^{\rm TLS\dagger}, \tag{D5b}$$

where

$$\chi_d(\omega) = \sqrt{\kappa}C(AC-|B|^2)^{-1}, \tag{D6a}$$

$$\chi_{\rm x}(\omega) = -\sqrt{\kappa}B(AC-|B|^2)^{-1}, \tag{D6b}$$

$$\chi_d^{\rm TLS}(\omega) = 2\sqrt{\kappa_N}\alpha^* C(AC-|B|^2)^{-1}, \tag{D6c}$$

$$\chi_{\rm x}^{\rm TLS}(\omega) = -2\sqrt{\kappa_N}\alpha B(AC-|B|^2)^{-1}. \tag{D6d}$$

If we assume that the thermal populations of the baths are given by $\langle a_{{\rm in},\omega}a_{{\rm in},\omega'}^\dagger\rangle = (n_{\rm th}+1)\delta(\omega-\omega')$ and $\langle a_{{\rm in},\omega}^{\rm TLS}a_{{\rm in},\omega'}^{\rm TLS\dagger}\rangle = (n_{\rm th}^{\rm TLS}+1)\delta(\omega-\omega')$, the cavity spectrum can be written as

$$\begin{aligned} S_\omega^\theta = {} & \tfrac{1}{4}[(|\chi_d(\omega)|^2 + |\chi_{\rm x}(-\omega)|^2)\langle\{a_{{\rm in},\omega}, a_{{\rm in},\omega}^\dagger\}\rangle + (|\chi_d(-\omega)|^2 + |\chi_{\rm x}(\omega)|^2)\langle\{a_{{\rm in},-\omega}^\dagger, a_{{\rm in},-\omega}\}\rangle] \\ & + \tfrac{1}{4}[(\chi_d(\omega)\chi_{\rm x}(-\omega)e^{-i2\theta} + \chi_d^*(\omega)\chi_{\rm x}^*(-\omega)e^{i2\theta})\langle\{a_{{\rm in},\omega}, a_{{\rm in},\omega}^\dagger\}\rangle \\ & + (\chi_d(-\omega)\chi_{\rm x}(\omega)e^{-i2\theta} + \chi_d^*(-\omega)\chi_{\rm x}^*(\omega)e^{i2\theta})\langle\{a_{{\rm in},-\omega}^\dagger, a_{{\rm in},-\omega}\}\rangle] \\ & + \tfrac{1}{4}\left[\left(\left|\chi_d^{\rm TLS}(\omega)\right|^2 + \left|\chi_{\rm x}^{\rm TLS}(-\omega)\right|^2\right)\left\langle\left\{a_{{\rm in},\omega}^{\rm TLS}, a_{{\rm in},\omega}^{\rm TLS\dagger}\right\}\right\rangle\right. \\ & \left. + \left(\left|\chi_d^{\rm TLS}(-\omega)\right|^2 + \left|\chi_{\rm x}^{\rm TLS}(\omega)\right|^2\right)\left\langle\left\{a_{{\rm in},-\omega}^{\rm TLS\dagger}, a_{{\rm in},-\omega}^{\rm TLS}\right\}\right\rangle\right] \\ & + \tfrac{1}{4}\left[\left(\chi_d^{\rm TLS}(\omega)\chi_{\rm x}^{\rm TLS}(-\omega)e^{-i2\theta} + \chi_d^{\rm TLS*}(\omega)\chi_{\rm x}^{\rm TLS*}(-\omega)e^{i2\theta}\right)\left\langle\left\{a_{{\rm in},\omega}^{\rm TLS}, a_{{\rm in},\omega}^{\rm TLS\dagger}\right\}\right\rangle\right. \end{aligned}$$

$$
\begin{aligned}
&+\left(\chi_d^{\mathrm{TLS}}(-\omega)\chi_{\mathrm{x}}^{\mathrm{TLS}}(\omega)e^{-i2\theta}+\chi_d^{\mathrm{TLS}*}(-\omega)\chi_{\mathrm{x}}^{\mathrm{TLS}*}(\omega)e^{i2\theta}\right)\left\langle\left\{a_{\mathrm{in},-\omega}^{\mathrm{TLS}\dagger},a_{\mathrm{in},-\omega}^{\mathrm{TLS}}\right\}\right\rangle]\\
&=\tfrac{1}{2}[|\chi_d(\omega)|^2+|\chi_d(-\omega)|^2+|\chi_{\mathrm{x}}(\omega)|^2+|\chi_{\mathrm{x}}(-\omega)|^2\\
&\quad+2\cos(\theta+\phi)|\chi_d(\omega)\chi_{\mathrm{x}}(-\omega)+\chi_d(-\omega)\chi_{\mathrm{x}}(\omega)|]\left(n_{\mathrm{th}}+\tfrac{1}{2}\right)\\
&\quad+\tfrac{1}{2}\left[\left|\chi_d^{\mathrm{TLS}}(\omega)\right|^2+\left|\chi_d^{\mathrm{TLS}}(-\omega)\right|^2+\left|\chi_{\mathrm{x}}^{\mathrm{TLS}}(\omega)\right|^2+\left|\chi_{\mathrm{x}}^{\mathrm{TLS}}(-\omega)\right|^2\right.\\
&\quad\left.+2\cos(\theta+\phi^{\mathrm{TLS}})\left|\chi_d^{\mathrm{TLS}}(\omega)\chi_{\mathrm{x}}^{\mathrm{TLS}}(-\omega)+\chi_d^{\mathrm{TLS}}(-\omega)\chi_{\mathrm{x}}^{\mathrm{TLS}}(\omega)\right|\right]\left(n_{\mathrm{th}}^{\mathrm{TLS}}+\tfrac{1}{2}\right),
\end{aligned}
\tag{D7}
$$

where $\phi^{(\mathrm{TLS})}=\mathrm{Arg}[\chi_d^{(\mathrm{TLS})}(\omega)\chi_{\mathrm{x}}^{(\mathrm{TLS})}(-\omega)+\chi_d^{(\mathrm{TLS})}(-\omega)\chi_{\mathrm{x}}^{(\mathrm{TLS})}(\omega)]$. In Fig. 5(a) we have plotted the cavity spectrum for the HP_-, and the spectrum related to HP_+ coupling derived from Eq. (8b) is presented in Fig. 5(b).

[1] A. J. Leggett, Science **307**, 871 (2005).
[2] W. H. Zurek, Phys. Today **44**, 36 (1991).
[3] A. J. Leggett, S. Chakravarty, A. T. Dorsey, M. P. A. Fisher, A. Garg, and W. Zwerger, Rev. Mod. Phys. **59**, 1 (1987).
[4] H.-P. Breuer and F. Petruccione, *The Theory of Open Quantum Systems* (Oxford University Press, Oxford, 2007).
[5] H. P. Breuer, E. M. Laine, J. Piilo, and B. Vacchini, Rev. Mod. Phys. **88**, 021002 (2016).
[6] A. Ishizaki, T. R. Calhoun, G. S. Schlau-Cohen, and G. R. Fleming, Phys. Chem. Chem. Phys. **12**, 7319 (2010).
[7] M. J. Leskinen, O. H. T. Nummi, F. Massel, and P Törmä, New J. Phys. **12**, 073044 (2010).
[8] F. Massel, A. Kantian, A. J. Daley, T. Giamarchi, and P. Törmä, New J. Phys. **15**, 045018 (2013).
[9] A. M. Visuri, D. H. Kim, J. J. Kinnunen, F. Massel, and P. Torma, Phys. Rev. A **90**, 051603 (2014).
[10] The Nobel Prize in Physics (2012), https://www.nobelprize.org/nobel_prizes/physics/laureates/2012/press.html.
[11] H. M. Wiseman and G. J. Milburn, *Quantum Measurement and Control* (Cambridge University Press, Cambridge, UK, 2010).
[12] M. A. Nielsen and I. L. Chuang, *Quantum Computation and Quantum Information*, 10th Anniversary ed. (Cambridge University Press, Cambridge, UK, 2010).
[13] A. A. Clerk, M. H. Devoret, S. M. Girvin, F. Marquardt, and R. J. Schoelkopf, Rev. Mod. Phys. **82**, 1155 (2010).
[14] B. P. Abbott *et al.* (LIGO Scientific Collaboration and Virgo Collaboration), Phys. Rev. Lett. **116**, 061102 (2016).
[15] A. Wallraff, D. I. Schuster, A. Blais, L. Frunzio, R. S. Huang, J. Majer, S. Kumar, S. M. Girvin, and R. J. Schoelkopf, Nature (London) **431**, 162 (2004).
[16] M. A. Sillanpää, J. I. Park, and R. W. Simmonds, Nature (London) **449**, 438 (2007).
[17] J. Majer *et al.*, Nature (London) **449**, 443 (2007).
[18] R. J. Schoelkopf and S. M. Girvin, Nature (London) **451**, 664 (2008).
[19] J. F. Poyatos, J. I. Cirac, and P. Zoller, Phys. Rev. Lett. **77**, 4728 (1996).
[20] J. D. Teufel, T. Donner, Dale Li, J. W. Harlow, M. S. Allman, K. Cicak, A. J. Sirois, J. D. Whittaker, K. W. Lehnert, and R. W. Simmonds, Nature (London) **475**, 359 (2011).
[21] E. E. Wollman, C. U. Lei, A. J. Weinstein, J. Suh, A. Kronwald, F. Marquardt, A. A. Clerk, and K. C. Schwab, Science **349**, 952 (2015).
[22] J. M. Pirkkalainen, E. Damskagg, M. Brandt, F. Massel, and M. A. Sillanpaa, Phys. Rev. Lett. **115**, 243601 (2015).
[23] F. Lecocq, J. B. Clark, R. W. Simmonds, J. Aumentado, and J. D. Teufel, Phys. Rev. X **5**, 041037 (2015).
[24] F. Massel, T. T. Heikkilä, J.-M. Pirkkalainen, S. U. Cho, H. Saloniemi, P. J. Hakonen, and M. A. Sillanpää, Nature (London) **480**, 351 (2011).
[25] C. F. Ockeloen-Korppi, E. Damskagg, J. M. Pirkkalainen, T. T. Heikkila, F. Massel, and M. A. Sillanpaa, Phys. Rev. X **6**, 041024 (2016).
[26] A. Metelmann and A. A. Clerk, Phys. Rev. X **5**, 021025 (2015).
[27] M. Mirrahimi, Z. Leghtas, V. V. Albert, S. Touzard, R. J. Schoelkopf, L. Jiang, and M. H. Devoret, New J. Phys. **16**, 045014 (2014).
[28] Z. Leghtas *et al.*, Science **347**, 853 (2015).
[29] G. Zolfagharkhani, A. Gaidarzhy, S. B. Shim, R. L. Badzey, and P. Mohanty, Phys. Rev. B **72**, 224101 (2005).
[30] O. Arcizet, R. Riviere, A. Schliesser, G. Anetsberger, and T. J. Kippenberg, Phys. Rev. A **80**, 021803 (2009).
[31] A. Eichler, J. Moser, J. Chaste, M. Zdrojek, I. Wilson-Rae, and A. Bachtold, Nat. Nanotechnol. **6**, 339 (2011).
[32] J. Suh, M. D. Shaw, H. G. LeDuc, A. J. Weinstein, and K. C. Schwab, Nano Lett. **12**, 6260 (2012).
[33] V. Singh, O. Shevchuk, Y. M. Blanter, and G. A. Steele, Phys. Rev. B **93**, 245407 (2016).
[34] R. W. Simmonds, K. M. Lang, D. A. Hite, S. Nam, D. P. Pappas, and J. M. Martinis, Phys. Rev. Lett. **93**, 077003 (2004).
[35] J. M. Martinis *et al.*, Phys. Rev. Lett. **95**, 210503 (2005).
[36] S. Ashhab, J. R. Johansson, and F. Nori, New J. Phys. **8**, 103 (2006).
[37] A. D. O'Connell *et al.*, Appl. Phys. Lett. **92**, 112903 (2008).
[38] J. Gao, M. Daal, J. M. Martinis, A. Vayonakis, J. Zmuidzinas, B. Sadoulet, B. A. Mazin, P. K. Day, and H. G. Leduc, Appl. Phys. Lett. **92**, 212504 (2008).
[39] C. Neill *et al.*, Appl. Phys. Lett. **103**, 072601 (2013).
[40] W. A. Phillips, Rep. Prog. Phys. **50**, 1657 (1987).
[41] C. M. Quintana *et al.*, Appl. Phys. Lett. **105**, 062601 (2014).
[42] R. N. Kleiman, G. Agnolet, and D. J. Bishop, Phys. Rev. Lett. **59**, 2079 (1987).
[43] J. Lindkvist and G. Johansson, New J. Phys. **16**, 055018 (2014).
[44] K. A. Fischer, L. Hanschke, J. Wierzbowski, T. Simmet, C. Dory, J. J. Finley, J. Vučković, and K. Müller, Nat. Phys. **13**, 649 (2017).
[45] G. J. Grabovskij, T. Peichl, J. Lisenfeld, G. Weiss, and A. V. Ustinov, Science **338**, 232 (2012).
[46] A. M. Holder, K. D. Osborn, C. J. Lobb, and C. B. Musgrave, Phys. Rev. Lett. **111**, 065901 (2013).
[47] G. Stefanucci and R. van Leeuwen, *Nonequilibrium Many-Body Theory of Quantum Systems* (Cambridge University Press, Cambridge, UK, 2014).

II

NUMERICAL SIMULATION OF KERR NONLINEAR SYSTEMS; ANALYZING NONCLASSICAL DYNAMICS

by

Agasti, Souvik (2019)

Journal of Physics Communications, 3 (10), 105004

https://doi.org/10.1088/2399-6528/ab4690

IOP Publishing J. Phys. Commun. 3 (2019) 105004 https://doi.org/10.1088/2399-6528/ab4690

Journal of Physics Communications

OPEN ACCESS

RECEIVED
10 July 2019

REVISED
18 September 2019

ACCEPTED FOR PUBLICATION
20 September 2019

PUBLISHED
7 October 2019

PAPER

Numerical simulation of Kerr nonlinear systems; analyzing non-classical dynamics

Souvik Agasti

Nanoscience center, Dept. of Physics, University of Jyväskylä, Finland
Photonics Laboratory, Physics Unit, Tampere University, Finland

E-mail: souvik.s.agasti@jyu.fi

Keywords: Kerr nonlinear system, bistability, second order correlation function, time-evolving block decimation algorithm

Abstract

We simulate coherent driven free dissipative Kerr nonlinear system numerically using Euler's method by solving Heisenberg equation of motion and time evolving block decimation (TEBD) algorithm, and demonstrate how the numerical results are analogous to classical bistability. The comparison with analytics show that the TEBD numerics follow the quantum mechanical exact solution obtained by mapping the equation of motion of the density matrix of the system to a Fokker-Plank equation . Comparing between two different numerical techniques, we see that the semi-classical Euler's method gives the dynamics of the system field of one among two coherent branches, whereas TEBD numerics generate the superposition of both of them. Therefore, the time dynamics determined by TEBD numerical method undergoes through a non-classical state which is also shown by determining second order correlation function.

Introduction

The Kerr effect was discovered by John Kerr in 1875 [1], which exhibits quadratic electro-optic (QEO) effect, is seen in almost all materials, but certain materials display more strongly than others, for example organic molecules and polymers [2], Se-based chalcogenide glasses [3] and silicon photonic devices [4]. The non-linear phenomenon introduced by Kerr effect has been observed experimentally and it has broad range application in many optical and magnetic devices. For example, the optical Kerr effects have been useful for nonlinear signal processing which has shown several applications including NRZ-to-RZ conversion [5], multi-casting, demultiplexing, regeneration, monitoring, multiple-wavelength source [6, 7], and many more. The magneto-optical Kerr effect (MOKE) has potential application in ultrathin magnetic devices, e.g. films [8], multilayers [9], and magnetic superlattices [10], and, the surface magneto-optic Kerr effect (SMOKE) has remain a powerful tool for *in situ* characterization [11] . All the setups have shown bistability as their predominant characteristics which causes due to nonlinear susceptibility.

The multistability in the steady state solution of Kerr nonlinearity has been encountered theoretically in two different ways: semiclassicaly where the state of the system is approximated to the nearest coherent state, and quantum mechanically where we estimate the exact solution from the master equation formalism of the density matrix of the system. The semicalssical solution of both dispersive and absorptive bistability has been derived by using the quantum Langevin equation [12, 13], and the theory of quantum mechanical solution for the absorptive case [14] and the dissipative case [15] has been obtained by mapping the master equation to the Fokker plank equation. Both the techniques have been used widely to study the dynamics of open quantum systems which is considered as one of the most fundamental problems in quantum mechanics.

The theoretical techniques for open quantum system have been developed over decades and applied successfully for detecting and preparing quantum states of matter and radiation [16], sensing electromagnetic fields [17], quantum communication [18] and detection of gravitational waves [19]. The recent development of nanoscale fabrication techniques, in general, circuit quantum electrodynamics (QED) setups exhibit the technological application of quantum mechanics, particularly in superconducting qubits and nanomechanical

resonators ([20, 21]). Within this framework, recently the theory has been used to study various nonlinear systems, e.g. two state systems [22, 23], microwave quantum optomechanics [24] and impurities in solid state systems [25]. In all cases, including Kerr nonlinear systems, linearized approximated theory has been implemented to study the dynamical behavior of the system, where one transforms the nonlinear Hamiltonian to a linear one by accounting the quantum fluctuation over nonlinear steady state field amplitude. Appreciating its simplicity, the technique, however, cannot provide a satisfactory platform. The limitation of the analytics provokes us for the numerical simulation of the time evolution of nonlinear systems, explicitly. In order to implement the numerical model, we transform the environmental degrees of freedom to a one dimensional many body system with nearest neighbor interaction and simulate the whole chain using time-adaptive density matrix renormalisation group (t-DMRG) method. The computational method consists of numerical diagonalization and renormalization process.

The t-DMRG technique is considered as one of the most powerful numerical schemes in optical, atomic and condensed matter physics to be applied on strongly-correlated many-body quantum systems. The technique have already been used for some of the renowned models of quantum mechanics, e.g. Hubbard model [26–29], Bose–Hubbard model [30–32] and Ising model [33–35], especially aiming to study the quenching dynamics, magnetization and phase transition properties.

In this paper, we introduce a TEBD numerical model for the simulation of open quantum system, and use the model for the first time to study the time dynamics of the Kerr nonlinear system. The article is composed by starting with the theoretical model that explains how the continuous modes of the bath together with the nonlinear system is transformed into a one dimensional discrete chain. Hereafter, we use two different numerical methods: time propagation of the system field by solving the Heisenberg equation of motion using Euler's method and TEBD numerical method to determine the time dynamics and steady state behavior of the system. We also compare between the numerics and with analytics, discussing in detail explaining the physical significance of our result.

Model: theory

The Hamiltonian of a system that describes the Kerr effect is,

$$H_S = \omega_S a^\dagger a + \chi'' a^{\dagger 2} a^2 + i(a^\dagger E e^{-i\omega_L t} - a E^* e^{i\omega_L t}), \tag{1}$$

where ω_S is the frequency of the cavity mode of oscillation, χ'' is the anharmonicity parameter which is dependent on the real part of the third order nonlinear susceptibility tensor ([15]), and $a^\dagger(a)$ are the creation (annihilation) operators of the system. E is the amplitude of an external driving field with an oscillation frequency ω_L, expressing as $\vec{E}(t) = \vec{E} e^{-i\omega_L t} + \vec{E}^* e^{i\omega_L t}$. In order to make the Hamiltonian time independent, we switch to the frame of the driving field. Eventually, the detuned cavity frequency becomes $\Delta = \omega_S - \omega_L$. Considering the system is coupled to a thermal reservoir, the total Hamiltonian is given by,

$$H_{tot} = H_S + H_B + H_{SB}, \tag{2}$$

where $H_B = \int_{-x_m}^{x_m} g(x) d^\dagger(x) d(x) \mathrm{d}x$ represents the Hamiltonian of a multimode bosonic reservoir which is at zero temperature, and $H_{SB} = \int_{-x_m}^{x_m} h(x)(a^\dagger d(x) + h.c.) \mathrm{d}x$ is the interaction Hamiltonian. We consider ω_S is the central frequency of the reservoir, $d_x^\dagger(d_x)$ are the creation (annihilation) operators, and $g(x)$ and $h(x)$ are the frequency of oscillation and the coupling strength between the system and environment, respectively, for the environmental mode x. The properties of bath can be characterized by a uniquely defined spectral density function $J(\omega)$. Considering the linear dispersion relation ($g(x) = g.x$, where g is the inverse of density of states), and implying wide band limit approximation ($h(x) = c_0$) [36], we get the spectral density function [37]

$$J(\omega) = \frac{1}{2}\gamma\theta(\omega + \omega_c)\theta(\omega_c - \omega), \tag{3}$$

where $\gamma = 2\pi c_0^2$ is the decay rate of the system and θ is the Heaviside step function. With this choice of hard cutoff, we fix the frequency limit $\omega_c = g.x_m$ to run over the entire spectrum of bath.

Model: tebd numerics

To simulate an open quantum system numerically, we transform the Hamiltonian of the system/bath coupling model to a semi-infinite chain model, by mapping the bath operators to the operators of lattice chain, using a unitary transformation: $b_n = \int_{-x_m}^{x_m} U_n(x) d(x) \mathrm{d}x$. In a case where the spectral density is defined by the equation (3), the normalized shifted Legendre polynomial is a natural choice as the unitary operator: $U_n(x) = \sqrt{\frac{(2n+1)}{2x_m}} L_n(x/x_m)$ which is defined in the range of $x \in [-x_m, x_m]$ and satisfies the orthogonality

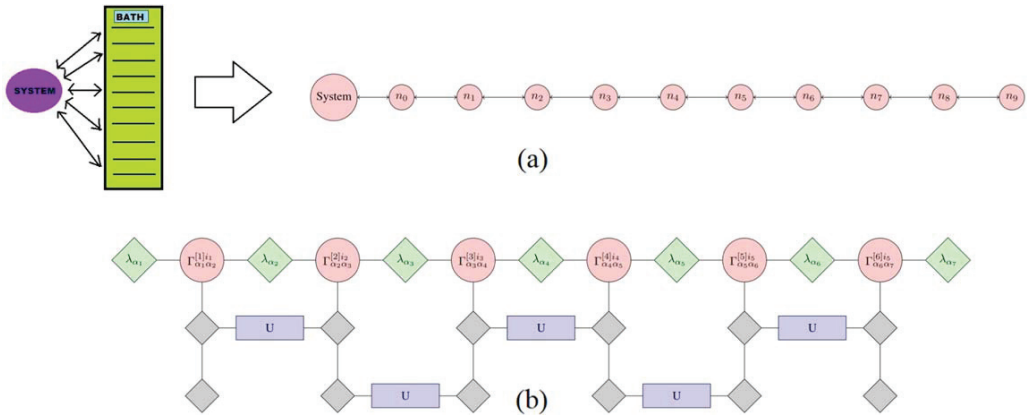

Figure 1. (a) Transformation of system/bath coupling Hamiltonian to a semi infinite chain Hamiltonian. (b) Diagrammatic expression of the real time evolution where the operators applied on alternating pair.

condition [38]. The transformed Hamiltonian of the semi infinite chain is

$$H_{chain} = H_S + \eta'(a^\dagger b_0 + a b_0^\dagger) + \lim_{N\to\infty}\left[\sum_{n=0}^{N}\omega_n b_n^\dagger b_n + \sum_{n=0}^{N-1}\eta_n(b_n^\dagger b_{n+1} + b_n b_{n+1}^\dagger)\right] \tag{4}$$

where the coefficients are $\eta' = c_0\sqrt{2\omega_c}$, $\omega_n = 0$ and, $\eta_n = \omega_c\left(\frac{n+1}{\sqrt{(2n+1)(2n+3)}}\right)$. The schematic diagram of the transformation is given in figure 1(a). Similar mapping is introduced recently in [38] to simulate open quantum systems aiming to be applied to spin-boson models [39] and biomolecular aggregates [40].

Hereafter, we express the state of the chain as a matrix product state (MPS) to do the numerical simulation using TEBD. The MPS state is expressed by ([41])

$$|\Psi\rangle = \sum_{\alpha_1,..,\alpha_{N+1}=0}^{\chi}\ \sum_{i_1...i_N=0}^{M}\lambda_{\alpha_1}^{[1]}\Gamma_{\alpha_1\alpha_2}^{[1]i_2}\lambda_{\alpha_2}^{[2]}\Gamma_{\alpha_2\alpha_3}^{[2]i_3}\cdots\cdot\lambda_{\alpha_N}^{[N]}\Gamma_{\alpha_N}^{[N]i_N}\lambda_{\alpha_{N+1}}^{[N+1]}|i_1, i_2 ,.., i_{N-1}, i_N\rangle. \tag{5}$$

The Γ and λ tensors are obtained through the Schmidt decomposition of the pure state of N sites where χ is the Schmidt number and M is the dimension of local Hilbert space. Figure 1(b) shows the method of numerical simulation for the real time evolution diagrammatically, where we choose 2nd order Suzuki Trotter (ST) expansion ([42]) which expresses the unitary evolution operator as

$$U_{dt} = e^{-idtH_{chain}} = e^{-iFdt/2}e^{-iGdt}e^{-iFdt/2} + O[dt^3], \tag{6}$$

where $F = \sum_{i\ \text{odd}} H_{chain}^{i,i+1}$ and $G = \sum_{i\ \text{even}} H_{chain}^{i,i+1}$. The ST expansion minimizes the error in 3rd order of the time step by evolving the pairs of alternate sites.

The simulation parameters are estimated by minimizing errors which appear in two ways: during the modeling of the S/B formalism to a 1D chain and the simulation of each step of the real time evolution. We discuss the errors extensively in appendix with an estimation of simulation parameters.

Model: time propagation of semi-classical equation

Since the bath is at zero temperature, the time dynamics of the system field is obtained by the Heisenberg equation of motion:

$$\dot{a} = -i\Delta a - \frac{\gamma}{2}a - 2i\chi\alpha^2 a^\dagger - 4i\chi|\alpha|^2 a \tag{7}$$

which is a first order differential equation. Therefore, using Euler's method ([43]), we do the time propagation of the system field numerically to obtain the time dynamics and steady state.

Results: steady state situation

The exact analytical expression of the moment calculating generalized functions of the system field operators are derived by mapping the master equation into the Fokker-Plank equation [15], which determines the steady-state field amplitude and second order correlation functions:

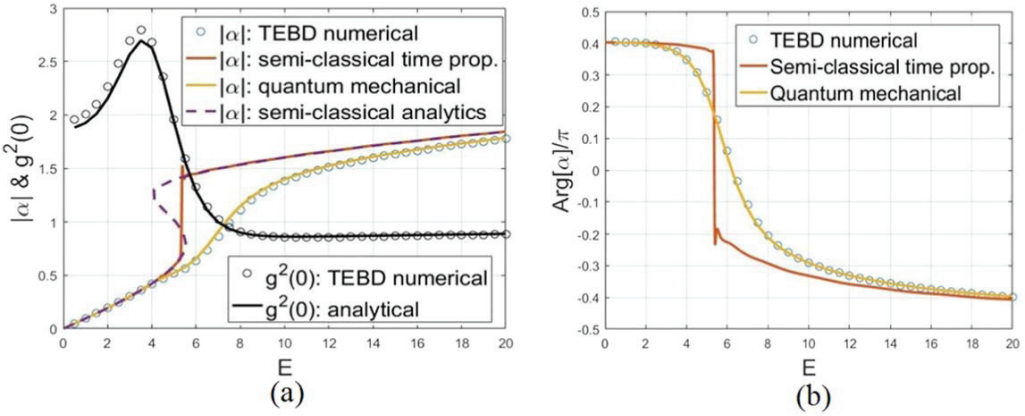

Figure 2. (a) Steady state field amplitude and second order correlation function, (b) phase plotted for $\Delta = -10$, $\chi'' = 3$, $\gamma = 6.3$ with the variation of driving field amplitude. All quantities are in the units of g and the TEBD simulation parameters: $N = 50$, $\chi = 25$, $M = 15$, $\delta t = 10^{-2}\, g^{-1}$.

$$\langle a \rangle = \left(-\frac{[E_0/i\chi'']F(p+1,\, q,\, 2[E_0/\chi'']^2)}{pF(p,\, q,\, 2[E_0/\chi'']^2)} \right). \tag{8a}$$

$$g^2(0) = \left(\frac{pqF(p,\, q,\, 2|E_0/\chi''|^2)F(p+2,\, q+2,\, 2[E_0/\chi'']^2)}{(p+1)(q+1)[F(p+1,\, q+1,\, 2[E_0/\chi'']^2)]^2} \right), \tag{8b}$$

where $E_0 = E = E^*$, $p = \left[\frac{\Delta}{\chi''} + \frac{\gamma}{2i\chi''}\right]$, $q = \left[\frac{\Delta}{\chi''} - \frac{\gamma}{2i\chi''}\right]$ and $F(p, q, z) = F([], [p, q], z)$ is the ${}_0F_2$ hypergeometric function. Furthermore, the relation between the input drive and the semi-classical stationary value of the system field, determined from the Heisenberg equation of motion given in equation (7), is given by

$$|E|^2 = |\alpha|^2 \left((\Delta + 2\chi''|\alpha|^2)^2 + \frac{\gamma^2}{4} \right), \tag{9}$$

where α is the steady state system field.

Since the TEBD numerical model for the Kerr nonlinear system is introduced for the first time, we justify its applicability by comparing with the analytically estimated results. Here, we plot the steady state system field and the second order correlation function in figure 2 which presents both the numerical results determined through TEBD and the time propagation of the system field using Euler's method, along with the analytically determined semi-classical and quantum mechanical solution, which shows how the TEBD numerical result is analogous to classical bistability. For the numerical simulation of the time dynamics, the initial state of the system is chosen to be in a ground state, and therefore, no photon existed initially. We see the stationary value of the system field loses its linear nature when the driving field is increased far. It is also to be noted that the semi classical solution exhibits bistability whereas the exact quantum mechanical solution does not. The peak in the plot of $g^2(0)$ indicates the increase of the quantum fluctuations near the transition point, which happens due to the superposition of two coherent states in the quantum mechanical solution; and, as the coherent states are not mutually orthogonal, the state loses its classical nature. The TEBD determined numerical result matches to the quantum mechanical exact analytical solution, whereas the numerical time propagation of the system field using Euler's method follows the analytically determined semi-classical solution, and the branch shift occurs within the boundary of analytically predicted transition region. The extent to which bistability is observed depends on the fluctuations of the input driving field, which in turn determine the time for random switching from one branch to the other. The time scale of the change of driving field must be larger than time intervals of the random switching between branches.

Results: time dynamics

The time dynamics of the Kerr nonlinear system is generally estimated analytically by linearizing the quantum fluctuation over nonlinear steady state field amplitude. Anticipating its simplicity, however, this does not provide accuracy when the impact of nonlinearity is predominant which is observed, especially when the system is driven by a stronger pump. Even though an effort to study the classical dynamics of Kerr system has been made in [44], but this does not provide sufficient information regarding quantum dynamics; which provokes us to opt

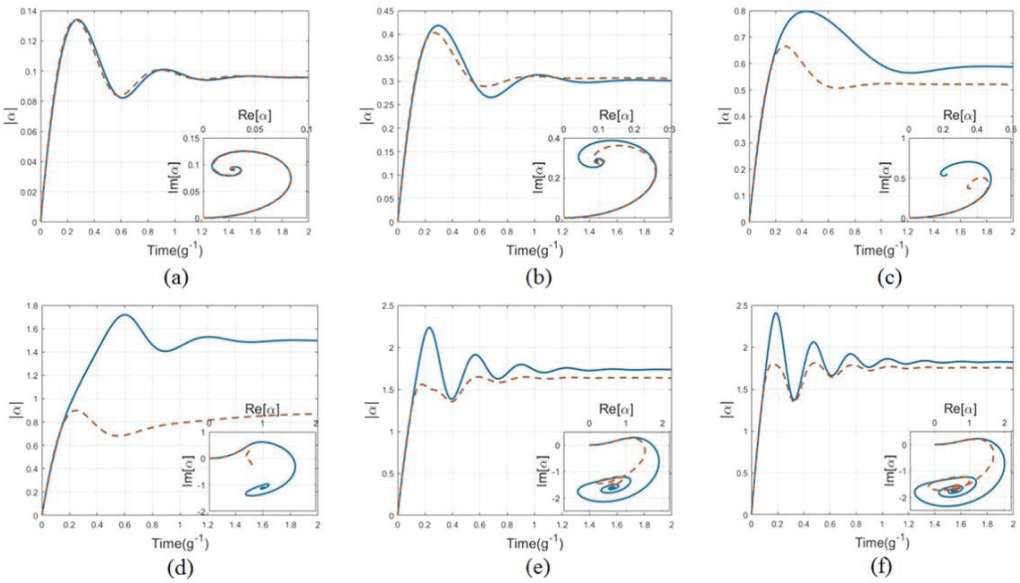

Figure 3. Time dynamics of the system field with the variation of driving field amplitude ((a)1, (b)3, (c)5, (d)7, (e)15, (f)19). The blue solid line and the red dashed lines correspond to the time propagation using Euler's method and TEBD numerical method, respectively. In inset we plot the trajectory of the system field, along with the phase. All other parameters remain same with figure 2.

numerical methods. We plot the time dynamics of system field in figure 3 which shows that the field stabilizes after suffering initial oscillation . However, the plots exhibit difference for two different methods, which comes from the fact that the semi-classical Euler's method determines the coherent field of the system which lies on one among two branches, whereas TEBD determined result gives the superposition of both the branches, and as a consequence, the difference enhances around the transition region (figures 3(c) and (d)) . The interesting phenomenon is also noticed when we plot the trajectory of the time evolution of the system field in phase space. From the plots given in insets, we see that two different branches reach different steady states following a completely opposite trajectory. However, in case of the TEBD numerical result, we don't find any particular pattern in the transition region, for the trajectory of the system field due to the dominant superposition of both the coherent states.

Results: second order correlation function

We also plot the time evolution of the second order correlation function using TEBD algorithm, in figure 4 which shows that the correlation function does not deviate much from unit value when the system relaxes closer to a stable classical branch. However, as anticipated due to the superposition of two coherent states, around the transition region, the time evolution of the correlation function differs much from the unit, which indicates that the evolution of the system goes through nonclassical states.

Conclusion

We have used TEBD numerical technique and Euler's method successfully for the time propagation of the system field of a Kerr nonlinear system, and studied how the numerical results are analogous to classical bistability. Analyzing the steady state behavior of the system, we see that the TEBD numerical result follows the quantum mechanical exact solution obtained by mapping the equation of motion of the density matrix of the system to a Fokker-Plank equation, whereas the time propagation of the system field obtained using Euler's method follows the semi-classical solution of the Heisenberg equation of motion. The time dynamics determined by two different numerical techniques show that the semi-classical Euler's method determines the coherent field of the system which lies one among two branches, whereas TEBD determined numerical result keeps the superposition of both of them. As a result, there comes a difference in the system field for two different methods, which enhances around the classical transition region. The TEBD determined second order correlation function does not evolve as unit valued, especially around the transition region which is an indication of the generation of non-classical state due to the superposition of the two coherent states. The

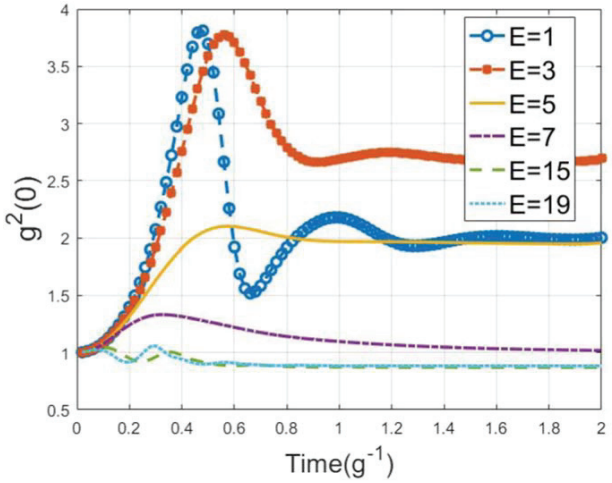

Figure 4. Plot of the second order correlation function with the variation of the driving field. All other parameters remain same with figure 2.

importance of our work, the analysis of the dynamical behavior of the externally driven Kerr nonlinear system, has been visualized in recent experiments. For example, studding the influence of different magnetic fields on electrical conductivity in a nonlinear media has drawn attention for exhibiting interesting quantum effects [45, 46]. Analyzing the performance of the numerical techniques, we conclude by saying that the techniques chosen here are quite promising to work with for the analysis of nonlinear systems, and could be useful for the investigation of nonlinear dynamics reported in [24, 25].

Acknowledgments

This work was supported by the Academy of Finland under contract no. 275245.

Appendix: Errors in tebd simulation and estimation of parameters

We investigate the error here introduced due to the finite values of the simulation parameters, and show how they modify with the variation of those parameters. This study will help us to estimate and optimize the parameters in order to do the simulation efficiently.

Modeling error

The modeling error is contributed by the canonical transformation of S/B coupling to 1D chain. In practice, we choose a model where the chain has a finite length considering the fact that the number of modes of the bath is finite, which causes the recurrence of the particle from the end of the chain. Here, we discuss how the recurrence time changes when those parameters change.

- *Length of the chain:* The recurrence time is dependent on the group velocity which is defined by $v_g = \frac{\delta\omega}{\delta k_N}$, where ω is the frequency, and k_N is the wavenumber determined by the number of lattice sites ($k_N \propto N$). In figure A1(a), we see the recurrence time increases with the increment of the length of the chain, which happens due to the fact that the increment of the number of sites reduces the group velocity for the particle to travel.
- *Cut off frequency:* The increment of the cutoff frequency increases the group velocity, forcing the particle to travel faster in the lattice, causing the reduction of the recurrence time which is seen in the figure A1(b).

Numerical error

Apart from modeling error, there are two other major sources of simulation error appears due to the finite sizes of the time step and the truncation of the Hilbert space.

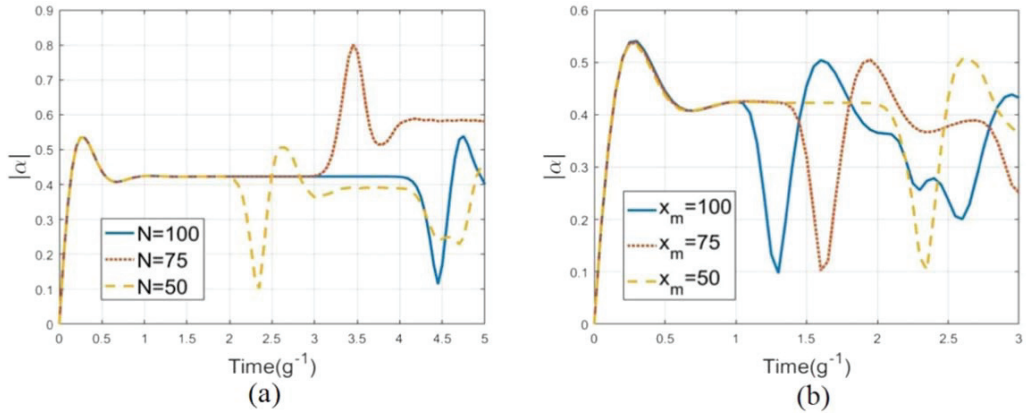

Figure A1. Variation of recurrence time with the variation of (a) number of sites, (b) cutoff frequency. $E = 4$ and all other parameters remain same with figure 2.

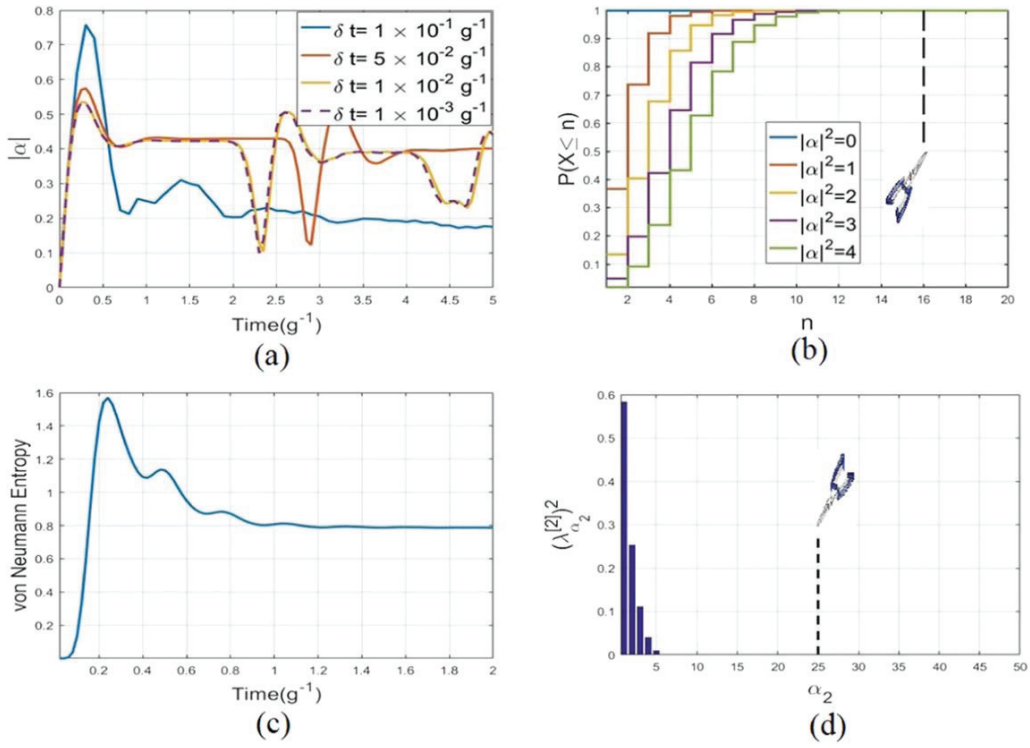

Figure A2. (a) Time evolution of the system field with the variation of step size in TEBD simulation. (b) Plot of cumulative probability of a regular Poisson distribution for different mean values. The black line shows the truncation point in the Hilbert space. (c) Plot of the time evolution of the von Neumann entropy of the first site. (d) Plot of the eigenvalues of the reduced density matrix when the entanglement is maximized, and the black line shows the truncation point. For (a) $E = 4$ and (c, d) $E = 20$, and all other parameters remain same with figure 2.

- *Suzuki Trotter error:*In case of real time evolution, the Suzuki-Trotter error which is introduced due to the finite size of the time step, tends to concentrate in the overall phase ([42]). In figure A2(a), we show how the accuracy of the simulation improved with the reduction time step. As time step decreases the curves approach each other, and beyond the time step $10^{-2}\,g^{-1}$, we do not see any substantial improvement in the plot of cavity field amplitude.
- *Truncation error:*The TEBD numerical method is involved with the truncation of Hilbert space in every step of time evolution ([41]). The *reasonable size* of Hilbert space is such a size that has the ability to express the cavity field with negligible error. The coherent field generated in the system has a Poisson probability distribution

which demands infinite local Hilbert space to complete the set which is clearly not possible. The occupation probability of boson of a coherent field ($|n\rangle$) is distributed in Fock basis according to $|\langle n|\alpha\rangle|^2 = \frac{1}{n!}(|\alpha|^{2n}e^{-|\alpha|^2})$. The cumulative probability distribution is shown in figure A2(b), which estimates the reasonable size of local Hilbert space, anticipating accuracy upto a significant extent.

In order to estimate a reasonable size of the Schmidt number, we plot the von Neumann entropy associated with the entanglement between the system and the first site ($S = -\sum_{\alpha_2}(\lambda_{\alpha_2}^{[2]})^2 \log_2(\lambda_{\alpha_2}^{[2]})^2$) in figure A2(c). As the evolution of the state starts from a product state, the von Neumann entropy was zero at the beginning. It increases initially and reaches to the maximum value, and then, reduces with time.

We estimate the Schmidt number when the entanglement is maximized. The Schmidt number should be chosen in such a way that the eigenvalues after truncation contribute so less that they can easily be neglected. In figure A2(d) we plot the eigenvalues of the reduced density matrices when the entanglement is maximum between the system and the first site of the chain. The truncation line shows that the choice of Schmidt number is reasonable in this case.

ORCID iDs

Souvik Agasti https://orcid.org/0000-0002-9863-2203

References

[1] Kerr J 1875 *The London, Edinburgh, and Dublin Philosophical Magazine and Journal of Science* **50** 337–48
[2] Nalwa H S and Miyata S 1997 *Nonlinear Optics of Organic Molecules and Polymers* (Boca Raton, FL: CRC Press)
[3] Lenz G, Zimmermann J, Katsufuji T, Lines M, Hwang H, Spälter S, Slusher R, Cheong S, Sanghera J and Aggarwal I 2000 *Opt. Lett.* **25** 254–62
[4] Leuthold J, Koos C and Freude C 2010 *Nat. Photonics* **4** 535–44
[5] Kuo B P-P, Chui P C and Wong K K-Y 2008 *J. Lightwave Technol.* **26** 3770–5
[6] Chen S and Xun L 2017 Research on cavity solitons in kerr combs with pump feedback for flat broadband multi-wavelength source *Frontiers in Optics 2017* (Washington, D.C: Optical Society of America) p JW4A.50 www.osapublishing.org/abstract.cfm?uri=FiO-2017-JW4A.50
[7] Liao P *et al* 2019 *J. Lightwave Technol.* **37** 579–84
[8] Loughran T H J, Keatley P S, Hendry E, Barnes W L and Hicken R J 2018 *Opt. Express* **26** 4738–50
[9] Kaihara T, Ando T, Shimizu H, Zayets V, Saito H, Ando K and Yuasa S 2015 *Opt. Express* **23** 11537–55
[10] Buda B, Dahl M, von Truchsess N and Waag A 1994 *J. Cryst. Growth* **138** 652–5
[11] Qiu Z Q and Bader S D 2000 *Rev. Sci. Instrum.* **71** 1243–55
[12] McCall S L 1974 *Phys. Rev.* A **9** 1515–23
[13] Agrawal G P and Carmichael H J 1979 *Phys. Rev.* A **19** 2074–86
[14] Carmichael H J and Walls D F 1977 *J. Phys. B: At. Mol. Phys.* **10** L685–91
[15] Drummond P D and Walls D F 1980 *J. Phys. A: Math. Gen.* **13** 725 p
[16] Solomon P A 2011 *Contemp. Phys.* **52** 162–3
[17] Clerk A A, Devoret M H, Girvin S M, Marquardt F and Schoelkopf R J 2010 *Rev. Mod. Phys.* **82** 1155–208
[18] Nielsen M and Chuang I 2010 *Quantum Computation and Quantum Information* 10th edn (Cambridge: Cambridge University Press) (https://doi.org/10.1017/CBO9780511976667)
[19] Abbott B P *et al* 2016 *Phys. Rev. Lett.* **116** 061102 p
[20] Wallraff A, Schuster D I, Blais A, Frunzio L, Huang R-S, Majer J, Kumar S, Girvin S M and Schoelkopf R J 2004 *Nature* **431** 162–7
[21] Sillanpää M A, Park J I and Simmonds R W 2007 *Nature* **449** 438
[22] Leggett A J, Chakravarty S, Dorsey A T, Fisher M P A, Garg A and Zwerger W 1987 *Rev. Mod. Phys.* **59** 1–85
[23] Spohn H 1989 *Comm. Math. Phys.* **123** 277–304
[24] Pirkkalainen J-M, Damskägg E, Brandt M, Massel F and Sillanpää M A 2015 *Phys. Rev. Lett.* **115** 243601
[25] Manninen J, Agasti S and Massel F 2017 *Phys. Rev.* A **96** 063830 p
[26] Arita R, Kuroki K, Aoki H and Fabrizio M 1998 *Phys. Rev.* B **57** 10324–7
[27] Sakai O and Kuramoto Y 1994 *Solid State Commun.* **89** 307–11
[28] Mielke A 1993 *Phys. Lett.* A **174** 443–8
[29] Sorella S and Tosatti E 1992 *EPL (Europhysics Letters)* **19** 699
[30] Freericks J K and Monien H 1996 *Phys. Rev.* B **53** 2691–700
[31] Läuchli A M and Kollath C 2008 *J. Stat. Mech: Theory Exp.* **2008** P05018 p
[32] Zwerger W 2003 *J. Opt. B: Quantum Semiclassical Opt.* **5** S9
[33] Juozapavičius A, Caprara S and Rosengren A 1997 *Phys. Rev.* B **56** 11097–101
[34] Glauber R J 1963 *J. Math. Phys.* **4** 294–307
[35] Baker G A 1961 *Phys. Rev.* **124** 768–74
[36] Stefanucci G and van Leeuwen R 2014 *Many-Body Theory of Quantum Systems* (Cambridge: Cambridge University Press) (https://doi.org/10.1017/CBO9781139023979)
[37] Leggett A J, Chakravarty S, Dorsey A T, Fisher M P A, Garg A and Zwerger W 1987 *Rev. Mod. Phys.* **59** 1–85
[38] Chin A W, Rivas A, Huelga S F and Plenio M B 2010 *J. Math. Phys.* **51** 092109 p
[39] Chin A W, Prior J, Huelga S F and Plenio M B 2011 *Phys. Rev. Lett.* **107** 160601
[40] Huelga S and Plenio M 2011 *Procedia Chemistry* **3** 248–57 22nd Solvay Conference on Chemistry
[41] Vidal G 2003 *Phys. Rev. Lett.* **91** 147902

[42] Hatano N and Suzuki M 2005 Finding exponential product formulas of higher orders *Quantum Annealing and Other Optimization* ed A Methods, Das and B K Chakrabarti (Berlin, Heidelberg: Springer Berlin Heidelberg) pp 37–68
[43] Butcher J C 2016 *Numerical Methods for Ordinary Differential Equations* (New York: Wiley)
[44] Rigo M, Alber G, Mota-Furtado F and O'Mahony P F 1997 *Phys. Rev.* A **55** 1665–73
[45] García-Merino J A, Martínez-González C L, Miguel C R T S, Trejo-Valdez M, Martínez-Gutiérrez H and Torres-Torres C 2016 *Opt. Express* **24** 19552–7
[46] García-Merino J A, Mercado-Zúñiga C, Martínez-González C L, Torres-SanMiguel C R, Vargas-García J R and Torres-Torres C 2017 *Mater. Res. Express* **4** 035601 p

III

SIMULATION OF MATRIX PRODUCT STATES FOR DISSIPATION AND THERMALIZATION DYNAMICS OF OPEN QUANTUM SYSTEMS

by

Agasti, Souvik (2020)

Journal of Physics Communications, 4 (1), 015002

https://doi.org/10.1088/2399-6528/ab6141

Journal of Physics Communications

OPEN ACCESS

RECEIVED
10 October 2019

REVISED
18 November 2019

ACCEPTED FOR PUBLICATION
12 December 2019

PUBLISHED
3 January 2020

PAPER

Simulation of Matrix Product States For Dissipation and Thermalization Dynamics of Open Quantum Systems

Souvik Agasti

Nanoscience center, Dept. of Physics, University of Jyväskylä, Finland
Photonics Laboratory, Physics Unit, Tampere University, Finland

E-mail: souvik.s.agasti@jyu.fi

Keywords: open quantum system, thermal bath, time-evolving block decimation algorithm, minimally entangled typical thermal states

Abstract

We transform the system/reservoir coupling model into a one-dimensional semi-infinite discrete chain through unitary transformation to simulate the open quantum system numerically with the help of time evolving block decimation (TEBD) algorithm. We apply the method to study the dynamics of dissipative systems. We also generate the thermal state of a multimode bath using minimally entangled typical thermal state (METTS) algorithm, and investigate the impact of the thermal bath on an empty system. For both cases, we give an extensive analysis of the impact of the modeling and simulation parameters, and compare the numerics with the analytics.

Introduction

Open quantum systems—i.e. quantum systems which are described as separate entities from the surrounding environment while being somehow coupled to it— have drawn attention over the decades because of their applicability in the foundation of statistical mechanics, quantum mechanics, and the realization of optical, atomic and molecular physics. The dynamics of open quantum systems is one of the most fundamental problems in quantum mechanics, encompassing concepts such as the boundary between quantum and classical physics [1], and the measurement paradox [2]. On general grounds, the system/bath (S/B) interaction represents an important aspect of the physics of condensed matter [3, 4], and complex systems, ranging from the energy transport in photosynthetic complexes [5] to the physics of ultracold gases [6, 7].

The theory of open quantum systems has been merged with experimental activities in the field of quantum computation and decoherence measurement in a two-level system, which has extensive applications in quantum networks [8, 9] of mesoscopic systems, including superconducting circuits [10], ion traps [11, 12], and photonic crystals [13]. The uses of the coupling between system and environment is rooted in measurement and sensing applications, ranging from electromagnetic fields [14] to gravitational waves [15]. On the other side, the impact of the external environment on the system represents a source of noise and dissipation when we look at from the quantum-dynamical perspective. However, the technological applications of quantum mechanics have been observed in the relatively recent development of nanoscale fabrication techniques, particularly in superconducting qubits, nanomechanical resonators and, more in general, circuit quantum electrodynamics (QED) setups [16, 17], where the dynamical quantum property shows dependency on the characteristic scales, which is affected by the presence of coupling to the surrounding environment. Within this framework, it was recently observed that a specific quantum state of the system can be generated by manipulating the properties of the environment or even the nature of the system environment coupling itself, which is known as reservoir engineering [18]. For example, the manipulation led to the possibility of measurement and control [19] of quantum states, and to protecting certain quantum states (cat states) from decoherence by designing a specific coupling (nonlinear) between system and environment [20, 21].

The dissipative dynamics of a Markovian system and the noise interference due to the linear coupling between the system and environment have been described in terms of linear quantum Langevin equations (QLE) [19], which are an extension of the classical Langevin equation to the quantum regime. However, the linear

coupling between the system and the environment does not appear as the most general situation; for instance, nanomechanical resonators [22, 23], circuit QED setups [16, 17], optomechanical systems [24, 25] and the impurity affected solid state systems [26]. In these cases, the theory has been implemented after transforming the nonlinear Hamiltonian to a linear one by linearizing the quantum fluctuation over a nonlinear steady state field amplitude. Appreciating its simplicity, this model, however, does not provide a satisfactory platform to obtain exact dynamical behavior. The interesting effects, e.g. non-classical behavior of the nonlinear systems [27], are often overlooked when we cannot handle the interaction between two systems in a perturbative manner. Apart from nonlinear S/B coupling, the analytical model is also limited to providing the exact solution in case of non-Markovian dynamical phenomenon, for instance phase transition in a two level system (TLS) between dynamically localized and delocalized states, at zero temperature for Ohmic and sub-Ohmic reservoirs [3, 28–30]. The limitation of the analytics explicitly provokes us to simulate the time evolution numerically. The numerical approach consists of transforming the environmental degrees of freedom to many body systems and simulate it in order to obtain the time evolution. The computational method includes a numerical diagonalization and renormalization process.

The time-adaptive density matrix renormalization group (t-DMRG) is considered as one of the most powerful methods in atomic, optical and condensed matter physics to study strongly correlated many-body quantum system. The method have often been used for some renowned models of quantum mechanics, such as the Ising model [31, 32], the Hubbard model [33–35] and the Bose–Hubbard model [36–38], especially aiming to study the magnetization, quenching dynamics and phase transition properties. In order to implement it in this case, we map the canonical S/B model to a one-dimensional harmonic chain with nearest neighbor interactions.

Here, we present a numerical model for the analysis of the simple coupling between the system and environment, along with the consequences associated with the modeling and the numerical simulation. We start with simulating the dissipative dynamics of an open quantum system, an then we study the thermalization of the system in the presence of a thermal bath.

According to quantum statistical mechanics, the thermal state is a mixed state, and therefore, it is represented by an ensemble of pure states. It is naturally expressed by using density matrix $\rho_\beta = \exp(-\beta H)$ for the inverse temperature β and Hamiltonian H. A few numerical approaches have been employed to study the impact of thermal bath on an interactive system, e. g. quasi adiabatic propagator path integral algorithm (QUAPI) [39, 40] or solving hierarchical equations of motion (HEOM) [41], but in all cases, the influence of the bath on the dynamics of the system is taken care analytically using well defined Feynman-Vernon influence functional. The influence functional appears to be different for different types of coupling between system and environment, and in some cases, it becomes extremely difficult to determine, especially when nonlinear coupling appears. However, the method we discuss here has the ability to overcome this problem. This includes generation of thermal bath numerically and evaluation of time dynamics of both the system and environment. Even though the DMRG technique is designed to determine the ground state [42] and the time evolution of many body systems, a different method has been used to study the thermal state. Here, we introduce a complementary approach which includes taking a large number of sample pure states and determine an observable by averaging over them, instead of expressing the state by a density matrix. The states whose ensemble collectively generates the impact of thermal state, are determined through imaginary time evolution and projective measurements, typically known as minimally entangled typical thermal states (METTS) [43]. In this article, we impose the algorithm for the first time to generate the thermal bath, parameterize it and investigate the consequences to study the thermalization of open quantum system.

Theoretical model

In this article, we discuss the dynamics of a simple coupling model between the system and the reservoir. We start with the Hamiltonian of the system coupled to a thermal environment, which is given by

$$H_{tot} = H_S + H_B + H_{SB}, \tag{1}$$

where $H_S = \omega_c c^\dagger c$ is the Hamiltonian of the isolated system, ω_c is the frequency, and $c^\dagger(c)$ are the bosonic creation (annihilation) operators corresponding to the mode of the system. $H_B = \sum_{k=-N}^{N} \omega_k d_k^\dagger d_k$ and $H_{SB} = \sum_{k=-N}^{N} g_k (c^\dagger d_k + c d_k^\dagger)$ represent the Hamiltonian of a multimode bosonic reservoir and the interaction Hamiltonian, respectively, where $d_k^\dagger (d_k)$ are the creation (annihilation) operators, and ω_k and g_k are the frequency of oscillation and the coupling strength between the system and environment, respectively, for the environmental mode k. The frequency range of the reservoir, $\omega_k \in [\omega_c - \epsilon, \omega_c + \epsilon]$, is chosen to be symmetric around the system mode (ω_c). The idea behind kind of modeling is the fact that, realistically, the system couples to the few modes of the environment around its resonating mode (ω_c). The model also includes consideration of the linear dispersion relation of the modes of the bath ($\omega_k \propto k$).

In order to characterize the properties of the bath, we define the spectral density function $J(\omega_k)$ [30], implying the hard cutoff limit of the reservoir and wide band limit approximation ($g_k = c_0$) [44], as

$$J(\omega_k) = \frac{1}{2}\gamma\theta(N-k)\theta(N+k), \tag{2}$$

where θ is the Heaviside step function, and $\gamma = 2\pi D c_0^2$ is the decay rate of the system where $D = \frac{\delta k}{\delta\omega_k} = \frac{N}{\epsilon}$ is the density of states (DOS). In case of a large cutoff limit ($\epsilon \to \infty$), the quantum Langevin equation (QLE) is [19]

$$\dot{c}(t) = -i\omega_c c(t) - \frac{\gamma}{2}c(t) + \sqrt{\gamma}c_{in}(t), \tag{3}$$

where $c_{in}(t) = -i\sqrt{\frac{1}{2\pi D}}\sum_k e^{-i\omega_k t}d_k(0)$ is the input field to the system. If the reservoir remains at zero temperature, no input field has contributed to the system. Therefore, the Heisenberg equation of motion (HEM) of the system mode is $\dot{c}(t) = -i\omega_c c(t) - \frac{\gamma}{2}c(t)$, which determines the free dissipative nature of the system population ($n(t) = \langle c^\dagger(t)c(t)\rangle$) as

$$n(t) = e^{-\gamma t}n(0). \tag{4}$$

TEBD numerical model

Transformation of the Hamiltonian

We transform the S/B coupling Hamiltonian to a one-dimensional lattice chain Hamiltonian for the numerical simulation. The transformation is done by mapping the bath operators into the operators of the lattice chain by defining a unitary transformation: $b_n = \sum_{k=-N}^{N} U_n^k d_k$. The normalized shifted Hahn polynomial is a natural choice for the spectral density defined by equation (2) as the unitary operator $U_n^k = \frac{1}{\rho_n}Q_n[(k+N)/2, N]$, where $Q_n(k, N)$ is the Hahn polynomial, and $\rho_n = (-1)^n(N!)\sqrt{\frac{(2n+1)}{(N+n+1)!(N-n)!}}$ is the normalization coefficient. The transformed Hamiltonian of the 1-D lattice chain is

$$H_{chain} = H_S + \eta'(a^\dagger b_0 + a b_0^\dagger) + \sum_{n=0}^{N}\omega_n b_n^\dagger b_n + \sum_{n=0}^{N-1}\eta_n(b_n^\dagger b_{n+1} + b_n b_{n+1}^\dagger) \tag{5}$$

where the coefficients are $\eta' = c_0\sqrt{2N}$, $\omega_n = \omega_c$ and $\eta_n = \left(\frac{(n+1)\sqrt{(N-n)(N+n+2)}}{D\sqrt{(2n+1)(2n+3)}}\right)$. The schematic diagram of the transformation is shown in figure 1(a). Recently, similar mapping was introduced in [45] to simulate open quantum systems aiming to be applied to spin-boson models [46] and biomolecular systems [47]. In all cases, the model had remain successful to overcome the complexity of the deduction of non-Markovian dynamical phenomenon, but the bath was considered to be at zero temperature. But, in the following section, we introduce METTS algorithm for the first time, for the generation of thermal bath at finite temperature and the evolution of system in the presence of the thermal bath.

Real-time evolution

We use time-evolving block decimation algorithm (TEBD) to do the numerical simulation, which requires expressing the state of the full chain as a matrix product state (MPS):

$$|\Psi\rangle = \sum_{\alpha_1,,,\alpha_{N+1}=0}^{\chi}\sum_{i_1\ldots i_N=0}^{M}\lambda_{\alpha_1}^{[1]}\Gamma_{\alpha_1\alpha_2}^{[1]i_2}\lambda_{\alpha_2}^{[2]}\Gamma_{\alpha_2\alpha_3}^{[2]i_3}\cdot\ldots\cdot\lambda_{\alpha_N}^{[N]}\Gamma_{\alpha_N}^{[N]i_N}\lambda_{\alpha_{N+1}}^{[N+1]}|i_1, i_2, .., i_{N-1}, i_N\rangle \tag{6}$$

The MPS state is obtained through the Schmidt decomposition of the pure state of N sites where M is the dimension of local Hilbert space and χ is the Schmidt number [48]. The method of numerical simulation for the real-time evolution is shown diagrammatically in figure 1(b), where we choose the second order Suzuki Trotter (ST) expansion [49], which minimizes the error in third order of the time step by evolving the pairs of alternate sites. Using ST expansion, we express the unitary evolution operator as

$$U_{dt} = e^{-idtH_{chain}} = e^{-iFdt/2}e^{-iGdt}e^{-iFdt/2} + O[dt^3] \tag{7}$$

where, $F = \sum_{i\ \mathrm{odd}} H_{chain}^{i,i+1}$ and $G = \sum_{i\ \mathrm{even}} H_{chain}^{i,i+1}$.

The simulation parameters are estimated by looking at errors which can appear in two ways: while modeling the S/B formalism to a one-dimensional chain and simulating each step during the real-time evolution. The errors are discussed extensively afterwards to estimate the parameters for numerical simulation.

Algorithm for thermal state

We imply the METTS algorithm by sampling over a huge number of pure quantum states [43]. Overall, these samples contain physical properties of the system for a given temperature, which approximates thermal

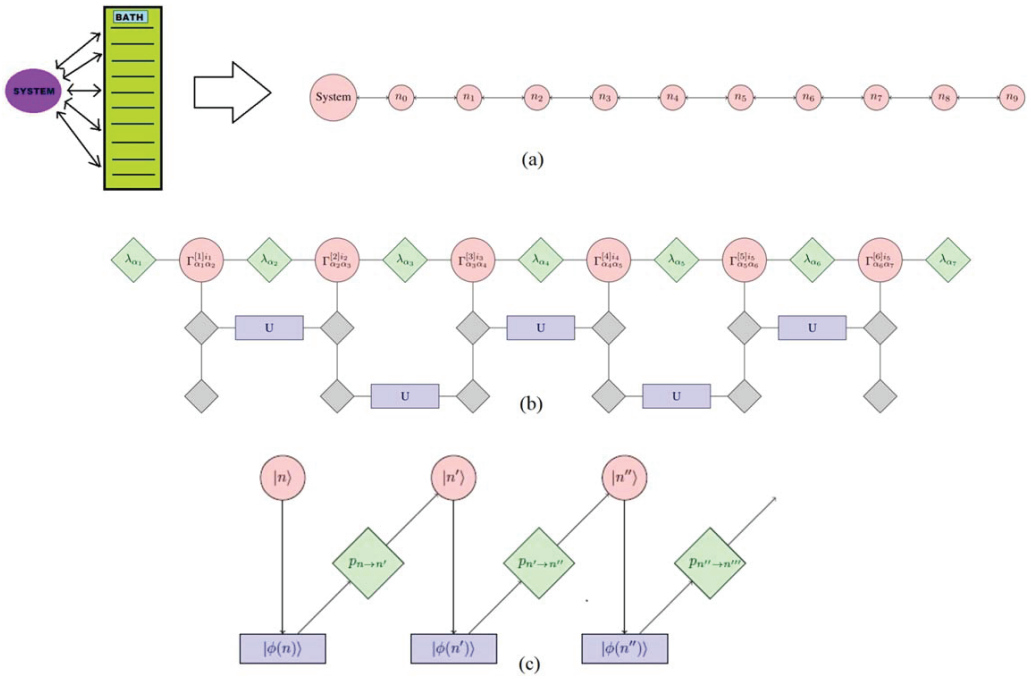

Figure 1. (a) Transformation of Hamiltonian from system/bath coupling model to semi-infinite chain model (b) Time evolution operation on alternating pairs (c) Generation of a set of METTS through imaginary time evolution and projective measurement.

expectation values of any observable $\langle\hat{O}\rangle_\beta$, are determined using a set of orthonormal basis $\{|\mathbf{n}\rangle\}$ of classical product states (CPS): $|\mathbf{n}\rangle = \bigotimes_i |n_i\rangle$, where $|n_i\rangle$ is an arbitrary orthonormal basis state of the lattice site i. The thermal expectation value of an operator is

$$\langle\hat{O}\rangle_\beta = \frac{1}{Z_\beta}\sum_n \langle\mathbf{n}|e^{-\beta H/2}\hat{O}e^{-\beta H/2}|\mathbf{n}\rangle, \tag{8}$$

where Z_β is the partition function. The CPS $|\mathbf{n}\rangle$ becomes a matrix product state (MPS) $|\phi_n\rangle$ after the imaginary time evolution with the probabilities P_n as

$$|\phi_n\rangle = \frac{1}{\sqrt{P_n}}e^{-\beta H/2}|\mathbf{n}\rangle, \qquad P_n = \langle\mathbf{n}|e^{-\beta H}|\mathbf{n}\rangle. \tag{9}$$

In the next step, the METTS $|\phi_n\rangle$ collapses to a new CPS $|n'\rangle$ through a projective measurement with an arbitrary measurement basis from which one can subsequently compute a new METTS $|\phi_{n'}\rangle$, and, this process keeps on going on to generate a large set of MPS which typically represents a thermal state altogether. Thus, the generation of METTS samples undergoes a Markov process which is illustrated in figure 1(c). In this framework, the thermal average is determined from the set of imaginary time evolved normalized MPS states ($|\phi_n\rangle$) with the probabilities P_n/Z_β

$$\langle\hat{O}\rangle_\beta = \frac{1}{Z_\beta}\sum_n P_n\langle\phi_n|\hat{O}|\phi_n\rangle\rangle. \tag{10}$$

The algorithm has been used widely to simulate the spin chain at finite temperatures [50–52]. However, we use the technique to study the thermalization of the open quantum system numerically for the first time, which includes generation of the thermal bath using the METTS algorithm, and afterwards, evolve an empty system in the presence of the thermal bath.

The computation cost of TEBD increases with the entanglement of the quantum state, and hence the CPS is the natural choice to start with for having least entanglement. The entanglement of the obtained MPS states remains relatively low during real time evolution, which makes the simulation efficient.

Free dissipative system

We check the applicability of the TEBD algorithm in the dynamics of open quantum systems by comparing it with the analytics of a simple system/bath coupling model, where we assume that one photon is kept initially in

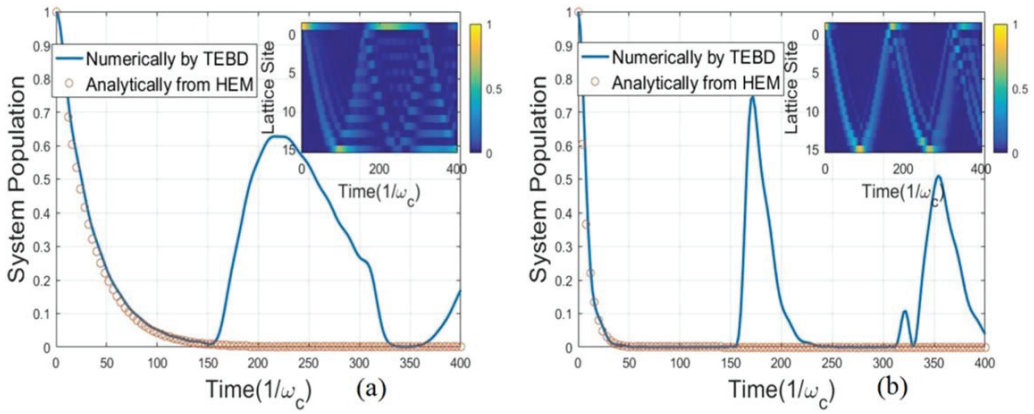

Figure 2. Plot of system population determined numerically by TEBD and analytically from the solution of QLE for different rates of dissipation (a) $\gamma = 0.031\ 4\omega_c$ and (b) $\gamma = 0.125\ 6\omega_c$. The parameters for TEBD simulation are cutoff frequency $\epsilon = 0.3\omega_c$; total number of sites, including system and bath: $N = 17$; Schmidt number $(\chi) = 5$; size of local Hilbert space $(M) = 2$; time step $\delta t = 0.5\omega_c^{-1}$. In the inset, the image plot of the population on the sites shows how the particle reflects back from the boundary.

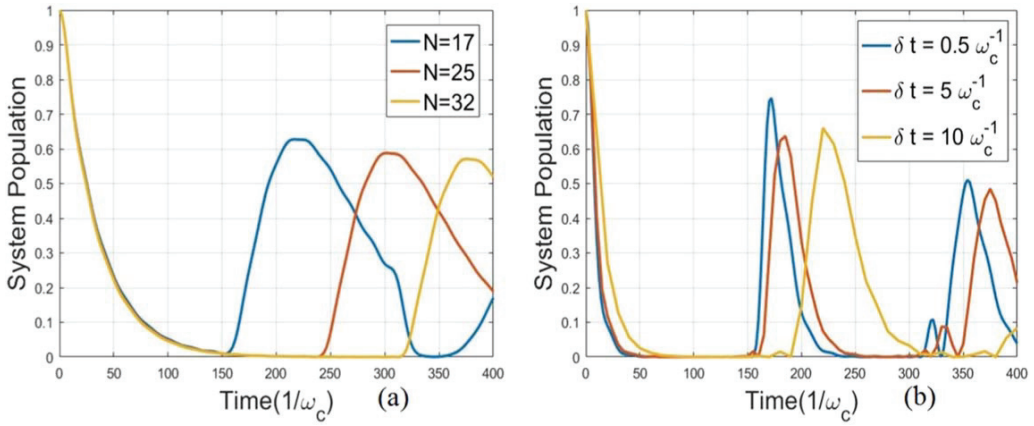

Figure 3. (a) Plot of time evolution of a free dissipative system for the variation of DOS, which is obtained by fixing the cutoff frequency and changing number of modes/lattice sites ($\gamma = 0.031\ 4\omega_c$). (b)Plot of time evolution of a free dissipative system for different time steps ($\gamma = 0.125\ 6\omega_c$). All other parameters remain same for both the figures (a) and (b) with figure 2.

the system and the bath is completely empty at zero temperature. Transforming the modes of the bath to a chain, we see that the first site is populated by a single quantum and all other sites remain empty. In figure 2, the dissipative nature of the system, which is obtained numerically by doing real-time evolution of the full chain, is compared with the analytics determined from the Heisenberg equation of motion (HEM) given by equation (4). We see an increment in the system population obtained in the numerical result after a certain time due to the reflection of the particle from the end of the chain, which is visible explicitly from the plots of the population of the full chain given in the insets of figure 2.

Recurrence time and density of states

The recurrence time decreases with the increment of the group velocity, causing the phonon to travel faster in the lattice. The group velocity is defined by $v_g = \frac{\delta\omega_k}{\delta k_N}$, where ω_k is the frequency, and k_N is the wavenumber determined by the number of lattice sites ($k_N \propto N$). Eventually, the group velocity is inversely proportional to the density of states ($v_g \propto D^{-1}$), and therefore, the recurrence time increases linearly with the increment of DOS, which is seen in figure 3(a), where we increased the DOS by increasing the number of sites, keeping the cutoff frequency fixed.

Errors and estimation of parameters

The case of real-time evolution, the ST expansion introduces time error, which tends to concentrate in the overall phase [49]. In figure 3(b), we show how the accuracy of the simulation improved while reducing the time step.

Truncation of the Hilbert space is also an issue in TEBD simulation. However, we chose the size of local Hilbert space to be 2 for having a single particle, and therefore the set is complete and we do not expect any error associated with the truncation of local Hilbert space. Because the time evolution started from an initial product state, the entanglement of the sites remains relatively low, and therefore the impact of the truncation in the Schmidt spectrum is also negligible.

Thermalization of an open quantum system

Analytics of the thermalization of a system

Accounting for the back action of the environment, we determine the time dynamics of the field operator of the system by integrating QLE of a simple S/B coupling model, given in equation (3) as

$$c(t) = -i\sqrt{\frac{\gamma}{2\pi D}}\sum_k \frac{d_k(0)}{-i(\omega_k-\omega_c)+\frac{\gamma}{2}}\{e^{-i\omega_k t}-e^{-(i\omega_c+\gamma/2)t}\}. \tag{11}$$

The initial thermal population distribution of the bath is

$$\langle d_k^\dagger(0)d_k(0)\rangle = \frac{1}{e^{\beta\omega_k}-1}, \tag{12}$$

which determines the population of the system as

$$n(t) = \sum_{\omega_k=\omega_c-\epsilon}^{\omega_c+\epsilon} AI_k + BJ_k, \tag{13}$$

where

$$\begin{aligned} I_k &= \frac{\gamma/2\pi D}{\left[(\omega_k-\omega_c)^2+\left(\frac{\gamma^2}{4}\right)\right]}\frac{1}{[e^{\beta\omega_k}-1]}, \\ J_k &= \frac{(\gamma/2\pi D)\cos((\omega_k-\omega_c)t)}{\left[(\omega_k-\omega_c)^2+\left(\frac{\gamma^2}{4}\right)\right]}\frac{1}{[e^{\beta\omega_k}-1]}, \end{aligned} \tag{14}$$

and

$$A = (1+e^{-\gamma t}), \qquad B = -2e^{-\gamma t/2}. \tag{15}$$

As the coefficient B goes to zero at the steady state, the population of the system is determined by the function I_k given in equation (14). Realistically, the population dynamics of the system are dependent on a few modes of the bath around the resonating mode of the system, and therefore, the cutoff limit (ϵ) should be considered in such a way that the contribution of the modes of the bath, those which far away from the system mode, can be marginalized. Hence, the function I_k is expected to converge when the frequency (ω_k) goes far away from ω_c. However, figure 4 shows that even though the function I_k exhibits a peak at the resonating frequency of the system, it rises up again when the frequency of the bath mode is much lower than the frequency of the system mode ($\omega_k \ll \omega_c$), which comes from the fact that the exponential function of the thermal population distribution of the bath $\left(\frac{1}{[e^{\beta\omega_k}-1]}\right)$ dominates over the Lorentzian function $\left(\frac{\gamma/2\pi D}{\left[(\omega_k-\omega_c)^2+\left(\frac{\gamma^2}{4}\right)\right]}\right)$. The acceptance up to the limit of the second order perturbation for the theoretical formulation of an open quantum system, is essentially based on the weak coupling between system and environment, ensuring the Lorentzian function acts like a delta function around ω_c.

It is also seen from figure 4 that I_k rises up faster towards the lower cutoff limit in the case of a bath which is at a lower temperature than it does in the case of a high temperature. Such situations can even be bypassed by reducing ϵ, but that increases the ratio between γ and ϵ. However, we can solve this issue by reducing the value of γ, but that demands more time for the system to reach the stationary state, and hence it might not be possible at times to reach the steady state before the recurrence of the particle from the boundary. In that case, we increase the recurrence time by increasing the density of states. However, in the case of a zero temperature bath, the thermal population remains zero for all modes. Therefore, the relaxation of the system to the ground state is not affected by the cutoff frequency.

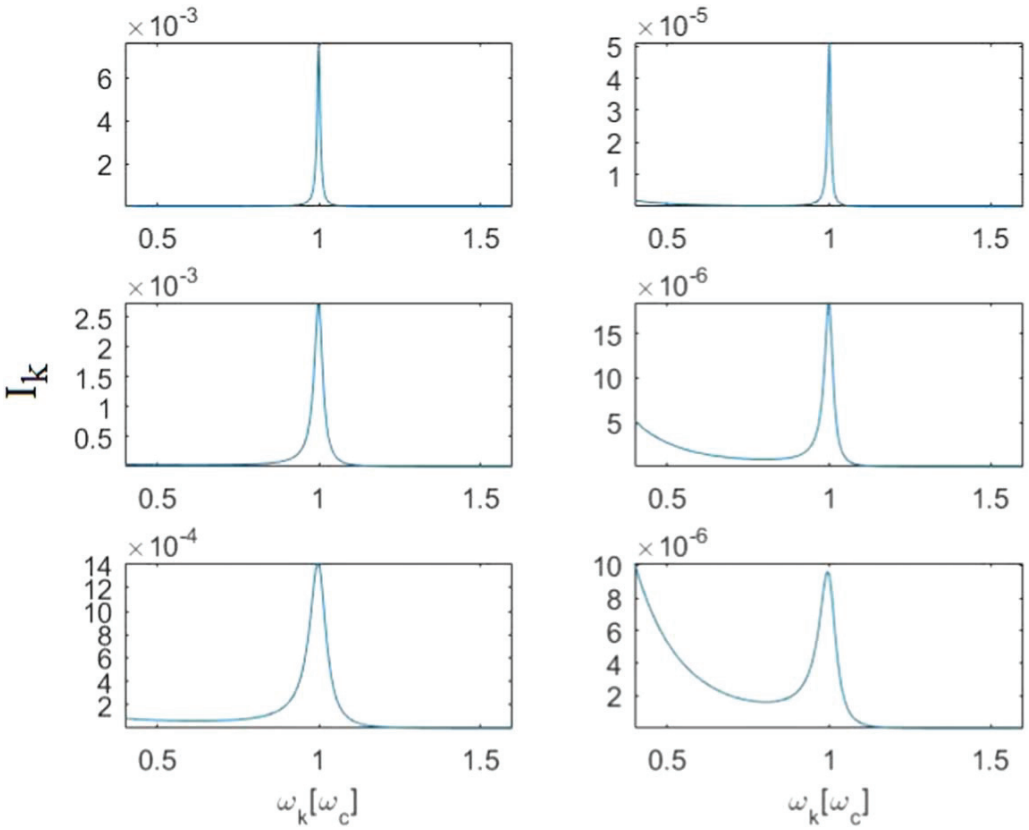

Figure 4. Plot of the function I_k for different temperatures and rates of dissipation of the system. The temperature is fixed for all plots in columns: $\beta = 5{,}10[1/\omega_c]$ for the first and second column respectively, and the dissipation rate changes over rows. $\gamma = 0.011\ 3{,}0.031\ 4{,}0.061\ 6\omega_c$ for the first, second and third row respectively.

Anticipating the fact that the Lorentzian function becomes a delta function for a given condition $\gamma << \epsilon$, the steady state population of the system is approximated to

$$n(\infty) = \frac{1}{e^{\beta\omega_c} - 1}, \tag{16}$$

which is the thermal population of the bath corresponding to the mode of the system. So the steady state population of the system is approximated to the population of the bath corresponding to the mode of the system.

Generation of the thermal bath

The quality of the thermal state generated by the METTS algorithm is dependent on two crucial parameters: temperature and number of samples. The frequency spectrum of the thermal population of the bath is plotted in figure 5(a), which determines that in the case of lower temperatures, as the thermal population reduces rapidly, the fewer modes are required to be taken into account to express a thermal state. This is also suggested by figure 5(b), which shows that the cumulative probability saturates faster for the low temperature bath, reducing the requirement of number of METTS samples to represent the thermal state. The consequence is observed in figure 5(c), where the plot of population distribution becomes smooth, and therefore defines a significant pattern while reducing the temperature for a fixed number of METTS, which indicates a better quality of the preparation of thermal state. In table 1 we compare the thermal population obtained analytically and numerically by taking average over 50 METTS samples. However, anticipating better performance of the METTS algorithm at low temperatures, it is also seen that the overall thermal population reduces so significantly that after a certain range, the number is not reliable for numerical simulation. Therefore, we prefer to generate a thermal state higher temperature in order to obtain the thermal population to a significant level, which forces us to take a large number of METTS samples into account while doing real time evolution. In figure 5(d), we show how the increment of the number of METTS samples modifies the population distribution over the entire lattice chain. As anticipated, the quality of the preparation of the bath improves while increasing the number of METTS samples, which is indicated by the improvement of the smoothness of the plot.

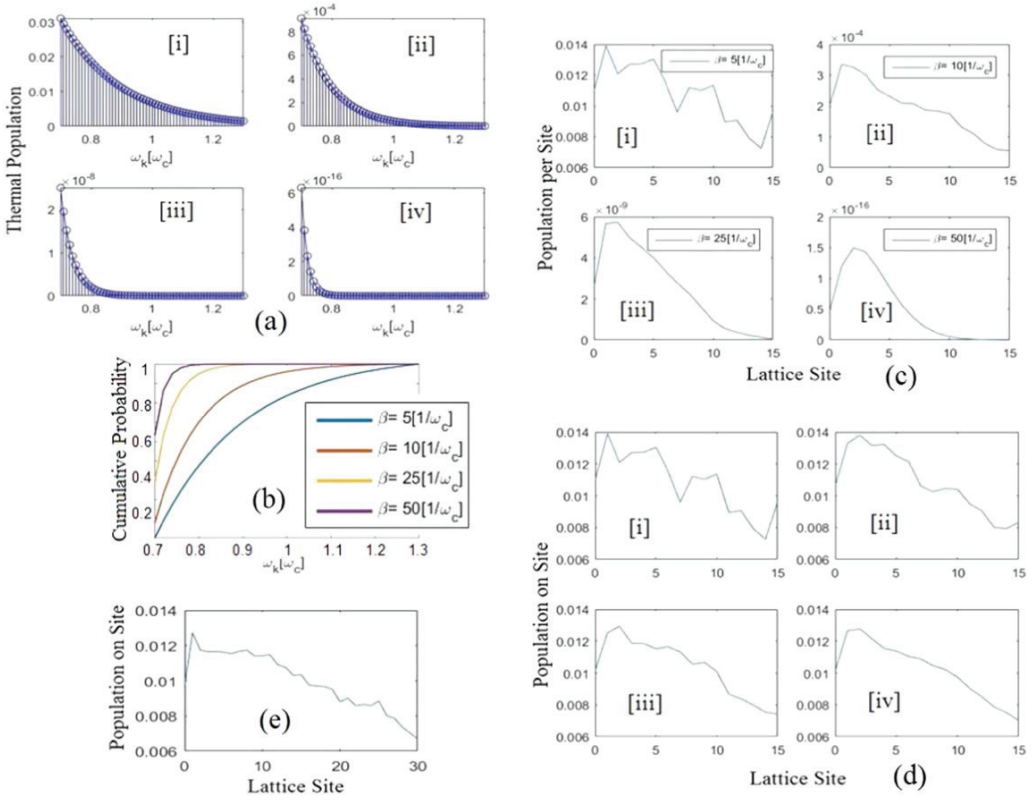

Figure 5. (a) Population spectra, (b) cumulative probability distribution of photon occupation, and (c) population variation on the lattice sites for different temperatures ($\beta = 5, 10, 25, 50\,[1/\omega_c]$). The number of METTS samples is 50. (d) Population variation on the lattice sites with the variation of the number of METTS samples (50, 100, 500, 1000) for a fixed temperature ($\beta = 5\,[1/\omega_c]$). Density of states (DOS) is $25[1/\omega_c]$ for all cases. (e) Population distribution on lattice sites for higher density of states ($DOS = 50[1/\omega_c]$). The number of METTS samples is 1000, inverse temperature $\beta = 5\,[1/\omega_c]$. The frequency range of the reservoir is $\omega_k \in [0.7,\ 1.3]\omega_c$, fixed in all cases.

Table 1. Population of a thermal bath for different temperatures in the frequency range $\omega_k \in [0.7,\ 1.3]\omega_c$. The density of states ($DOS = 25[1/\omega_c]$) and the number of METTS samples ($METTS = 50$) are kept fixed for all cases.

$\beta\,[1/\omega_c]$	Analytical population	TEBD population
5	0.162 6	0.173 0
10	0.002 8	0.003 0
25	$3.972\,3 \times 10^{-8}$	$3.967\,7 \times 10^{-8}$
50	$7.292\,0 \times 10^{-16}$	$7.952\,4 \times 10^{-16}$

As we increase the density of states for a fixed frequency range, the number of modes and number of lattice sites also increase, which essentially demands more METTS samples to represent a thermal state. Therefore, we see a poor population distribution in figure 5(e) compared to figure 5(d)[iv], when we doubled the DOS and keep the number of METTS fixed. However, the increase of the density of states increases the total population of the bath, which is shown in table 2.

Real-time propagation of systems coupled to thermal bath

Hereafter, we study the thermalization of an empty system in the presence of a thermal bath at inverse temperature $\beta = 5[1/\omega_c]$. The time evolution of the system population for different cutoff frequencies and rates of dissipation are shown in figure 6. As anticipated from equation (13), the oscillation in the population of the system is introduced by the left tail of figure 4. The extension of the lower cutoff frequency contributes more oscillation to the dynamics, and more population in the stationary state of the system, which is visible when we compare figures 6(a) and (b). The higher value of γ also contributes more oscillation as an error to the dynamics

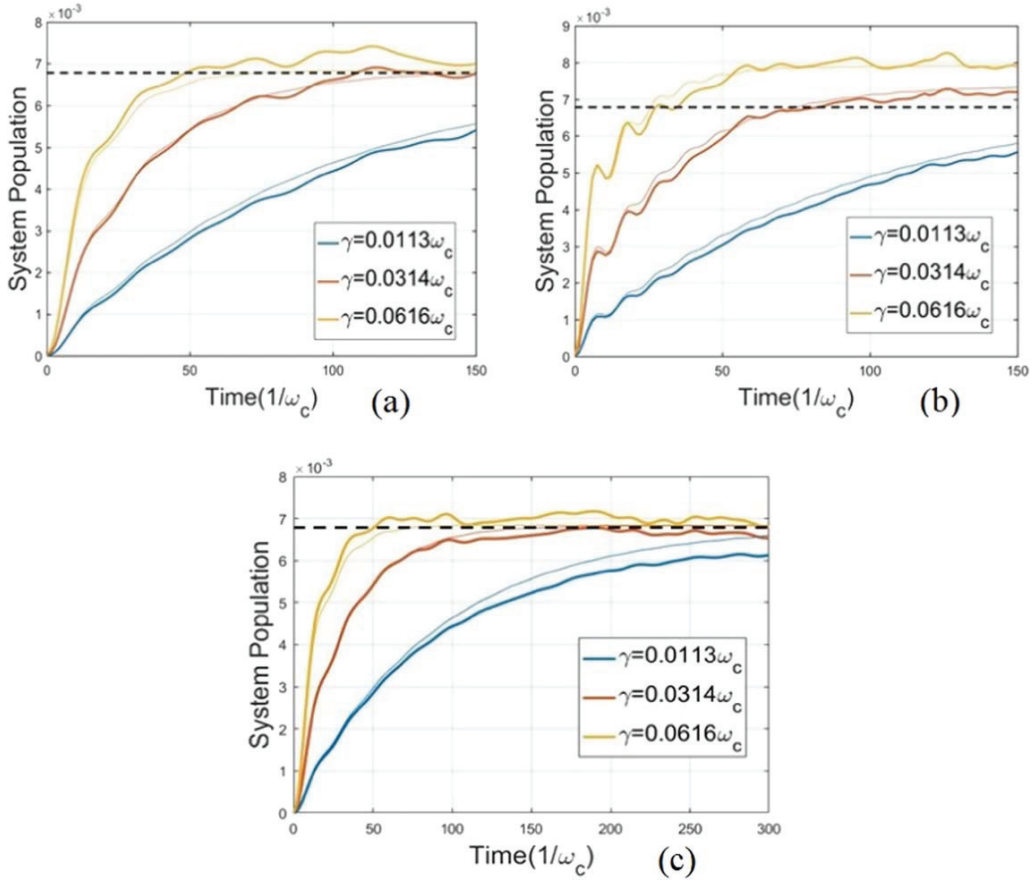

Figure 6. (a), (b) Plot of the time evolution of the system population for different cutoff frequency: (a)$\epsilon = 0.3\omega_c$ is and (b)$\epsilon = 0.6\omega_c$. The length of the chain of the bath is 16 and 31, respectively, keeping the DOS fixed $DOS = 25[1/\omega_c]$. (c) Plot of the time evolution of the system population increasing the density of state $DOS = 50[1/\omega_c]$. The length of the chain of the bath is 31, and the cutoff frequency is ($\epsilon = 0.3\omega_c$) . The temperature ($\beta = 5[1/\omega_c]$) and number of METTS samples (4000) are kept fixed in all cases. Thick lines correspond to the TEBD numerical result and the thin lines represent analytical results obtained from equation (13). The black dashed line stands for the thermal population corresponding to the mode of the system expressed in equation (16).

Table 2. Population of a thermal bath for different density of states in the frequency range $\omega_k \in [0.7,\ 1.3]\omega_c$ and temperature $\beta = 5[1/\omega_c]$. The number of METTS samples is kept fixed at 1000 for all cases.

DOS $[1/\omega_c]$	Analytical population	TEBD population
25	0.162 6	0.163 0
50	0.308 2	0.308 8

of the system population. We see the steady state population of the system is comparable to the thermal population at ω_c, which is indicated by equation (16). In both figures 6(a) and (b), the system has not been able to achieve the steady state for the slow dissipation rate (especially $\gamma = 0.011\ 3\omega_c$). Therefore, we extend the recurrence time by increasing the DOS in figure 6(c), which gives sufficient freedom to the system to relax to the steady state.

The numerical technique, therefore proves a promising scheme to study the open quantum dynamics. In order to investigate its applicability in the physics of quantum Brownian motion, we plot real-time dynamics of the quadrature fluctuations in figure 7 with a comparison to its analytics. The arbitrary quadrature is defined as $X_\theta(t) = e^{i\theta}c(t) + e^{-i\theta}c^\dagger(t)$. As $\langle d_k(0)\rangle = \langle d_k^\dagger(0)\rangle = \langle d_k^2(0)\rangle = \langle d_k^{\dagger 2}(0)\rangle = 0$, the quadrature fluctuation becomes phase (θ) independent ($\delta X_\theta(t) = \sqrt{1 + 2n(t)}$), and its time dynamics gives a pattern similar to the population dynamics.

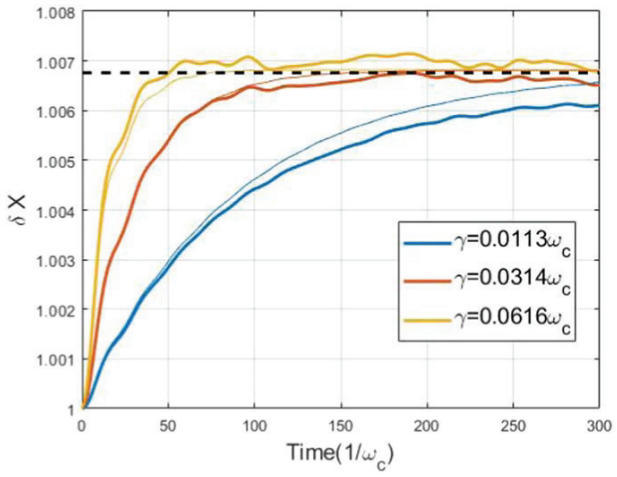

Figure 7. Plot of the time evolution of the quadrature fluctuation for different rate of dissipation. All other parameters are kept same with figure 6(c). Thick lines correspond to the TEBD numerical result and the thin lines represent their corresponding analytics. The black dashed line stands for the quadrature fluctuation corresponding to the mode of the system at same temperature.

Conclusion

In this article, we intended to investigate the applicability of METTS algorithm in the thermalization dynamics of open-quantum systems, anticipating the fact that the DMRG technique has the ability to extract out exact dynamics without linearizing nonlinear Hamiltonians. The consequences of this approach are demonstrated in terms of the efficiency of the algorithm with a discussion of advantages and disadvantages of this simulation. In this spirit, we also compare the numerical result with analytical result determined using Heisenberg equation of motion. We started with presenting a model that transforms the Hamiltonian of a quantum system coupled linearly to a discrete set of modes of a bosonic reservoir, to a Hamiltonian of a one-dimensional chain with nearest-neighbour interactions. We then used the model to study free dissipation and thermalization of that open quantum system. We found the recurrence time of the real-time evolution increases linearly with the increment of density of states. Our results also show that even though the minimally entangled typical thermal states (METTS) algorithm performs better at lower temperatures, we preferred to work at higher temperature in order to obtain the thermal population at a significant level and avoid unwanted error in the population dynamics of the system contributed by the lower cutoff frequency limit. Therefore, more METTS samples are taken into account, which consume more computation resources. In conclusion, one can say that the numerically generated thermal bath shows promise, but, this requires a compromise between the quality of the result and the computation resources. The numerical scheme presented here was mainly motivated by an attempt to determine the exact solution in the case of nonlinear coupling between the system and the environment [26], non-classical dynamics of non-linear systems [27], and reach out single photon limit in optomechanical systems [24, 25]. The combination of real and imaginary time evolution of open quantum system will allow us to investigate quantum Brownian motion of topological quantum matter [53, 54]. In addition, the method will be useful to study the non-Markovian dynamics and critical behaviors of the sub-ohmic or ohmic spin-Bosson coupling models [3, 4, 28, 29].

Acknowledgments

This work was supported by the Academy of Finland under grant no. 275245.

ORCID iDs

Souvik Agasti https://orcid.org/0000-0002-9863-2203

References

[1] Zurek W H 1991 *Phys. Today* **44** 3644
[2] Leggett A J 2005 *Science* **307** 871–2

[3] Leggett A J, Chakravarty S, Dorsey A T, Fisher M P A, Garg A and Zwerger W 1987 *Rev. Mod. Phys.* **59** 1–85
[4] Breuer H-P, Laine E-M, Piilo J and Vacchini B 2016 *Rev. Mod. Phys.* **88** 021002
[5] Ishizaki A, Calhoun T R, Schlau-Cohen G S and Fleming G R 2010 *Phys. Chem. Chem. Phys.* **12** 7319–37
[6] Leskinen M J, Nummi O H T, Massel F and Törmä P 2010 *New J. Phys.* **12** 073044
[7] Massel F, Kantian A, Daley A J, Giamarchi T and Törmä P 2013 *New J. Phys.* **15** 045018
[8] Kimble H J 2008 *Nature* **453** 1023
[9] Felinto D, Chou C W, Laurat J, Schomburg E W, de Riedmatten H and Kimble H J 2006 *Nat. Phys.* **2** 844–8
[10] You J Q and Nori F 2011 *Nature* **474** 589
[11] Ospelkaus C, Warring U, Colombe Y, Brown K R, Amini J M, Leibfried D and Wineland D J 2011 *Nature* **476** 181
[12] Barreiro J T, Müller M, Schindler P, Nigg D, Monz T, Chwalla M, Hennrich M, Roos C F, Zoller P and Blatt R 2011 *Nature* **470** 486
[13] O'Brien J L, Furusawa A and Vuckovic J 2009 *Nat. Photonics* **3** 687
[14] Clerk A A, Devoret M H, Girvin S M, Marquardt F and Schoelkopf R J 2010 *Rev. Mod. Phys.* **82** 1155–208
[15] Abbott B P *et al* 2016 *Phys. Rev. Lett.* **116** 061102
[16] Wallraff A, Schuster D I, Blais A, Frunzio L, Huang R-S, Majer J, Kumar S, Girvin S M and Schoelkopf R J 2004 *Nature* **431** 162–7
[17] Sillanpää M A, Park J I and Simmonds R W 2007 *Nature* **449** 438
[18] Poyatos J F, Cirac J I and Zoller P 1996 *Phys. Rev. Lett.* **77** 4728–31
[19] Howard G J M and Wiseman M 2009 *Quantum Measurement and Control* 1st edn (Cambridge: Cambridge University Press)
[20] Mirrahimi M, Leghtas Z, Albert V V, Touzard S, Schoelkopf R J, Jiang L and Devoret M H 2014 *New J. Phys.* **16** 045014
[21] Leghtas Z *et al* 2015 *Science* **347** 853–7
[22] Zolfagharkhani G, Gaidarzhy A, Shim S-B, Badzey R L and Mohanty P 2005 *Phys. Rev.* B **72** 224101
[23] Arcizet O, Rivière R, Schliesser A, Anetsberger G and Kippenberg T J 2009 *Phys. Rev.* A **80** 021803
[24] Nunnenkamp A, Børkje K and Girvin S M 2011 *Phys. Rev. Lett.* **107** 063602
[25] Pirkkalainen J-M, Damskägg E, Brandt M, Massel F and Sillanpää M A 2015 *Phys. Rev. Lett.* **115** 243601
[26] Manninen J, Agasti S and Massel F 2017 *Phys. Rev.* A **96** 063830
[27] Agasti S 2019 *Journal of Physics Communications* **3** 105004
[28] Spohn H 1989 *Commun. Math. Phys.* **123** 277–304
[29] Kehrein S K and Mielke A 1996 *Phys. Lett.* A **219** 313–8
[30] Bulla R, Lee H-J, Tong N-H and Vojta M 2005 *Phys. Rev.* B **71** 045122
[31] Juozapavičius A, Caprara S and Rosengren A 1997 *Phys. Rev.* B **56** 11097–101
[32] Baker G A 1961 *Phys. Rev.* **124** 768–74
[33] Arita R, Kuroki K, Aoki H and Fabrizio M 1998 *Phys. Rev.* B **57** 10324–7
[34] Mielke A 1993 *Phys. Lett.* A **174** 443–8
[35] Sorella S and Tosatti E 1992 *EPL (Europhysics Letters)* **19** 699
[36] Freericks J K and Monien H 1996 *Phys. Rev.* B **53** 2691–700
[37] Läuchli A M and Kollath C 2008 *J. Stat. Mech: Theory Exp.* **2008** P05018
[38] Zwerger W 2003 *J. Opt. B: Quantum Semiclassical Opt.* **5** S9
[39] Nalbach P, Ishizaki A, Fleming G R and Thorwart M 2011 *New J. Phys.* **13** 063040
[40] Nalbach P and Thorwart M 2009 *Phys. Rev. Lett.* **103** 220401
[41] Tanimura Y and Kubo R 1989 *J. Phys. Soc. Jpn.* **58** 101–14
[42] White S R 1992 *Phys. Rev. Lett.* **69** 2863–6
[43] Stoudenmire E M and White S R 2010 *New J. Phys.* **12** 055026
[44] Stefanucci G and van Leeuwen R 2014 *Many-Body Theory of Quantum Systems* (Cambridge: Cambridge University Press)
[45] Chin A W, Rivas A, Huelga S F and Plenio M B 2010 *J. Math. Phys.* **51** 092109
[46] Chin A W, Prior J, Huelga S F and Plenio M B 2011 *Phys. Rev. Lett.* **107** 160601
[47] Huelga S and Plenio M 2011 *Procedia Chemistry* **3** 248–57 22nd Solvay Conf. on Chemistry
[48] Vidal G 2003 *Phys. Rev. Lett.* **91** 147902
[49] Hatano N and Suzuki M 2005 Finding exponential product formulas of higher orders *Quantum Annealing and Other Optimization Methods* ed A Das and B K Chakrabarti (Berlin, Heidelberg: Springer Berlin Heidelberg) pp 37–68
[50] Feiguin A E and White S R 2005 *Phys. Rev.* B **72** 220401
[51] Binder M and Barthel T 2015 *Phys. Rev.* B **92** 125119
[52] Bruognolo B, von Delft J and Weichselbaum A 2015 *Phys. Rev.* B **92** 115105
[53] Quelle A, Cobanera E and Smith C M 2016 *Phys. Rev.* B **94** 075133
[54] Cobanera E, Kristel P and Morais Smith C 2016 *Phys. Rev.* B **93** 245422

IV

NUMERICAL SIMULATION OF FREE DISSIPATIVE OPEN QUANTUM SYSTEM AND ESTABLISHMENT OF A FORMULA FOR π

by

Agasti, Souvik

Accepted to be published in AIP Conf. Proceedings.

Numerical Simulation of Free Dissipative Open Quantum System and Establishment of a Formula for π

Souvik Agasti[1,2,a)]

[1]*Nanoscience center, Dept. of Physics, University of Jyväskylä*
[2]*Photonics Laboratory, Physics Unit, Tampere University*

[a)]Corresponding author: souvik.s.agasti@jyu.fi

Abstract. We transform the system/reservoir coupling model into a one-dimensional semi-infinite discrete chain with nearest neighbor interaction through a unitary transformation, and, simulate the dynamics of free dissipative open quantum system. We investigate the consequences of such modeling, which is observed as finite size effect causing the recurrence of particle from the end of the chain. Afterwards, we determine a formula for π in terms of the matrix operational form, which indicates a robustness of the connection between quantum physics and basic mathematics.

Introduction

An open quantum system (OQS), described to be a separate entity from its surrounding environment while being coupled with it, has shown importance due to its applicability in the foundation of quantum mechanics, statistical mechanics and atomic, molecular, optical and bio-physics. The theory of OQS has remained useful to describe experimental activities in the field of decoherence measurement and quantum computation, which has applications in quantum networks [1, 2] in mesoscopic systems, which includes photonic crystals [3], ion traps [4, 5] and superconducting circuits [6]. The coupling of system mode to the environment has been used in the sensing and measurement related applications, in a broad range from electromagnetic fields [7] to gravitational waves [8].

The dissipative dynamics of OQS due to the system/bath (S/B) coupling, has been studied with the help of quantum master equation and Heisenberg-Langevin equation [9]. Both the equations are extensions of their classical counterpart, in the quantum regime. Despite of their simplicity, these techniques exhibit limitations while extracting out exact solution when OQS suffers non-Markovianity in the dynamical behavior or non-linearity in the Hamiltonian. For example, the non-Markovian dynamical phenomena has been observed in a type of quantum phase transition between dynamically localized and delocalized states of two level system (TLS) for zero temperature sub-Ohmic and Ohmic baths [10, 11, 12, 13], where one cannot treat effective interaction between oscillator and TLS in a perturbative manner. On another side, the non-linear Hamiltonian appears in case of Kerr nonlinear system [14] or cavity coupled TLS systems [15], where the theory of OQS has been implemented after linearizing the Hamiltonian over nonlinear steady state field amplitude. Therefore, the interesting effects are often missed out, and the limitation of analytics provokes us explicitly to do numerical simulation. The numerical method requires transformation of the degrees of freedom of the environmental modes to a many body system with nearest neighbor interactions.

The idea of such mapping was first introduced in Ref. [13] where a recursive numerical technique was performed on discretised environment, and truncated to form a many body chain. Furthermore, using the properties of orthogonal polynomials, an exact unitary transformation has been presented that maps the Hamiltonian of a linearly coupled system to a continuum of bosonic or fermionic modes, to a Hamiltonian that describes a one-dimensional chain with only nearest-neighbor interactions [16]. Considering applicability, the time-adaptive density matrix renormalisation group (t-DMRG) [17] has been considered recently as one of the most useful tools in optical, atomic and condensed matter physics for the numerical simulation of one-dimensional systems with short-range interactions.

In this paper we present how the S/B coupling model is mapped to a semi infinite chain with nearest neighbor interactions. We construct the Hamiltonian matrix for a single particle located in the entire chain, and use that to simulate the free dissipative OQS. We also discuss the recurrence of particle which comes from the finite size effect

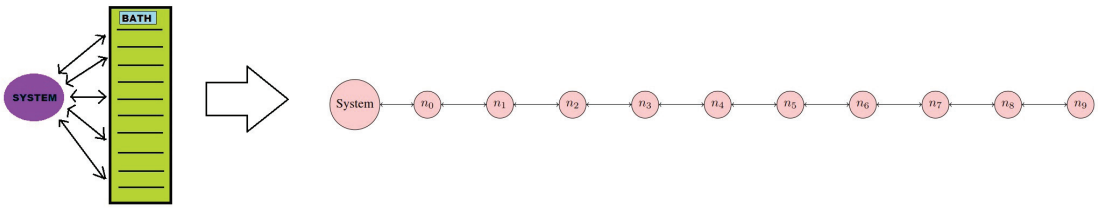

FIGURE 1. Transformation of Hamiltonian from system/bath coupling model to semi infinite chain model.

of the chain. Afterwards, we show that the famous quantity π can be computed from the dissipation dynamics of the OQS, in terms of matrix operational form.

THEORETICAL MODEL

In order to discuss the dissipative dynamics of an OQS, we start with the full Hamiltonian

$$H = H_S + H_B + H_{int} \tag{1}$$

Here, the Hamiltonian of the isolated system is $H_S = \omega_c a^\dagger a$, where ω_c is the frequency, and $a(a^\dagger)$ are the annihilation (creation) operator of the system mode. The Hamiltonian of the bath is represented by a set of bosonic modes $H_B = \sum_{k=-N}^{N} \omega_k b_k^\dagger b_k$, and, the interaction Hamiltonian between system and environment is $H_{int} = \sum_{k=-N}^{N} g_k(b_k^\dagger a + a^\dagger b_k)$, where $b_k(b_k^\dagger)$ are the annihilation (creation) operators, and ω_k is the frequency of k^{th} mode of the environmental field. g_k is the coupling strength between the system and k^{th} mode of the bath. The frequency of the bath changes linearly with the change of mode $k : \omega_k \propto k$, and the range is chosen to be symmetric around the system mode (ω_c) due to the fact that, in most of the realistic situation, the system is coupled to the modes of the environment around its own resonating mode (ω_c). Moving to a rotating frame of frequency ω_c, the frequency range of the bath is accepted to be $\omega_k \in [-\epsilon, \epsilon]$.

The dynamics of the bipartite system is determined by a positive function of the mode of the bath, is known as spectral density [13]. In case of a hard cutoff range of the modes of the reservoir, implying wide band limit approximation, i.e. the coupling strength is independent of the mode of the bath ($g_k = c_0$) [18], we obtain the spectral density function as

$$J_k = c_0^2 D\theta(N-k)\theta(N+k) \tag{2}$$

where θ is the Heaviside step function and $D = \frac{\delta k}{\delta \omega_k} = \frac{N}{\epsilon}$ is the density of states (DOS) of the bath.

In case of an empty bath, considering a large cutoff window ($\epsilon \to \infty$), the dynamics of the system is determined by the Heisenberg equation of motion (HEM): $\dot{a}(t) = -\frac{\gamma}{2}a(t)$ [9], which gives a dissipative nature of the system population ($n_S = \langle a^\dagger a \rangle$) as $n_S(t) = e^{-\gamma t} n_S(0)$, where $\gamma = 2\pi D c_0^2$ is the rate of dissipation of the system. Therefore, if the initial state of the system is a Fock state of only one particle, the occupation probability of the particle decays down exponentially with time as

$$P_S(t) = \exp(-\gamma t) \tag{3}$$

NUMERICAL MODEL

Here, we transform the S/B coupling Hamiltonian to a semi-infinite chain model, using a unitary transformation of the operators of the bath: $d_n = \sum_{k=-N}^{N} U_n(k) b_k$ [16]. In a case where the spectral density is defined by Eq. (2), normalized shifted Hahn polynomial is a the natural choice as the unitary operator: $U_n^k = \frac{1}{\rho_n} Q_n[(k+N)/2, N]$, where $Q_n(k, N)$ is the Hahn polynomial, and $\rho_n = (-1)^n (N!) \sqrt{\frac{(2n+1)}{(N+n+1)!(N-n)!}}$ is the normalization coefficient. One can check that the

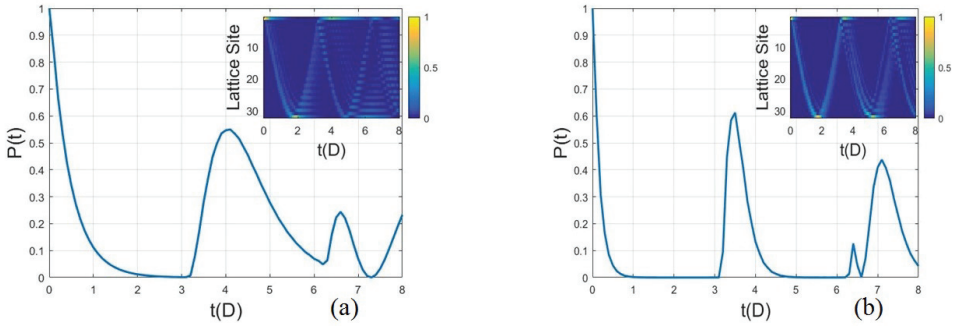

FIGURE 2. Occumation probability in system determined numerically for different rates of dissipation (a)$c_0 = 0.6D^{-1}$ and (b)$c_0 = 1D^{-1}$. Total number of modes of the bath $N = 30$. In the inset the image plot is given for the population on the sites which shows how the particle reflects back from the boundary.

new modes of the bath satisfy bosonic commutation relation $[d_n, d_m^\dagger] = \delta_{mn}$. Essentially, the transformed Hamiltonian becomes

$$\tilde{H} = \eta' \left(a^\dagger d_0 + a d_0^\dagger\right) + \sum_{n=0}^{N-1} \eta_n (d_n^\dagger d_{n+1} + d_{n+1}^\dagger d_n) \tag{4}$$

The diagrammatic representation of this transformation is shown in Fig. 1. Using the recurrence relation of Hahn polynomial [16, 19], the coefficients are determined as $\eta' = c_0\sqrt{2N}$ and $\eta_n = \frac{(n+1)}{D}\sqrt{\frac{(N-n)(N+n+2)}{(2n+1)(2n+3)}}$. The mapping is useful for the simulation of the time dynamics of OQS using DMRG method. Recently, similar mapping was introduced in Ref. [16] aiming to be applied on spin-boson models [20] and biomolecular systems [21]. However, instead of using DMRG, we use the Hamiltonian for a system where one particle of boson is located in entire chain.

FREE DISSIPATIVE SYSTEM

In a situation where only one particle located in the entire system and environment, which is initially localized in system, leaving the bath completely empty, the state of the corresponding 1-D chain is represented by $|S\rangle = [1\,0\,0\,0\,.....]^T$. Essentially, the corresponding matrix representation of the chain Hamiltonian gives

$$\tilde{H} = \begin{bmatrix} 0 & \eta' & & & & & 0 \\ \eta' & 0 & \eta_0 & & & & \\ & \eta_0 & 0 & \eta_1 & & & \\ & & \eta_1 & . & & & \\ & & & & . & & \\ & & & & & . & \eta_{N-1} \\ 0 & & & & & \eta_{N-1} & 0 \end{bmatrix} \tag{5}$$

After time t, the occupation probability of the particle in the system is determined from the time evolved state $|S_t\rangle = e^{-i\tilde{H}t}|S\rangle$ as $P_S(t) = |\langle S|S_t\rangle|^2$. We determine the time evolved state numerically, and plot the dissipative nature of the system population in Fig. 2, where we observe that the system population increases again after a certain time, which comes from the fact that the particle reflects back from the end of the chain, which is visible from the population plot of the entire chain shown in the inset of Fig. 2. The recurrence of the particle is dependent on the DOS, which is explained explicitly in appendix.

Comparing to the Eq. (3), we estimate the rate of dissipation from the numerically determined population dynamics of the system as

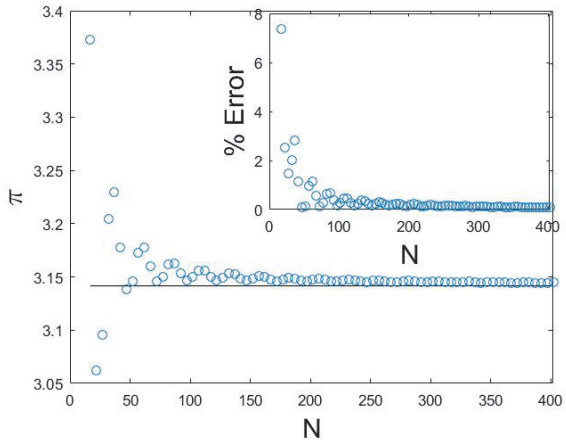

FIGURE 3. Plot of the value of π determined numerically, for incresing size of matrix. The black line corresponds to the actual value. In the inset, % error is calculated for incresing size of matrix.

$$\gamma = -\frac{\delta \ln(P_S(t))}{\delta t}|_{t<\text{recurrence time}} \tag{6}$$

In the next step, we fix $D = 1, c_0 = 1$ and $t = 1$ (which satisfies the condition $t <$ recurrence time), in order to get the simplest formula of π in terms of the matrix operational form. It is to be noted that Eq. (3) is obtained by considering a large cutoff frequency which is ideally infinite. Therefore, the accuracy of the value of π determined by this new formula, is anticipated when we increase the size of the matrix, which indicates consistency between numerical modeling and analytical formulation of open quantum system. Fig. 3 presents a comparison between actual and numerically determined value of π, which shows how the numerically determined value gets closer to actual one when we increase the size of matrix.

Remark: Note that the unitary transformation of S/B coupling Hamiltonian is done using Hahn polynomial which is given by $Q_n(k; N) = {}_3F_2(-n, -k, n+1; 1, -N+1; 1)$, where ${}_3F_2$ is generalized hyper-geometric function which is constructed by Gamma function [19]. Therefore, the value of π has not been used anywhere in the process of transformation of Hamiltonian to 1-D chain. On the other side, in the analytically determined dynamics of open quantum system, the quantity π appears in the rate of dissipation from the Fourier transformation of delta function.

CONCLUSION

We present a model that represents the transformation of Hamiltonian of an OQS coupled linearly to a discrete set of modes of bosonic reservoir, to a Hamiltonian of a one-dimensional chain having nearest-neighbour interactions. Using the model, we study free dissipation of a particle, located initially in the system, to a zero temperature empty bath. We observe that the finite length of the chain causes recurrence of particle from the end. The mapping seems promising to investigate the dynamics of OQS through the numerical simulation of many body systems. We also determine a formula for π in terms of matrix operations through this method. As anticipated from the fact that system bath coupling model considers a large cutoff frequency, the accuracy increases as the size of the matrix increases. Such kind of formulation indicates the robustness of the establishment of quantum physics and its connection to the fundamental mathematics.

ACKNOWLEDGMENTS

I would like to thank Subrata Chakraborty for his suggestion and comments while preparing the manuscript. This work was supported by the Academy of Finland under contract no. 275245.

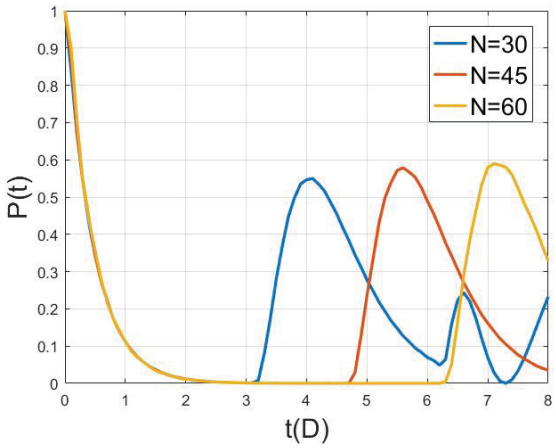

FIGURE 4. Plot of time evolution of a free dissipative system for the variation of DOS ($1D, 3/2D$ and $2D$), which is obtained by fixing the cutoff frequency ($30D^{-1}$) and changing number of lattice sites. $\gamma = 2.2619D^{-1}$ (the actual value of π has been used here).

Appendix

The recurrence time of the particle is dependent on the group velocity in the lattice. The group velocity is defined by $v_g = \frac{\delta\omega_k}{\delta k_N}$, where k_N is the wavenumber determined by the number of lattice sites ($k_N \propto N$), and ω_k is the frequency. The higher group velocity causes the phonon traveling faster in lattice. However, the group velocity is inversely proportional to the density of states ($v_g \propto D^{-1}$), and therefore, the recurrence time increases linearly when the DOS increases. In the Fig. 4, we increased the DOS by increasing the number of sites keeping the cutoff frequency fixed. The increment of DOS forces to take more number of lattice into account, and therefore, which causes an increment in the recurrence time.

REFERENCES

[1] H. J. Kimble, Nature **453**, 1023 EP –Jun (2008).

[2] D. Felinto, C. W. Chou, J. Laurat, E. W. Schomburg, H. de Riedmatten, and H. J. Kimble, Nature Physics **2**, 844–848 (2006).

[3] J. L. O'Brien, A. Furusawa, and J. Vuckovic, Nature Photonics **3**, 687 EP –Dec (2009), review Article.

[4] C. Ospelkaus, U. Warring, Y. Colombe, K. R. Brown, J. M. Amini, D. Leibfried, and D. J. Wineland, Nature **476**, 181 EP –Aug (2011).

[5] J. T. Barreiro, M. Müller, P. Schindler, D. Nigg, T. Monz, M. Chwalla, M. Hennrich, C. F. Roos, P. Zoller, and R. Blatt, Nature **470**, 486 EP –Feb (2011), article.

[6] J. Q. You and F. Nori, Nature **474**, 589 EP –Jun (2011), review Article.

[7] A. A. Clerk, M. H. Devoret, S. M. Girvin, F. Marquardt, and R. J. Schoelkopf, Rev. Mod. Phys. **82**, 1155–1208Apr (2010).

[8] B. P. Abbott, et. al., Phys. Rev. Lett. **116**, p. 061102Feb (2016).

[9] C. W. Gardiner and M. J. Collett, Phys. Rev. A **31**, 3761–3774Jun (1985).

[10] A. J. Leggett, S. Chakravarty, A. T. Dorsey, M. P. A. Fisher, A. Garg, and W. Zwerger, Rev. Mod. Phys. **59**, 1–85Jan (1987).

[11] H. Spohn, Communications in Mathematical Physics **123**, 277–304Jun (1989).

[12] S. K. Kehrein and A. Mielke, Physics Letters A **219**, 313 – 318 (1996).

[13] R. Bulla, H.-J. Lee, N.-H. Tong, and M. Vojta, Phys. Rev. B **71**, p. 045122Jan (2005).

[14] P. D. Drummond and D. F. Walls, Journal of Physics A: Mathematical and General **13**, p. 725 (1980).

[15] J. Manninen, S. Agasti, and F. Massel, Phys. Rev. A **96**, p. 063830Dec (2017).

[16] A. W. Chin, A. Rivas, S. F. Huelga, and M. B. Plenio, Journal of Mathematical Physics **51**, p. 092109 (2010), https://doi.org/10.1063/1.3490188 .

[17] G. Vidal, Phys. Rev. Lett. **91**, p. 147902Oct (2003).
[18] G. Stefanucci and R. van Leeuwen, *Many-Body Theory of Quantum Systems* (Cambridge University Press, 2014).
[19] R. Koekoek and R. F. Swarttouw, The askey-scheme of hypergeometric orthogonal polynomials and its q-analogue, 1998.
[20] A. W. Chin, J. Prior, S. F. Huelga, and M. B. Plenio, Phys. Rev. Lett. **107**, p. 160601Oct (2011).
[21] S. Huelga and M. Plenio, Procedia Chemistry **3**, 248 – 257 (2011), 22nd Solvay Conference on Chemistry.